
STRONGLY INTERACTING
LOW-DIMENSIONAL RYDBERG
LATTICE GASES IN AND OUT OF
EQUILIBRIUM

BY
SIYUAN JI, MSci.

Thesis submitted to the University of Nottingham
for the degree of Doctor of Philosophy

February 2015

Abstract

Recent achievements in ultra-cold experiments have made quantum simulation of interacting many-body systems possible in a well controllable environment. Of many candidates as quantum simulators, Rydberg atoms have been extensively utilised due to its exaggerated and fascinating atomic properties. Example includes high susceptibility to electric fields and relatively long life time in comparison to atoms in low-lying states. The tunable interaction between Rydberg atoms have made them even more versatile in simulating quantum many-body systems, e.g. interacting spin-1/2 particles. We will start the thesis by reviewing these properties of Rydberg atoms and explain how they lead to the Rydberg lattice gases that of interest.

Following the review of the essential knowledge of Rydberg atoms, we first study the ground states of interacting Rydberg lattice gases in both one-dimension and two-dimensions. The many-body system we are interested in is initially prepared in a Mott-insulator state, with each lattice site containing one atom that is laser coupled to its highly excited Rydberg state. The extremely huge van der Waals interactions between Rydberg atoms at close distance leads to an interesting Rydberg blockade effect. As we shall show, these strong interactions lead to rich phases and critical behaviours in the ground states of the many-body Hamiltonians that describes the systems. The aim of the first three chapters is to analyse these ground states in detail.

Having investigated the static properties, we then move on to study the dynamical behaviour of a class of generic spin models which can in principal be realised by Rydberg lattice gases with tunable blockade radius. By deriving an effective master equation, and comparing it to the exact calculation, we will demonstrate how different pure initial states eventually evolve to the same equilibrium state and analysed in detail the time evolution and the steady state.

List of Publications

Some of the results present in this thesis are also published in the following manuscripts:

Chapter 3:

1. Siyuan Ji, Viraj Sanghai, Cenap Ates, and Igor Lesanovsky, *Inhomogeneities and impurities in a dense one-dimensional Rydberg lattice gas*, Phys. Rev. A **89**, 021404(R) (2014).

Chapter 4:

2. Siyuan Ji, Cenap Ates, and Igor Lesanovsky, , *Two-dimensional Rydberg gases and the quantum hard-Squares model*, Phys. Rev. Lett. **107**, 060406 (2011).

Chapter 5:

3. Siyuan Ji, Cenap Ates, Juan P. Garrahan and Igor Lesanovsky, *Equilibration of quantum hard rods in one-dimension*, J. Stat. Mech.: Theory Expt. P02005, (2013).

Acknowledgements

Of all the people that I am grateful, I want to firstly express my deepest gratitude to my supervisor, Prof. Igor Lesanovsky. Igor first introduced me to ultra-cold atoms and many-body physics right before my master degree. Since then, my interest in these areas of physics had been greatly enlarged which eventually led to this PhD degree. As my mentor, his wisdom and passion has profoundly affected me during the past years. In addition, during my hardest days, he has shown understandings that I would never expect. Thank you very much.

I owe a very important debt to Dr. Cenap Ates, who has now unfortunately left science. Dr. Ates has been keen in helping me to develop various skills in achieving not only a successful postgraduate degree, but also essential abilities in continuing my career in science. His patience and enthusiasm have supported me in many difficult days during my PhD study. I would also like to thank Dr. Beatriz Olmos who has been always encouraging and providing helpful feedbacks on my works; Dr. Weibin Li, who shares the same cultural background with me and made the office even more friendly; Dr. Sam Genway, who gave an introductory lecture on ETH to me and spend much time on proofreading my works; Prof. Juan Garrahan and Prof. Peter Krüger for being my annual report advisors and providing helpful feedbacks on my works; and Dr. Lucia Hackermüller who gave me the chance to co-organizing a postgraduate student conference.

My appreciation also goes to PhD students including Matthew Jones, Sonali Warriar, and Asaf Paris-Mandoki. I really had an enjoyable time together with you fellows in organising the student conference, QuaCS. Thanks to James Hickey and Benjamin Everest who have made my thesis writing up less difficult by creating a lot of inspiring chats in the office. Thanks to Viraj Sanghai, an undergraduate student who I have collaborated with during his summer research with Igor. He had contributed significantly to Chapter 3 of my thesis. And thanks to Jennifer Gaskell who I had some exchanges with on the analytical calculations made in Chapter 5.

I now want to offer my special thanks to people who had been always supportive in my life outside of studying. Firstly, thanks to my girlfriend, Jingjing, who though is not interested in science, but has been accompanied me all the time and brought so much joy to me. And last but not least, of course, many thanks to my parents. I have been a lucky person who have received all kinds of supports from them. Their love is most precious to me.

Contents

Abstract	2
List of Publications	3
Acknowledgements	4
1 Introduction	18
2 The Rydberg Lattice Gases	22
2.1 Rydberg Atoms	22
2.1.1 Hydrogen Atom	23
2.1.2 Alkali-metal Atoms	26
2.1.3 Properties of Rydberg Atoms	28
2.1.4 Photoexcitation of a Rydberg Atom	31
2.1.5 Interacting Rydberg Atoms	36
2.2 Rydberg Lattice Gases	41
2.2.1 Strategy for Finding the Approximate Ground State	43
2.2.2 Hamiltonian of the Rokhsar-Kivelson Type	44
2.3 A Homogeneous One-dimensional Rydberg Lattice Gas	46
2.3.1 Brief Review of Statistical Physics	49
2.3.2 Partition Function of the Hard-dimers Lattice Gas	50
2.3.3 Application of the Partition Function	52
2.3.4 Exact Numerical Calculation of $ G\rangle$ in One-dimension	54
2.4 Conclusion	56
3 The Ground State of Inhomogeneous One-dimensional Rydberg Lattice Gas	59
3.1 Introduction	59
3.2 The Inhomogeneous Rydberg Lattice Gases in One-dimension	61
3.2.1 The System	61
3.2.2 The Hamiltonian and the Approximate Ground State	62
3.3 An Impurity in the Lattice	64

3.3.1	Identification of a Critical Point	66
3.3.2	Long Range Tails of the van der Waals Interaction	69
3.3.3	Effective Hamiltonian near the Critical Point	71
3.4	Conclusion and Outlook	80
4	Two Dimensional Rydberg Lattice Gases	82
4.1	Introduction	82
4.2	The System	85
4.3	The Quantum Hard-squares Model	86
4.4	The Analytical Ground State of $H_{R-K_{\text{sqr}}}$	87
4.4.1	Partition Function of Hard-Squares	88
4.4.2	Classical Observables	90
4.4.3	Density-density Correlation	92
4.5	Connection to the Rydberg Lattice Gas	95
4.6	The Numerical Ground States of $H_{R_{\text{Yd}}_{\text{sqr}}}$ and $H_{R-K_{\text{sqr}}}$	97
4.7	$ \xi\rangle_{\text{sqr}}$ as a Variational Ansatz	101
4.8	Phase Diagram of the Rydberg Lattice Gas in Square Lattice	105
4.9	Quarter-filling Variational State	107
4.10	Conclusion and Outlook	110
5	Quantum Dynamics of the Quantum Hard-rods Model	112
5.1	Introduction	112
5.2	The System	115
5.3	Configuration Network	117
5.3.1	Structure	117
5.3.2	Properties of the Configuration Network	117
5.4	Derivation of the master Equation	120
5.4.1	Configuration States and Probability Distribution	120
5.5	Time Evolution and the Steady State of the master Equation	125
5.6	Exact Numerical Quantum Evolution	127
5.6.1	Quasi-momentum Basis States	127
5.6.2	Comparison to the solutions of the master Equation	130
5.6.3	Eigenstate Thermalisation Hypothesis	133
5.7	Conclusion and Outlook	136
	Appendices	139
	A Interaction Picture and the Effective Hamiltonian	139
	B Expectation Values of the Observables in the Limiting Cases	142

C	Configuration Energy of the Quarter Filling State	145
D	Calculation of Configuration Network Properties	147
	D.1 The Combinatorial Method	147
	D.2 Transfer Matrix Method	148
E	Derivation of a master Equation from a General Hamiltonian	151
	E.1 Unitary Transformation and the Interaction Picture	151
	E.2 The von Neumann Equation in the Interaction Picture	153
	E.3 An Exact master Equation	154
F	Partition Function of a Hard-trimer Gas	155
	Bibliography	157

List of Figures

2.1	Energy levels of a Sodium (Na) atom (left) and a Hydrogen (H) atom (rightmost). The energies of the electronic states are taken from Ref. [55] and converted into electron Volts. The value of the principal quantum number ν is written next to the respective energy levels. The angular momentum quantum number l to the respective energy level is indicated in the horizontal-axis. The ionisation threshold ($\nu \rightarrow \infty$) is illustrated as a dashed line toward the top of the diagram.	25
2.2	Semi-classical (elliptical) orbit followed by the valence electron of the atom with low angular momentum. The ionic core is located at one of the focal points of the ellipse. (a) The electron orbit in the absence of the quantum defect. The electron sees the ion core as an entity that has a net charge of +1; (b) The electron orbit in the presence of the quantum defect. The electron, when it travels near to the inner turning point, can penetrate through the ion core. . . .	27
2.3	a) A three-level system, with the three states denoted by $ g\rangle$, $ m\rangle$, and $ R\rangle$. The two states, $ g\rangle$ and $ m\rangle$ have a transition frequency of ω_{gm} and are coupled by a laser with frequency of ω_a and detuning δ_a ; and the two states, $ m\rangle$ and $ R\rangle$ have a transition frequency of ω_{mR} and are coupled by a laser with frequency of ω_b and detuning δ_b . The two transition lasers are parameterised by the Rabi-frequency Ω_a and Ω_b respectively. b) By carrying out a rotating wave approximation and adiabatically eliminate the intermediate state $ m\rangle$, it is possible to reduce the system to an effective two-level system coupled by an effective laser with Rabi-frequency, Ω and detuning Δ (see text for more details).	32
2.4	A schematic diagram of two indistinguishable Rydberg atoms showing the displacement vectors used in deriving the dipole-dipole interaction between the two atoms. The larger red dot represents the a singly charged ion core and the smaller blue dot represents the highly excited electron.	36

2.5	(a) The relevant energy levels of the two interacting Rydberg atoms with the energy of the $ \nu s\rangle$ -state set to zero. (b) The same system represented in the pair-state basis that is introduced in the main text for the derivation of the van der Waals interaction.	38
2.6	Excitation energy $E(r)$ of two atoms as a function of interatomic distance, r . The energy required to excite either atom to its Rydberg state is given by the energy different between the two levels, denoted as $\hbar\omega$ in SI units. However, to simultaneously excite both of the atoms to their Rydberg state requires an extra r -dependent energy due to the van der Waals interaction between the two atoms in the Rydberg state. The blue region represents the laser linewidth which is determined by the Rabi-frequency Ω for strong laser driving. The blockade happens at a distance where the energy required for simultaneous excitation is above the blue region. The analytical expression of blockade radius is given by $R_b \approx (C_6/\Omega)^{1/6}$	40
2.7	A Rydberg ring to visualise a periodic one-dimensional lattice. Each lattice is occupied by one atom and the atomic spacing is given by a . In the system considered, we set the Rydberg blockade radius such that the Rydberg atom exactly blocks excitation of its nearest neighbours, i.e. $R_b \gtrsim a$. Here, a Rydberg atom located on the k -th lattice site prevents possible excitations in its two nearest neighbours on $k + 1$ -th and $k - 1$ -th lattice sites.	41
2.8	The ξ -manifold as introduced in Eq. (2.42) is plotted in the ω, δ -plane defined in the content. The red dot marks the location at where $\xi = 1$. As ξ approaches infinity, the curve lies exactly on the δ -axis at $\delta = -3$	47
2.9	A graphical illustration of the ground state of $H_{R-K}(\xi)$, $ \xi\rangle$. Here, each grey dot represents a lattice site occupied by a ground state atom (down-spin) and a blue dot represents a lattice site occupied by a Rydberg atom (up-spin). Each configuration is associated with a probability amplitude given by $(-\xi)$	49
2.10	Fractional Rydberg density as a function of ξ in the ξ -manifold for a lattice size $L = 12$. The analytical result obtained in Eq. (2.65) is plotted black, and the numerical result obtained by diagonalising H_{Ryd} is depicted in dash red.	55

- 3.1 Schematics of the one-dimensional lattice with spacing, a . Each site contains a single atom whose ground state $|\downarrow\rangle_k$ is coupled to a Rydberg νs -state $|\uparrow\rangle_k$ via a laser parameterised by a site-dependent Rabi-frequency Ω_k and detuning Δ_k . (a) Rydberg lattice gas with a single impurity present on the j -th site. The impurity atom is irradiated by a laser (orange) of different parameters ($\Omega_{\text{imp}}, \Delta_{\text{imp}}$) compare to the rest of the system (blue, and parameterised by $\Omega_{\text{sys}}, \Delta_{\text{sys}}$). (b) Alternating lasers are introduced to investigate the breaking of the sublattice symmetry. On odd (even) lattice sites, a laser parameterised by Ω_{odd} (Ω_{even}) and Δ_{odd} (Δ_{even}) is used to excite atoms to Rydberg states. 61
- 3.2 Pictorial representation of the ground state given by Eq. (3.4). The state $|\{\xi_k\}\rangle$ is a superposition of all possible arrangement of Rydberg atoms with the nearest-neighbour blockade constraint. Each arrangement has a weight which is determined by the number of Rydberg atoms and the position of them. The normalisation constant is given by $Z_{\{\xi_k\}}$ which can be determined by transfer matrix method in principle. 63
- 3.3 Rydberg density for a lattice with 41 sites and an impurity placed at site $j = 21$. The fugacity parameter of the impurity is given by $\xi_{\text{imp}} = 5$ (black dash) and the fugacity parameter of the remaining spins ξ_{sys} is varied from 0 to 10. With increasing ξ_{sys} the system's correlation length l_c (plotted at the cyan diagonal lines) increases. The many-body state of the system atoms becomes more strongly correlated and the presence of the impurity affects the state of more and more distant atoms. Note that for $\xi_{\text{sys}} = \xi_{\text{imp}}$ the density is homogeneous in space due to the translational symmetry of the system. 65
- 3.4 We plot the analytical result obtained from Eq. (3.7) in black and compare it to the numerically obtained $\langle n \rangle_{\text{odd}}$ from diagonalising Hamiltonian (2.40) within the ξ_k -manifold given in Eq. (2.42), with $\xi_s = 5 < L$ in (a) and with $\xi_s = 20 > L$ in (b). In (a), we see an excellent agreement and a clear convergence of the numerical results toward the analytical one with increasing lattice size. However, in (b), the results disagree due to the fact that the correlation length given by $\eta_c = \xi_s/2$ is beyond the lattice size and a large ξ_s and relatively small L leads to non-negligible contribution from the 2nd eigenvalues of the transfer matrix [c.f. Sec. 2.3.2] for more details) 67

3.5	(a) Mean density of the odd sublattice as a function of ξ_d . Here, with $\xi_s = 5$, we have plotted the analytical result given in Eq. (3.7) in black and the numerical result obtained from diagonalising Hamiltonian (3.1) in red (with circles) with $L = 14$. The latter shows a significantly steeper switching of the sublattice populations at $\xi_d = 0$. (b) Susceptibility $\chi_{\text{odd}}(\xi_s = 5, \xi_d)$ for different lattice sizes: $L = 10$ (red circles), $L = 12$ (blue triangles), and $L = 14$ (black squares). The data suggests a divergence of the susceptibility at $\xi_d = 0$ in the limit of large lattice sizes L	68
3.6	The scaling behaviour of the variance at ξ_d close to critical value $\xi_d = 0$. The dashed line indicates the boundary of the scaling region for the $L = 18$ curve. From the left to the right, we have corresponding lattice size $L = 18, 16, 14, 12$. The gradient seems to not depend on the lattice size.	69
3.7	The plot shows the sublattice density of the odd sites (colour code) for varying V_3 and ξ_d . As one can see, the sharp transition does not emerge immediately when V_3 is turned on, but actually, slowly emerges. The red dash indicates the possible critical value of V_3 where the smooth transition becomes sharp.	71
3.8	Stylized phase diagram of the homogeneous Rydberg lattice gas Hamiltonian (3.1) with $\Omega_k = \Omega$ and $\Delta_k = \Delta$. The curve parameterised by Eqs. (2.42) approaches in the limit $\xi \rightarrow \infty$ the critical point $\{\Omega = 0, \Delta = -3V_2\}$ which is located between a classical crystalline phase with Rydberg density $1/2$ and one with density $1/3$. Inset: In our analysis we approach the critical point $\{\xi_d = 0, \xi_s^{-1} = 0, V_3 = 0\}$ from different directions: One experiences a 2D-Ising type transition by approaching the critical point from finite ξ_d , while one experiences a AFM-PM transition by approaching from finite V_3	72
3.9	a) Equivalence between the spin representation and the fictitious particle-hole representation introduced in the text. b) The pictorial description of how configurations in the particle-hole representation are related in terms of the effective hopping, J , chemical potential, μ_{eff} and the interaction between adjacent particles, U_{eff} , i.e. the three bare parameters in the effective Hamiltonian, H_{xxz} near the previously obtained critical point.	73

4.1	Strongly interacting Rydberg atoms in a square lattice with lattice spacing, a . Atom are labeled by two indices, k, m . Each atom, like in the one-dimensional system, is approximated by a two level atom with a ground state and a Rydberg state which are coupled by a site-independent Rabi-frequency, Ω , and detuning, Δ . In the strongly interacting regime, where $V \gg \Omega$, a Rydberg atom prevents the exaction of its four adjacent atoms to their Rydberg states. In the quantum hard-squares model that we introduce in Sec. 4.3, each Rydberg atom is effectively treated as a hard-square. Long range tails that are beyond next-nearest neighbours in the van der Waals interaction will be neglected in the calculation. This is indicated by the blue region around each Rydberg atom.	85
4.2	Comparison between quantities obtained from $ \xi\rangle_{\text{num}}$ of $H_{\text{R-Ksq}}$ (in red boxes) and $ \xi\rangle$ through the partition function of hard-squares (in blue lines): (a) Density of Rydberg atom, and (b) Variance of the density of Rydberg atoms of a 4-by-4 square lattice. The red squares lie exactly on top of the blue lines which indicate that $ \xi\rangle_{\text{num}}$ is exactly equivalent to $ \xi\rangle$	90
4.3	Variance of the density of Rydberg atoms obtained with lattice size N-by-N with N being 4 to 16 in step of 2. The black vertical line demonstrates the critical fugacity at $N \rightarrow \infty$ as predicted in the classical Baxter's hard-square. The plots demonstrate the ability of the transfer matrix to solve the partition function of hard-squares for large lattice sizes. Moreover, the increasing peak value of the variance with increasing lattice size suggests a possible divergence at the thermodynamic limit where $N \rightarrow \infty$. Thus, the peak value of each curve indicates the critical fugacity for the corresponding lattice size.	91

4.4	<p>a) Expectation values of density-density correlation for adjacent hard-squares. We compare the results obtained directly from the quantum hard-squares model described by $H_{R-K_{\text{sqr}}}$ (red squares) with that from the partition function of the classical hard-squares (blue line). An exact overlap further proves the validity of the classical hard-squares model; b) Expectation values of density-density correlation for hard-squares that are increasingly further apart within a row. The separation of two hard-squares is presented by the number in the horizontal axis, e.g. 2 represents two hard-squares that are separated by two lattice sites. The vertical axes indicates an increasing fugacity to show how these density-density correlation varies with the fugacity. The colour code works in the following way: white for an expectation value of 0 (non-correlated) and black for an expectation value of 1 (fully correlated). Long range order in the correlation pattern starts to emerge after ξ reaches critical fugacity (red line).</p>	93
4.5	<p>All possible configurations of single/many-body interactions derived from the added H_ξ. All solid dots represent atoms in the Rydberg state where the green dot shows the reference site, $\{k, m\}$. The ξ-dependent weight is given on the side of the corresponding configuration. Identical configurations due to translational invariance of the lattice are included into the weight coefficients. Notice that there are configurations that include nearest neighbour excitations which are forbidden in the physical subspace.</p>	98
4.6	<p>Overlap between the true ground state $G\rangle_{\text{sqr}}$ and the approximate ground state $\xi\rangle_{\text{num}}$ on the ξ-manifold for a 4-by-4 square lattice. The overlap never drops below 0.5 for all ξ. The curve indicates that the two ground states are very close to each other and even almost identical at small and large fugacity.</p>	98
4.7	<p>Comparison of the quantities obtained from $\xi\rangle_{\text{num}}$ and $G\rangle_{\text{sqr}}$ of a 4-by-4 square lattice: results obtained from the ground state, $G\rangle_{\text{sqr}}$ of Rydberg Hamiltonian $H_{R_{\text{yd}}_{\text{sqr}}}$ are plotted in black solid and results obtained from the ground state, $\xi\rangle_{\text{num}}$ of $H_{R-K_{\text{sqr}}}$ are plotted in dashed red. (a) Density of Rydberg atoms; (b) Ground state energy per atom (red solid shows result after applying perturbation theory to the red dash); (c) Density-density correlation between Rydberg atoms that are next nearest neighbours; (d) Variance of the quantity in (a).</p>	99

- 4.8 Expectation values of the observables appearing in the Hamiltonian (4.22) and the ground state energy: (a) Expectation value of $\sigma_{k,m}^x$ (b) Density of Rydberg atoms; (c) Density-density correlation of Rydberg atoms which are next nearest neighbours; (d) Ground state energy. Results for lattice size from 4-by-4 to 14-by-14 are plotted in different colours with index given on the right hand side of the energy plots. In the limiting cases, it is observed that $\langle \sigma_{k,m}^x \rangle_{\xi \rightarrow 0} = 0$, $\langle \sigma_{k,m}^x \rangle_{\xi \rightarrow \infty} = 0$; $\langle n_{k,m} \rangle_{\xi \rightarrow 0} = 0$, $\langle n_{k,m} \rangle_{\xi \rightarrow \infty} = 0.5$; $\langle n_{k,m} n_{k+1,m+1} \rangle_{\xi \rightarrow 0} = 0$, $\langle n_{k,m} n_{k+1,m+1} \rangle_{\xi \rightarrow \infty} = 0.5$. In addition, as shown in the insets, the enlarged parts of the curves appear to be converging as lattice size increase. 103
- 4.9 Comparing the quantities obtained from the optimised variational method to the same quantities obtained numerically from a 6-by-6 lattice on the ξ -manifold [32]. (a) Energy (main plot) and density per site (inset): exact ground state energy/density of $H_{\text{Ryd}_{\text{sqr}}}$ is plotted in red; energy/density obtained from $|\xi\rangle_{\text{sqr}}$ in the same manifold is plotted in black; energy/density obtained with the optimisation method to minimise $\langle \eta | H_{\text{Ryd}_{\text{sqr}}}(\xi) | \eta \rangle$ is plotted in black squares. (b) Red curve: overlap between $|\xi\rangle_{\text{sqr}}$ and $|G\rangle_{\text{sqr}}$; Black squares: overlap between $|\eta\rangle$ and $|G\rangle_{\text{sqr}}$; Inset: the optimising parameter η as a function of ξ 103
- 4.10 Phase diagram (in terms of density of Rydberg atoms) generated using the optimisation method with the variational state as a function of $\omega = \Omega/V$ and $\delta = \Delta/V$ for a 16-by-16 square lattice. The red dash indicates results on the ξ -manifold which is calculated in Fig. 4.9; The black line draws the phase transition line and the yellow line draws the transition line where only nearest neighbour interactions are included. The insets illustrate the energy functional at the corresponding points A, B and C, where one sees a shift in the global minimum as one crosses the transition line. 104

- 4.11 The variational energy $\langle H_{\text{Ryd}_{\text{sqr}}} \rangle_{\eta}$ as function of η . At fixed ω values where in a) $\omega \approx \omega_2$, and in b) $\omega < \omega_2$. The green line depicts the critical fugacity of the Baxter’s hard-squares model. The black curve is the connected global minimum of each energy functional. The red curve indicates the approximate position where the first order transition occurs. As one can see, the only blue curves in graph (a) that have double maxima are the ones that are near the transition point. The double minima slowly merges into a single minima as one goes away from the critical point. This feature is seen more clearly in (b) where the double minima feature is completely gone at all values of δ for $\omega < \omega_2$ 106
- 4.12 Phase diagram in the same fashion as Fig. 4.10, but with a quarter filling region determined by introducing a quarter filling state $|\phi\rangle$. Within the quarter filling lobe, the configuration energy $\langle \phi | H_{\text{Ryd}_{\text{sqr}}} | \phi \rangle_{1/4}$ is lower than the minimised variational energy $\langle \eta | H_{\text{Ryd}_{\text{sqr}}} | \eta \rangle$ for the same parameters, Ω/V and Δ/V . The circle indicates where the discontinues phase transition ends, and the dashed line illustrates the numerically obtained “extended phase boundary” described in the content. 107
- 5.1 (a) Graphical representation of possible spin configuration for blockade length $\lambda = 1$ and $\lambda = 2$. Spin configurations can be also illustrated in the pictures of hard-rods where each up-spin is effectively mapped to a hard-rod occupying $\lambda + 1$ lattice sites. (b) An example of the configuration network in detail with $L = 8$ and $\lambda = 1$. Each node represents a specific classical spin configurations denoted by $|n\mathcal{C}_n\rangle$ with n being the number of up-spins in the configuration and \mathcal{C}_n uniquely labels the spin configuration. Two examples $|3\ 1\rangle$ and $|4\ 2\rangle$ are provided to show how the labelling works. Edge between adjacent nodes indicates that the nodes are directly coupled by H_{Ω} . Each column can be seen as the graphical interpretation of the expectation value of the observable, i.e. $p_n = \langle P_n \rangle$, defined in the text in Sec. 5.4. The non-zero matrix elements in the adjacency matrix \mathcal{M}^2 [see Sec. 5.4] identifies three types of transitions that describe a two-steps transition (two-spin flip operation): loop (green), reflection (orange) and transmission (red). 116

- 5.2 (a,b) Graphical illustration of the reflection processes. Two configurations can at most be connected by two reflection pathways (a). However, since rods must not overlap, the path containing an additional hard rod during the intermediate step is often forbidden (b). (c) For the numerical study we fix the physical system length l and the critical radius r_c . The parameter λ is varied by increasing the number of lattice sites. 118
- 5.3 The time evolution of the distribution functions $p_n(t)$ by solving the master equation with nearest neighbour blockade only, i.e. $\lambda = 1$. The system considered has a lattice length to blockade length ratio $l/r_c = 120$. p_n are drawn at the time intervals: $\Omega t = 0.02, 0.1, 0.2, 0.3, 0.4, 0.5, 0.6, 0.8$ and $\Omega t = 2$ (blue) from left to right, as shown in (a). The initial distribution function used is $p_0 = 1$ which is a delta function. The steady state distribution is explicitly demonstrated in (b) in blue and compared with the numerical results obtained directly from Eq. (5.17) (red circles). The two curves match perfectly. To investigate the dependence of the time-evolution on initial distributions, we start with distributions with different densities ranging from $\rho = 0$ ($p_0 = 1$) to $\rho = 0.5$ ($p_{60} = 1$). As seen, the steady state is independent of the chosen initial state. . 125
- 5.4 In (a), to see the dependence on the blockade length, we show the time-evolution of the distribution function $p_0 = 1$ with different blockade radii $\lambda = 1$ (blue), $\lambda = 9$ (green) and $\lambda = 59$ (red). The densities of the steady states are explicitly plotted in (b) to further demonstrate the increase of density of the steady state with increasing blockade length. Values of λ in the plot include 1 (blue), 2, 3, 5, 7, 9 (green), 19, 29, 39, and 59 (red). At particular blockade length where $\lambda = 1, 9$, and 59, distribution functions at equilibrium ($\Omega t = 2$) are plotted in blue, green and red respectively in (c). The Mandel Q-factor has been calculated for all steady state distributions and illustrated in (d) with x-axis being the natural log of λ . The Mandel Q-factor saturates to -1 at large blockade length. . . . 126
- 5.5 For $\lambda = 3$ and $l/r_c = 10$, the quantum evolution of the density of a randomly chosen spin configuration in $k = 0$ momentum subspace (red dash) and in complete momentum subspace (blue). The initial pin configuration has 3 up-spins and does not have translational symmetry (see text). 127

- 5.6 (a) Quantum evolution of microstates in complete momentum space and (b) the distribution functions of the steady states. In vertical direction, we increase the blockade radius where $\lambda = 1, 2, 3$ with a fixed $l/r_c = 10$. In all plots, the temporal evolutions described by the master equation and the distribution function of the steady states are plotted in black. For each blockade radius, we randomly chose 3 different initial states for the numerical simulation of the quantum evolution. Then the quantum evolution and the distribution functions of the resultant steady states are illustrated in red, green, and blue respectively for each of the initial states. 131
- 5.7 Long time quantum evolution of the hard rod density starting from a randomly chosen initial state with $n_0 = 3$ hard rods for $\lambda = 4$ and $l/r_c = 9$. The evolution predicted by the master equation is plotted in black. To highlight the shift, the time evolution from $\Omega t = 0.5$ to $\Omega t = 20$ is enlarged and shown in the left inset, and the evolution from $\Omega t = 80$ to $\Omega t = 100$ is enlarged and shown in the right inset. . 133
- 5.8 Histogram of the parameter \mathcal{D} , defined in Eq. (5.26), for the three parameter sets used in Fig. 5.6. The numbers in the parentheses show the dimension of the Hilbert space and the number of initial states used to create the histogram, respectively. For the bottom panel we also show the distribution of the number of hard rods contained in the initial states as an inset. The black dashed line with blue cross marks in the inset shows the microcanonical steady state distribution of the number of hard rods for comparison. . . . 134
- 5.9 Histogram of the overlap \mathcal{D}_{ETH} , defined in 5.29. The parameter sets are equivalent to those in 5.8. The histogram is constructed using all eigenstates for the respective parameter set. 135

Chapter 1

Introduction

One of the central problems in physics over the past few decades is to enhance our understandings of the quantum many-body problem. Many-body systems exhibit pronounced collective phenomena that manifest in quantum phase transitions, the formation of strongly correlated ground states as well as intricate dynamical behaviour.

In recent years, great attention has been placed on the experimental study of many-body effects in systems of ultra-cold atomic gases [1]. Atomic ensembles can be trapped in almost arbitrarily tailored potential landscapes and their inter-atomic interaction properties can be manipulated by the help of external fields. This high degree of experimental control has granted insights into a number of collective phenomena, ranging from the first realisation of a Bose-Einstein condensate (BEC) [2, 3, 4] and degenerate atomic Fermi gas [5] to the demonstration of the Mott-Insulator – superfluid quantum phase transition [6] and the Bardeen-Cooper-Schrieffer (BCS) – BEC crossover [7, 8, 9].

What makes the physics of many-body systems non-trivial is the fact that the individual microscopic components interact. The interactions imply a huge increase of complexity in comparison to a single-body problem. This becomes already evident in classical mechanics: Two-body interactions in a system consisting of three bodies already make a general solution intractable [10]. Analytical solutions can then only be found in special cases [11].

For quantum systems, in comparison to classical systems, the situation is quite similar, but further complications might arise which can be illustrated as follows. In a classical system one might encounter a situation where an initially strongly interacting arrangement of particles evolves into a configuration where particles are weakly interacting. Here, the motion of the individual component is approximately given by a free solution of Newton's equations of motion, which might be analytically tractable. In quantum mechanics, however, this might not be necessarily true as quantum correlations can persist even if particles are non-interacting.

Quantum features like this make many-body quantum systems intriguing and at the same time more difficult to understand in comparison to classical systems.

Theoretical studies of many-body quantum systems are often carried out by investigating the underlying Hamiltonian and the corresponding Schrödinger equation. Finding analytical solutions is often unfeasible. Yet, there are a few models for which analytical solutions exist. Examples of soluble models include but are not limited to, the one-dimensional spin-1/2 Heisenberg Model [12], the quantum XY-model [13], the Heisenberg-Ising model [13], the Majumdar-Ghosh model [14], and the Affleck-Kennedy-Lieb-Tasaki spin model [15]. In almost all other cases, approximate analytical or numerical methods have to be employed. These include perturbation theory, the use of variational principles, or mean-field theory all of which have contributed to our understandings of the quantum many-body problem.

A more straight forward approach to solve a quantum many-body problem is a direct numerical-diagonalisation of its Hamiltonian. However, as the dimension of the Hilbert space typically grows exponentially with increasing number of particles, the numerical calculation is restricted to relatively small system sizes. There are some numerical techniques allowing us to overcome this limitations. Examples include density matrix renormalisation group technique [16], density functional theory [17], and quantum Monte-Carlo methods [18]. Despite the array of techniques mentioned, simulating the dynamics of many-body systems numerically remains a formidable task.

Motivated by the eagerness to enhance our theoretical understanding of the many-body quantum problem, the goal of this thesis is to study a group of many-body quantum systems that relate to the current experimental effort in the domain of ultra-cold atomic physics.

The specific system we are considering features two central ingredients. The first one is constituted by ultra-cold atoms in highly excited states, so-called Rydberg atoms. These atoms possess a valence-electron which is excited to an electronic state with high principle quantum number [19]. In an ultra-cold atomic experiment, these atoms can be prepared by a laser that drives a transition between the electronic ground state and the desired highly excited electronic state [20, 21]. Rydberg atoms have fascinating properties and have been extensively studied both theoretically and experimentally. The properties that are crucial for the many-body physics explored in this thesis are their strong and tunable interactions which can easily bridge distances of a few micrometers as well their long life time in comparison to atoms being excited to low-lying electronic states.

The second central ingredient is an optical lattice. The basic principle for creating an optical lattice is to utilise the interference pattern of two counter-

propagating laser beams to create a periodic potential [22]. The periodic potentials then permit the trapping of ultra-cold atoms. Eventually a situation can be achieved in which there is a single atom occupying each lattice site.

In this thesis we explore the physics of Rydberg atoms trapped in such regular lattice geometries. In particular we are interested in the interplay between the strong interaction of Rydberg atoms and the laser excitation of Rydberg states. Both give rise to intricate statics and rich dynamical behaviours.

Since the first proposal of using Rydberg atoms for the implementation of quantum information protocols [23], the field of ultra-cold atomic physics with Rydberg atoms has been flourishing. For instance, the realisation of a quantum gate among two atoms was demonstrated experimentally in Ref. [24, 25]. The coherent properties of these strongly interacting Rydberg gases have been studied in a number of experiments such as Ref. [26, 27], and the Rydberg blockade mechanism has been observed in Ref. [28, 29]. On the theoretical side, it has been predicted that there exists rich quantum many-body phenomena in these Rydberg gases, such as quantum critical behaviours [30].

More recently, Rydberg lattice gases have become the focus of a number of recent theoretical and experimental investigations. The analytical treatment of a Rydberg lattice gas are discussed in Ref. [31] and since then, a vast number of theoretical studies on the ground state properties of Rydberg lattice gases have been performed. Examples include but are not limited to the numerical and approximate analytical studies of the ground states of Rydberg lattice gases in low-dimensions with and without inhomogeneities [32, 33, 34, 35, 36, 37], excited states of the one-dimensional Rydberg lattice gas [38, 39], and the correlation and entanglement properties of the lattice gases [40, 41]. On the experimental side, a number of experiments have been performed to realise Rydberg excitations in optical lattice [21, 42] which has paved the way for the possibility of realising the ground states of the Rydberg lattice gases.

The dynamical behaviour of the Rydberg lattice gases has also been of strong interest recently. Numerical and approximate analytical studies on the time-evolution of Rydberg lattice gases can be found in Ref. [43, 44]. A number of theoretical studies have shown that the excitation dynamics of Rydberg atoms in the optical lattice can lead to crystalline structures [45, 46, 47, 48, 49]. And it is only until recently that an ordered structure of Rydberg excitations in an optical lattice has been observed experimentally [50].

We start the thesis by giving a brief review on the properties of Rydberg atoms that are relevant to the Rydberg lattice gases. The Hamiltonians that describe the Rydberg lattice gases are derived. We proceed by reviewing the approximate analytical methods used in solving the one-dimensional homogeneous

Rydberg lattice gas [31] and demonstrate the agreement between the analytics and numerics obtained from direct diagonalisation of the Hamiltonian. In Chapter 3, for the one-dimensional system, we move on to investigate how ground states are effected by various inhomogeneities that are introduced through the local variation of the laser parameters. In particular, we study two situations: the system with a single impurity, and with staggered laser fields which alternate from site to site. In the latter case where the sublattice symmetry is essentially broken, we are able to identify a critical point and to study how critical properties are affected by the influence of long-range interactions [36]. In Chapter 4, we explore the ground state of the Rydberg lattice gas in a two-dimensional square lattice. By introducing a quantum version of Baxters hard-squares model, we are able to obtain an approximate analytical ground state that captures the exact ground state properties in a particular parameter regime [32, 51]. Further using this ground state as a variational ansatz, we determine an approximate phase diagram of the system in the whole parameter range. The system is found to undergo a first order phase transition from an ordered phase to a liquid phase. In Chapter 5, we move on to study the dynamical behaviours of the system. In brief, by introducing a hard-rod representation in which the effective dynamics of interacting Rydberg atoms can be described by coherent deposition and removal of the hard rods from a lattice, we derive an approximate master equation for the evolution of the number of hard rods on the lattice [52]. The equation captures an equilibrium steady state which strongly resembles a microcanonical ensemble of classical hard rods. With numerical comparison, the master equation is found to also capture the non-equilibrium evolution from the majority of initial states to the steady state. In summary, both of the static and dynamical properties of the strongly interacting Rydberg lattice gases in low-dimensions are investigated. The results obtained provide us insightful understandings on the properties of correlated ground states of many-body quantum systems and on how closed many-body quantum systems relax to equilibrium.

Chapter 2

The Rydberg Lattice Gases

2.1 Rydberg Atoms

Rydberg atoms are atoms having one valence electron excited to a state with very high principal quantum number ν^1 [19]. The binding energy of the valence electron is described by the famous equation known as the Rydberg formula,

$$E_e = -\frac{Z^2 Ry}{(\nu - \delta_l)^2}, \quad (2.1)$$

where δ_l is known as the quantum defect that depends on the angular momentum quantum number l and the choice of the element. The universal constant, Ry is known as the Rydberg constant which is given by $Ry = \frac{k_e^2 e^4 m_e}{2\hbar^2}$, where $k_e = \frac{1}{4\pi\epsilon_0}$ is the Coulomb's constant with ϵ_0 being the permittivity of free space, Z is the number of protons, e is the elementary charge, and m_e is the mass of an electron. The Rydberg formula is named after the atomic physicist, Johannes Robert Rydberg for his discovery of the pattern in the spectrum of various elements and the generalisation of this pattern into the empirical formula, the Rydberg formula [53]. Neglecting the effect of the quantum defect at the moment, one notices that the binding energy of a Rydberg atom would become very small due to the ν^{-2} scaling. The binding energy hence indicates that the valence electron is very loosely bound to the ion core, a property that is very distinct from atoms being excited to low-lying states. More interestingly, like the binding energy, many properties of Rydberg atoms, as shown later, can be described by a power-law in terms of ν . To understand these properties of Rydberg atoms and eventually utilise them to construct the system of interest, we will start by reviewing briefly the physics of a Hydrogen atom in the following section.

¹In common quantum mechanical text books, the notation used for the principal quantum number is often n , but to avoid confusion with later use of n as an operator, we use ν in this thesis to denote the principal quantum number instead.

Fundamental Constants	Symbol	Atomic Units	SI units (3 s.f.)
Electron mass	m_e	1	$9.11 \times 10^{-31} \text{kg}$
Elementary charge	e	1	$1.60 \times 10^{-19} \text{C}$
Reduced Planck's constant	\hbar	1	$1.05 \times 10^{-34} \text{Js}$
Coulomb's constant	k_e	1	$8.99 \times 10^9 \text{Nm}^2\text{C}^{-2}$

Table 2.1: The values of some fundamental constants in atomic units and in SI units.

2.1.1 Hydrogen Atom

Perhaps the simplest model one can use to understand the basic properties of a Hydrogen atom is through the well known semi-classical model, Bohr's model of an atom [54]. The idea is to model the valence electron orbiting around the ion classically according to Newton's law of motion, but at the same time, treating the angular momentum quantum mechanically by quantising it in terms of the reduced Planck's constant \hbar , i.e. $m_e v r_e = \nu \hbar$, with ν being a positive integer. Bohr's model predicts the total energy of the electron to be $E_e = -\frac{k_e^2 e^4 m_e}{2\nu^2 \hbar^2}$ which coincides with the Rydberg formula in the absence of the quantum defect. From the above calculation, Bohr's model also predicts an orbital radius of the electron to be $r_e = \frac{\nu^2 \hbar^2}{e^2 m_e k_e}$. Hence, one notices that the orbital radius has a ν^2 -scaling behaviour. This scaling indicates that the size of a Rydberg atom is much larger than the size of a ground state atom and atoms being excited to low-lying states. For instance, the orbital radius of the electron in Hydrogen being excited to the $\nu = 2$ state is about 0.2 nm, whereas the orbital radius is about 132 nm when being excited to $\nu = 50$ state. Therefore, from Bohr's model, one can already conclude that Rydberg atoms are not only very loosely bound to the ion core, but also have very large sizes.

For simplicity, we will adopt atomic units from now on. By the definition of atomic units, the electron mass, the elementary charge, the reduced Planck's constant, and the Coulomb's constant are unity, i.e. $m_e = e = \hbar = k_e = 1$. Adopting atomic units, as an example, the electronic energy of a Hydrogen atom as predicted by Bohr's model reads, $E_e = -\frac{1}{2\nu^2}$. In Table (2.1), the values of these fundamental constants in atomic units and SI units are provided.

Although Bohr's model nicely introduces the idea of quantisation which turns out to be successful in understanding both qualitatively and quantitatively the electronic structure of a Hydrogen atom, it does not provide explanation for the complete quantum mechanical behaviour of it. Hence, to go beyond the semi-classical picture, let us briefly review the determination of the wavefunction of the valence electron, ψ_e from the time-independent Schrödinger equation for a

Hydrogen in spherical coordinates,

$$\left(-\frac{\nabla^2}{2} - \frac{1}{r_e}\right)\psi_e = E_e\psi_e. \quad (2.2)$$

where ∇^2 is the Laplacian operator that determines the kinetic energy of the electron and in spherical coordinates it reads,

$$\nabla^2 \equiv \frac{1}{r_e^2} \frac{\partial}{\partial r_e} \left(r_e^2 \frac{\partial}{\partial r_e} \right) + \frac{1}{r_e^2 \sin \theta} \frac{\partial}{\partial \theta} \left(\sin \theta \frac{\partial}{\partial \theta} \right) + \frac{1}{r_e^2 \sin^2 \theta} \frac{\partial^2}{\partial \phi^2}, \quad (2.3)$$

and we have considered a standard Coulomb potential felt by the electron in the second term. The equation can be solved by separating the wavefunction into a radial part, $\mathcal{R}_{\nu,l}(r_e)$, and an angular part $\mathcal{Y}_{l,m}(\theta, \phi)$, i.e. $\psi_e(r_e, \theta, \phi) = \mathcal{R}_{\nu,l}(r_e)\mathcal{Y}_{l,m}(\theta, \phi)$, where the indices ν, l , and m will become clear later. The solution to the latter part, $\mathcal{Y}_{l,m}(\theta, \phi)$, is known as the normalised spherical harmonics,

$$\mathcal{Y}_{l,m}(\theta, \phi) = \sqrt{\frac{(2l+1)(l-m)!}{4\pi(l+m)!}} P_{l,m}(\cos \theta) e^{im\phi}, \quad (2.4)$$

where $P_{l,m}(\cos \theta)$ are associated Legendre polynomials. The angular wavefunction depends on two integers, l and m , where l , known as the angular momentum quantum number, is a non-negative integer, while m , known as the magnetic quantum number, may take integral values from $-l$ to l .

The solution to the radial wavefunction for a bound electron satisfying the appropriate boundary condition where the wavefunction vanishes as $r_e = \infty$ and remains finite at $r_e = 0$ reads,

$$R_{\nu,l}(r_e) = \sqrt{\frac{4(\nu-l-1)!}{\nu^4(\nu+l)!^3}} \left(\frac{2r_e}{\nu}\right)^l L_{\nu-l-1}^{2l+1}(2r_e/\nu) e^{-\frac{r_e}{\nu}}, \quad (2.5)$$

with ν being the already mentioned principal quantum number, and $L_{\nu-l-1}^{2l+1}$ are the Laguerre polynomials. Taking the electronic ground state, i.e. $\nu = 1, l = 0, m = 0$, as an example, the wavefunction of the electron reads,

$$\psi_e = \frac{1}{\sqrt{\pi}} e^{-r_e}. \quad (2.6)$$

The eigenenergy is obtained to be exactly $E_e = -\frac{1}{2\nu^2}$, coinciding with the Rydberg formula for the case of a Hydrogen atom. This allows one to obtain the electronic energy levels which is depicted in the rightmost column in Fig. 2.1. It is worth to note that the energy levels are independent of l , i.e. electronic states of the same ν with different l are degenerate. As we will see later for Alkali-metal

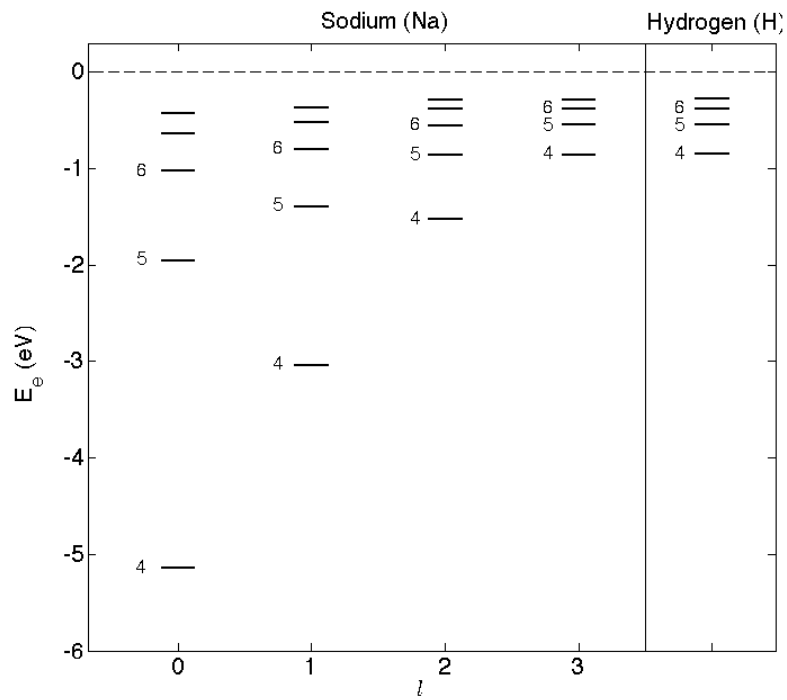


Figure 2.1: Energy levels of a Sodium (Na) atom (left) and a Hydrogen (H) atom (rightmost). The energies of the electronic states are taken from Ref. [55] and converted into electron Volts. The value of the principal quantum number ν is written next to the respective energy levels. The angular momentum quantum number l to the respective energy level is indicated in the horizontal-axis. The ionisation threshold ($\nu \rightarrow \infty$) is illustrated as a dashed line toward the top of the diagram.

atoms, the l -dependent quantum defect, δ_l breaks this degeneracy, and hence making electronic state energies also l -dependent. For $\nu \rightarrow \infty$, the binding energy approaches zero, which is known as the ionisation limit, and an electron having an energy beyond this threshold is no longer bound to the ion core and becomes a free electron leaving the atom positively charged.

Having demonstrated the quantum mechanical derivation of the electron wavefunction, one can start to utilise it to study properties of Rydberg atoms. For instance, for a highly excited electron, the expectation value of the orbital radius, $\langle \hat{r}_e \rangle$, with \hat{r}_e being the radial operator in spherical coordinates, can be calculated from the wavefunction with given ν and l . The solution yields [56],

$$\langle \hat{r}_e \rangle = \frac{1}{2}[3\nu^2 - l(l+1)], \quad (2.7)$$

agreeing with the ν^2 -dependence obtained from Bohr's model as we have seen previously. However, the angular momentum l -dependence is new compared to Bohr's model. Now, let us proceed further with the quantum mechanical description of a Hydrogen atom, and explain the origin of the quantum defect, δ_l seen in the Rydberg formula in the next section.

2.1.2 Alkali-metal Atoms

Noticeably, in the definition of Rydberg atoms, there is no specification for the choice of the element. Hence, Rydberg atoms should possess similar properties despite the choice of the element in producing them. This can be explained by the simple picture where the highly excited electron sees the entire ion core and the remaining electrons as an entity that has a net charge of +1, hence making it effectively a hydrogen like atom as shown in Fig. 2.2(a). However, for different elements, the properties of Rydberg atoms vary slightly with respect to the quantum defect, δ_l . In this section, we will look beyond the Hydrogen atom to explain the origin of the quantum defects from a simple semi-classical picture of the orbiting valence electron.

We choose Alkali-metal atoms in particular for reason that they have exactly one valence electron which in this way, makes them similar to that of a Hydrogen atom. For other elements, the situation will become even more complicated, but the arguments that we give later still apply. To proceed, let us take Sodium (Na) as an example, and illustrate its electronic structure of the valence electron. As shown in the diagram in Fig. 2.1 [19, 20], the ν and l - dependent energy levels are drawn as horizontal lines with the ν -value written next to each line and l -value illustrated in the horizontal axis. The binding energies of the electronic levels are

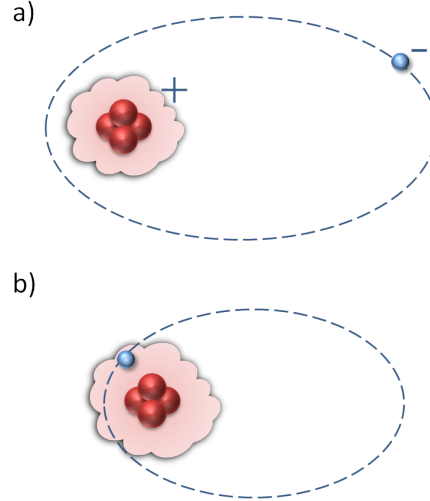


Figure 2.2: Semi-classical (elliptical) orbit followed by the valence electron of the atom with low angular momentum. The ionic core is located at one of the focal points of the ellipse. (a) The electron orbit in the absence of the quantum defect. The electron sees the ion core as an entity that has a net charge of $+1$; (b) The electron orbit in the presence of the quantum defect. The electron, when it travels near to the inner turning point, can penetrate through the ion core.

taken from Ref. [55] and converted into electron Volts.

The first thing to be noticed in this diagram is the level spacing between states with the same angular momentum l . One sees a large gap initially between the first two electronic states, but such a gap quickly shrinks as ν becomes large due to the inverse quadratic relation given in Eq. (2.1). Approaching the ionisation threshold, the energy levels (not shown) hence become very close to each other and are almost continuous. Secondly, one observes that the electronic states with the same ν can have different energies due to different angular momentum. This is a consequence of the presence of the angular momentum dependent quantum defect. For increasing angular momentum, in comparison to the Hydrogen atom, the corresponding binding energy of the electron eventually becomes degenerate with a valence electron in a Hydrogen atom, hence indicating $\delta_l \approx 0$ for high l . If one chooses a different Alkali-metal atom, e.g. Rubidium (Rb), or element beyond the Alkali-metals group, although the exact energy of each electronic state would be different, the two patterns observed still remain similar [57]. Altogether, these observations lead to the conclusion that the properties of Rydberg atoms are almost independent of the choice of the element and it is sufficient, in many cases, to describe a Rydberg atom by using the highly excited Hydrogen atom. The advantage of the latter inference is that it allows us to apply the analytical knowledge of a Hydrogen atom to study many properties of Rydberg atoms as we will see later.

Now, let us look at the quantum defect from a more physical point of view and explain the origin of the defect. Considering again an Alkali-metal atom where the number of protons is greater than one. In a semi-classical representation, rather than following a circular motion, as displayed in Fig. 2.2, the valence electron at small angular momentum will orbit around the ion core by following an elliptical path with the ion core located at one of the focal points. In Fig. 2.2(a), we illustrate the situation where the quantum defect is neglected. In this case, the electron sees the ion core and the inner electron cloud as an entity that has a net charge of $+1$. Effectively, this makes it a Hydrogen-like atom with a non-zero angular momentum, i.e. $l > 0$. As depicted in Fig. 2.2(b), where one considers the effect of the quantum defect, the orbit of the valence electron changes. As one sees, when the valence electron orbits toward the closer end of the ion core, it has certain possibility to penetrate through the inner electron cloud [19]. The penetration leads to a modification to the Coulomb potential that the valence electron feels. As shown in Ref. [19], the modification of the potential leads to a phase shift in the wavefunction which is the mathematical origin of the quantum defect. The values of the quantum defect were first analysed as the Rydberg and Ritz coefficients in the Rydberg-Ritz formula by Robert Jastrow [58] and can be accurately measured experimentally [59, 60]. For large angular momentum where the valence electron follows an approximately circular orbit, and as we have already seen from Fig. 2.1, the binding energy of the valence electron in Rydberg atoms is degenerate with that in the Hydrogen atom.

To summarize, the quantum defect observed in Alkali-metal atoms leads to a correction to the single electron wavefunction obtained from the hydrogen model. As a result, the properties of Rydberg atoms will depend on the magnitude of the quantum defect, and hence, its angular momentum. Nonetheless, by introducing an effective quantum principle number $\nu^* = \nu - \delta_l$, one finds that Rydberg atoms still preserve the same ν^* -scaling behaviours for all their properties. For simplicity, since it is only the power law scalings of these properties of Rydberg atoms that matter, we will not consider the effect of the quantum defect, and simply continue utilising the single electron wavefunction obtained from the Hydrogen model to study the other properties of Rydberg atoms. Eventually, we will show how certain properties scale with the principal quantum number, ν .

2.1.3 Properties of Rydberg Atoms

A selection of properties of Rydberg atoms along with their ν -scaling is summarised in Table (2.2)[20]. These properties are important and useful in understanding the Rydberg lattice gases that we study in the later sections. In Sec. 2.1

we have already shown the ν -scaling of the electronic binding energy, E_e , and the orbital radius, r_e of a Rydberg atom. In this section, we will further discuss other properties of Rydberg atoms including the energy level spacing, ΔE_e which scales as ν^{-3} , radiative lifetime, τ which scales as ν^3 and the polarisability, α which scales as ν^7 .

The energy level spacing, i.e. the energy difference between adjacent energy levels, of a Rydberg atom can be calculated based on the already obtained expression of the electronic level energy as,

$$\begin{aligned} \Delta E_e = E_e^{\nu+1} - E_e^\nu &= \frac{1}{2} \left(\frac{1}{\nu^2} - \frac{1}{(\nu+1)^2} \right) \\ &= \frac{2\nu+1}{2(\nu^4 + 2\nu^3 + \nu^2)} \\ &\stackrel{\nu \gg 1}{\approx} \nu^{-3} \end{aligned} \quad (2.8)$$

This scaling explains what we have observed in Fig. 2.1 where adjacent energy levels become closer to each other as ν increases.

Before we proceed to illustrate the ν -scaling of radiative lifetime of a Rydberg atom, let us first briefly analyse the radial transition dipole moment matrix elements (or dipole matrix element) between electronic states, and the selection rule.

The dipole matrix element quantifies the coupling strength between two states, and it is often denoted as $\langle \nu' l' | \hat{\mathbf{d}} | \nu l \rangle$ with $\hat{\mathbf{d}} = -e\hat{\mathbf{x}}$ being the dipole operator in SI unit, where e is the electron charge and $\hat{\mathbf{x}}$ being the three-dimensional position operator in Cartesian coordinates. The two coupled states are the electron wavefunction denoted by their corresponding quantum numbers in the bra-ket notation. The analytical expressions for transition dipole moments involving different quantum numbers are in general difficult to obtain. For situations where the principle quantum number is conserved, i.e. $\nu' = \nu$, and the angular momentum quantum numbers obey $l' = l + 1$, a simple analytical expression for the radial transition dipole matrix element reads [19, 56],

$$\langle \nu l | \hat{r}_e | \nu(l+1) \rangle = \frac{-3\nu\sqrt{\nu^2 - l^2}}{2}, \quad (2.9)$$

where \hat{r}_e is the same radial operator in spherical coordinates used previously. This radial dipole matrix element with conserved principle quantum number, ν , illustrates a ν^2 -scaling behaviour. This scaling will be useful in deriving the scaling behaviour of the van der Waals coefficient, C_6 , as demonstrated later in Sec. 2.1.5. Another important property regarding the dipole matrix element with conserved principle quantum number is that for situation where $l' = l$, the dipole matrix

Property	Symbol	ν -scaling
binding energy	E_e	ν^{-2}
orbital radius	r_e	ν^2
energy spacing	ΔE_e	ν^{-3}
radial transition dipole moment	$\langle \nu l \hat{r}_e \nu(l+1) \rangle$	ν^2
radiative lifetime	τ	ν^3
polarisability	α	ν^7
van der Waals coefficient	C_6	ν^{11}

Table 2.2: Selected properties of Rydberg atoms which are discussed in the content. The properties scale as functions of the principal quantum ν according to power laws [19]. These scalings give rise to bizarre properties at large ν which form the foundation of the Rydberg lattice gases.

element is zero due to the parity conservation between the two coupled states, [61]. This induces a selection rule that states, $\Delta l = l' - l = \pm 1$ when $\nu = \nu'$.

One interesting and at the same time counterintuitive property of Rydberg atoms is that they have much longer radiative lifetime when compared to atoms being excited to low-lying states. Intuitively, one might expect the contrary because highly excited atoms are obviously energetically unfavourable. However, according to the given scaling, where $\tau \sim \nu^3$, one notices that the higher the excited state the longer the lifetime of a Rydberg atom, and this lifetime can be orders of magnitude higher than atoms in low-lying excited states. To see the origin of the long radiative lifetime of a Rydberg atom, one can calculate the radiative life time of a Rydberg atom in a $|\nu l\rangle$ state by

$$\tau_{\nu l} = \left[\sum_{\nu' l'} A_{\nu' l', \nu l} \right]^{-1}, \quad (2.10)$$

where $A_{\nu' l', \nu l}$ is the well known Einstein A -coefficient that quantifies the rate of spontaneous decay from a highly excited state, $|\nu l\rangle$ to a low-lying state, $|\nu' l'\rangle$. The coefficient can be expressed in terms of the radial transition dipole moment as [56],

$$A_{\nu' l', \nu l} = \frac{4\omega_{\nu' l', \nu l}^3 l_{\max}}{3(2l+1)} |\langle \nu' l' | \hat{r}_e | \nu l \rangle|^2, \quad (2.11)$$

where $l_{\max} = \max(l, l')$, and $\omega_{\nu' l', \nu l}$ is the transition frequency between the two electronic states. The Einstein A -coefficient, as seen, scales as ω^3 . This means that the sum in Eq. (2.10) is dominated by the term with the highest ω , and this corresponds to the decay channel to the lowest low-lying state allowed by selection rule. For such transition, the corresponding radial dipole matrix element scales as $\nu^{-3/2}$ due to the normalisation of the Rydberg state wavefunction [19]. Hence, the radiative lifetime of a Rydberg state roughly scales as ν^3 . Typically, with ^{85}Rb as

an example, it has been reported both theoretically and experimentally that the radiative life time of Rydberg atom in the $\nu > 40$ s -states can reach $60\mu s$ whereas typical lifetime for an electron in the low-lying states, i.e. $\nu \sim 10$ is on the order of hundreds of nanoseconds to a few microseconds [62, 63]. In short, the long lifetime of Rydberg atoms permits them to be studied in ultra-cold atomic experiments and this enables many studies in the field of atomic physics, many-body physics, and quantum information.

Another important property of Rydberg atoms is the polarisability α which is defined as the ratio of an induced dipole moment of an atom to the electric field that create this dipole moment [64]. It quantifies how strongly an atom responds to an external electric field. Within the framework of the quantum defect theory and the quasi-classical approach, a detailed derivation of the ν -scaling behaviour of the polarisability of Rydberg atom is nicely given in Ref. [65]. The ν^7 scaling indicates that a Rydberg atom has a giant polarisability which makes it very susceptible to electric fields. One of the consequences of the huge polarisability of Rydberg atoms is that they can polarise each other. This gives rise to strong interactions between the atoms which can reach out to very long distances. Consequently, the interaction leads to an interesting many-body phenomenon - *Rydberg Blockade* - which forms the basis of the entire thesis. More details on this interaction and the blockade mechanism will be discussed in Sec. 2.1.5. Having discussed some interesting properties of Rydberg atoms, let us now review how a Rydberg atom is excited via lasers in the following section.

2.1.4 Photoexcitation of a Rydberg Atom

Before the 70s, Rydberg atoms were produced collisionally via so-called charge exchange [66, 67, 68] and electron impact [69, 70, 71], where both methods rely on collision process involving charged particles. Both of these collision-dependent methods have one thing in common which is that they are unable to select a specific Rydberg state to be populated. This is because during the collision between the charged particles, the amount of energy of the incident particles being transferred to the target valence electrons cannot be precisely controlled, thus leading to the electrons being excited to different Rydberg states according to the energy absorbed. In modern experiments, Rydberg atoms are produced by using optical excitation which allows specifying a particular Rydberg state to be excited. This is done by using dye lasers [72, 73]. By specifying the photon energy, i.e. laser frequency, the target electrons will absorb the photons with exactly the photon energy and hence be excited to the particular Rydberg state of interest. This optical method is often referred to as photoexcitation.

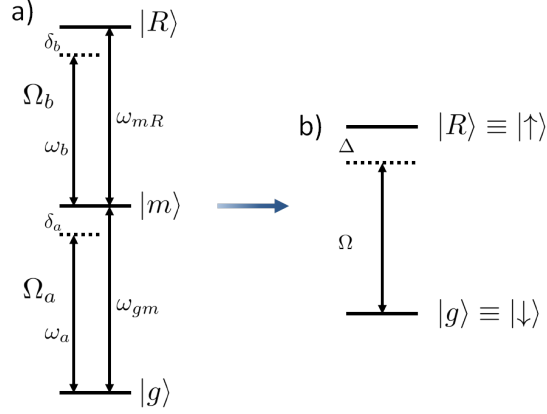


Figure 2.3: a) A three-level system, with the three states denoted by $|g\rangle$, $|m\rangle$, and $|R\rangle$. The two states, $|g\rangle$ and $|m\rangle$ have a transition frequency of ω_{gm} and are coupled by a laser with frequency of ω_a and detuning δ_a ; and the two states, $|m\rangle$ and $|R\rangle$ have a transition frequency of ω_{mR} and are coupled by a laser with frequency of ω_b and detuning δ_b . The two transition lasers are parameterised by the Rabi-frequency Ω_a and Ω_b respectively. b) By carrying out a rotating wave approximation and adiabatically eliminate the intermediate state $|m\rangle$, it is possible to reduce the system to an effective two-level system coupled by an effective laser with Rabi-frequency, Ω and detuning Δ (see text for more details).

Although atoms have a complicated energy level structure, photoexcitation allows one to concentrate only on excited states of interest, and eventually neglect all other energy levels. This is true when the laser frequency is close to the transition frequency between the ground state and the excited states [74]. This condition of the laser frequency is often called near-resonance. In practice, it is very difficult to produce Rydberg atom via a single laser due to restriction of laser frequencies to meet the transition frequency between the electronic ground state and the target Rydberg state. Also, due to the selection rules, exciting an electron from its electronic ground state, i.e. ν_0s -state, to a highly excited νs -state is not allowed since the difference in angular momentum of the two states has to be ± 1 . Therefore, Rydberg states in ultra-cold experiments are often populated through a two-photon process as shown in Fig. 2.3 [75]. In detail, we have three energy levels: the electronic ground state $|g\rangle$, an intermediate state $|m\rangle$, and a Rydberg state $|R\rangle$ with two coupling lasers with laser frequencies ω_a and ω_b . The transition frequency between $|g\rangle$ and $|m\rangle$ is denoted as ω_{gm} and between $|m\rangle$ and $|R\rangle$ is denoted as ω_{mR} . Here, we introduce detuning terms that quantify the difference between the laser frequency and the transition frequency, i.e. $\delta_a = \omega_{gm} - \omega_a$, and $\delta_b = \omega_{mR} - \omega_b$. If the two laser detunings are set very small with respect to the transition frequencies ω_{gm} and ω_{mR} , i.e. both coupling lasers are near-resonant with the corresponding transition frequency, we can safely approximate the complex electronic structure by an effective picture involving only these three energy levels. In the following,

we will show how to obtain an effective two-level description via rotating wave approximation and adiabatic elimination.

We start by deriving the Hamiltonian of the three-level system irradiated by the two lasers. The Hamiltonian consists of two parts: the atomic part H_{atom} which accounts for the energy of the free atom, and the interaction part denoted as $H_{\text{atom-laser}}$ which accounts for the interaction between the atom and the laser. Writing this Hamiltonian in a matrix form with the use of $|g\rangle$, $|m\rangle$ and $|R\rangle$ as the basis states, we have,

$$H_{\text{one-atom}} = \sum_{i,j} \langle i | (H_{\text{atom}} + H_{\text{atom-laser}}) | j \rangle | i \rangle \langle j |, \quad (2.12)$$

where i, j denotes the three different basis states. For the atomic part of the Hamiltonian, the basis states are eigenstates of H_{atom} , e.g. $H_{\text{atom}} |g\rangle = \epsilon_g |g\rangle$. Without losing generality, one can set the electronic ground state energy to be zero, i.e. $\epsilon_g = 0$ for simplicity. A non-zero ϵ_g can be thought as an overall energy shift to the system. We then have $\langle g | H_{\text{atom}} |g\rangle = 0$, $\langle m | H_{\text{atom}} |m\rangle = \omega_{gm}$, and $\langle R | H_{\text{atom}} |R\rangle = \omega_{gm} + \omega_{mR}$. Due to orthogonality of the basis states, i.e. $\langle i | j \rangle = 0$ for $i \neq j$, the off-diagonal elements in H_{atom} are zeros. Hence, the matrix elements of the atomic part of $H_{\text{one-atom}}$ reads,

$$H_{\text{one-atom}} = |g\rangle \langle g| + \omega_{gm} |m\rangle \langle m| + (\omega_{gm} + \omega_{mR}) |R\rangle \langle R| \quad (2.13)$$

For the interaction part of the Hamiltonian, within a dipole approximation¹, the interaction energy between the atom and the laser can be approximated by an energy of an electric dipole in an electric field as,

$$H_{\text{atom-laser}} = -\hat{\mathbf{d}}_{gm} \cdot \hat{\epsilon}_{gm} - \hat{\mathbf{d}}_{mR} \cdot \hat{\epsilon}_{mR}, \quad (2.14)$$

where $\hat{\mathbf{d}} = -\hat{\mathbf{x}}$ is the previously introduced dipole operator in atomic unit with $\hat{\mathbf{x}}$ being the three-dimensional position operator, and $\hat{\epsilon} = \epsilon \hat{p} \cos(\omega t)$ is the classical monochromatic electric field generated by the laser at the position of the atom with ϵ being the electric field amplitude at the position of the atom and \hat{p} being the unit polarisation vector that is perpendicular to the direction of the propagation of the electric field. The subscript gm (mR) denotes the interaction involving the two energy levels $|g\rangle$ and $|m\rangle$ ($|m\rangle$ and $|R\rangle$). Therefore, the interaction Hamiltonian

¹This is a valid approximation when the wavelength of the electric field is much longer than the size of the atom, so that the spatial variation of the field over the extent of the atom can be neglected.

is further calculated as,

$$\begin{aligned}
H_{\text{atom-laser}} &= 2 \cos(\omega_a t) (\Omega_a \langle g | m \rangle + \Omega_a^* \langle m | g \rangle) \\
&\quad + 2 \cos(\omega_b t) (\Omega_b \langle m | R \rangle + \Omega_b^* \langle R | m \rangle), \tag{2.15}
\end{aligned}$$

where $\Omega_{a,b}$ are known as the Rabi-frequencies defined as $\Omega_a = \varepsilon_{gm} \langle g | \hat{\mathbf{x}}_{gm} \cdot \hat{\mathbf{p}}_{gm} | m \rangle / 2$ and $\Omega_b = \varepsilon_{mR} \langle m | \hat{\mathbf{x}}_{mR} \cdot \hat{\mathbf{p}}_{mR} | R \rangle / 2$, and ω_a and ω_b are the corresponding laser frequencies. In the matrix representation, one realises that $H_{\text{atom-laser}}$ only contains off-diagonal elements. This is due to the previously discussed selection rule based on parity argument where $\langle i | \hat{\mathbf{x}} | i \rangle = 0$.

Having the matrix elements of $H_{\text{one-atom}}$ determined in Eqs. (2.13) and (2.15), and further assuming the Rabi-frequencies are real for the sake of simplicity, $H_{\text{one-atom}}$ becomes,

$$H_{\text{one-atom}} = \begin{pmatrix} \omega_{gm} + \omega_{mR} & 2\Omega_b \cos(\omega_b t) & 0 \\ 2\Omega_b \cos(\omega_b t) & \omega_{gm} & 2\Omega_a \cos(\omega_a t) \\ 0 & 2\Omega_a \cos(\omega_a t) & 0 \end{pmatrix}. \tag{2.16}$$

Now, we transform $H_{\text{one-atom}}$ into a rotating frame by performing an unitary transformation of the form,

$$U = \begin{pmatrix} e^{-i(\omega_a + \omega_b)t} & 0 & 0 \\ 0 & e^{-i\omega_a t} & 0 \\ 0 & 0 & 1 \end{pmatrix}, \tag{2.17}$$

on the time-dependent Schrödinger equation, one then obtains an effective Hamiltonian describing the one-atom system as,

$$\begin{aligned}
H'_{\text{one-atom}} &= U^\dagger H_{\text{one-atom}} U - iU^\dagger \partial_t U \\
&= \begin{pmatrix} \delta_a + \delta_b & \Omega_b(1 + e^{-i2\omega_b t}) & 0 \\ \Omega_b(1 + e^{-i2\omega_b t}) & \delta_a & \Omega_a(1 + e^{-i2\omega_a t}) \\ 0 & \Omega_a(1 + e^{-i2\omega_a t}) & 0 \end{pmatrix}, \tag{2.18}
\end{aligned}$$

where $\delta a = \omega_{gm} - \omega_a$ and $\delta b = \omega_{mR} - \omega_b$ are the laser detunings of the coupling lasers respectively.

Provided that the lasers are near-resonant, i.e. $\delta_a, \delta_b \ll \omega_a, \omega_b$, the four exponential terms in the above equation are quickly oscillating compared to the rest of the terms and hence quickly average to zero. This allows us to apply the rotating wave approximation to neglect these exponential terms. The Hamiltonian then

reduces to,

$$H'_{\text{one-atom}} \approx \begin{pmatrix} \delta_a + \delta_b & \Omega_b & 0 \\ \Omega_b & \delta_a & \Omega_a \\ 0 & \Omega_a & 0 \end{pmatrix}. \quad (2.19)$$

The rotating wave approximation allows one to neglect the time-dependence and eventually obtain an effective Hamiltonian that describes the energy levels in a rotating frame.

Since we are only interested in exciting the atom to the Rydberg state, ideally, one would make the intermediate state remain unpopulated. To proceed, we now look at the time-dependent Schrödinger equation, $i\partial_t |\phi(t)\rangle = H'_{\text{one-atom}} |\phi(t)\rangle$ where the time-dependent wavefunction can be written as a superposition of the three basis states as, $|\phi(t)\rangle = C_g(t) |g\rangle + C_m(t) |m\rangle + C_R(t) |R\rangle$, where $C_g(t)$, $C_m(t)$, and $C_R(t)$ are time-dependent probability amplitudes for their corresponding basis states. In the systems that we will consider in later chapters of this thesis, we are only interested in the ground state and the Rydberg state, hence, we want to eliminate the intermediate state, $|m\rangle$ through a mathematical adiabatic elimination, which amounts to having $i\dot{C}_m(t) = 0$ such that the population of the intermediate state remains unchanged over time. Hence, if the intermediate state is unpopulated initially, it will remain unpopulated. In practice, this can be achieved by making the first laser far-detuned, i.e. $\delta_a \gg \Omega_a, \Omega_b$ which will become apparent later. Solving the differential equations of the time-dependent probability amplitudes with the condition $i\dot{C}_m(t) = 0$, one obtains a solution for $C_m(t)$, where

$$C_m(t) = -\frac{1}{\delta_a} (\Omega_b C_r(t) + \Omega_a C_g(t)). \quad (2.20)$$

Here, one sees that with the condition $\delta_a \gg \Omega_a, \Omega_b$, the small magnitude of the probability amplitude of $C_m(t)$ indicates that the system can be effectively described by a two-level Hamiltonian. Substituting the results of $C_m(t)$ to the other two differential equations for $\dot{C}_g(t)$ and $\dot{C}_R(t)$, the effective two-level Hamiltonian reads,

$$\begin{aligned} H_{\text{eff-one-atom}} &= \begin{pmatrix} \delta_a + \delta_b & -\frac{\Omega_a \Omega_b}{\delta_a} \\ -\frac{\Omega_a \Omega_b}{\delta_a} & 0 \end{pmatrix} \\ &= \begin{pmatrix} \Delta & \Omega \\ \Omega & 0 \end{pmatrix}, \end{aligned} \quad (2.21)$$

where we have defined an effective detuning, $\Delta = \delta_a + \delta_b$, and an effective Rabi-frequency, $\Omega = -\frac{\Omega_a \Omega_b}{\delta_a}$. Notice that in deriving this effective Hamiltonian, we have neglected an overall energy shift of $-\Omega_a^2/\delta_a$ as this does not alter the two-level description. In terms of the Pauli spin matrices and by further introducing a

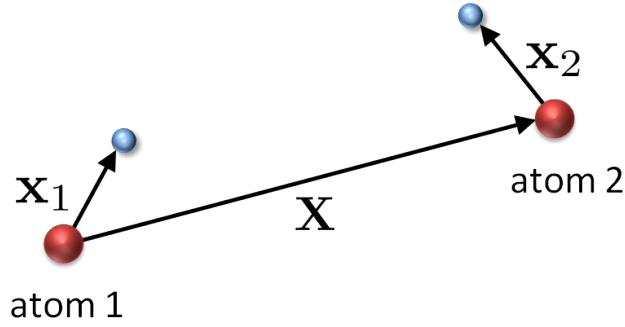


Figure 2.4: A schematic diagram of two indistinguishable Rydberg atoms showing the displacement vectors used in deriving the dipole-dipole interaction between the two atoms. The larger red dot represents the a singly charged ion core and the smaller blue dot represents the highly excited electron.

projection operator, $n = |R\rangle\langle R|$ that projects onto the Rydberg state, we can rewrite $H_{\text{eff-one-atom}}$ as,

$$H_{\text{eff-one-atom}} = \Omega\sigma^x + \Delta n. \quad (2.22)$$

In the language of spins, we formally establish the atom-spin equivalence here by introducing $|\downarrow\rangle \equiv |g\rangle$ and $|\uparrow\rangle \equiv |R\rangle$. The spin representation will prove to be very helpful in later section when we deal with systems contains more than one atom. The one-atom Hamiltonian can also be interpreted as a spin-1/2 particle in a transverse field Ω , and a longitudinal field, Δ .

2.1.5 Interacting Rydberg Atoms

The van der Waals Interaction

In this section, we will briefly discuss how two Rydberg atoms interact with each other via the van der Waals interaction. There are different ways to derive this interaction. Here, as depicted in Fig. 2.4, we will review a standard electrostatic approach by considering the two Rydberg atoms separated by a distance, $r = |\mathbf{X}|$ where \mathbf{X} is the displacement vector of the second atom from the first atom. The displacement vectors of the valence electrons of each of the Rydberg atoms from their associated nuclei are denoted as \mathbf{x}_1 and \mathbf{x}_2 respectively. We will consider the regime where the separation between the two nucleus is much greater than the orbital radii of the two valence electrons in Rydberg states, i.e. $r \gg |\mathbf{x}_1|, |\mathbf{x}_2|$. Then, treating the two nuclei as positive charges with fixed positions, the complete Coulomb interaction potential can be expressed as,

$$U_{\text{dd}} = \frac{1}{|\mathbf{X}|} - \frac{1}{|\mathbf{X} + \mathbf{x}_2|} - \frac{1}{|\mathbf{X} - \mathbf{x}_1|} + \frac{1}{|\mathbf{X} + \mathbf{x}_2 - \mathbf{x}_1|}, \quad (2.23)$$

where the first term is the Coulomb interaction between the two nuclei, the second (third) term is the Coulomb interaction between the first (second) nucleus and the valence electron of the second (first) atom, and the last term is the Coulomb interaction between the two electrons. In the regime where $r \gg |\mathbf{x}_1|, |\mathbf{x}_2|$, one can Taylor expand U_{dd} about $|\mathbf{x}_1|, |\mathbf{x}_2| = 0$, and obtain

$$U_{\text{dd}} \approx \frac{\mathbf{x}_1 \cdot \mathbf{x}_2}{r^3} - \frac{3(\mathbf{x}_1 \cdot \mathbf{X})(\mathbf{x}_2 \cdot \mathbf{X})}{r^5}. \quad (2.24)$$

This is essentially a dipole-dipole interaction where the two Rydberg atoms can be effectively treated as two dipoles that are interacting. In the following content, we will illustrate how one can arrive at the van der Waal interaction from the dipole-dipole interaction, U_{dd} by considering a simple situation where the vector \mathbf{X} is along the z-axis, i.e. $\mathbf{X} = r\hat{z}$ with \hat{z} being the unit vector in the z-direction. As a result, the dipole-dipole interaction simplifies to,

$$U_{\text{dd}} = \frac{\mathbf{x}_1 \cdot \mathbf{x}_2 - 3(\mathbf{x}_1 \cdot \hat{z})(\mathbf{x}_2 \cdot \hat{z})}{r^3}. \quad (2.25)$$

The dipole-dipole interaction can cause dipole transition to other electronic states. Although there are infinite number of states that the electron can transit to, the most probable transitions are the ones to the closest two states in energy. To proceed, let us construct the energy levels involved in the most probable transitions. Initially, both of the atoms are excited to the same Rydberg state denoted by $|\nu s\rangle$, i.e. $l = 0$. Considering a simple situation where the closest energy levels to the $|\nu s\rangle$ state are the $|\nu p\rangle$ state and $|(\nu - 1)p\rangle$ with relative energies to the zero energy state $|\nu s\rangle$ being $E_{\nu p}$ and $E_{(\nu - 1)p}$ respectively¹. These energy levels are depicted in Fig. 2.5(a).

Now, we introduce a pair-state basis representation. As depicted in Fig. 2.5(b), the case with two atoms both in the initial Rydberg- νs state is now represented by the $|\nu s \nu s\rangle$ state; the pair-states that are coupled to the $|\nu s \nu s\rangle$ state are the $|\nu p \nu p\rangle$ state, i.e. both atoms are in the νp -state; the $|(\nu - 1)p(\nu - 1)p\rangle$ state where both atoms are in the $(\nu - 1)p$ -state; and finally the $|\nu p(\nu - 1)p\rangle$ state where one atom is in the νp -state and the other atom is in the $(\nu - 1)p$ -state². The energies of

¹Here we introduce an overall energy shift to the electronic states such that the energy of $|\nu s\rangle$ is zero.

²Note that $|\nu p(\nu - 1)p\rangle \equiv |(\nu - 1)p\nu p\rangle$ due to the two Rydberg atoms are indistinguishable.

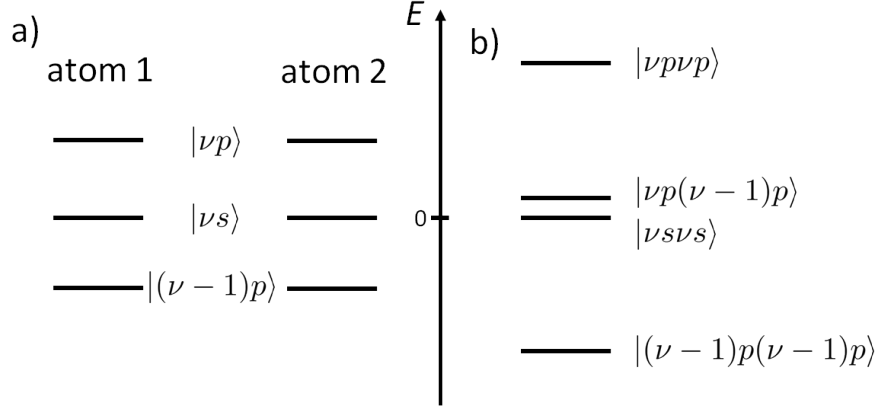


Figure 2.5: (a) The relevant energy levels of the two interacting Rydberg atoms with the energy of the $|\nu s\rangle$ -state set to zero. (b) The same system represented in the pair-state basis that is introduced in the main text for the derivation of the van der Waals interaction.

these pair-states can be obtained as,

$$\begin{aligned}
 E_{\nu s \nu s} &= 0 \\
 E_{\nu p \nu p} &= 2E_{\nu p} \\
 E_{(\nu-1)p(\nu-1)p} &= 2E_{(\nu-1)p} \\
 \text{and } E_{\nu p(\nu-1)p} &= E_{\nu p} + E_{(\nu-1)p}.
 \end{aligned} \tag{2.26}$$

Since $|E_{\nu p}| \approx |E_{(\nu-1)p}|$ with $E_{\nu p} > 0$ and $E_{(\nu-1)p} < 0$, one notices that $|E_{\nu p(\nu-1)p}| \ll |E_{\nu p \nu p}|, |E_{(\nu-1)p(\nu-1)p}|$, which can be observed in Fig. 2.5(b). This enables us to neglect the couplings to both $|\nu p \nu p\rangle$ and $|(\nu-1)p(\nu-1)p\rangle$. Then, the Hamiltonian that describes the two atoms in the pair-state basis can be effectively described by a two-level system where

$$\begin{aligned}
 H_{\text{pair-state}} &\approx \begin{pmatrix} E_{\nu p(\nu-1)p} & \langle \nu p(\nu-1)p | U_{\text{dd}} | \nu s \nu s \rangle \\ \langle \nu s \nu s | U_{\text{dd}} | \nu p(\nu-1)p \rangle & 0 \end{pmatrix} \\
 &\equiv \begin{pmatrix} E_{\nu p(\nu-1)p} & \frac{\gamma}{r^3} \\ \frac{\gamma}{r^3} & 0 \end{pmatrix},
 \end{aligned} \tag{2.27}$$

with $\gamma = \langle \nu s \nu s | \mathbf{x}_1 \cdot \mathbf{x}_2 - 3(\mathbf{x}_1 \cdot \hat{\mathbf{z}})(\mathbf{x}_2 \cdot \hat{\mathbf{z}}) | \nu p(\nu-1)p \rangle$ and the two off-diagonal matrix elements are essentially equal. One immediately notices that from the definition of dipole matrix element, γ is essentially proportional to the product of two dipole matrix elements, and hence, has a ν -scaling of ν^4 . The eigenenergies

of $H_{\text{pair-state}}$, which can be obtained by a straightforward diagonalisation, read,

$$\lambda_{\pm} = \frac{E_{\nu p(\nu-1)p} \pm \sqrt{E_{\nu p(\nu-1)p}^2 + 4\gamma^2/r^6}}{2}. \quad (2.28)$$

In the regime where the interaction energy is much smaller than the energy difference between the two involved states, i.e. $\langle \nu s \nu s | U_{\text{dd}} | \nu p(\nu-1)p \rangle \ll E_{\nu p(\nu-1)p}$, the eigenenergy, λ_- , which corresponds to the situation where both atoms are in the Rydberg νs -state initially, can be approximated as,

$$\lambda_- \approx -\frac{\gamma^2}{(E_{\nu p} + E_{(\nu-1)p})r^6}. \quad (2.29)$$

Further introducing a coefficient, $C_6 = -\gamma^2/(E_{\nu p} + E_{(\nu-1)p})$, known as the van der Waals coefficient, we have arrived at the van der Waals type of interaction,

$$V(r) = \frac{C_6}{r^6}. \quad (2.30)$$

As previously stated, C_6 typically scales as ν^{11} . This can be now understood with the fact that γ^2 scales as ν^8 and $E_{\nu p} + E_{(\nu-1)p}$ is roughly an energy level spacing, and hence scales as ν^{-3} as shown in Eq. (2.8). Therefore, combining the scalings, we arrive at the result that C_6 scales as ν^{11} . This dramatic scaling indicates that an interaction strength between two highly excited Rydberg atoms is about ten orders of magnitude stronger than the interaction strength between two ground state atoms. Hence, when Rydberg atoms are at close range, the van der Waals interaction plays a very important role. As we will see in the following sub-section, this leads to the so-called Rydberg blockade mechanism. The other interesting feature of the van der Waals interaction is that the interaction strength quickly decays with increasing distance, r between the Rydberg atoms due to the inverse power law, r^{-6} . This is important in later study of the Rydberg lattice gases as it allows one to neglect van der Waals interactions between Rydberg atoms that are very far away.

The Rydberg Blockade

With the spin-1/2 description of the Rydberg atom demonstrated in previous section, and knowing that Rydberg atoms interact via the van der Waals interaction, we can now write down a Hamiltonian describing two atoms separated by a distance, r , and both coupled to the same Rydberg states as,

$$H_{\text{two-atoms}} = \Omega\sigma_1^x + \Delta n_1 + \Omega\sigma_2^x + \Delta n_2 + \frac{C_6}{r^6}n_1n_2. \quad (2.31)$$

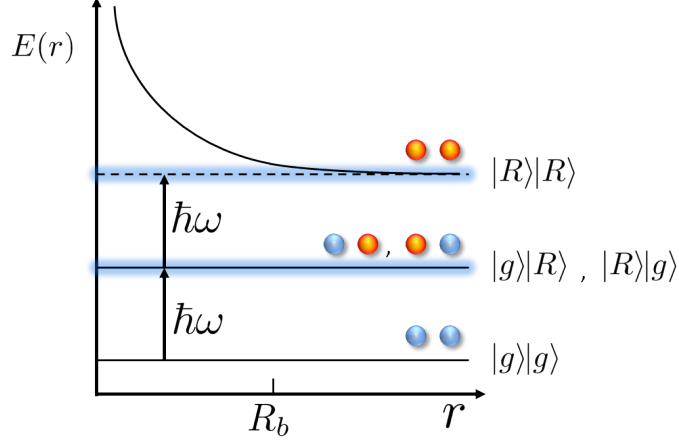


Figure 2.6: Excitation energy $E(r)$ of two atoms as a function of interatomic distance, r . The energy required to excite either atom to its Rydberg state is given by the energy different between the two levels, denoted as $\hbar\omega$ in SI units. However, to simultaneously excite both of the atoms to their Rydberg state requires an extra r -dependent energy due to the van der Waals interaction between the two atoms in the Rydberg state. The blue region represents the laser linewidth which is determined by the Rabi-frequency Ω for strong laser driving. The blockade happens at a distance where the energy required for simultaneous excitation is above the blue region. The analytical expression of blockade radius is given by $R_b \approx (C_6/\Omega)^{1/6}$.

The first four terms are single body terms accounting for individual laser couplings of the atom to the Rydberg state. The last term stands for the discussed van der Waals interaction present in the case of having both atoms are in the Rydberg state. Adopting the spin product state as the basis state, the Hilbert space consists of four states which are $|\downarrow\downarrow\rangle$, $|\downarrow\uparrow\rangle$, $|\uparrow\downarrow\rangle$, and $|\uparrow\uparrow\rangle$. To see how van der Waals interaction affects the system, let us consider resonant lasers where $\Delta = 0$, and look at the energies of the basis states as a function of the separation between the two atoms, r . As depicted in Fig. 2.6, the van der Waals interaction leads to a r -dependent configuration energy for the doubly excited state. In detail, in comparison to the dashed line that corresponds to the absence of van der Waals interaction, the shift in the energy of $|\uparrow\uparrow\rangle$ state is huge for small r due to the extremely large C_6 coefficient. For instance, for ^{87}Rb atom excited to $53s$ -state, the experimentally measured C_6 is about $13.7 \text{ GHz}\mu\text{m}^6$ [76]. Since typical spacing between Rydberg atoms trapped in optical lattice is on the order of micrometers, this means that C_6/r^6 is much greater than typical Rabi-frequencies ranging from $2\pi \times 0.5 \text{ MHz}$ to $2\pi \times 5 \text{ MHz}$. Therefore, the doubly excitation is strongly suppressed in this regime. This phenomenon is often referred to as the *Rydberg blockade* [23, 77, 78] and has been successfully demonstrated in ultra-cold experiments [79, 80]. Such a mechanism leads to rich many-body phenomena and has

lattice with lattice constant a . Each lattice site is occupied by only one atom and the electronic ground state of the atom on the \mathbf{k} -th lattice site is coupled to its Rydberg state by a site-dependent laser with Rabi-frequency $\Omega_{\mathbf{k}}$ and detuning $\Delta_{\mathbf{k}}$. The system can be realised in ultra-cold experiments with optical lattices where the typical lattice constant ranges from 0.5 micrometers to 10 micrometers [21]. In these optical lattices, the atom traps created by the standing waves are often deep such that the atoms are well confined. The atoms are considered to be fixed in space since the typical displacement of the atom is much less than the atomic spacing. This regime is often referred to as the frozen gas [83, 84] allowing the approximation of neglecting external degrees of freedom. For simplicity, we will always consider a periodic boundary condition, but this is not a necessity. In one-dimension, the periodicity can be visualised by a ring lattice [31, 78] as shown in Fig. 2.7 and in two-dimensions, the system can be visualised by a torus. According to the Hamiltonian derived for the two atoms case in Eq. (2.31), for a system containing L atoms, the general Hamiltonian which describes the system reads,

$$H_{\text{Ryd}} = \sum_{\mathbf{k}}^L \Omega_{\mathbf{k}} \sigma_{\mathbf{k}}^x + \sum_{\mathbf{k}}^L \Delta_{\mathbf{k}} n_{\mathbf{k}} + \frac{1}{2} \sum_{\mathbf{k}, \mathbf{m}}^L V_{|\mathbf{k}-\mathbf{m}|} n_{\mathbf{k}} n_{\mathbf{m}}. \quad (2.33)$$

Here, the interaction strength between two Rydberg atoms that are separated by $a|\mathbf{k}-\mathbf{m}|$ is denoted by $V_{|\mathbf{k}-\mathbf{m}|} = V|\mathbf{k}-\mathbf{m}|^{-6}$, where $V = C_6/a^6$ parameterises the van der Waals interaction at nearest neighbour distance. The factor of one half in front of the interaction terms ensures that the interaction between every two Rydberg atoms is only counted once. Note that the indices in Hamiltonian (2.33) are vectors, e.g. $\mathbf{k} = (k_x, k_y)$ in two-dimensions, and L always indicates the total number of sites on the lattice. The first two terms in the Rydberg Hamiltonian simply represent L non-interacting two-level atoms driven by laser fields. The last terms reflects the van der Waals interactions between every two Rydberg atoms. In studying the ground state properties of Rydberg lattice gases, we consider the regime where $V \gg \Omega$ such that the system exhibits ideal nearest neighbour blockade, i.e. simultaneous excitation of adjacent atoms is strictly forbidden. This is also illustrated in Fig. 2.7 with $R_b \gtrsim a$. However, the Rydberg Hamiltonian H_{Ryd} , as one observes, does not explicitly demonstrate this nearest neighbour blockade mechanism. In later sections, we will show how one can make this mechanism manifest by transforming H_{Ryd} into its interaction picture with respect to nearest neighbour interactions.

2.2.1 Strategy for Finding the Approximate Ground State

In principle, given the Hamiltonian of a system, one can always solve the Schrödinger equation numerically by performing exact diagonalisation. However, for quantum many-body systems, the dimension of the Hilbert space grows exponentially with increasing atom number. Thus, exact diagonalisation becomes quickly unmanageable as system size grows. To deal with such a restriction and eventually go beyond the numerical limits, for the system described by Hamiltonian (2.33), we present an analytical approach which will allow us to obtain an approximate ground state solution. In this section, we will lay out the general principles of this analytical treatment. They will serve as a foundation for investigating the system in specially designed situations, e.g. presence of an impurity as well as in various lattice geometries, e.g. square lattice.

Now let us start by transforming the Rydberg Hamiltonian into an interaction picture with respect to the nearest neighbour interaction. The motivation to perform such transformation is inspired by the Rydberg blockade mechanism. Since no simultaneous nearest neighbour Rydberg excitations are allowed due to $V \gg \Omega_{\mathbf{k}}, \Delta_{\mathbf{k}}$, it is reasonable to make the blockade mechanism manifest in the Hamiltonian. The details of the transformation are provided in Appendix A, and one eventually obtains an effective Hamiltonian for the system in the regime $V \gg \Omega_{\mathbf{k}}$ as,

$$H_{\text{eff}} = \sum_{\mathbf{k}}^L \Omega_{\mathbf{k}} \mathcal{P}_{\mathbf{k}} \sigma_{\mathbf{k}}^x + \sum_{\mathbf{k}}^L \Delta_{\mathbf{k}} n_{\mathbf{k}} + \frac{1}{2} \sum_{\substack{\mathbf{k}, \mathbf{m} \\ |\mathbf{k}-\mathbf{m}| > 1}}^L V_{|\mathbf{k}-\mathbf{m}|} n_{\mathbf{k}} n_{\mathbf{m}}, \quad (2.34)$$

where $\mathcal{P}_{\mathbf{k}}$ is a plaquette operator defined as $\mathcal{P}_{\mathbf{k}} = \prod_{\mathbf{m}} [1 - n_{\mathbf{m}}]$ with the indices \mathbf{m} being the nearest neighbours of \mathbf{k} , and the rest of the symbols have their usual meanings. The first term in H_{eff} is a quantum many-body term that effectively demonstrates the blockade mechanism. For instance, a Rydberg excitation on the \mathbf{k} -th lattice site can only take place if atoms in all its neighbouring sites are in the electronic ground state, i.e. $\mathcal{P}_{\mathbf{k}} = 1$. As a result, the Hilbert space is split into uncoupled blocks, e.g. the basis state $|\uparrow\downarrow\downarrow \dots\rangle$ is not coupled to the basis state $|\uparrow\uparrow\downarrow \dots\rangle$ since excitation on the second lattice site is not allowed due to the presence of an up-spin on the first lattice site. We will focus on the subspace where nearest neighbour excitations, e.g. $|\uparrow\uparrow\downarrow \dots\rangle$, are strictly forbidden, and this subspace will be referred to as the physical subspace. The second term in H_{Ryd} is unaffected by the transformation. However, comparing with H_{Ryd} , the last term in H_{eff} now no longer contains nearest neighbour interactions as it explicitly appears in the first term of H_{eff} .

To carry on, we will approximate the Rydberg gas Hamiltonian by a frustration

free Hamiltonian which is of the so-called Rokhsar-Kivelson (R-K) type [85, 86]. The ground state of this type of Hamiltonian can be constructed explicitly due to special properties of the Hamiltonian which will be discussed later. We then write the effective Hamiltonian (2.34) into a Hamiltonian of a R-K type, $H_{\text{R-K}}$, such that the ground state of $H_{\text{R-K}}$ can be treated as an approximate ground state of the Rydberg Hamiltonian (2.33). To do so, we firstly add a parameter dependent Hamiltonian, $H_{\xi_{\mathbf{k}}}$ and subsequently subtracting it such that the overall Hamiltonian stays unchanged. The parameter dependent Hamiltonian, $H_{\xi_{\mathbf{k}}}$ takes the following form,

$$H_{\xi_{\mathbf{k}}} = \sum_{\mathbf{k}} \mathcal{P}_{\mathbf{k}}[\xi_{\mathbf{k}}^{-1}n_{\mathbf{k}} + \xi_{\mathbf{k}}(1 - n_{\mathbf{k}})], \quad (2.35)$$

where $\mathcal{P}_{\mathbf{k}}$ is the same plaquette operator and $\xi_{\mathbf{k}}$ is a free parameter associated with the \mathbf{k} -th lattice site. By rearranging the terms, one can rewrite the effective Hamiltonian as

$$H_{\text{eff}} = E_0(\xi_{\mathbf{k}}) + H_{\text{R-K}}(\xi_{\mathbf{k}}) + H'(\xi_{\mathbf{k}}), \quad (2.36)$$

where $E_0(\xi_{\mathbf{k}})$ effectively acts as the approximate ground state energy of the system, $H_{\text{R-K}}(\xi_{\mathbf{k}})$ is the Hamiltonian that is of the R-K type with a ground state known exactly, and $H'(\xi_{\mathbf{k}})$ contains all of the rest of the terms that acts as a perturbation. Notice that all terms are now $\xi_{\mathbf{k}}$ dependent. The task then is to minimise the perturbing term, $H'(\xi_{\mathbf{k}})$, such that the ground state of $H_{\text{R-K}}(\xi_{\mathbf{k}})$ effectively becomes the approximate ground state of Hamiltonian (2.33). The perturbing Hamiltonian will mainly depend on the system dimension and the lattice geometry as shown in later chapters. In the simple one-dimensional situation with homogeneous system, we will demonstrate that $H'(\xi_{\mathbf{k}})$ can be almost neglected completely within a specific parameter regime. In higher dimensions, this is no longer possible even with introducing such parameter regime due to non-negligible effective many-body terms. An alternative treatment will be applied to deal with this difficulty. For now, let us assume that the impact of $H'(\xi_{\mathbf{k}})$ on the ground state of the Rydberg lattice gas is small in general, such that this ground state is well described by the ground state of $H_{\text{R-K}}(\xi_{\mathbf{k}})$. In the following section, we will focus on the properties of $H_{\text{R-K}}(\xi_{\mathbf{k}})$ and analyse its ground state.

2.2.2 Hamiltonian of the Rokhsar-Kivelson Type

Since the ground state of the Rokhsar-Kivelson Hamiltonian will act effectively as the approximate ground state of the Rydberg Hamiltonian, we now analyse $H_{\text{R-K}}$ and its ground state in detail. By definition, a Hamiltonian of the R-K type can be expressed as a sum of positive-semidefinite Hermitian operators, $h_{\mathbf{k}}$, that is

equal to the square of it, i.e. $h_{\mathbf{k}} = h_{\mathbf{k}}^\dagger h_{\mathbf{k}}$ [86],

$$H_{\text{R-K}} = \sum_{\mathbf{k}} h_{\mathbf{k}}^\dagger h_{\mathbf{k}}. \quad (2.37)$$

This type of Hamiltonian is essentially a frustration free Hamiltonian in which the ground state of the total Hamiltonian is also the ground state of each local Hamiltonian, i.e. the ground state of $H_{\text{R-K}}$ is also the ground state for each and every $h_{\mathbf{k}}$ in this case. This is a convenient property as it allows the ground state to be constructed analytically by finding the wavefunction that is annihilated by each and every one of these Hermitian operators, $h_{\mathbf{k}}$, i.e. $h_{\mathbf{k}}|G\rangle = 0$. Then, due to $H_{\text{R-K}}$ being a frustration free Hamiltonian, $|G\rangle$ is then the ground state of $H_{\text{R-K}}$. Another very important property of the Hamiltonian of R-K type is that, often, the normalisation constant in the ground state is equivalent to the partition function of a classical system defined over the Hilbert space [86].

For the Rydberg lattice gases considered in this thesis, we construct a set of ξ -dependent $h_{\mathbf{k}}$ that allows us to approximate H_{Ryd} effectively by $H_{\text{R-K}}$ despite the choice of $\xi_{\mathbf{k}}$ locally and the dimensionality of the system. The constructed Hamiltonian of the R-K type, $H_{\text{R-K}}$ takes the form of Eq. (2.37), with

$$h_{\mathbf{k}} = (\xi_{\mathbf{k}}^{-1} + \xi_{\mathbf{k}})^{-1/2} \mathcal{P}_{\mathbf{k}}[\sigma_{\mathbf{k}}^x + \xi_{\mathbf{k}}^{-1} n_{\mathbf{k}} + \xi_{\mathbf{k}}(1 - n_{\mathbf{k}})]. \quad (2.38)$$

It can be shown that $h_{\mathbf{k}}^\dagger h_{\mathbf{k}} = h_{\mathbf{k}}$. Since the ground state is annihilated by all $h_{\mathbf{k}}$, we construct the ground state $|G\rangle \equiv |\{\xi_{\mathbf{k}}\}\rangle$ as [31, 38],

$$|\{\xi_{\mathbf{k}}\}\rangle = \frac{1}{\sqrt{Z_{\xi_{\mathbf{k}}}}} \prod_{\mathbf{k}} (1 - \xi_{\mathbf{k}} \sigma_{\mathbf{k}}^+ \mathcal{P}_{\mathbf{k}}) |\downarrow\downarrow \cdots \downarrow\rangle, \quad (2.39)$$

where $|\{\xi_{\mathbf{k}}\}\rangle$ depends on the choice of the parameters set $\{\xi_{\mathbf{k}}\}$, $Z_{\xi_{\mathbf{k}}}$ is a normalisation constant, and $\sigma_{\mathbf{k}}^+ = (\sigma_{\mathbf{k}}^x + i\sigma_{\mathbf{k}}^y)/2$ is a spin creation operator. By expanding this state in the spin product basis, one sees that this state is a coherent superposition of all spin states which do not contain adjacent up-spins. Each allowed configuration is associated with a particular $\xi_{\mathbf{k}}$ -dependent probability amplitude. Therefore, the choices of the set of parameters $\xi_{\mathbf{k}}$ plays an important role in the determination of the ground state since they can suppress (enhance) the weight of particular spin configurations. For a large system size, L , we see that it is unfeasible to expand the ground state and write it in full due to the exponentially increasing number of states with increasing lattice size. Based on the property of the ground state of the Hamiltonian of R-K type in which the normalisation constant, $Z_{\xi_{\mathbf{k}}}$ is exactly equivalent to the partition function of a corresponding classical system, it is then possible to analyse the ground state by establishing the

formal connection to the classical counterpart and obtain its partition function. Due to the nearest neighbour blockade mechanism adopted in the Rydberg lattice gas and with each atom being effectively treated as a two-level atom (spin-1/2 particle), the classical counterparts, as we will demonstrate in latter parts of the thesis, correspond to classical hard-object lattice models [31, 32].

In the following section, we will study a homogeneous Rydberg lattice gas in a one-dimensional lattice by adopting the strategy discussed in the previous section and the R-K approximation technique discussed in this section. This study is based on the study carried out in Ref. [31] and will serve as an example in applying the discussed strategy and technique.

2.3 A Homogeneous One-dimensional Rydberg Lattice Gas

In Sec. 2.2.1, we outlined a strategy for finding the approximate ground state of the Rydberg lattice gas with arbitrary dimensionality and with site dependent laser couplings. To demonstrate how the strategy is adopted in detail and, in particular, to show how the system is eventually connected to a lattice gas of hard-objects (hard-object lattice model), let us take the one-dimensional homogeneous Rydberg lattice gas as an example and analyse its static properties by following Ref. [31, 38]. By “homogeneous”, we mean that the laser parameters are no longer site-dependent, i.e. $\{\Omega_{\mathbf{k}}, \Delta_{\mathbf{k}}\} \rightarrow \{\Omega, \Delta\}$, and therefore become spatially homogeneous. Referring to Hamiltonian (2.34), and taking the index \mathbf{k} to be a scalar quantity as for one-dimension, we arrive at the system Hamiltonian,

$$H_{\text{eff1D}} = \Omega \sum_k^L \mathcal{P}_k \sigma_k^x + \Delta \sum_k^L n_k + \frac{1}{2} \sum_{|k-m|>1}^L V_{|k-m|} n_k n_m, \quad (2.40)$$

with $\mathcal{P}_k = P_{k-1} P_{k+1}$ and $P_k = (1 - n_k)$. Now, following the procedure given previously, by adding a term, $\sum_k \mathcal{P}_k [\xi^{-1} n_k + \xi(1 - n_k)]$ to H_{eff1D} , and subsequently subtracting it, we arrive at,

$$H_{\text{eff1D}} = E_0(\xi) + H_{\text{R-K}\xi} + H'(\xi),$$

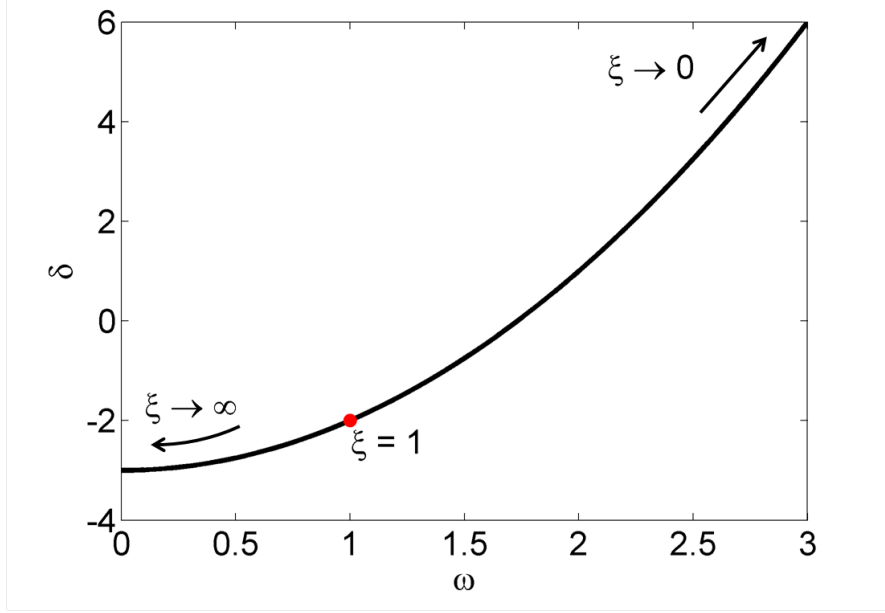


Figure 2.8: The ξ -manifold as introduced in Eq. (2.42) is plotted in the ω, δ -plane defined in the content. The red dot marks the location at where $\xi = 1$. As ξ approaches infinity, the curve lies exactly on the δ -axis at $\delta = -3$.

where,

$$\begin{aligned}
E_0(\xi) &= -\Omega L \xi; \\
H_{\text{R-K}}(\xi) &= \Omega \sum_k^L h_k^\dagger h_k, \\
\text{with } h_k &= (\xi^{-1} + \xi)^{-1/2} P_{k-1} P_{k+1} [\sigma_k^x + \xi^{-1} n_k + \xi(1 - n_k)]; \\
H'(\xi) &= \sum_k^L [\Delta + \Omega(3\xi - \xi^{-1}) + (2^{-6}V - \Omega\xi)n_{k+2}]n_k \\
&\quad + V \sum_{m>k+2}^L \frac{n_k n_m}{|k-m|^6} \\
&\quad - \Omega(\xi - \xi^{-1}) \sum_k n_k n_{k+1} (2 - n_{k+2}). \tag{2.41}
\end{aligned}$$

To proceed, we will now minimise $H'(\xi)$ such that $E_o(\xi)$ will effectively act as the approximate ground state energy of H_{eff1D} and the ground state of $H_{\text{R-K}}(\xi)$ will act as an approximate ground state to the exact ground state of H_{eff1D} . To minimise $H'(\xi)$, we firstly introduce the following relations between the laser parameters, V , and ξ ,

$$(i) \Delta = -\Omega(3\xi - \xi^{-1}); \quad (ii) V = 2^6 \Omega \xi. \tag{2.42}$$

By substituting these relations into $H'(\xi)$, one immediately sees that the first line in $H'(\xi)$ vanishes exactly. These parameters relation defines a manifold in which

$H'(\xi)$ is minimal and hence $H_{\text{R-K}}$ is closest to H_{eff1D} . We will refer Eqs. (2.42) as a ξ -manifold since it relates all parameters to ξ , a parameter in which the meaning of it becomes clearer and important later when constructing the ground state of $H_{\text{R-K}}(\xi)$. Solving Eq. (i) above for ξ , we arrive at

$$\xi = \frac{1}{6} \left[-\frac{\Delta}{\Omega} + \sqrt{\left(\frac{\Delta}{\Omega}\right)^2 + 12} \right], \quad (2.43)$$

which relates the free parameter ξ to experimentally accessible laser parameters Ω and Δ and allows an analytical expression for the approximate ground state energy, $E_0(\xi)$. This ξ -manifold is also illustrated in Fig. 2.8 (black) in a (ω, δ) - plane, where $\omega = 2^6\Omega/V$ and $\delta = 2^6\Delta/V$. Away from the ξ -manifold, i.e. where the combination of the laser parameters, $\{\Omega, \Delta\}$ does not fulfil Eq. (2.43), the first line of $H'(\xi)$ will no longer be zero. For parameters combinations that are sufficiently close to the ξ -manifold, the contribution of $H'(\xi)$ to H_{eff1D} can be studied perturbatively. Far away from this manifold, (c.f. Chapter 4), techniques such as variational approach can be adopted.

The second line in $H'(\xi)$ accounts for interactions at separation larger than two lattice sites, thus has very small contributions due to the quickly decaying van der Waals interaction. We can thus neglect these long range tails in the interaction terms. The last term is exactly zero when $\xi = 1$. Away from this condition, the last term in $H'(\xi)$ can still be neglected in the physical subspace since $n_k n_{k+1}$ accounts for simultaneous excitation of neighbouring atom which are excluded in this particular subspace of the Hilbert space. Therefore, one can safely neglect $H'(\xi)$ within the ξ -manifold, and hence, allowing us to approximate the exact ground state of the Rydberg Hamiltonian by the ground state, $|\xi\rangle$ of $H_{\text{R-K}}(\xi)$.

Let us now concentrate on $H_{\text{R-K}}(\xi)$ and its analytical ground state which according to Eq. (2.39), can be constructed as [31, 38],

$$|\xi\rangle = \frac{1}{\sqrt{Z_\xi}} \prod_k^L (1 - \xi \sigma_k^+ \mathcal{P}_k) |\downarrow\downarrow \cdots \downarrow\rangle. \quad (2.44)$$

Comparing it with Eq. (2.39), one immediately sees that the ground state now only depends on a global parameter, ξ . Expanding the product, we illustrate $|\xi\rangle$ graphically in Fig. 2.9 where one sees that the ground state is simply a superposition of all possible configurations of arrangement of Rydberg atoms under the restriction of nearest neighbour exclusion. Here, each allowed configuration is associated with a probability amplitude of $(-\xi)^n$ with n being the number of Rydberg atoms in the lattice, or equivalently, the number of up-spins in the spin configu-

$$|\xi\rangle = \frac{1}{\sqrt{Z_\xi}} \prod_k^L (1 - \xi P_{k-1} \sigma_x^k P_{k+1}) |\downarrow\downarrow\downarrow\downarrow\dots\downarrow\rangle$$

Figure 2.9: A graphical illustration of the ground state of $H_{\text{R-K}}(\xi)$, $|\xi\rangle$. Here, each grey dot represents a lattice site occupied by a ground state atom (down-spin) and a blue dot represents a lattice site occupied by a Rydberg atom (up-spin). Each configuration is associated with a probability amplitude given by $(-\xi)^{n_k}$.

ration. Therefore, the likelihood of Rydberg excitation is controlled by the choice of ξ . Referring to Fig. 2.9 together with Fig. 2.8, for instance, in the limiting case where $\xi \rightarrow 0$, the only surviving state is the all spin-down state (spin vacuum), and hence no Rydberg excitation; for $\xi \gg 1$ on the other hand, $|\xi\rangle$ is dominated mainly by states with high number of Rydberg excitations, and in the limiting case, where $\xi \rightarrow \infty$, the ground state can be approximated by a superposition of two anti-ferromagnetic spin states as $|\xi\rangle|_{\xi \rightarrow \infty} \approx \frac{1}{\sqrt{2}}(|\uparrow\downarrow\uparrow\downarrow\uparrow\downarrow\dots\rangle + |\downarrow\uparrow\downarrow\uparrow\downarrow\dots\rangle)$. Hence, one expects an expectation value of the fractional density of Rydberg atoms defined as,

$$\langle n \rangle = \frac{1}{L} \sum_k^L n_k, \quad (2.45)$$

to be approximately 0.5 due to nearest neighbour blockade. At the end of the previous section, we briefly brought up the idea of mapping the Rydberg lattice gas to a hard-object model. With the aid of Fig. 2.9, let us now discuss this mapping in detail for the one-dimensional Rydberg lattice gas. Firstly, for all possible Rydberg arrangements on the lattice, due to the nearest neighbour blockade, each Rydberg atom is always accompanied by a ground state atom on each of its sides. This allows us to effectively treat each Rydberg atom as a hard-dimer with a length of $2a$ and with the centre located on the lattice site. Then, one immediately notices that the partition function is equivalent to the counting of all possible hard-dimers arrangement on a one-dimensional lattice with each hard-dimer weighted by a fugacity factor given by ξ^2 . In the following sections, starting with a brief review of statistical physics on partition functions, we will demonstrate how this partition function can be analytically obtained by using the so-called transfer matrix method by following Ref. [87].

2.3.1 Brief Review of Statistical Physics

In this section, we will briefly introduce the formalisation of partition functions. The canonical partition function of a classical system of fixed volume and number

of particles in the content of statistical physics is defined as,

$$Z = \sum_c e^{-\beta E_c}, \quad (2.46)$$

where $\beta = 1/(k_b T)$ is the inverse temperature with k_b being the Boltzmann constant and T being the temperature of the system, and E_c is the energy of the system in the microstate denoted by c .

With known knowledge of the partition function, it is then possible to obtain expectation value of thermodynamic quantities such as energy, E_c , by,

$$\langle E_c \rangle = \frac{\sum_c E_c e^{-\beta E_c}}{Z} \quad (2.47)$$

As one notices so far, the partition function that describes a thermal system is a function of temperature. However, temperature is irrelevant in the calculation performed in the rest of thesis as we will use partition function in a more generalised manner where β is parameter such that $e^{-\beta H_c}$ is interpreted as the likelihood that a configuration indexed by c with energy functional H_c would occur in the system. And we will set $\beta = 1$ for the sake of simplicity such that the probability of the occurrence of the configuration is only dependent on their energies. And we shall no longer include it in the calculation in partition function so that,

$$Z = \sum_{\{c\}} e^{-H_c}, \quad (2.48)$$

with H_c being unitless. Another important quantity we will frequently refer to is the fugacity, ξ . Fugacity, in a general content is often defined as an effective pressure that is proportional to the mechanical pressure of the system. It is related to the chemical potential by $e^{\beta\mu}$ where μ is the chemical potential. The particular definition of the fugacity used in this thesis will be given later.

2.3.2 Partition Function of the Hard-dimers Lattice Gas

Adopting the previous mapping from the partition function Z_ξ of the wavefunction $|\xi\rangle$ onto the hard-dimer gas, let us now introduce a hard-dimer gas on a one-dimensional lattice with periodic boundary conditions. The Hamiltonian of such a hard-dimer gas can be constructed as follows,

$$H_{\text{h-d}} = V \sum_k^L n_k n_{k+1} - 2 \ln(\xi) \sum_k^L n_k. \quad (2.49)$$

In the hard-dimer regime, we have $V \rightarrow \infty$, where simultaneous occupation of particles on adjacent lattice sites k and $k+1$ is restricted. Moreover, the effective chemical potential $-2 \ln(\xi)$, as we will show later, will yield the fugacity term $\xi^{(2n)}$ for n hard-dimers present in a configuration. With this Hamiltonian, the partition function is calculated by,

$$Z = \sum_{\{n_k\}} e^{-(V \sum_k^L n_k n_{k+1} - 2 \ln(\xi) \sum_k^L n_k)}, \quad (2.50)$$

with the summation $\sum_{\{n_k\}} \equiv \sum_{n_1} \sum_{n_2} \cdots \sum_{n_L}$ and assuming that the system obeys periodic boundary condition i.e., $n_{L+1} = n_1$. Before carrying out any further calculation, let us take a closer look at the associated weights of the hard-dimers in the limit of $V \rightarrow \infty$. In particular, an excitation (hard-dimer) is weighted by the term $e^{2 \ln(\xi)} = \xi^2$. For n hard-dimers present in the configuration, we have a weight of ξ^{2n} .

To carry on with the calculation of the partition function, we now expand the sums in the exponentials which allows us to rewrite Z as,

$$Z = \sum_{n_1} \sum_{n_2} \cdots \sum_{n_L} [e^{-V n_1 n_2 + \ln(\xi)(n_1 + n_2)}] [e^{-V n_2 n_3 + \ln(\xi)(n_2 + n_3)}] \cdots [e^{-V n_L n_1 + \ln(\xi)(n_L + n_1)}]. \quad (2.51)$$

We then construct the transfer matrix by considering possible values of each of the exponential terms as the matrix elements of a transfer matrix. Mathematically, we have

$$T_{n_1 n_2} = e^{-V n_1 n_2 + \ln(\xi)(n_1 + n_2)}, \quad (2.52)$$

with n_1 and n_2 being the labels of the matrix elements, where n_k takes the value of either 0 for unoccupied lattice site k (down-spin), or 1 for an occupied lattice site k (up-spin). In matrix representation, we have,

$$\mathbf{T} = \begin{pmatrix} T_{11} & T_{10} \\ T_{01} & T_{00} \end{pmatrix} = \begin{pmatrix} e^{2 \ln(\xi) - V} & e^{\ln(\xi)} \\ e^{\ln(\xi)} & 1 \end{pmatrix} \stackrel{V \rightarrow \infty}{=} \begin{pmatrix} 0 & \xi \\ \xi & 1 \end{pmatrix}, \quad (2.53)$$

where in the last step we have applied the hard-dimer regime where $V \rightarrow \infty$. Then, each of the exponential terms in the partition function can be expressed in terms of the above transfer matrix with unique labels, and the partition function becomes the sums over a product of L matrices. According to the rule of matrix multiplication, where the matrix element A_{ij} of the matrix $\mathbf{A} = \mathbf{B} \cdot \mathbf{C}$ is given by $A_{ij} = \sum_k B_{ik} C_{kj}$, we see that the sum series in the partition function, $\sum_{n_2} \cdots \sum_{n_L}$ is equivalent to a matrix multiplication. This allows us to simplify the partition

function as,

$$Z = \sum_{n_1} (T^L)_{n_1 n_1}. \quad (2.54)$$

Then, by the definition of a trace where $\text{Tr} \mathbf{A} = \sum_i A_{ii}$, one observes that the partition function is nothing but the trace of the matrix \mathbf{T} to the power of L , i.e.

$$Z = \text{Tr}(\mathbf{T}^L). \quad (2.55)$$

However, it is rather problematic to perform the matrix power \mathbf{T}^L as the matrix contains non-zero off-diagonal elements. Since the trace is basis-independent, this problem can be resolved by an unitary transformation, S , that diagonalises the matrix, i.e. $\mathbf{T}' = S^{-1} \mathbf{T} S = \begin{pmatrix} \lambda_1 & 0 \\ 0 & \lambda_2 \end{pmatrix}$, where S contains the eigenvectors of \mathbf{T} with corresponding eigenvalues λ_1 and λ_2 . Then, the partition function can be simplified as

$$Z = \text{Tr}[(\mathbf{T}')^L] = \lambda_1^L + \lambda_2^L, \quad (2.56)$$

with the two eigenvalues,

$$\lambda_1 = \frac{1}{2}(1 - \sqrt{1 + 4\xi^2}); \quad \lambda_2 = \frac{1}{2}(1 + \sqrt{1 + 4\xi^2}). \quad (2.57)$$

In the large system limit where $L \gg 1$, the contribution of λ_1 to the partition function can be neglected since $\lambda_2^L \gg \lambda_1^L$, and hence,

$$Z_\xi = \left[\frac{1}{2} + \frac{\sqrt{1 + 4\xi^2}}{2} \right]^L. \quad (2.58)$$

Neglecting λ_1 allows a neater mathematical form of the partition function as well as the fractional density that will be calculated in the proceeding section. However, we emphasise here that neglecting λ_1 is not a necessity in the analytical calculations performed in the rest of the thesis. In fact, for finite lattice size, particularly for small lattice size where numerical simulation is feasible, one observes that the contribution of λ_1 is no longer negligible. Therefore, one has to take the contribution of λ_1^L into consideration, and the effect of such term will be further discussed in Chapter 3 when studying the inhomogeneous Rydberg lattice gas.

2.3.3 Application of the Partition Function

In this section, we demonstrate a few quantities which can be calculated now by using the previously obtained partition function, Z_ξ and the transfer matrix

method. Let's start with calculating the fractional density as defined previously,

$$\frac{\langle N \rangle}{L} = \frac{\sum_k^L \langle \xi | n_k | \xi \rangle}{L} = \langle \xi | n_k | \xi \rangle \equiv \langle n_k \rangle. \quad (2.59)$$

The idea is to follow the standard partition function formalism to calculate expectation values of classical observables. For instance, to calculate $\langle \hat{O} \rangle$ with \hat{O} being arbitrary operator, we have $\langle \hat{O} \rangle = \sum_s \hat{O} e^{-H(s)} / Z$. Hence, to obtain $\langle n_k \rangle$, we have,

$$\langle n_k \rangle = \frac{1}{Z_\xi} \sum_{n_1} \sum_{n_2} \dots \sum_{n_L} n_k e^{-(V \sum_k^L n_k n_{k+1} - 2 \ln(\xi) \sum_k^L n_k)}. \quad (2.60)$$

Noticing that the part $e^{-(V \sum_k^L n_k n_{k+1} - 2 \ln(\xi) \sum_k^L n_k)}$ can be expressed in terms of the transfer matrix as described in previous section, we can simplify the expectation value as,

$$\langle n_k \rangle = \frac{1}{Z_\xi} \sum_{n_1} \sum_{n_2} \dots \sum_{n_L} [T_{n_1 n_2} T_{n_2 n_3} \dots T_{n_{k-1} n_k} n_k T_{n_k n_{k+1}} \dots T_{n_L n_1}], \quad (2.61)$$

with $n_k = \begin{pmatrix} 1 & 0 \\ 0 & 0 \end{pmatrix}$. The sums again, are equivalent to a trace, which allow us to write

$$\langle n_k \rangle = \text{Tr}[T_{n_1 n_2} T_{n_2 n_3} \dots T_{n_{k-1} n_k} n_k T_{n_k n_{k+1}} \dots T_{n_L n_1}], \quad (2.62)$$

and further using the cyclic property of the trace, we have,

$$\langle n_k \rangle = \text{Tr}(n_k \mathbf{T}^L), \quad (2.63)$$

with \mathbf{T} being the transfer matrix obtained in the previous section. Using the diagonalised transfer matrix where $\mathbf{T}' = S^{-1} \mathbf{T} S$, $\langle n_k \rangle$ becomes,

$$\langle n_k \rangle = \frac{1}{Z_\xi} \text{Tr}[S^{-1} n_k S (S^{-1} \mathbf{T} S)^L] = \frac{\text{Tr}[S^{-1} n_k S \mathbf{T}'^L]}{\text{Tr}[\mathbf{T}'^L]}, \quad (2.64)$$

with the partition function, Z_ξ also expressed in terms of the transfer matrix according to result in previous section. One finds that in the limit of L approaches infinity,

$$\langle n_k \rangle = \frac{1}{2} - \frac{1}{2\sqrt{1+4\xi^2}}. \quad (2.65)$$

Using similar ideas, we can also construct density-density correlation, $\langle n_k n_m \rangle$. In this case, the operator of interest will be $n_k n_m$, and the expectation value can

be obtained as,

$$\begin{aligned} \langle n_k n_m \rangle = & \frac{1}{Z_\xi} \sum_{n_1} \sum_{n_2} \cdots \sum_{n_L} [T_{n_1 n_2} T_{n_2 n_3} \cdots T_{n_{k-1} n_k} n_k T_{n_k n_{k+1}} \\ & \cdots T_{n_{m-1} n_m} n_m T_{n_m n_{m+1}} \cdots T_{n_L n_1}]. \end{aligned} \quad (2.66)$$

Following the identical procedure by turning the series of summations into matrix representation where the sum becomes the trace of the diagonalised matrix, we have the following formalisation,

$$\langle n_k n_m \rangle = \frac{\text{Tr}[S^{-1} n_k S(\mathbf{T}')^m S^{-1} n_m S(\mathbf{T}')^{L-m}]}{\text{Tr} \mathbf{T}'^L}, \quad (2.67)$$

with the partition function also expressed in terms of the transfer matrix, the expression yields the following result:

$$\langle n_k n_m \rangle = \frac{1 - \sqrt{1 + 4\xi^2} + 2\xi^2 \left(1 + \frac{-1 - 2\xi^2 + \sqrt{1 + 4\xi^2}}{2\xi^2}\right)^{m-k+1}}{2 + 8\xi^2}. \quad (2.68)$$

The transfer matrix method also allows one to obtain expectation values of higher moments.

2.3.4 Exact Numerical Calculation of $|G\rangle$ in One-dimension

In this section, we will briefly explain how numerical calculation of the ground state, $|G\rangle$ of the Rydberg lattice Hamiltonian, H_{Ryd} is performed. The idea is to write the Hamiltonian in a matrix representation and then solve the matrix for its eigenvalues and eigenvectors. The ground state is the eigenvector that corresponds to the lowest eigenvalue. The matrix size will be 2^L -by- 2^L for L atoms.

To construct the matrix, we will first write the operators in Hamiltonian H_{Ryd} in matrix forms, where

$$n_k = \begin{pmatrix} 1 & 0 \\ 0 & 0 \end{pmatrix}; \quad \sigma_k^x = \begin{pmatrix} 0 & 1 \\ 1 & 0 \end{pmatrix}. \quad (2.69)$$

Then, the summations in H_{Ryd} can be expanded using Kronecker product. Using two atoms as an example, the first term in H_{Ryd} reads,

$$\sum_k^2 \Omega_k \sigma_k^x = \Omega_1 \sigma_1^x \otimes \mathbb{1}_2 + \Omega_2 \mathbb{1}_1 \otimes \sigma_2^x, \quad (2.70)$$

where $\mathbb{1}$ is an identity matrix, and in the homogeneous Rydberg lattice case considered in the previous sections, $\Omega_1 = \Omega_2$. The other terms in H_{Ryd} can be expanded

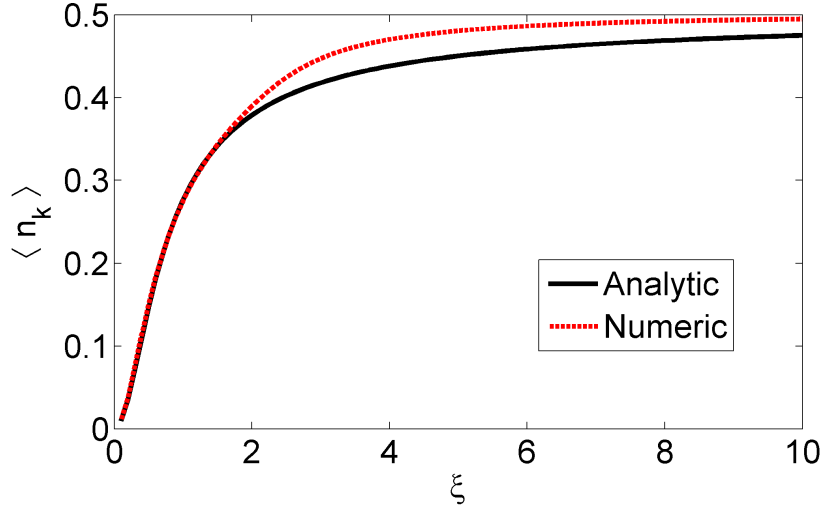


Figure 2.10: Fractional Rydberg density as a function of ξ in the ξ -manifold for a lattice size $L = 12$. The analytical result obtained in Eq. (2.65) is plotted black, and the numerical result obtained by diagonalising H_{Ryd} is depicted in dash red.

in a similar way. For L atoms, we have, with the first summation as an example,

$$\begin{aligned} \sum_k^L \Omega_k \sigma_k^x &= \Omega_1 \sigma_1^x \otimes \mathbb{1}_2 \otimes \cdots \otimes \mathbb{1}_L + \Omega_2 \mathbb{1}_1 \otimes \sigma_2^x \otimes \cdots \otimes \mathbb{1}_L + \cdots \\ &\quad + \Omega_L \mathbb{1}_1 \otimes \mathbb{1}_2 \otimes \cdots \otimes \sigma_L^x. \end{aligned} \quad (2.71)$$

This method is very straight forward, but lacks of computational convenience as it takes significant amount of computational time due to the amount of loops required to carry out these summations and the fact that the matrix changes its size each time a Kronecker product is performed. An alternative numerical method is to use a convenient basis and write the Hamiltonian in this basis. For instance, one can use the spin product basis, where each Rydberg arrangement in the lattice corresponds to a particular spin product state. This further allows one to utilise certain symmetries in the system to write the matrix in a block diagonal form [88]. As a result, one can diagonalise each block at a time instead of diagonalising the entire matrix to reduce computational effort. This idea of block diagonalisation is further explained in Chapter 5.

To demonstrate the numerical results and compare them with the approximate analytical results obtained in previous sections, for a lattice size, $L = 12$, we plot Rydberg fractional density in Fig. 2.10 as a function of the fugacity, ξ in the ξ -manifold. The analytical result given in Eq. (2.65) is plotted in black and the exact numerical result obtained by diagonalising H_{Ryd} is plotted in dash red. The exceptionally good agreement at small fugacity shows that the validity of the analytical treatment provided. The small discrepancy at larger ξ can be explained

by finite size effects. For larger system size and further comparison between the numerics and the analytical results, please refer to Ref. [31].

2.4 Conclusion

In this chapter, we started with reviewing some of the essential properties of Rydberg atoms in relevant to this thesis. Then, with these properties in mind, we introduced the systems, the strongly interacting Rydberg lattice gases, that have been studied in this thesis. To show how one can both approximately analytically and numerically investigate the ground state properties of the Hamiltonian, H_{Ryd} that describes the Rydberg lattice gas, we used a one-dimensional homogeneous Rydberg lattice gas as an example to provide the general methodology which will be used in later chapters. The methods presented in this chapter were also discussed in Ref. [31], and we refer the readers to this work for further details on the phase diagram and Ref. [38] for the analytical construction of the first excited state of the homogeneous Rydberg lattice gas.

One of the key steps in the approximate analytical treatment of the Rydberg lattice gas is the use of the Hamiltonian that has the Rokhsar-Kivelson form in which the ground state can be constructed analytically. By mapping the Hamiltonian of the Rydberg lattice gas onto the Hamiltonian of the Rokhsar-Kivelson form, and by introducing a ξ -manifold, we are able to use the ground state of $H_{\text{R-K}}$ to approximate the exact ground state of H_{Ryd} . There are a few limitations in the utilisation of $H_{\text{R-K}}$. Firstly, the ground state $|\{\xi_{\mathbf{k}}\}\rangle$ of this Hamiltonian is only closest to the true ground state of H_{Ryd} in the ξ -manifold. Away from this manifold, the approximation is expected to work less well. As shown in Chapter 4 later, other techniques such as variational approach are necessary to study the ground state of H_{Ryd} beyond the manifold. Another limitation is to do with the analytical calculation of the normalisation constant Z_{ξ} in the ground state $|\xi\rangle$. As we have demonstrated in Sec. (2.3.2), Z_{ξ} is equivalent to the partition function of the hard-dimers lattice gas and can be analytically obtained by using a transfer matrix method. One essential approximation in deriving Z_{ξ} in Eq. (2.58) is that $L \gg 1$, i.e. very large system size. This large system limit suggests that Eq. (2.58) is less accurate when considering small systems since the contribution of λ_1 in Eq. (2.56) is no longer negligible. This problem arises later in the study of an inhomogeneous Rydberg lattice gas in Sec. 3.3.1. Last, when we consider a Rydberg lattice gas in two-dimensions later on in Sec. 4.4, the analytical calculation of the normalisation constant in the ground state of $H_{\text{R-K}}$ is no longer possible and the system size is limited by the corresponding numerical technique adopted. Though having these limitations, the Rokhsar-Kivelson description is still powerful

in studying the Rydberg lattice gases as we will continuously demonstrate.

In potential experimental realisation of the Rydberg lattice gas, there are a few practical imperfections which require consideration. Laser fields in the experiment are in real life never homogeneous. Therefore, the intensity of the laser fields will have spatial variations. These variations then induce fluctuations in the laser parameters, $\{\Omega, \Delta\}$, that are used in describing the Rydberg lattice gas. Therefore, strictly speaking, the ξ -manifold is almost never fulfilled due to these fluctuations. However, provided that these fluctuations is small enough, the approximated mapping from the Hamiltonian that describes the Rydberg lattice gas to the Hamiltonian of the R-K type is still considered to be valid. Moreover, this mapping should enable perturbative studies of the Rydberg lattice gas not far away from the ξ -manifold. More on this randomness in the laser parameters will be discussed toward the end of the next chapter.

In discussing the radiative lifetime of Rydberg atoms in Sec. 2.1.3, a significant contribution to the actual lifetime has not been discussed. This contribution comes from the black-body radiation, and has significant impact on Rydberg atoms in current ultra-cold atomic experiments that are operated under room-temperature conditions [19]. The black-body radiation induces transitions from the populated Rydberg state to nearby states due to small energy differences and the large transition dipole moment between the populated Rydberg state and nearby states[89]. On the one hand, this effect will lead to a much more complicated level structure of the Rydberg atom. On the other hand, with increasing principle quantum number, ν , the blackbody radiation that reduces the lifetime of the excited electron generally becomes more and more significant [90]. The decrease in the lifetime of a Rydberg atom can reach 40% at room-temperature as claimed in Ref. [91]. With this reduction in the lifetime, however, the actual lifetime of an atom in a highly excited electronic state is still on the order of tens of microseconds [92]. In comparison to the excitation dynamic timescale, i.e. Rabi-oscillation of the atom from its ground state to Rydberg state, which is a few microseconds in typical ultra-cold atomic experiments [93, 94], the lifetime of Rydberg atoms is sufficiently long for potential experimental realisation of the Rydberg lattice gas even with the consideration of black-body radiation. Therefore, it is safe to neglect the contribution of the black-body radiation to the systems of interest, which eventually ensures the validity of the two-level approximation of the atoms by avoiding the complicated decay channels induced by the black-body radiation.

In the next Chapter, we will begin to investigate the system with more complexity emerging through the introduction of inhomogeneities into the system. As one will see, the method described in this chapter is also applicable to inhomogeneous Rydberg lattice gas and permits an approximate analytical treatment.

Moreover, the inhomogeneities will lead to interesting physics such as symmetry breaking and transition behaviours.

Chapter 3

The Ground State of Inhomogeneous One-dimensional Rydberg Lattice Gas

In the previous chapter, we demonstrated the capability of using a frustration-free Hamiltonian to obtain approximate ground states of the Rydberg lattice gases. By following Ref. [31] and reviewing the homogeneous one-dimensional Rydberg lattice gas, it was clear from the results that this approximate analytical solution obtained from the introduced quantum hard-object model based on the frustration-free Hamiltonian very successfully described the actual Rydberg lattice gas, particularly in the ξ -manifold. However, what remains unclear was whether the frustration free-Hamiltonian is still applicable to a more general situation where the Rydberg lattice gas takes the generic form given in Eq. (2.33) in which parameters can vary site-to-site. Intrigued by this unanswered question, we will investigate deliberately designed inhomogeneous Rydberg lattice gases in a one-dimensional setup in this chapter [36]. Surprisingly, as one shall see later, despite the presence of arbitrary choices of inhomogeneities, the construction of a generic frustration-free Hamiltonian permits the approximate analytical study of the ground state properties of these inhomogeneous system.

3.1 Introduction

The study of inhomogeneities in many-body physics has been always an active and flourishing field of research for many reasons. For instance, the presence of inhomogeneities in a many-body system, for example, can smear out characteristic sharp features of phase transitions and (de-)enhance correlations in the ground state[95, 96]. Many-body systems subject to external fields that are inhomoge-

neous have been extensively studied in the past [95, 96, 97, 98, 99, 100, 101, 102]. To understand the effects of these type of inhomogeneities, both analytical and numerical approach have been developed to theoretically investigate inhomogeneous many-body systems such as the Ising model with random exchange energies [96, 97]. Recently, with the tremendous boost in ultra-cold experiments, simulations of many-body systems, such as the Bose-Hubbard model with inhomogeneous external fields became feasible experimentally [103]. One of the very recent breakthrough experiments with Rydberg atoms, as beautifully reported in Ref. [94], has shown that single site addressing of atoms is achievable. The experiment on one hand permits direct visualisation of correlations of Rydberg atoms while on the other hand, provides precise control on the external fields experienced by individual atom in the optical lattice. Hence, it enables the possibility to deliberately implement inhomogeneous laser fields to the Rydberg lattice gases proposed in the previous chapter.

Despite its fundamental interest and experimental realizability discussed so far, inhomogeneities are also very important due to its unavoidable presence in natural physical systems. Examples include the presence of impurities and disorder. For instance, spatial variations in the external fields (lasers) used in ultra-cold experiments are intrinsic properties of the experimental setup. Therefore, considering only the homogeneous situation theoretically does not provide a complete picture of a system that will be observed in an experiment, and our understandings of the effects of these inhomogeneities are of immediate importance and relevance to on-going researches. Motivated by these reasons, we therefore decided to go beyond the homogeneous Rydberg lattice gases and investigate the effects of inhomogeneities. The inhomogeneities we are mainly interested in are induced by the variation of the laser fields that couple the ground state atoms to the Rydberg state and controlled by the laser parameters, i.e. the Rabi-frequency and the detuning. The details of how exactly they can be varied will be discussed in later sections.

The chapter is organised as follows. We start by considering the generic Rydberg lattice gases in one-dimension and show that approximated analytical solutions exist despite the choices of inhomogeneous laser fields. Then, in Sec. 3.3, we consider one of the simplest inhomogeneities that can be included into the lattice gas, which is a single impurity. The effect of the local perturbation on the impurity site is analysed in terms of the correlations between Rydberg atoms. We show that the impurity can lead to a breaking of the ground state symmetry. Motivated by this result, we introduce staggered laser fields where the atoms are radiated by two alternating lasers into the system and the results are studied in detail in Sec. 3.3.1. With the system in the staggered laser field, we demonstrate that the

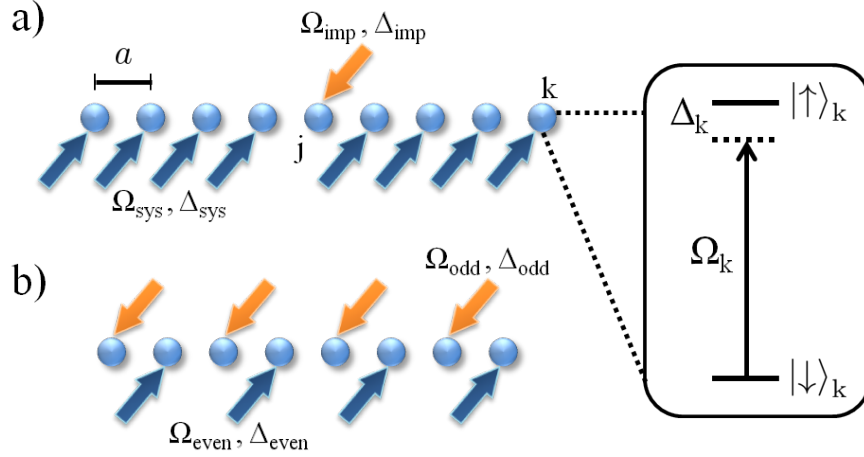


Figure 3.1: Schematics of the one-dimensional lattice with spacing, a . Each site contains a single atom whose ground state $|\downarrow\rangle_k$ is coupled to a Rydberg νs -state $|\uparrow\rangle_k$ via a laser parameterised by a site-dependent Rabi-frequency Ω_k and detuning Δ_k . (a) Rydberg lattice gas with a single impurity present on the j -th site. The impurity atom is irradiated by a laser (orange) of different parameters ($\Omega_{\text{imp}}, \Delta_{\text{imp}}$) compare to the rest of the system (blue, and parameterised by $\Omega_{\text{sys}}, \Delta_{\text{sys}}$). (b) Alternating lasers are introduced to investigate the breaking of the sublattice symmetry. On odd (even) lattice sites, a laser parameterised by Ω_{odd} (Ω_{even}) and Δ_{odd} (Δ_{even}) is used to excite atoms to Rydberg states.

system exhibits transition behaviour at a particular point in the parameter space when long range tails of the van der Waals interaction are considered. As shown in the subsequent sections, in order to gain insight in how long range tails induce the observed transition behaviour, we derive an effective Hamiltonian, known as the spin-1/2 Heisenberg XXZ model in an external magnetic field, to describe the system near the critical point. A conclusion of the results and possible future directions of research are given towards the end of the chapter.

3.2 The Inhomogeneous Rydberg Lattice Gases in One-dimension

3.2.1 The System

The inhomogeneous Rydberg lattice gases in one-dimension can be pictured with the aid of the ring lattice illustrated in Fig. 2.7 in the previous Chapter. The modifications here are the lasers irradiated on the atoms which now can vary site-to-site. Since in later sections, two specific choices of these lasers will be studied, we illustrate these two situations schematically in Fig. 3.1 to help visualising how inhomogeneities are introduced. In Fig. 3.1(a), we illustrate the single impurity

which will be discussed in Sec. 3.3, where the impurity is introduced on the j -th lattice site with a laser (orange) that is in general different from the rest of the system (blue). Similarly, in 3.1(b), we demonstrate the system with staggered laser field as introduced in Sec. 3.3.1. The lasers radiating on the odd lattice sites (orange) is in general different from the lasers radiating on the even lattice sites (blue). In general, to conveniently denote these inhomogeneous systems, we introduce site-dependent Rabi-frequency, Ω_k and Detuning, Δ_k to couple the ground state and the Rydberg state of the atom on the k -th lattice site. Though, the two cases are illustrated with a chain of atoms, we still consider periodic boundary condition for convenience.

3.2.2 The Hamiltonian and the Approximate Ground State

According to Hamiltonian (2.33), the Hamiltonian of the generic inhomogeneous Rydberg lattice gases in one-dimension is given by

$$H_{\text{Ryd}} = \sum_k^L \Omega_k \sigma_k^x + \sum_k^L \Delta_k n_k + \frac{1}{2} \sum_{k,m}^L V_{|k-m|} n_k n_m, \quad (3.1)$$

where parameters have their usual meanings. It is worth to note that though Rabi-frequency and detuning now becomes site-dependent, we still fix the Rydberg-Rydberg interaction strength at nearest neighbour distance to be constant, i.e $V = C_6/a^6$ is fixed. By following the strategy provided in Chapter 2.2.1, we introduce a frustration-free Hamiltonian of the R-K type that reads,

$$H_{\text{R-K}} = \sum_k^L \Omega_k h_k^\dagger h_k, \quad (3.2)$$

with

$$h_k = (\xi_k^{-1} + \xi_k)^{-1/2} \mathcal{P}_k [\sigma_k^x + \xi_k^{-1} n_k + \xi_k (1 - n_k)], \quad (3.3)$$

such that $h_k^\dagger h_k = h_k$. In brief, as previously discussed in Sec. 2.2.1, and further illustrated in Chapter 2.3 with the example of a homogeneous one-dimensional Rydberg lattice gas, the system Hamiltonian H_{Ryd} , in principle, can be approximated by $H_{\text{R-K}}$, hence allowing us to use the ground state of $H_{\text{R-K}}$ as an approximate ground state of the system. $H_{\text{R-K}}$ has a ground state that can be constructed based on Eq. (2.39) in one-dimension as,

$$|\{\xi_k\}\rangle = \frac{1}{\sqrt{Z_{\{\xi_k\}}}} \prod_k^L (1 - \xi_k \sigma_k^+ \mathcal{P}_k) |\downarrow\downarrow \cdots \downarrow\rangle. \quad (3.4)$$

$$|\{\xi_k\}\rangle = \frac{\dots + \xi_1 \xi_3 \dots + \xi_2 \xi_4 \dots}{\sqrt{Z_{\{\xi_k\}}}}$$

Figure 3.2: Pictorial representation of the ground state given by Eq. (3.4). The state $|\{\xi_k\}\rangle$ is a superposition of all possible arrangement of Rydberg atoms with the nearest-neighbour blockade constraint. Each arrangement has a weight which is determined by the number of Rydberg atoms and the position of them. The normalisation constant is given by $Z_{\{\xi_k\}}$ which can be determined by transfer matrix method in principle.

One can show that $|\{\xi_k\}\rangle$ best describes the actual ground state of H_{Ryd} within the ξ_k -manifold defined as,

$$(i)\Delta_k = -\Omega_k(3\xi_k - \xi_k^{-1}); \quad (ii)V = 2^6\Omega_k\xi_k, \quad (3.5)$$

where one notices that instead of fulfilling global conditions as it was the case in the homogeneous situation as shown in Eq. (2.42), the laser parameters have to be fulfilled locally and for every atom.

The ground state, $|\{\xi_k\}\rangle$, unlike in the homogeneous situation where the ground state is only dependent on a single and global parameter, the ground state $|\{\xi_k\}\rangle$ depends on a set of fugacity parameters $\{\xi_k\}$. To illustrate this, we use a pictorial representation for the ground state in Fig. 3.2. Here, the ground state is a superposition of all possible arrangement of Rydberg atoms compatible with nearest-neighbour blockade mechanism, i.e. no adjacent Rydberg atoms allowed in an arrangement. The probability amplitude associated with each arrangement is simply given by a product of fugacity parameters depending on how many Rydberg atoms are present in the arrangement and where they are. For instance, if a configuration has two Rydberg atoms on the 1st and 3rd lattice site (top right configuration), the corresponding weight is given by $\xi_1\xi_3$.

Comparing with the homogeneous situation where one has the control of only one free fugacity parameter, and changing the value of ξ results in changes of the weights of all spin configuration, now in the inhomogeneous case, one has more degrees of control to enhance (suppress) the probability amplitude of a particular or a set of configurations by altering fugacity parameters locally. More importantly, from Fig. 3.2, we notice that instead of writing down the full ground state at chosen set of ξ_k , one only needs to obtain the ξ_k -dependent normalisation con-

stant similar to the homogeneous Rydberg lattice gas. This is because all the information on the ground state is again encoded in this normalisation constant. Unsurprisingly, the variation of ξ_k from site to site leads to an increase in the complexity in calculating the normalisation constant $Z_{\{\xi_k\}}$. $Z_{\{\xi_k\}}$ now corresponds to a partition function of a hard-dimer gas with each hard-dimer has a site-dependent fugacity, ξ_k , i.e.,

$$H'_{\text{h-d}} = V \sum_k^L n_k n_{k+1} - 2 \sum_k^L \ln(\xi_k) n_k. \quad (3.6)$$

By following the transfer matrix method given previously, one finds that the partition function no longer depends on a single transfer matrix, $T_{n_i n_j}$, but L -different transfer matrices which depends on the local fugacity, ξ_k . This dramatically increases the complexity in the analytical calculation of the partition function. Nonetheless, the calculation is still feasible analytically if one only considers very few independent fugacity parameters. For example, in the following sections where we will study the effect of an impurity and staggered laser fields, one sees that in both situations, only two independent fugacity parameters are necessary.

3.3 An Impurity in the Lattice

Having the analytical ground state of the inhomogeneous system and the knowledge on how to use transfer matrix method to obtain thermodynamic quantities with arbitrary inhomogeneities, we will now investigate the effect of an impurity in the Rydberg lattice gas. This is done by preparing a system with all atoms but the j -th irradiated by the same system laser field parameterised by Ω_{sys} and Δ_{sys} with the corresponding fugacity parameter ξ_{sys} , satisfying the ξ_k -manifold given in Eq. (2.42). The impurity is then introduced on the j -th lattice site by applying a laser field characterised by Ω_{imp} and Δ_{imp} which are in general different from the system laser field. The corresponding fugacity is then ξ_{imp} , which in an experimental setting can be achieved by single site addressing as experimentally demonstrated in Ref. [94]. A schematic of the system in the presence of an impurity is illustrated in Fig. 3.1(a). Although the diagram shows a linear chain of atoms, we apply periodic boundary conditions as usual. As a result, the choice of j does not qualitatively alter the results. Thus, we will conveniently choose the middle site in the lattice as the impurity site.

To see the effect of the impurity, in the following calculation, we fix the impurity fugacity parameter to be $\xi_{\text{imp}} = 5$. The spatial density distribution across the lattice is then calculated with varying the system fugacity (vertical axis) as demonstrated in Fig. 3.3. Initially for very small ξ_{sys} , a peak of high density is

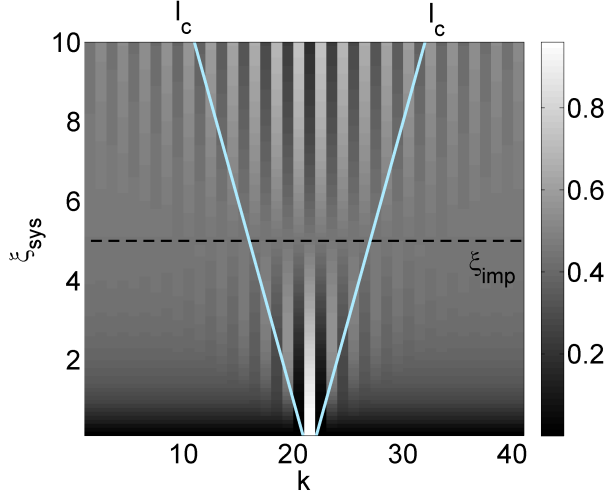


Figure 3.3: Rydberg density for a lattice with 41 sites and an impurity placed at site $j = 21$. The fugacity parameter of the impurity is given by $\xi_{\text{imp}} = 5$ (black dash) and the fugacity parameter of the remaining spins ξ_{sys} is varied from 0 to 10. With increasing ξ_{sys} the system's correlation length l_c (plotted at the cyan diagonal lines) increases. The many-body state of the system atoms becomes more strongly correlated and the presence of the impurity affects the state of more and more distant atoms. Note that for $\xi_{\text{sys}} = \xi_{\text{imp}}$ the density is homogeneous in space due to the translational symmetry of the system.

visible at the site of the impurity. Referring to the ground state given in Eq. (3.4), the excitation probability at site j is enhanced due to the fact that $\xi_{\text{imp}} \gg \xi_{\text{sys}}$. As one increases ξ_{sys} , a density oscillation pattern emerges around the impurity site, and this pattern becomes more profound as ξ_{sys} keeps increasing. The oscillation is due to the nearest neighbour blockade mechanism so that Rydberg atom can only present on every second site around the impurity site. This pattern indicates the onset of stronger and stronger correlations in the ground state. As calculated in Ref. [31], the correlation length of the system spins is given by $l_c = \xi_{\text{sys}}$ for a homogeneous system. This length is plotted as the cyan diagonal lines in the figure showing that the impurity indeed determines the state of the system atoms located within a distance l_c . Keeping increasing ξ_{sys} until $\xi_{\text{sys}} \sim \xi_{\text{imp}}$, one observes that the density modulations disappear. This is because the system becomes homogeneous as $\xi_{\text{sys}} = \xi_{\text{imp}}$, and is now translationally invariant. Since at $\xi_{\text{sys}} = 5$ is sufficiently large for the system favouring a high Rydberg density, the ground state according to Eq. (3.4), can be approximated by a superposition of two anti-ferromagnetic state as $|G\rangle \approx \frac{1}{\sqrt{2}}(|\uparrow\downarrow\uparrow\downarrow \dots\rangle + |\downarrow\uparrow\downarrow\uparrow \dots\rangle)$. If the impurity was absent, and the fugacity parameter ξ_{sys} is increased towards infinity - a limit which is achieved when Ω_{sys} approaches zero - the ground state (2.44) of the homogeneous system, i.e. is indeed a superposition of the two anti-ferromagnetic states as discussed previously in Sec. 2.3. With the impurity, when $\xi_{\text{sys}} > \xi_{\text{imp}}$, the ground state, as seen in Fig.

3.3, appears to be one of the anti-ferromagnetic states with a down-spin at the impurity site. One can also prove this by expanding Eq. (3.4). Therefore, we see that the presence of an impurity reduces the symmetry of the system by breaking the sublattice symmetry of the system when $\xi_{\text{sys}} > \xi_{\text{imp}}$.

From the above results, we see that in the vicinity of $\xi_{\text{sys}} = \xi_{\text{imp}}$, interesting physics such as symmetry breaking can occur. However, based on the calculation so far, whether the qualitative change in the spatial density distribution indicates transition behaviour remains unclear. Thus, in order to gain better understanding of the system, we will enhance the inhomogeneity by introducing a staggered laser fields that vary from odd sites to even sites. Experimentally, this is equivalent to having one laser, parameterised by ξ_{odd} , irradiate on the odd sites while having, in general, a different laser, parameterised by ξ_{even} , irradiate on the even sites. The staggered laser fields, in comparison to a single impurity, shall further reduce the symmetry of the system. Our hope is that this deliberately designed situation shall enhance, if it exists, the transition observed near the parameter regime where the two laser fields merge to a single one, i.e. $\xi_{\text{odd}} \approx \xi_{\text{even}}$.

3.3.1 Identification of a Critical Point

Carrying on with the idea of introducing staggered laser fields to the system, in this section, we will demonstrate that a critical point has been identified from numerical simulation. The system, with the staggered laser field, is depicted in Fig. 3.1(b). Here, to make it clear, the sublattice fugacity parameter ξ_{odd} (ξ_{even}), is related to the laser parameters, $\{\Omega_{\text{odd}}, \Delta_{\text{odd}}\}$ ($\{\Omega_{\text{even}}, \Delta_{\text{even}}\}$) through Eqs. (3.5). For the upcoming analysis, it is convenient to define the difference $\xi_d = \xi_{\text{odd}} - \xi_{\text{even}}$ and the sum $\xi_s = \xi_{\text{odd}} + \xi_{\text{even}}$ of the two sublattice fugacity parameters.

To investigate the effect of the staggered laser fields, let us now specifically study the expectation value of the Rydberg density on the odd sublattice $\langle n \rangle_{\text{odd}} = \sum_{k=\text{odd}} n_k / L$. Using the ground state (3.4) and following the transfer matrix method one finds,

$$\langle n \rangle_{\text{odd}} = \frac{1}{2} \left[1 + \frac{\xi_d - \xi_s^{-1}}{\sqrt{(1 + \xi_s^{-2})(1 + \xi_d^2)}} \right]. \quad (3.7)$$

To verify the analytical results, we numerically diagonalise Hamiltonian (2.40) to obtain the sublattice density, $\langle n \rangle_{\text{odd}}$, and compare it to Eq. (3.7) with fixed $\xi_s = 5$ and $\xi_s = 20$. The numerical diagonalisation used here is very similar to the one that we introduced in Sec. 5.6. In short, we write H_{Ryd} in a matrix representation that is calculated from the sum of the tensor products in this Hamiltonian. e.g. $\sum_k^2 \Omega_k \sigma_k^x = \Omega_1 \sigma_1^x \otimes \mathbf{1}_2 + \Omega_2 \mathbf{1}_1 \otimes \sigma_2^x$. For the laser parameters, Ω_k and Δ_k , we

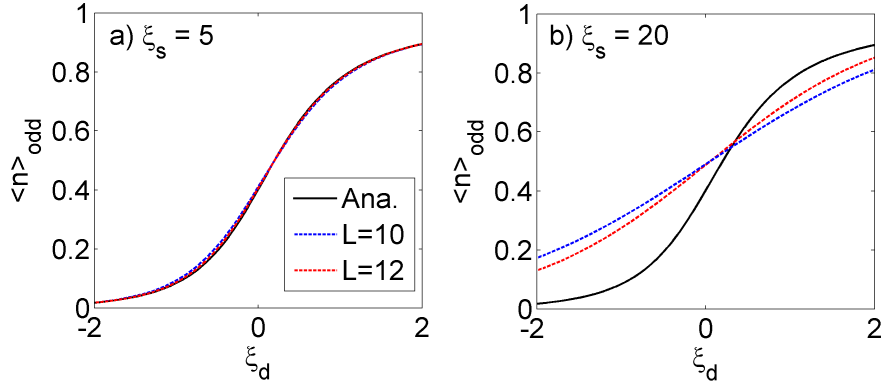


Figure 3.4: We plot the analytical result obtained from Eq. (3.7) in black and compare it to the numerically obtained $\langle n \rangle_{\text{odd}}$ from diagonalising Hamiltonian (2.40) within the ξ_k -manifold given in Eq. (2.42), with $\xi_s = 5 < L$ in (a) and with $\xi_s = 20 > L$ in (b). In (a), we see an excellent agreement and a clear convergence of the numerical results toward the analytical one with increasing lattice size. However, in (b), the results disagree due to the fact that the correlation length given by $\eta_c = \xi_s/2$ is beyond the lattice size and a large ξ_s and relatively small L leads to non-negligible contribution from the 2nd eigenvalues of the transfer matrix [c.f. Sec. 2.3.2] for more details)

express them in terms of ξ_k in the ξ_k -manifold introduced in Eqs. (3.5). One can then obtain classical observables such as $\langle n \rangle_{\text{odd}}$ with the numerical ground state obtained from the diagonalisation.

The results are compared in Fig. 3.4. In (a), we see the analytical result is in good agreement with the numerics. As one increases the lattice size in the numerical calculation, a convergence of the results toward the analytical results is also found. However, in plot (b) where $\xi_s = 20$ the numerics and analytic are no longer in agreement. We notice that the major difference between the two cases is the choice of ξ_s in respect with the value of the lattice size, L . With further investigation of different combination of ξ_s and L , we find that as long as $\xi_s < L$, the results are in good agreement. To physically explain this, one can show that the correlation length $\eta_c = \xi_s/2$ at $\xi_d = 0$ meaning that for $\xi_s > L$, the correlation length of the system is beyond the lattice size. Another reason is due to the finite size where the approximation used in the transfer matrix method is not well justified. For instance, as demonstrated in Sec. 2.3.2, when calculating the partition function of the hard-dimer gases, one of the eigenvalues in the transfer matrix has been neglected in the thermodynamic limit. Nonetheless, for small system size and large ξ_s , one notices that the two eigenvalues are on the same orders of magnitudes. Therefore, in the following calculations, we restrict ourselves to relatively large L with ξ_s always smaller than L .

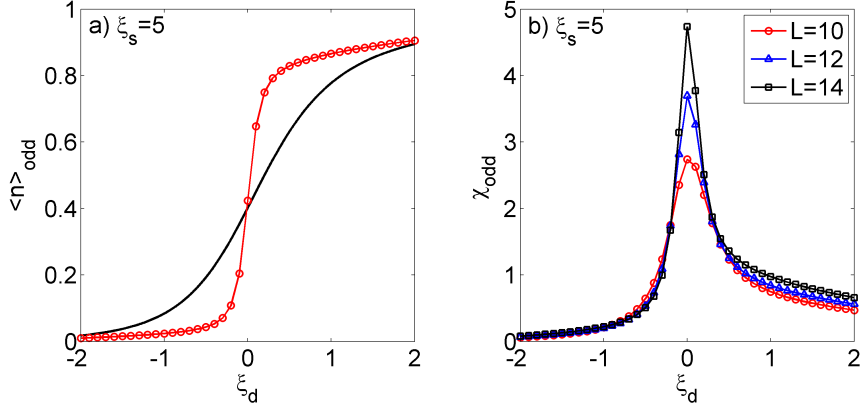


Figure 3.5: (a) Mean density of the odd sublattice as a function of ξ_d . Here, with $\xi_s = 5$, we have plotted the analytical result given in Eq. (3.7) in black and the numerical result obtained from diagonalising Hamiltonian (3.1) in red (with circles) with $L = 14$. The latter shows a significantly steeper switching of the sublattice populations at $\xi_d = 0$. (b) Susceptibility $\chi_{\text{odd}}(\xi_s = 5, \xi_d)$ for different lattice sizes: $L = 10$ (red circles), $L = 12$ (blue triangles), and $L = 14$ (black squares). The data suggests a divergence of the susceptibility at $\xi_d = 0$ in the limit of large lattice sizes L .

Having justified the analytical results obtained in Eq. (3.7), now let us discuss the features in Fig. 3.4(a) in more details. For small ξ_s^{-1} Eq. (3.7) predicts a transition between two states in which Rydberg atoms predominantly occupy the odd/even sublattice which takes place when the difference between the sublattice fugacity parameters vanishes $\xi_d = 0$ [see Fig. 3.5(a)]. This is expected since for $\xi_s^{-1} = 0$ and $\xi_d = 0$ both $|\uparrow\downarrow\uparrow\downarrow\dots\rangle$ and $|\downarrow\uparrow\downarrow\uparrow\dots\rangle$ are ground states and any non-zero value of ξ_d will favour one over the other. Note, that according to Eq. (3.7), which is plotted in Fig. 3.5 in black, this switching between the two anti-ferromagnetic ground states is smooth as the susceptibility, which can be calculated as,

$$\chi_{\text{odd}}(\xi_s, \xi_d) = \partial\langle n_{\text{odd}} \rangle / \partial\xi_d, \quad (3.8)$$

saturates at a value $1/2$ at the “transition point” $\{\xi_d = 0, \xi_s^{-1} = 0\}$ [see Eq. (3.7)]. Since a tiny perturbation to the system would lead to a symmetry breaking, e.g. an impurity, one would naturally expect the transition occurring at $\xi_d = 0$ to be sharp rather than a crossover. Therefore, although the frustration-free Hamiltonian (2.40) excellently describes the Rydberg gas along the curve parameterised by Eqs. (2.42) as shown in Ref. [31], it is very questionable whether this Hamiltonian and Eq. (3.7) faithfully describe the actual sublattice occupation of the ground state of the Rydberg gas Hamiltonian (3.1) in one-dimension at the “transition point”. The suspicion is confirmed by numerically calculating $\langle n_{\text{odd}} \rangle$ in the ground state of H_{Ryd} . This data is shown as the one with red circles in Fig. 3.5(a) and

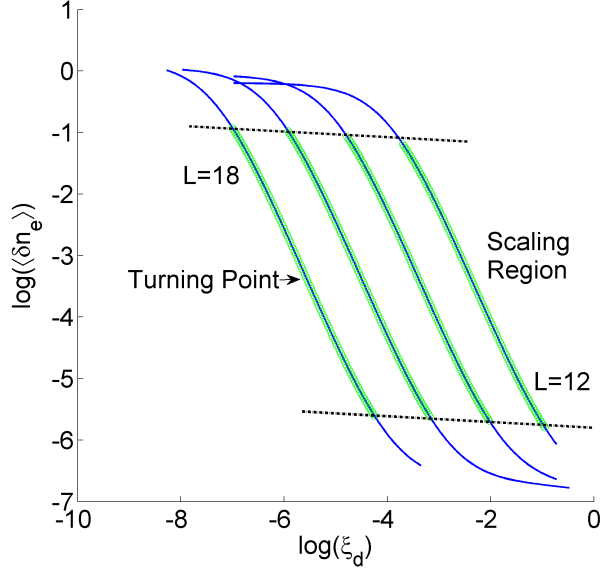


Figure 3.6: The scaling behaviour of the variance at ξ_d close to critical value $\xi_d = 0$. The dashed line indicates the boundary of the scaling region for the $L = 18$ curve. From the left to the right, we have corresponding lattice size $L = 18, 16, 14, 12$. The gradient seems to not depend on the lattice size.

clearly displays a significantly sharper transition. Moreover, as shown in Fig. 3.5(b), one can anticipate a diverging behaviour of the susceptibility $\chi_{\text{odd}}(\xi_s, \xi_d)$ with increasing lattice sizes.

This strongly suggests that $\{\xi_d = 0, \xi_s^{-1} = 0\}$ is a critical point of the Rydberg gas Hamiltonian (3.1) in one-dimension which is not captured by the ground state of the frustration-free approximation (2.40). To investigate the nature of this point, we will perform a scaling analysis in the next section by using the results shown in Fig. 3.5(b).

3.3.2 Long Range Tails of the van der Waals Interaction

Following the previous section, we now analyse the susceptibility $\chi_{\text{odd}}(\xi_s, \xi_d)$ plotted in Fig. 3.5(b). We will then further investigate the cause of this sharp transition. Near the critical point, one can express the susceptibility as $\chi_{\text{odd}} \sim (\xi_d - \xi_d^c)^{-\gamma}$ with critical exponent γ and ξ_d^c being the critical value of ξ_d at where the transition occurs, we now show how γ can be numerically extracted in the vicinity of $\xi_d = 0$. Since $\xi_d^c = 0$, we simply have $\chi_{\text{odd}} = \alpha \xi_d^{-\gamma}$, with α being the proportionality. Taking the logarithm of both sides, we have $\log \delta \chi_{\text{odd}} = \log \alpha - \gamma \log \xi_d$. One immediately sees that γ can be simply extracted by fitting the function linearly. However, the linear behaviour, as shown in Fig. 3.6 only happens within a so called scaling region[87], and the choice of boundaries which define this region will have impact on the gradient of the fitted line. Here, we provide a possible but not the

only appropriate way to define this region in the following: We first find the turning point of this curve and use data points within the upper and lower boundaries defined by $\log \xi_d \pm 1.35$ (green circles). The gradients of the fitted lines, i.e. the value of the critical exponent, is found to be $\gamma \approx 1.76 \pm 0.05$. This result suggests that the second order transition belongs to the 2D-Ising universality class [87].

Having found strong evidence that $\{\xi_d = 0, \xi_s^{-1} = 0\}$ indeed corresponds to a critical point, we now want to explore the origin of it. The major difference between the red and black in Fig. 3.5(a) is the fact that the exact diagonalisation of Hamiltonian (3.1) (in red) includes long ranged tails of the van der Waals interaction whereas the analytical results obtained in Eq. (3.7) from the transfer matrix method (in black) only considers nearest neighbour interactions. After further investigation of the inclusion of these long range tails, we are able to observe two things:

(i) When we include interactions up to next-next-nearest neighbours, V_3 while keeping longer ranged tails in the van der Waals interaction at zero, i.e. $V_i = 0$ for $i > 3$, the sharp transition observed in Fig. 3.5 emerges. This suggests that the sharp transition behaviour is triggered by the inclusion of van der Waals interaction at next-next-nearest neighbours.

(ii) In previous parameter choices, we always have $V_3 = V/3^6$ to ensure that interaction strength falls off according to the quickly decaying van der Waals interaction. However, when we deliberately assign values for V_3 that does not obey $V_3 = V/3^6$, the sharp transition observed in Fig. 3.5 still present as long as V_3 is sufficiently large.

To see the latter observation in more detail, in Fig. 3.7, at fixed $\xi_s = 10$, we have plotted sublattice density (colour code) at different values of V_3 against ξ_d . As one observes, the sharp transition emerges after V_3 become sufficiently large (above the red dash), although this 'critical value' of V_3 seems to be very small. Then, we change the value of ξ_s to see if one obtains the same critical V_3 . Interestingly, it seems that the 'critical value' of V_3 depends on the value of ξ_s where for increasing ξ_s , the 'critical value' of V_3 becomes smaller. Since for all numerical simulations, we have finite size effect, one cannot make a solid conclusion on what is the value of V_3 needed to turn on the transition behaviour. Rather, according to what we have obtained so far, one can predict that for $\xi_s \rightarrow \infty$, 'critical value' of V_3 is approaching zero.

Knowing that including long range tails in the van der Waals interaction is sufficient to change the transition behaviour of the system, we now briefly comment on why this is the case. At the critical point, we have $\xi_d = 0$ and therefore $\xi_{\text{odd}} = \xi_{\text{even}}$ which means that the fugacity parameter is site independent, $\xi_k = \xi$.

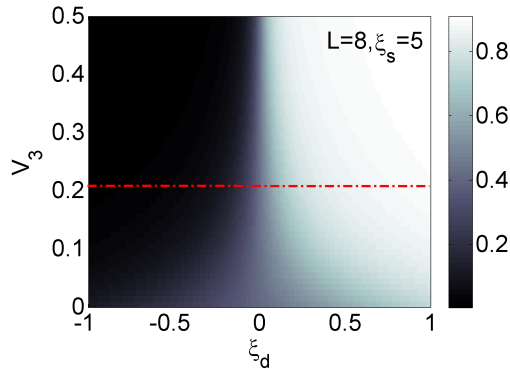


Figure 3.7: The plot shows the sublattice density of the odd sites (colour code) for varying V_3 and ξ_d . As one can see, the sharp transition does not emerge immediately when V_3 is turned on, but actually, slowly emerges. The red dash indicates the possible critical value of V_3 where the smooth transition becomes sharp.

To understand the limits of the validity of the frustration-free Hamiltonian (2.40) and to gain further insights into the critical point, it is therefore instructive to have a closer look at the phase diagram of the Hamiltonian (3.1) in the one-dimensional homogeneous case. A stylized version of this diagram is depicted in Fig. 3.8. Here one sees that the curve, which is parameterised by Eqs. (2.42) hits the point $\{\Omega = 0, \Delta_c = -3V_2\}$, i.e. $\xi \rightarrow \infty$, where the phase boundaries of a classical phase with Rydberg density $1/3$ and one with density $1/2$ coalesce. An inspection of the frustration-free Hamiltonian (2.40) shows that in the limit $\xi \rightarrow \infty$ this approximate Hamiltonian does not energetically discriminate between configurations of the form $|\uparrow\downarrow\uparrow\downarrow\uparrow\downarrow \dots\rangle$ and $|\uparrow\downarrow\downarrow\uparrow\downarrow\downarrow \dots\rangle$ due to the lack of the next-next-nearest neighbour interaction V_3 . This explains why its ground state (3.4) fails to describe properties, such as the sublattice density of the Rydberg lattice gas, in the vicinity of the critical point.

3.3.3 Effective Hamiltonian near the Critical Point

In order to understand the change in the transition behaviour we observed previously, which is apparently associated with the inclusion of long range tails in the van der Waals interaction, in this section, we will investigate the system near the critical point, $\{\xi_d = 0, \xi_s^{-1} = 0\}$ with finite V_3 . Instead of approaching the critical point from finite ξ_d to $\xi_d = 0$ with $V_3 = 0$, we will now approach the critical point along the V_3 axis while fixing ξ_d to be zero. This idea of approaching the same critical point from different axis is illustrated in Fig. 3.8 as an inset. By following Refs. [33, 104], we will show that the a spin-1/2 Heisenberg XXZ model with an

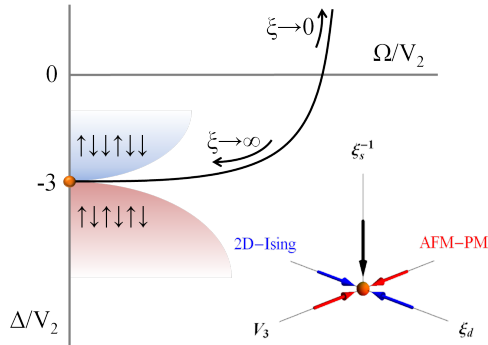


Figure 3.8: Stylized phase diagram of the homogeneous Rydberg lattice gas Hamiltonian (3.1) with $\Omega_k = \Omega$ and $\Delta_k = \Delta$. The curve parameterised by Eqs. (2.42) approaches in the limit $\xi \rightarrow \infty$ the critical point $\{\Omega = 0, \Delta = -3V_2\}$ which is located between a classical crystalline phase with Rydberg density $1/2$ and one with density $1/3$. Inset: In our analysis we approach the critical point $\{\xi_d = 0, \xi_s^{-1} = 0, V_3 = 0\}$ from different directions: One experiences a 2D-Ising type transition by approaching the critical point from finite ξ_d , while one experiences a AFM-PM transition by approaching from finite V_3 .

external magnetic field effectively describes the system near the critical point.

Since the transition occurs exactly at $\xi_d = 0$, i.e. at the point where the system recovers homogeneity, the following derivation starts by considering a global fugacity parameter, ξ where $\xi = \xi_s/2$. Hence, $\xi^{-1} = 0$ since $\xi_s^{-1} = 0$ at the critical point. We then include next-next-nearest neighbour interactions, $V_3 \sum_k^L n_k n_{k+3}$ into the frustration free Hamiltonian to give,

$$H_{nnn} = \sum_k^L \{\xi P_{k-1} P_k P_{k+1} + \xi^{-1} n_k + P_{k-1} \sigma_k^x P_{k+1} + V_3 n_k n_{k+3}\}, \quad (3.9)$$

with symbols have their usual meanings. This Hamiltonian can be separated into two parts as $H_{nnn} = H_0 + H_\sigma$ with $H_\sigma = \sum_k P_{k-1} \sigma_k^x P_{k+1}$ being the off-diagonal part of the Hamiltonian and H_0 being the rest of the Hamiltonian that is diagonal. The idea now is to treat H_σ perturbatively and look at the configuration energies in the limit $\xi \rightarrow \infty$.

To conveniently study the system, as demonstrated in Fig. 3.9(a), we introduce a fictitious particle that represents three adjacent spins having $\uparrow\downarrow\downarrow$ configuration and a fictitious hole that represents two adjacent spins having $\uparrow\downarrow$ configuration. We then use $\mathbb{1}$ to label these fictitious particles and $\mathbb{0}$ to label the fictitious holes. These particles and holes will lie on fictitious lattice with the total number of fictitious lattices sites $L_e = m + n$ and actual number of lattice sites $L = 3m + 2n$ with m being number of $\mathbb{1}$'s and n being number of $\mathbb{0}$'s. There are obviously three equivalent choices for the particles and two equivalent choices for holes. Nonetheless, for the calculation of configuration energies shown later on, it is not necessary to con-

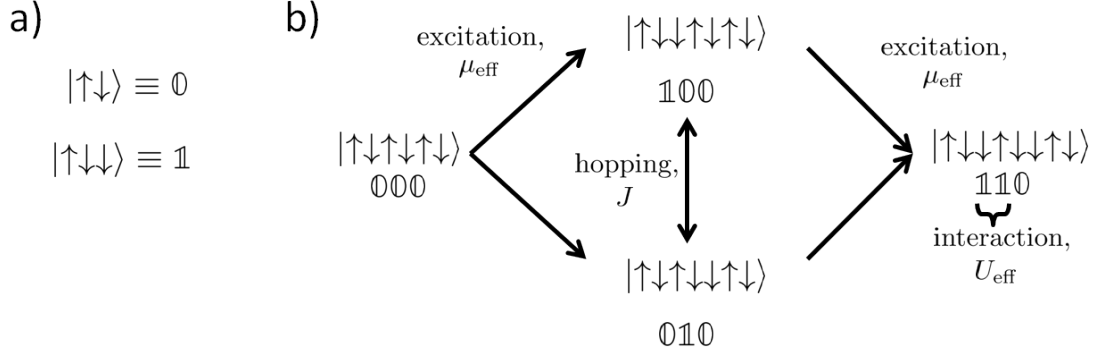


Figure 3.9: a) Equivalence between the spin representation and the fictitious particle-hole representation introduced in the text. b) The pictorial description of how configurations in the particle-hole representation are related in terms of the effective hopping, J , chemical potential, μ_{eff} and the interaction between adjacent particles, U_{eff} , i.e. the three bare parameters in the effective Hamiltonian, H_{xxz} near the previously obtained critical point.

sider different choices because they will have degenerate configuration energy due to periodic boundary condition. The reasons for introducing fictitious particles and holes are the following: Due to the nearest neighbour blockade mechanism, it is thus not possible to have two adjacent up-spins in any spin-configuration. In addition, in the limit of $\xi \rightarrow \infty$, the first term in H_{nnn} indicates an infinite configuration energy if three adjacent down spins, $\downarrow\downarrow\downarrow$ is presented in the configuration. Therefore, these two constraints leads to only two possible choices of local spin configurations namely the 'particles' and the 'holes'. Moreover, states composed out of any combinations of $\mathbb{1}$ and $\mathbb{0}$ are strictly degenerate at $\{V_3 \rightarrow 0, \xi^{-1} = 0\}$. For finite values of V_3 and ξ , the degeneracy breaks down due to the presence of virtual transitions of the type $\uparrow\downarrow\downarrow \leftrightarrow \downarrow\uparrow\downarrow$.

Configuration Energies

Now, instead of using the \uparrow and \downarrow spin notation, we use the previously introduced $\mathbb{1}$ and $\mathbb{0}$, i.e. fictitious particles and holes, to label the spin configurations and begin to obtain the configuration energy in the absence of H_σ . Starting with the configuration that contains no fictitious particles, we find that the configuration energy is simply given as $\frac{L}{2\xi}$ since there is no interaction between two adjacent $\mathbb{0}$'s, and there are total of $L/2$ holes with each hole having a configuration energy $1/\xi$. Now let us place one particle on the fictitious lattice. It is then convenient to label the fictitious lattice by the index j , and one can place the particle in any of the $j = 1, 2, \dots, L_e$ sites. Interestingly, it is easy to prove that no matter where we place the particle, the configuration energy is the same, which is given by $\frac{L-1}{2\xi} + V_3$, i.e. there are total of $(L-1)/2$ up-spins that each has an energy

$1/\xi$ and an interaction energy of V_3 between the particle on the j -th site and the hole on the $(j + 1)$ -th site. Carrying on with the calculation, we find that the configuration energy depends on the number of $\mathbb{1}$'s in the fictitious lattice, but is independent of the exact locations of these particles. Therefore, we conclude a general formula to calculate the configuration energy as,

$$\epsilon_m = \frac{L - m}{2\xi} + mV_3. \quad (3.10)$$

Now, we come back to the situation where H_σ is finite. We apply canonical van Vleck perturbation theory (VVPT) [105] up to second order to obtain the correction to the configuration energies. It is worth to note that VVPT also allows one to obtain the effective coupling strength between configurations.

For instance, it was found that the energy correction to ϵ_0 is given by $\delta\epsilon_0 = \frac{L/2}{1/\xi - \xi}$ from the VVPT up to second order. Taylor expanding $\delta\epsilon_0$ around $\xi^{-1} = 0$ and keeping terms up to second order, we find $\delta\epsilon_0 \approx -\frac{L}{2\xi}$. For consistency, unless stated otherwise, the following Taylor expansions are all performed about $\xi^{-1} = 0$. Then, the corrected configuration energy for zero particles reads,

$$E_0 = \epsilon_0 + \delta\epsilon_0 = 0. \quad (3.11)$$

For $m = 1$, we find that

$$\delta\epsilon_1 = \frac{2}{\frac{1}{\xi} + V_3 - 2\xi} + \frac{n - 1}{\frac{1}{\xi} - \xi}, \quad (3.12)$$

where the number of holes n can be calculated as $n = (L - 3m)/2 = (L - 3)/2$. To interpret this energy correction, let us look at what happens when σ_k^x acts on the system, i.e. a spin flip. For configurations having only one particle, a spin flip operation can only result in two situations. Let us have the particle lying on the j -th site of the fictitious lattice, and the up-spin in the particle is on the k -th site of the original lattice. Then, flipping the spin at k -th site or the $(k + 3)$ -th site (destroying the particle at j -th fictitious lattice site or destroying the hole at $(j + 1)$ -th fictitious lattice site respectively) corresponds to a transition to a configuration that contains four adjacent down-spins which gives an energy of 2ξ . The energy correction from this type of spin-flip gives the first term in $\delta\epsilon_1$. Spin-flips at all other lattice sites will destroy a fictitious hole and will create a local configuration containing three adjacent down-spins with an energy of ξ . With $n - 1$ different but equivalent ways of making this type of spin-flip, we have the second term in the energy correction to $\delta\epsilon_1$. Performing a Taylor expansion, we

find that,

$$\delta\epsilon_1 \approx -\frac{1}{\xi} - \frac{L-5}{2\xi} \approx -\frac{L-3}{2\xi}, \quad (3.13)$$

and thus, the corrected energy of one-particle configuration reads,

$$\begin{aligned} E_1 &= \epsilon_1 + \delta\epsilon_1 \\ &\approx \left(\frac{L-1}{2\xi} + V_3 \right) - \frac{L-3}{2\xi} \\ &\approx \frac{1}{\xi} + V_3. \end{aligned} \quad (3.14)$$

Now with the VVPT method, one can calculate all configuration energies up to second order correction. Here, we give the corrected configuration energy for the 1/2-filling configuration, i.e. $0101\dots$ and fully occupied configuration, i.e. $1111\dots$, as these energies will be used to calculate chemical potential and effective interaction between neighbouring 1 's later.

For the 1/2-filling configuration, the number of particle is equal to the number of holes, i.e. $m = n$. Since $L = 2n + 3m$, we have $m = L/5$. Using VVPT, one finds that the corrected energy for $m = L/5$ is calculated as,

$$\begin{aligned} E_{L/5} &= \frac{2L}{5\xi} + \frac{L}{5}V_3 + \delta\epsilon_{L/5} \\ &= L \left[\frac{2}{5\xi} + \frac{V_3}{5} + \frac{2}{5 \left(\frac{1}{\xi} + V_3 - 2\xi \right)} \right] \\ &\approx L \left(\frac{1}{5\xi} + \frac{V_3}{5} \right). \end{aligned} \quad (3.15)$$

For the fully occupied configuration, since $n = 0$, $L = 3m$ which yields $m = L/3$. Again, with VVPT, the configuration energy, $E_{L/3}$ reads,

$$\begin{aligned} E_{L/3} &= \frac{L}{\xi} + \frac{L}{3}V_3 + \delta\epsilon_{L/3} \\ &= L \left[\frac{1}{3\xi} + \frac{V_3}{3} + \frac{1}{3 \left(\frac{1}{\xi} + 2V_3 - 3\xi \right)} \right] \\ &\approx L \left(\frac{2}{9\xi} + \frac{V_3}{3} \right). \end{aligned} \quad (3.16)$$

Effective Hopping, Chemical Potential, and Interaction between Fictitious Particles

In this section, we will show how configurations are related each other in terms of their energy differences and effective couplings. A pictorial description of the

results obtained in this section is depicted in Fig. 3.9(b), where an excitation, i.e. a creation of a particle, requires an energy of μ_{eff} ; particles can hop around the fictitious lattice with an effective hopping amplitude given by J ; and for two adjacent particles, there is an effective interaction which is denoted as U_{eff} . These parameters will form the basis of the effective Hamiltonian that describes the system near the critical point observed in Sec. 3.3.1, and the detailed calculation of these parameters in relation to ξ and V_3 will be given in this section.

When determining the configuration energies, the VVPT method also allows direct calculation of the effective coupling between configurations in the particle/hole representation that are translationally invariant. For instance, the $\mathbb{1}000\dots$ with the $\mathbb{1}$ on the j -th site and $0\mathbb{1}00\dots$ with the $\mathbb{1}$ on the $(j+1)$ -th site has an effective coupling calculated from VVPT that reads,

$$t = \frac{1}{\frac{1}{\xi} + V_3 - 2\xi} \approx -\frac{1}{2\xi}, \quad (3.17)$$

Physically, this effective coupling can be interpreted as a hopping amplitude for particles hopping on the fictitious lattice. The energy contribution to this hopping then can be expressed by the Hamiltonian as $H_{\text{hop}} = t \sum_j (\alpha_j^\dagger \alpha_{j+1} + \alpha_j \alpha_{j+1}^\dagger)$ with α_j^\dagger (α_j) being the creation (annihilation) operator that creates (destroys) a fictitious particle on site j .

Clearly, from the difference seen in the configuration energies of configurations containing different number of particles, it is expected that there is a chemical potential associated with the particle excitation, i.e. the system requires certain energy to create a particle. To deduce this chemical potential, we use two configurations with different number of m and both of them interaction free. Here, the interaction free means that the configurations do not contain adjacent particles. The effective interaction between particles will be made clearer later. Choosing configurations with $m = 0$ and $m = 1$ respectively. Then, one has $\mu\Delta m = E_1 - E_0$ where $\Delta m = 1$, and using the fact that E_0 is zero, we obtain

$$\mu = E_1 = \frac{1}{\xi} + V_3. \quad (3.18)$$

To be consistent, we check our result by using a different set of configurations, where we use two configurations with $m = 0$ and the half-filling configuration, i.e. $0\mathbb{1}0\mathbb{1}\dots$, with $m = n = L/5$. We emphasise here that the latter configuration is also interaction free. In this case the chemical potential can be calculated by

using the relation, $\mu L/5 = E_{L/5} - E_0$. Using $E_{L/5}$ obtained previously, we find

$$\begin{aligned}\mu &= \frac{5}{L} (E_{L/5} - E_0) \\ &= \frac{1}{\xi} + V_3,\end{aligned}\tag{3.19}$$

which is exactly the same μ as obtained before. Now, let us look at configurations involving adjacent particles. We denote the interaction between adjacent particles as U . We will obtain this term with the aid of the obtained chemical potential as follows. Firstly, let us look at the fully occupied configuration, i.e. $1111\cdots$ and compare it with the empty configuration, i.e. $0000\cdots$. The difference in particle number is $L/3$ and contributes an energy difference of $\frac{L}{3}\mu$. In the $1111\cdots$ configuration, each particle effectively interacts with its neighbouring particle which make an energy contribution of U . Since there are total of $L/3$ particles, to avoid double counting, the total interaction energy for $1111\cdots$ can hence be denoted as $\frac{L}{3}U$. On the other hand, the energy contribution from interaction is zero in $0000\cdots$ since adjacent particles are absent in this configuration. Therefore, the total difference in the energy between $0000\cdots$ and $1111\cdots$ is given by $E_{L/3} - E_0 = (\mu + U)L/3$. Using perviously obtained $E_{L/3}$ and μ , we find,

$$\begin{aligned}U &= \frac{3}{L} (E_{L/3} - E_0) - \mu \\ &= \frac{3}{L} \left(\frac{2L}{9\xi} + \frac{V_3L}{3} \right) - \left(\frac{1}{\xi} + V_3 \right) \\ &= -\frac{1}{3\xi}.\end{aligned}\tag{3.20}$$

Using creation (annihilation) operators α^\dagger (α) introduced perviously when we write down the hopping Hamiltonian, we can also write down the Hamiltonian associate with the chemical potential and effective nearest neighbour interaction, which reads, $H_\mu = \mu \sum_j \alpha_j^\dagger \alpha_j$ and $H_U = U \sum_j \alpha_j^\dagger \alpha_j \alpha_{j+1}^\dagger \alpha_{j+1}$. Combining these two with H_{hop} , we arrive at an effective Hamiltonian describing H_{nmn} in the vicinity of the critical point that reads,

$$\begin{aligned}H_{\text{particle-hole}} &= H_{\text{hop}} + H_\mu + H_U \\ &= t \sum_j (\alpha_j^\dagger \alpha_{j+1} + \alpha_j \alpha_{j+1}^\dagger) + \mu \sum_j \alpha_j^\dagger \alpha_j + U \sum_j \alpha_j^\dagger \alpha_j \alpha_{j+1}^\dagger \alpha_{j+1},\end{aligned}\tag{3.21}$$

with the hopping amplitude t , chemical potential μ , and nearest neighbour interaction strength U shown in Eq. (3.17), (3.19), and (3.20) respectively.

Mapping to the Heisenberg-XXZ Model

In this section, we will map $H_{\text{particle-hole}}$ onto the Heisenberg-XXZ Model. To begin with, let us look at the creation and annihilation operators in $H_{\text{particle-hole}}$. Within the description in which the system is illustrated by fictitious particles and holes sitting in a fictitious lattice with lattice index, j , for the creation and annihilation operator acting on the j -th site, we have,

$$\begin{aligned}\alpha_j^\dagger |0\rangle_j &= |\mathbb{1}\rangle_j; & \alpha_j^\dagger |\mathbb{1}\rangle_j &= 0; \\ \alpha_j |\mathbb{1}\rangle_j &= |0\rangle_j; & \alpha_j |0\rangle_j &= 0,\end{aligned}\tag{3.22}$$

where $|\mathbb{1}\rangle$ ($|0\rangle$) is a state vector that denotes a fictitious particle (hole) on the j -th fictitious lattice site. In another word, the fictitious particles and holes description enables us to effectively treat a local particle-hole representation by a two-level scheme where the state vectors for a fictitious particle and a fictitious hole can be written as,

$$|\mathbb{1}\rangle_j = \begin{pmatrix} 1 \\ 0 \end{pmatrix}_j; \quad |0\rangle_j = \begin{pmatrix} 0 \\ 1 \end{pmatrix}_j.\tag{3.23}$$

Therefore, the solution to these local operators α_j^\dagger and α_j for Eqs. (3.22) in the matrix representation reads,

$$\alpha_j^\dagger = \begin{pmatrix} 0 & 1 \\ 0 & 0 \end{pmatrix}_j; \quad \alpha_j = \begin{pmatrix} 0 & 0 \\ 1 & 0 \end{pmatrix}_j.\tag{3.24}$$

One immediately realises that these creation and annihilation operators are equivalent to the raising and lowering spin operators introduced in Eq. (2.39), i.e. $\sigma_k^\pm = (\sigma_k^x \pm i\sigma_k^y)/2$. Therefore, with the two-level representation, and replacing the creation and annihilation operators by the equivalent spin raising and lowering operators, i.e. $\alpha^\dagger \equiv \sigma^+$ and $\alpha \equiv \sigma^-$, H_{eff} can be written as,

$$\begin{aligned}H_{\text{particle-hole}} &= H_{\text{hop}} + H_\mu + H_U \\ &= t \sum_j (\sigma_j^+ \sigma_{j+1}^- + \sigma_j^- \sigma_{j+1}^+) + \mu \sum_j \sigma_j^+ \sigma_j^- + U \sum_j \sigma_j^+ \sigma_j^- \sigma_{j+1}^+ \sigma_{j+1}^-.\end{aligned}\tag{3.25}$$

A general spin-1/2 Heisenberg XXZ Model in an external magnetic field is given by,

$$H_{\text{XXZ}} = J \sum_j (S_x^j S_x^{j+1} + S_y^j S_y^{j+1}) + \mu_{\text{eff}} \sum_j S_z^j + U_{\text{eff}} \sum_j S_z^j S_z^{j+1}.\tag{3.26}$$

Now, in order to map the effective Hamiltonian onto the XXZ-model, we first relate the Cartesian components of the spin-operators to the Pauli spin matrices, and the spin raising and lowering operators, σ^\pm as the following,

$$\begin{aligned} S_x &= \frac{1}{2}\sigma_x = \frac{1}{2}(\sigma^- + \sigma^+); \\ S_y &= \frac{1}{2}\sigma_y = \frac{i}{2}(\sigma^- - \sigma^+); \\ S_z &= \frac{1}{2}\sigma_z = \sigma^+\sigma^- - \frac{\mathbb{1}}{2}. \end{aligned} \tag{3.27}$$

Using these relations, one obtains

$$\begin{aligned} S_x^j S_x^{j+1} + S_y^j S_y^{j+1} &= \frac{1}{4}(\sigma_j^- \sigma_{j+1}^- + \sigma_j^+ \sigma_{j+1}^+ + \sigma_j^- \sigma_{j+1}^+ + \sigma_j^+ \sigma_{j+1}^-) \\ &\quad - \frac{1}{4}(\sigma_j^- \sigma_{j+1}^- + \sigma_j^+ \sigma_{j+1}^+ - \sigma_j^- \sigma_{j+1}^+ - \sigma_j^+ \sigma_{j+1}^-) \\ &= \frac{1}{2}(\sigma_j^- \sigma_{j+1}^+ + \sigma_j^+ \sigma_{j+1}^-); \end{aligned} \tag{3.28}$$

$$\begin{aligned} S_z^j S_z^{j+1} &= (\sigma_j^+ \sigma_j^- - \frac{\mathbb{1}}{2}) \cdot (\sigma_{j+1}^+ \sigma_{j+1}^- - \frac{\mathbb{1}}{2}) \\ &= \sigma_j^+ \sigma_j^- \sigma_{j+1}^+ \sigma_{j+1}^- - \frac{1}{2} \sigma_j^+ \sigma_j^- - \frac{1}{2} \sigma_{j+1}^+ \sigma_{j+1}^- + \frac{\mathbb{1}}{4}; \end{aligned} \tag{3.29}$$

and,

$$S_z^j = \sigma_j^+ \sigma_j^- - \frac{\mathbb{1}}{2}. \tag{3.30}$$

Now one only needs to equate the relevant terms. Also, one can safely drop the identities terms $\mathbb{1}$ as they contribute to a constant energy shift. Moreover, due to periodic boundary conditions, where the system is translationally invariant, we have $\sum_j \sigma_j^+ \sigma_j^- = \sum_j \sigma_{j+1}^+ \sigma_{j+1}^-$. Therefore, one finds the exchange energy, J reads

$$J = 2t = -\frac{1}{\xi}. \tag{3.31}$$

For the other two terms, according to the relation we obtained above, one finds

$$U_{\text{eff}} \sum_j S_z^j S_z^{j+1} + \mu_{\text{eff}} \sum_j S_z^j = U_{\text{eff}} \sum_j \sigma_j^+ \sigma_j^- \sigma_{j+1}^+ \sigma_{j+1}^- + (\mu_{\text{eff}} - U_{\text{eff}}) \sum_j \sigma_j^+ \sigma_j^-. \tag{3.32}$$

Equating with Eq. (3.25), one finds that

$$U_{\text{eff}} = U = -\frac{1}{3\xi}, \tag{3.33}$$

and,

$$\mu_{\text{eff}} = U_{\text{eff}} + \mu = \frac{2}{3\xi} + V_3. \quad (3.34)$$

Summarising the results, we obtain a spin-1/2 Heisenberg XXZ model in an external magnetic field,

$$H_{\text{xxz}} = \sum_j \left[-\frac{1}{\xi} (S_x^j S_x^{j+1} + S_y^j S_y^{j+1}) + \frac{\delta}{\xi} S_z^j S_z^{j+1} + \frac{\mu}{\xi} S_z^j \right],$$

with $\delta = -1/3$ and $\mu = 2/3 + \xi V_3$. With respect to the pseudo-spin degree of freedom, i.e. $|\uparrow\rangle_k$, and $|\downarrow\rangle_k$, this model exhibits a critical transition between an anti-ferromagnetic (AFM) and a paramagnetic (PM) phase at $\mu = \delta + 1$ [106], i.e. when $\xi V_3 = 0$. This transition can also be pictured in terms of the fictitious particles and holes, where crossing $\xi V_3 = 0$, the system goes from $\mathbb{1}\mathbb{1}\mathbb{1}\mathbb{1}\dots$ to random combinations of $\mathbb{1}$ and $\mathbb{0}$. Hamiltonian H_{nmn} has thus a critical point at $\{V_3 = 0, \xi^{-1} = 0\}$. This corroborates the previous analysis of the numerical data displayed in Fig. 3.5 which suggested a second order transition of the Rydberg lattice gas Hamiltonian (3.1) in one-dimension to occur at $\{\xi_d = 0, \xi_s^{-1} = 0\}$. In fact due to the finite nearest-neighbour and next-next-nearest neighbour interaction which is inevitably present in practice the Rydberg gas will never be strictly at the critical point. However, due to the smallness of V_3 , stemming from the r^{-6} -scaling of the van der Waals interaction, observable exhibits a scaling behaviour (as for example shown in Fig. 3.5 which will be interesting to be explored experimentally pursuing the route in Refs. [107, 108]).

3.4 Conclusion and Outlook

In this chapter, we presented a detailed analysis of the static properties of inhomogeneous one-dimensional Rydberg lattice gases. We started by showing a generic frustration-free Hamiltonian of the Rokhsar-Kivelson type that permits the approximate analytical investigation of inhomogeneous Rydberg lattice gases. We then utilised the ground state property of this frustration-free Hamiltonian to study two different inhomogeneities in detail. The first situation considered was the presence of an impurity in the system. In this system, we investigated the effect of the impurity on the correlation property of the ground state and showed that the impurity can break the sub-lattice symmetry. Inspired by this result, we further introduced staggered lasers fields. A critical point was identified in the parameter space. A scaling analysis indicated that the 2nd order transition, crossing the critical point, belongs to 2D-Ising universality class. Moreover, we also studied the effect of the long range tails of the van der Waals interactions

on the transition by deriving an effective model to describe the system near this critical point. As shown, the Heisenberg XXZ-model in an external magnetic field confirmed the criticality and might enable the experimental implementation and study of impurities immersed in Luttinger liquids along the lines of Ref. [109].

As discussed, there are two different inhomogeneities being investigated in this chapter, but the employed approach is not limited to those two. In fact, the generic Rydberg Hamiltonian H_{Ryd} allows the implementation of various inhomogeneities through the variations of the laser parameters from site-to-site, and they might lead to fascinating results. One particular example, which is relevant to practical experimental setups, is the inclusion of disorder caused by random potentials in the optical lattice and by fluctuations in the laser parameters. These randomness will correspond to the practical situation in potential experimental implementation of Rydberg lattice gas [94]. Interestingly, the fluctuations in the laser parameters eventually lead to a breakdown of the R-K approximation as the laser parameters might not fulfil the relations described by the ξ -manifold. Nonetheless, provided that the laser parameters are sufficiently close to the ξ -manifold, the Hamiltonian of the R-K type can be used as a reasonable approximation to enable the study of systems beyond the ξ -manifold.

With the implementation of inhomogeneities, it is also possible to look at the effect of the finite width of the spatial wavefunction of the trapped atom in the optical lattice. It would be therefore interesting to see if a detail study of such Rydberg lattice gas would agree with the results claimed by Ref. [110] in which the statistics, i.e. the averaged behaviour is believed to be not contributing to a modification of the interaction strength between the trapped atoms.

Another direction worth consideration in this system could be introducing non-ideal nearest neighbour blockade where adjacent atoms, though unfavourably, can still be simultaneously excited to Rydberg state. The homogeneous situation of such a system has been investigated in Refs. [33, 111]. Using perturbation theory it was shown that in the non-ideal blockade regime, virtual hopping processes modify the low energy part of the many-body energy spectrum, in particular the energy gap to the ground state, which in turn can change the transition behaviour of the system. Therefore, whether such a new blockade mechanism in the presence of inhomogeneities will reduce the stability of the transition behaviours remains an open and interesting question.

Chapter 4

Two Dimensional Rydberg Lattice Gases

Having considered both the one-dimensional homogeneous and inhomogeneous Rydberg lattice gases in previous chapters, we will now investigate the two-dimensional homogeneous Rydberg lattice gases in this Chapter. With a detailed study of the square lattice, we demonstrate that the construction of the frustration-free Hamiltonian allows us to approximately map the Rydberg lattice gas to Baxter's hard-squares model. Further, using the analytical ground state of the frustration-free Hamiltonian as a variational ansatz, we obtain a phase diagram where an order-disorder phase transition has been identified in parameter space.

4.1 Introduction

A quantum phase transition describes the change in the phases of a quantum system at absolute zero. It is fundamentally different from classical phase transitions as at zero Kelvin, thermal fluctuations are absent. Hence, it is believed that quantum phase transitions are driven by quantum fluctuations originating from the uncertainty principle. Moreover, since temperature does not play a role here, the transition often occurs due to the change of relevant physical parameters, e.g. the transverse magnetic field in a two-dimensional Ising model [112].

To understand the nature of quantum phase transition, one usually uses the concept of level crossing between the ground state and excited states [113]. To begin with, let us consider a Hamiltonian that describes a many-body system at absolute zero of the form $H(g) = H_0 + gH_1$, with g being a tunable dimensionless parameter. There can be two different situations and correspond to two different types of quantum phase transitions. The first case is when $[H_0, H_1] = 0$. As such,

the eigenstates of the Hamiltonian is independent of the parameter g since H_0 and H_1 can be simultaneously diagonalised whereas the eigenenergy is still a function of g . Then, there might exist a value of $g = g_c$ such that an excited state becomes the ground state, i.e. a level-crossing. And at $g = g_c$, the ground state energy becomes non-analytic. This is often referred to as a first-order quantum phase transition. The other situation is when H_0 and H_1 do not commute. In this case, for a finite lattice, the level-crossing is avoided when varying g . However, this avoided level-crossing at some value of $g = g_c$ can become sharper with increasing lattice size and eventually becomes a actual level-crossing in the thermodynamic limit. When this happens, the ground state energy again becomes non-analytic at $g = g_c$, indicating a quantum phase transition often referred to as continuous or second order quantum phase transition.

In this Chapter, we will show that within a model description of the strongly interacting Rydberg lattice gas on a square lattice, we can identify a first order phase transition.

The exploration of quantum phase transitions is difficult in practice as tuning a system down to an extremely low temperature where quantum fluctuations dominate is not an easy task. Thanks to the success in ultra-cold experiments where temperatures can be cooled down to nano-Kelvins nowadays, the investigation of changes in the ground state of many-body systems becomes possible. This has enabled many theoretical studies recently on quantum phase transitions in various many-body systems.

Also motivated by experimental realisability of the Rydberg lattice gas introduced previously, we would also like to identify possible quantum phase transitions in the system. However, since one-dimensional systems often do not exhibit phase transitions, yet with higher dimensions systems often possess rich phases, we will explore the Rydberg lattice gas in two-dimensions in this chapter. In particular, we will analyse in detail the ground state properties of a Rydberg lattice gas in a square lattice. We will show that by mapping the system to Baxter's hard-squares, one can identify a similar phase transition in parameter space.

This chapter is organised by the following structure. We start by introducing the Hamiltonian that describes the Rydberg lattice gases in a two dimensional square lattice, and depicting the blockade mechanism of nearest neighbours that we adopt in the system. To study this system, we first introduce a quantum version of Baxter's classical hard-squares model [51] in Sec. 4.3 which exhibits the same symmetry property of the Rydberg lattice gas. We refer to this model as the quantum hard-squares model. We then analyse the ground state of this model and demonstrate how to calculate the properties of this ground state via transfer matrix methods in Sec. 4.4. Having the knowledge of its ground state, we connect

the quantum hard-squares model to the Rydberg lattice gas in square lattice in Sec. 4.5, and further compare their numerical ground states in the subsequent section. The results enable us to use the ground state of the quantum hard-squares model as a variational ansatz to obtain the approximate ground state of Rydberg lattice variationally in Sec. 4.7 and eventually extend this variational approach to study the phase diagram in the entire parameter space described by the rescaled laser parameters $\{\Omega/V, \Delta/V\}$ in Sec. 4.8. Finally, in Sec. 4.9 to further obtain an expected quarter-filling phase in the phase diagram, we will deliberately introduce a quarter-filling variational state to study the quarter filling region. A summary of the results and possible future works are discussed in Sec. 4.10

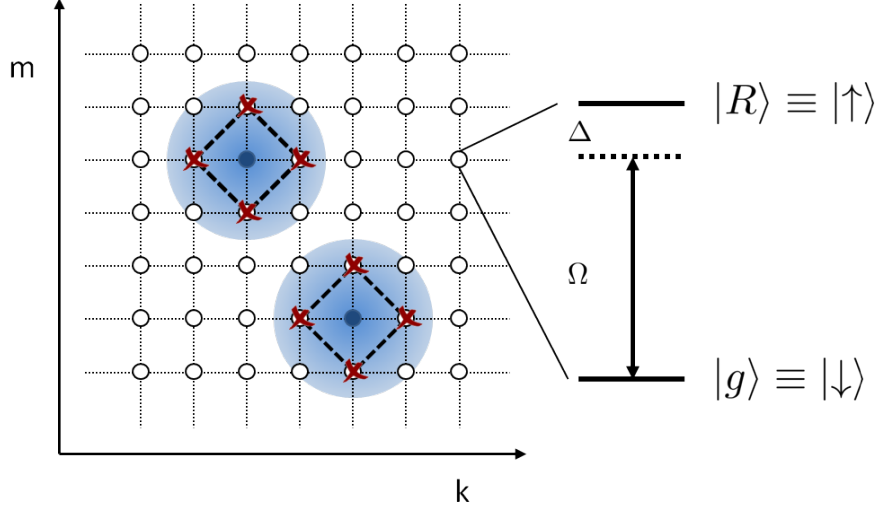


Figure 4.1: Strongly interacting Rydberg atoms in a square lattice with lattice spacing, a . Atoms are labeled by two indices, k, m . Each atom, like in the one-dimensional system, is approximated by a two-level atom with a ground state and a Rydberg state which are coupled by a site-independent Rabi-frequency, Ω , and detuning, Δ . In the strongly interacting regime, where $V \gg \Omega$, a Rydberg atom prevents the excitation of its four adjacent atoms to their Rydberg states. In the quantum hard-squares model that we introduce in Sec. 4.3, each Rydberg atom is effectively treated as a hard-square. Long range tails that are beyond next-nearest neighbours in the van der Waals interaction will be neglected in the calculation. This is indicated by the blue region around each Rydberg atom.

4.2 The System

We explore the two-dimensional Rydberg lattice gases by starting with the square lattice where the system is illustrated in Fig. 4.1. The system under consideration is very similar to the one-dimensional case in the following sense: For the lattice part, each lattice site contains only one atom which forms a Mott-insulator [6], and the lattice spacing is given by a . Periodic boundary condition is applied for the purpose of simplicity, but this is not a necessity. The lattice system with periodic boundary condition can be visualised by a torus. To label the lattice sites (atoms), according to Eq. (2.33), one can use a two-dimensional vector, i.e. $\mathbf{k} = \{k_x, k_y\}$, but for convenience, we use $\{k, m\}$ instead where k is the index in the horizontal direction while m is the index in the vertical direction. For a number of K sites in the horizontal direction and M sites in the vertical direction, the total number of lattice sites is given by $L = K \times M$. Unless stated otherwise, we always set $K = M$. Hence, the lattice size is given by L^2 . For the laser part, we do not introduce any inhomogeneity such that every atom is coupled to the same Rydberg state with the same laser characterised by the global laser parameters, Ω and Δ for Rabi-frequency and detuning respectively. As such, in reference to Eq.

(2.33), the Hamiltonian describing the system reads,

$$H_{\text{Ryd}_{\text{sqr}}} = \Omega \sum_{k,m}^L \sigma_{k,m}^x + \Delta \sum_{k,m}^L n_{k,m} + \frac{1}{2} \sum_{k,m;p,q}^L V_{k,m;p,q} n_{k,m} n_{p,q}, \quad (4.1)$$

where symbols have their usual meanings, and $V_{k,m;p,q} = V/(|p-k|^2 + |q-m|^2)^3$, with $V = C_6/a^6$ being the van der Waals interaction between Rydberg atoms at nearest neighbour distance, a .

In the following studies of the Rydberg lattice gas in the square lattice, we consider only the strongly interacting regime, where $V \gg \Omega$. In particular, similar to the one dimensional systems, we restrict ourselves in the nearest neighbour blockade regime, where a Rydberg atom prevents the (de-)excitation of its four adjacent atoms. Moreover, we will only consider the subspace where configurations containing Rydberg atoms in adjacent lattice sites are excluded. The system depicted in Fig. 4.1 is an example of an allowed configuration of Rydberg atoms. We will continue to adopt the spin notations to present the two levels of an atom, i.e. $|g\rangle \equiv |\downarrow\rangle$, and $|R\rangle \equiv |\uparrow\rangle$.

4.3 The Quantum Hard-squares Model

Before studying the two-dimensional Rydberg lattice gas described by $H_{\text{Ryd}_{\text{sqr}}}$, let us first look at a model which is a quantum version of Baxter's classical hard-squares model [51] on a square lattice. We refer to this particular model as the quantum hard-squares model in the rest of the chapter. The reasons for looking at this particular model are as follows. Firstly, the model's many-body ground state wave function is known analytically. And secondly, it possesses the same symmetry properties and the same quantum term as $H_{\text{Ryd}_{\text{sqr}}}$. With these properties, it is reasonable to use the ground state of the quantum hard-squares model as a variational input state to approximately determine the phase diagram of the Rydberg lattice gas.

The system of the quantum hard-squares model considers a square lattice with each lattice site either occupied by at most one particle or empty. For any lattice site being occupied, its nearest four neighbours cannot be occupied, which amounts to having an effective hard-square located at the occupied lattice site with a diagonal length equal to two times the lattice spacing. One then sees that how such a model possesses the same symmetry properties of the Rydberg lattice gas in the nearest neighbour blockade mechanism introduced previously. The quantum parts come from the operation of placing a hard-square into or removing one from the square lattice. And such an operation on the $\{k, m\}$ -th lattice site is exactly described by the mathematical term $\sigma_{k,m}^x$, which is seen in the Rydberg Hamilto-

nian, $H_{\text{Ryd}_{\text{sqr}}}$. Eventually, the Hamiltonian, $H_{\text{R-K}_{\text{sqr}}}$ of this quantum hard-squares model takes the Rokhsar-Kivelson, i.e.,

$$H_{\text{R-K}_{\text{sqr}}} = \Omega \sum_{k,m}^L h_{k,m}^\dagger h_{k,m},$$

with $h_{k,m} = (\xi^{-1} + \xi)^{-1/2} \mathcal{P}_{k,m} [\sigma_{k,m}^x + \xi^{-1} n_{k,m} + \xi(1 - n_{k,m})]$. (4.2)

where $h_{k,m}$ is a positive-semidefinite, self-adjoint operator and obey $h_{k,m}^\dagger h_{k,m} = h_{k,m}$. As discussed in previous chapters, the ground state energy for a Hamiltonian of the Rokhsar-Kivelson type is zero and the ground state wavefunction is annihilated by all $h_{k,m}$. This then allows us to construct the ground state, $|\xi\rangle_{\text{sqr}}$ of the quantum hard-squares model in the following form [32],

$$|\xi\rangle_{\text{sqr}} = \frac{1}{\sqrt{Z_{\text{sqr}}}} \prod_k^L (1 - \xi \mathcal{P}_{k,m} \sigma_{k,m}^+) |\downarrow\downarrow \dots \downarrow\rangle, \quad (4.3)$$

where Z_{sqr} is the normalisation constant. Simply expanding the product in this state, one finds that $|\xi\rangle_{\text{sqr}}$ is a coherent superposition of all spin states describing configurations of Rydberg atoms compatible with the nearest neighbour blockade mechanism. Each configuration is weighted by a factor $(-\xi)^n$, where n denotes the number of occupied lattice sites within the configuration. This state belongs to a class of states which is often named as projected entangled pair-state (PEPS) [114, 115, 116].

Finally, analogous to the homogeneous one-dimensional case where the normalisation of $|\xi\rangle$ is mapped onto the partition function of a hard-dimer gas, the normalisation constant here in $|\xi\rangle_{\text{sqr}}$, Z_{sqr} is found to be exactly equivalent to the partition function of Baxter's classical hard-squares model [32] with a fugacity ξ^2 . Knowing the normalisation constant allows one to obtain classical observables such as density. And the nice thing about this equivalence is that it is possible to obtain the partition function of Baxter's classical hard-squares model numerically for fairly large system size with manageable computational costs. In the following section, we will demonstrate how the partition function of the classical hard-squares is calculated.

4.4 The Analytical Ground State of $H_{\text{R-K}_{\text{sqr}}}$

In the previous section, we demonstrate, in Eq. (4.3), the analytical ground state of $H_{\text{R-K}}$ and its connection to Baxter's classical hard-squares. In this section, we start with illustrating how to obtain the partition function of the classical

hard-squares problem through a transfer matrix method. Then, we will use the result to obtain expectation values of classical observables such as density and density-density correlations.

4.4.1 Partition Function of Hard-Squares

In this section, we demonstrate how to obtain the partition function of Baxter's classical hard-squares in detail. The Hamiltonian of this classical model is given by,

$$H_{\text{h-sqr}} = V \sum_{k,m}^L n_{k,m} (n_{k+1,m} + n_{k,m+1}) - 2 \ln(\xi) \sum_{k,m}^L n_{k,m}. \quad (4.4)$$

In the hard-squares regime, the interaction strength V is set to infinity such that simultaneous occupation of nearest neighbours are forbidden. $2 \ln(\xi)$ here is an effective chemical potential. The partition function of this model is given by

$$Z_{\text{h-sqr}} = \sum_{k,m}^L e^{-[V \sum n_{k,m} (n_{k+1,m} + n_{k,m+1}) - 2 \ln(\xi) \sum n_{k,m}]}. \quad (4.5)$$

The partition function $Z_{\text{h-sqr}}$ can be calculated through a modified transfer matrix method as given in Ref. [117], and we will review the details as follows.

The first step is to rewrite the partition function in a product form. Using Taylor expansion of an exponential, we have $e^{-x} = 1 - x + \frac{x^2}{2!} - \dots$. Further using the property of a projection operator where $n_k^2 = n_k$, we arrive at $e^{-V n_{k,m} n_{k+1,m}} = 1 - n_{k,m} n_{k+1,m} (1 - e^{-V})$. Under the restriction where simultaneous occupation of nearest neighbours is forbidden, i.e. $V \rightarrow \infty$, we have $(1 - e^{-V}) = 1$. Therefore, one can make further simplification to obtain $e^{-V n_{k,m} n_{k+1,m}} = 1 - n_{k,m} n_{k+1,m}$. Substituting this simple relation back into $Z_{\text{h-sqr}}$, we have the partition function in a product form that read,

$$Z_{\text{h-sqr}} = \sum_{n_{k,m}} \sum_{n_{k+1,m}} \sum_{n_{k,m+1}} \dots \sum_{n_{K,M}} e^{2 \ln(\xi) \sum n_{k,m}} \prod_m^M \prod_k^K (1 - n_{k,m} n_{k+1,m}) (1 - n_{k,m} n_{k,m+1}), \quad (4.6)$$

with a square lattice of size of K-by-M. The periodic boundary condition is satisfied by the relations $n_{K+1} = n_1$ and $n_{M+1} = n_1$.

With $e^{2 \ln(\xi)} = \xi^2$, we define the transfer matrix, $T(n_{k,m}, n_{k,m+1})$ as

$$T(n_{k,m}, n_{k,m+1}) = \prod_k^K \xi^2 \sum_{n_{k,m}} (1 - n_{k,m} n_{k+1,m}) (1 - n_{k,m} n_{k,m+1}), \quad (4.7)$$

such that the partition function, $Z_{\text{h-sqr}}$ with expansion of the product \prod_m^M , reads

$$Z_{\text{h-sqr}} = \sum_{n_{k,1}} \sum_{n_{k,2}} \sum_{n_{k,3}} \dots \sum_{n_{k,M}} T(n_{k,1}, n_{k,2}) T(n_{k,2}, n_{k,3}) \dots T(n_{k,M}, n_{k,1}). \quad (4.8)$$

Accordinging the rule of matrix multiplication and the definition of a trace, the partition function is simply the trace of the transfer matrix to the power of M (see Sec. 2.3.2 for more details with the example of hard-dimers), i.e.

$$Z_{\text{h-sqr}} = \text{Tr } T^M. \quad (4.9)$$

Now to determine the partition function, one only needs to obtain the transfer matrix which is described by a matrix of size 2^K -by- 2^K . When constructing the matrix, one finds that many matrix elements in fact are zero due to the nearest neighbour blockade, i.e. $(1 - n_{k,m}n_{k+1,m})(1 - n_{k,m}n_{k,m+1}) = 0$. Using this fact, it is possible to reduce the matrix size by only considering none-zero entries in the matrix. To exclude all these configurations, we will adopt the following technique. Firstly, we consider the general situation where we do not take hard-squares into consideration yet, i.e. simultaneous occupation of adjacent sites is allowed at the moment. Here, one would naturally describe all configurations in terms of binary codings where an occupied lattice site is represented by 1 and an empty lattice site is represented by 0. As a result, configurations are described by binary numbers that correspond to decimal numbers starting from 0 to $2^N - 1$. For instance, the decimal number 0 corresponds to the all-site-empty configuration, and $2^N - 1$ is the all-site-occupied configuration. Then, we consider the hard-squares regime by excluding all configurations containing simultaneous occupation of adjacent sites. This is done by creating a detecting algorithm to scan through all configurations and exclude all the ones with the presence of `..11.` in the binary coding. As a consequence, after excluding all unallowed configurations, the reduced matrix has a dimension of $N_{1,3}$ -by- $N_{1,3}$ where $N_{1,3}$ is the N^{th} number of the Fibonacci sequence starting with 1 and 3. The method greatly reduces the dimensionality of the matrix. For instance, $2^N/N_{1,3} \approx 69$ for $N = 20$ [117].

So far, we have provided a numerical method to obtain the partition function for the classical hard-squares. Although the transfer matrix has been simplified with a reduced matrix size, the calculation of the partition function for two-dimensional lattices is still restricted by the lattice size since matrix size still scales exponentially with increasing lattice size. In comparison to exact numerical diagonalisation of the Rydberg Hamiltonian $H_{\text{Ryd}_{\text{sqr}}}$, as we will show later, a 6-by-6 lattice is already near the limit whereas the partition function with the same computational power allows one to go up to a 16-by-16 lattice. It is worth

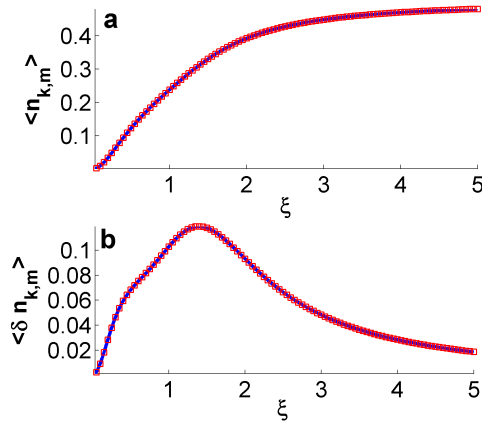


Figure 4.2: Comparison between quantities obtained from $|\xi\rangle_{\text{num}}$ of $H_{\text{R-K}_{\text{sqr}}}$ (in red boxes) and $|\xi\rangle$ through the partition function of hard-squares (in blue lines): (a) Density of Rydberg atom, and (b) Variance of the density of Rydberg atoms of a 4-by-4 square lattice. The red squares lie exactly on top of the blue lines which indicate that $|\xi\rangle_{\text{num}}$ is exactly equivalent to $|\xi\rangle$.

emphasising that though the partition function allows exact calculation of ground state properties of the quantum hard-squares model up to fairly large system size, the results, as we will discuss later, are only approximations to the exact solutions of the Rydberg lattice gas. With the knowledge of the partition function, it is possible to obtain expectation values of various classical observables. And this will be presented in detail in the upcoming section.

4.4.2 Classical Observables

Now, we demonstrate how to apply the known partition function of the classical hard-squares to obtain expectation values of classical observables. We will first start with two simple observables, the expectation value of the number of hard-squares present in the lattice, $\langle N_{k,m} \rangle$; and the variance of $\langle N_{k,m} \rangle$ defined as $\langle \delta N_{k,m} \rangle = \langle N_{k,m}^2 \rangle - \langle N_{k,m} \rangle^2$. In relation to partition function, these quantities can be calculated as,

$$\begin{aligned} \langle N_{k,m} \rangle &= \frac{\partial}{\partial \Xi} \ln Z_{\text{h-sqr}}; \\ \langle \delta N_{k,m} \rangle &= -\frac{\partial^2}{\partial \Xi^2} \ln Z_{\text{h-sqr}}, \end{aligned} \quad (4.10)$$

with $\Xi = 2\ln(\xi)$. The obtained results are summarised in Fig. 4.2 where we have rescaled these quantities by a factor of $1/L$, with $L = M \times N$ to give the fractional density of hard-squares, denoted as $\langle n_{k,m} \rangle$ and the corresponding variance denoted as $\langle \delta n_{k,m} \rangle$. In particular, with a 4-by-4 square lattice, as function of the

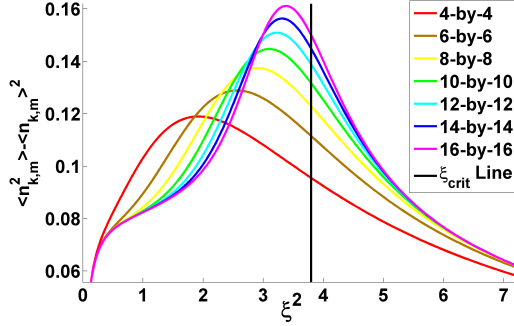


Figure 4.3: Variance of the density of Rydberg atoms obtained with lattice size N -by- N with N being 4 to 16 in step of 2. The black vertical line demonstrates the critical fugacity at $N \rightarrow \infty$ as predicted in the classical Baxter’s hard-square. The plots demonstrate the ability of the transfer matrix to solve the partition function of hard-squares for large lattice sizes. Moreover, the increasing peak value of the variance with increasing lattice size suggests a possible divergence at the thermodynamic limit where $N \rightarrow \infty$. Thus, the peak value of each curve indicates the critical fugacity for the corresponding lattice size.

fugacity, ξ , we compare the obtained $\langle n_{k,m} \rangle$ and $\langle \delta n_{k,m} \rangle$ via the partition function (blue) with the ones obtained using the numerical ground state of $H_{\text{R-Ksq}}$, e.g. $\langle \xi | n_{k,m} | \xi \rangle_{\text{num}}$ (red). As seen in the plots, the obtained values from different methods lie exactly on top of each as expected. This indicates that the transfer matrix method has correctly calculated the partition function and provides a numerical tool to obtain the exact solutions to the ground state properties of the quantum hard-squares model. We have also calculate the variance, $\langle \delta n_{k,m} \rangle$ with the use of the partition function for system size up to 16-by-16 and illustrate them in Fig. 4.3 with various colours. In the plots, firstly one observes that the magnitude of ξ where the peak value of the variance is located seems to saturate to a particular value. In addition, the peak value of the variance becomes larger as the lattice size increases. These patterns together suggests a divergence in $\langle \delta n_{k,m} \rangle$ as ξ approaches a critical value, ξ_c .

A divergence in the statistical fluctuation suggests a phase transition at the critical value where statistical fluctuation goes to infinity, e.g. at the critical fugacity in Baxter’s classical hard-squares model (indicated by the black vertical line at $\xi^2 \approx 3.6$ in Fig. 4.3. Although the transition only occurs in the thermodynamic limit where the lattice size approaches infinity, one can still extract the critical value by gradually increasing the lattice size and record how the maximum $\langle \delta n_{k,m} \rangle$ shifts its position in terms of ξ^2 .

4.4.3 Density-density Correlation

In the following, we will show how to obtain expectation values of two-body correlation by using a modified partition function. In particular, we will calculate the correlation between lattice sites which are next-nearest neighbours in the square lattice, e.g. $\langle n_{k,m}n_{k+1,m+1} \rangle$. The technique adopted is to firstly add the term, $\alpha \sum_{k,m} n_{k,m}n_{k+1,m+1}$ into the Hamiltonian of the classical hard-squares, $H_{\text{h-sqr}}$. The new Hamiltonian thus reads,

$$H'_{\text{h-sqr}} = H_{\text{h-sqr}} + \alpha \sum_{k,m} n_{k,m}n_{k+1,m+1}, \quad (4.11)$$

with $H_{\text{h-sqr}}$ given in Eq. (4.4). The new parameter, α can be physically interpreted as the interaction strength between a particle present on the $\{k, m\}$ -th site and its next-nearest neighbour located on the $\{k+1, m+1\}$ -th site (or alternatively, two adjacent classical hard-squares). Hence, this modified Hamiltonian describes a classical hard-squares model with nearest neighbour interactions between the hard-squares. $H'_{\text{h-sqr}}$ allows the construction of a new partition function where,

$$Z'_{\text{h-sqr}} = \sum_{k,m} e^{-(H_{\text{h-sqr}} + \alpha \sum_{k,m} n_{k,m}n_{k+1,m+1})}. \quad (4.12)$$

The aim is to obtain $\langle n_{k,m}n_{k+1,m+1} \rangle$, and this quantity can be determined by the following expression,

$$\langle n_{k,m}n_{k+1,m} \rangle = \frac{1}{Z'_{\text{h-sqr}}} \sum_{k,m} n_{k,m}n_{k+1,m} e^{-H'_{\text{h-sqr}}} = -\frac{1}{Z'_{\text{h-sqr}}} \frac{\partial Z'_{\text{h-sqr}}}{\partial \alpha} = -\frac{\partial \ln Z'_{\text{h-sqr}}}{\partial \alpha}. \quad (4.13)$$

The modified partition function, $Z'_{\text{h-sqr}}$ can be also calculated through the transfer matrix method. Firstly, writing in the product form, we have,

$$Z'_{\text{h-sqr}} = \sum_{\{n_{k,m}\}} e^{2\ln(\xi) \sum n_{k,m}} e^{\alpha \sum n_{k,m}n_{k+1,m+1}} \prod_m^N \prod_k^L (1 - n_{k,m}n_{k+1,m})(1 - n_{k,m}n_{k,m+1}), \quad (4.14)$$

where we have abbreviated the series of sums, $\sum_{k,m} \sum_{k+1,m} \cdots \sum_{K,M}$ by $\sum_{\{k,m\}}$. And by defining a new transfer matrix as,

$$T'_{\text{h-sqr}}(n_{k,m}, n_{k,m+1}) = \prod_k^L e^{2\ln(\xi) \sum n_{k,m}} e^{\alpha \sum n_{k,m}n_{k+1,m+1}} \times (1 - n_{k,m}n_{k+1,m})(1 - n_{k,m}n_{k,m+1}),$$

the partition function $Z'_{\text{h-sqr}}$ can eventually be obtained by $Z'_{\text{h-sqr}} = \text{Tr } T'^M$. The extra term present in T' , $e^{\alpha \sum n_{k,m}n_{k+1,m+1}}$ in comparison to T can be physically

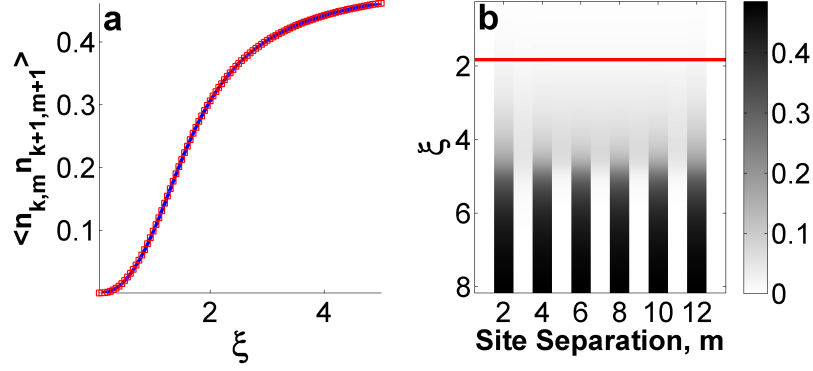


Figure 4.4: a) Expectation values of density-density correlation for adjacent hard-squares. We compare the results obtained directly from the quantum hard-squares model described by $H_{R-K_{\text{sqr}}}$ (red squares) with that from the partition function of the classical hard-squares (blue line). An exact overlap further proves the validity of the classical hard-squares model; b) Expectation values of density-density correlation for hard-squares that are increasingly further apart within a row. The separation of two hard-squares is presented by the number in the horizontal axis, e.g. 2 represents two hard-squares that are separated by two lattice sites. The vertical axes indicates an increasing fugacity to show how these density-density correlation varies with the fugacity. The colour code works in the following way: white for an expectation value of 0 (non-correlated) and black for an expectation value of 1 (fully correlated). Long range order in the correlation pattern starts to emerge after ξ reaches critical fugacity (red line).

interpreted as a α -dependent weight factor for configurations containing adjacent hard-square. For configurations absent of adjacent hard-squares, the extra term has no contribution to the partition function as $e^{\alpha \sum n_{k,m} n_{k+1,m+1}} = 1$. Considering the original Baxter's classical hard-squares situation where simultaneous diagonal occupation is interaction free, i.e. hard-squares do not interact, we have $\alpha = 0$. Therefore, the two-body correlation in Baxter's classical hard-squares can be calculated as

$$\langle n_{k,m} n_{k+1,m} \rangle = \left. \frac{\partial \ln Z'_{\text{h-sqr}}}{\partial \alpha} \right|_{\alpha=0} = \left. \frac{\partial \text{Tr}(T'_{\text{h-sqr}})^N}{\partial \alpha} \right|_{\alpha=0}. \quad (4.15)$$

To verify the validity of this new partition function, we compare $\langle n_{k,m} n_{k+1,m+1} \rangle$ obtained from the modified partition function (blue) with $\langle \xi | n_{k,m} n_{k+1,m+1} | \xi \rangle_{\text{num}}$ obtained from numerical diagonalisation of $H_{R-K_{\text{sqr}}}$ (red squares) in Fig. 4.4(a). As one sees, a perfect agreement between the two results has been observed for a 4-by-4 lattice, which confirms the validity of the transfer matrix calculation of the modified partition function, $Z'_{\text{h-sqr}}$.

The two-body correlation obtained is not the only type of configuration that corresponds to two adjacent hard-squares on a square lattice. The other possi-

ble configuration can be described by the operator $n_{k,m}n_{k+1,m-1}$. Nonetheless, carrying out the calculation of $\langle n_{k,m}n_{k+1,m-1} \rangle$ following the exact same method mentioned above, we obtain the result that $\langle n_{k,m}n_{k+1,m+1} \rangle = \langle n_{k,m}n_{k+1,m-1} \rangle$. This can be explained by the rotational symmetry of the lattice, i.e. the system is rotationally invariant under 90 degrees (anti-)clockwise rotation. To see this property of the system mathematically, we can introduce a rotational operator, \hat{R} , which upon acting on a spin state will rotate the configuration anti-clockwise by 90 degrees. For example,

$$R \left| \begin{pmatrix} \uparrow & \downarrow & \downarrow \\ \downarrow & \downarrow & \downarrow \\ \uparrow & \downarrow & \downarrow \end{pmatrix} \right\rangle = \left| \begin{pmatrix} \downarrow & \downarrow & \downarrow \\ \downarrow & \downarrow & \downarrow \\ \uparrow & \downarrow & \uparrow \end{pmatrix} \right\rangle. \quad (4.16)$$

It is easy to show that $\hat{R}|\xi\rangle_{\text{num}} = |\xi\rangle_{\text{num}}$ since a rotated configuration is still one of the substates in the ground state $|\xi\rangle_{\text{num}}$.

We now want to extend the calculation to determine two-body correlations along one direction in the lattice, i.e. $\langle n_{k,m}n_{k,m+1} \rangle$, $\langle n_{k,m}n_{k,m+2} \rangle$, and so forth. The same result is expected if one calculate two-body correlations along the other direction due to the rotation symmetry discussed. In Fig. 4.4(b), with the varying fugacity, ξ , we show the obtained two-body correlations in a row with a lattice size of 14-by-14. In the horizontal axis, the number corresponds to the distance between two spins. For small ξ , the system has no correlation pattern as the overall density of hard-squares is close to zero. As ξ increases, more hard-squares emerges, but no apparent long range order can be seen until a critical fugacity value is reached. Here, we have also indicated the expected critical ξ in red for reference. The results here coincide with the prediction made previously when discussing transition behaviour from the calculated variance, $\langle \delta n_{k,m} \rangle$. This is because correlation pattern in Fig. 4.4(b) indicates a phase transition from a unordered phase to an ordered one as ξ passes a critical value.

The results obtained in the section provides the following facts: firstly, as shown in Fig. 4.3, Fig. 4.4 (b), and Fig. 4.8, the transfer matrix method allows the determination of the partition function of classical hard-squares up to large system sizes containing more than 200 atoms. Knowing the partition function allows one to calculate expectation values of classical observables such as density and density-density correlation. This will prove to be very useful in later calculation of the Rydberg lattice gas. Secondly, Fig. 4.2 and Fig. 4.4(a) indicate that the partition function of the classical hard-squares allows a very accurate calculation of the properties of the quantum many-body ground state, $|\xi\rangle_{\text{sqr}}$ of the quantum hard-squares model described the Hamiltonian, $H_{\text{R-K}_{\text{sqr}}}$, which takes the Rokhsar-

Kivelson form.

4.5 Connection to the Rydberg Lattice Gas

Now, to use the knowledge of the quantum hard-squares model, in this section, we will show how we can connect the Rydberg lattice gas in the square lattice to the quantum hard-squares model. Starting from Hamiltonian (4.1), the first thing we do is to transform it into an interaction picture with respect to nearest neighbour interaction by following the procedure provided in Appendix A. The transformation leads to an effective Hamiltonian which explicitly demonstrates the nearest neighbour blockade mechanism. Keeping only interactions between Rydberg atoms which are within next-nearest neighbours, as illustrated by the blue region in Fig. 4.1, and neglecting anything beyond this region, the effective Hamiltonian of the Rydberg gas on the square lattice reads [32],

$$H_{\text{eff-sqr}} = \Omega \sum_{k,m}^L \sigma_{k,m}^x \mathcal{P}_{k,m} + \Delta \sum_{k,m}^L n_{k,m} + \frac{V}{8} \sum_{k,m}^L (n_{k,m} n_{k+1,m+1} + n_{k,m} n_{k+1,m-1}), \quad (4.17)$$

with the plaquette operator $\mathcal{P}_{k,m} \equiv P_{k+1,m} P_{k-1,m} P_{k,m+1} P_{k,m-1}$ and the rest of parameters having their usual meanings. The first term immediately illustrates the nearest-neighbour blockade mechanism: an (de-)excitation can only take place on site $\{k, m\}$ when all its four nearest neighbour atoms are in the local ground state. In the spin product basis, the Hilbert space is hence split into uncoupled blocks similar to the one-dimensional case, and we are interested only in the subspace without the presence of adjacent Rydberg atoms. We refer to this special subspace as the physical subspace. In the physical subspace, one can build up the connection to the quantum hard-squares model qualitatively as shown in Fig. 4.1. The idea is the following: since Rydberg excitation in adjacent lattice sites is strictly forbidden, each Rydberg atom is always accompanied by four ground state atoms in its four adjacent lattice sites. Hence, this allows us to effectively treat a Rydberg atom as a hard-square with the centre located at the lattice site and a diagonal length of $2a$. As such, the first term in Hamiltonian (4.17), being a quantum term, effectively places or removes one hard-square from the lattice located at the $\{k, m\}$ -th site. In the absence of this quantum term, the Hamiltonian will resemble the classical hard-squares model as described in Eq. (4.11) in the regime $V \rightarrow \infty$, with an effective chemical potential $\Delta = -2 \ln(\xi)$, and an interaction strength of $V/8 = \alpha$ between adjacent classical hard-squares. With this impression in mind, one sees that how closely our Rydberg lattice gas is related to the classical Baxter's hard-squares model. With the presence of the quantum term

appearing in Hamiltonian (4.17), we will continue to demonstrate how mathematically one can approximate it with the Hamiltonian of the quantum hard-squares model as described by Eq. (4.2).

To proceed, we follow method used previously in Sec. 2.2.1. The idea is to add a term, $H_\xi = \sum_{k,m} \mathcal{P}_{k,m}[\xi^{-1}n_{k,m} + \xi(1 - n_{k,m})]$ into $H_{\text{eff-sqr}}$ and subsequently subtract it so that $H_{\text{eff-sqr}}$ remains unchanged overall. However, by rearranging $H_{\text{eff-sqr}}$, we can arrive Hamiltonian of the following form,

$$H_{\text{eff-sqr}} = E_0 + H_{\text{R-K}_{\text{sqr}}} + H', \quad (4.18)$$

where the constant term $E_0 = -\Omega L\xi$ can be thought as an approximate ground state energy when H' is minimised. $H_{\text{R-K}_{\text{sqr}}}$ is exactly the Hamiltonian that describes the quantum hard-squares model. And finally, H' acts as a perturbing Hamiltonian which we want to minimise such that $H_{\text{eff-sqr}}$ is approximately $H_{\text{R-K}_{\text{sqr}}}$ with an energy offset. Mathematically, the perturbing Hamiltonian reads,

$$\begin{aligned} H' = & [\Delta - (\xi^{-1} - 5\xi)\Omega] \sum_{k,m}^L n_{k,m} \\ & + \left[\frac{V}{(\sqrt{2})^6} - \Omega\xi \right] \sum_{k,m}^L 2(n_{k+1,m+1} + n_{k+1,m-1})n_{k,m} \\ & + \Omega\xi \sum_{k,m}^L n_{k,m} (-(n_{k+2,m} + n_{k,m+2}) + n_{k+1,m+1}n_{k+1,m-1} \\ & + n_{k-1,m+1}n_{k-1,m-1} + n_{k+1,m+1}n_{k-1,m+1} \\ & \quad + n_{k+1,m-1}n_{k-1,m-1} - n_{k+2,m}n_{k+1,m+1}n_{k+1,m-1}) \\ & + \Omega(\xi^{-1} - \xi) \sum_{k,m}^L n_{k,m} [2(n_{k+1,m} + n_{k,m+1}) \\ & \quad - (n_{k+1,m}n_{k-1,m} + n_{k,m+1}n_{k,m-1} + n_{k+1,m}n_{k,m+1} \\ & \quad \quad + n_{k+1,m}n_{k,m-1} + n_{k-1,m}n_{k,m+1} + n_{k-1,m}n_{k,m-1}) \\ & \quad + (n_{k+1,m}n_{k-1,m}n_{k,m-1} + n_{k+1,m}n_{k-1,m}n_{k,m+1} \\ & \quad \quad + n_{k+1,m}n_{k,m+1}n_{k,m-1} + n_{k-1,m}n_{k,m+1}n_{k,m-1}) \\ & \quad - n_{k,m+1}n_{k,m-1}n_{k+1,m}n_{k-1,m}n_{k,m}]. \end{aligned} \quad (4.19)$$

The first line in H' consists of all single body terms and the second line contains two-body terms that describes Rydberg atoms which are at next-nearest neighbour distance. These two lines are exactly zero on the ξ_{sqr} -manifold defined as

$$(i)\Delta = -(5\xi - \xi^{-1})\Omega; \quad (ii)V = 8\Omega\xi. \quad (4.20)$$

The rest of the terms in H' describes many-body interactions with various configurations. To visualise these many-body interactions, we plot the corresponding configurations in Fig. 4.5 with the associated ξ -dependent weight given on the side. The green dot represents the reference Rydberg atom which is interacting simultaneously with neighbouring Rydberg atoms on the sites presented by the red dots. As shown, all configurations with an energy of $-\xi^{-1} + \xi$ contain Rydberg atoms which are located on adjacent lattice sites. In the physical subspace, these many-body terms in principle has zero contribution to the system as the corresponding spin product states are excluded in this subspace. The rest of the terms are still problematic as these many-body terms cannot be simply neglected and the contributions of them depends on ξ which in turn depends on the laser parameters $\{\Omega, \Delta\}$ within the ξ_{sqr} -manifold. However, these terms still have small contributions in two special cases in terms of the fractional Rydberg density, $\langle n \rangle$, defined as the number of Rydberg atoms present in the lattice divided by the total number of lattice, L :

(i) For a small $\langle n \rangle$, i.e. only a small amount of Rydberg atoms are randomly populated in the lattice, these Rydberg atoms are very unlikely to present at close range. Since the configurations as shown in Fig. 4.5 account for Rydberg atoms at close range, the contributions of these terms are therefore insignificant.

(ii) When the laser is sufficiently detuned to overcome the interaction energy between Rydberg atoms at next-nearest neighbours range, the system favours a maximally occupied state having a fractional Rydberg density of $\approx 1/2$. This density can only be achieved when the Rydberg atoms are ordered into a crystalline structure. As shown later the actual ground state of the Rydberg Hamiltonian, $H_{\text{Ryd}_{\text{sqr}}}$, is well described by the ground state of $H_{\text{R-K}_{\text{sqr}}}$ in this case. Therefore, we conclude that H' is minimised within the ξ_{sqr} -manifold and predict that the ground state of $H_{\text{Ryd}_{\text{sqr}}}$ should be very well described by the ground state of $H_{\text{R-K}_{\text{sqr}}}$ in the ξ_{sqr} -manifold. We will justify our results in the next section by numerically obtaining the ground states of the above two Hamiltonians and comparing them.

4.6 The Numerical Ground States of $H_{\text{Ryd}_{\text{sqr}}}$ and $H_{\text{R-K}_{\text{sqr}}}$

In this section, to justify the assumption made previously where $H_{\text{Ryd}_{\text{sqr}}}$ can be approximated by $H_{\text{R-K}_{\text{sqr}}}$ in the ξ_{sqr} -manifold, we will simply perform direct diagonalisation of the two Hamiltonians with small lattice size to obtain the ground state of each Hamiltonian. It is worth to note here that such diagonalisation is restricted by the lattice size as for a system containing 16 particles, i.e. 4-by-4

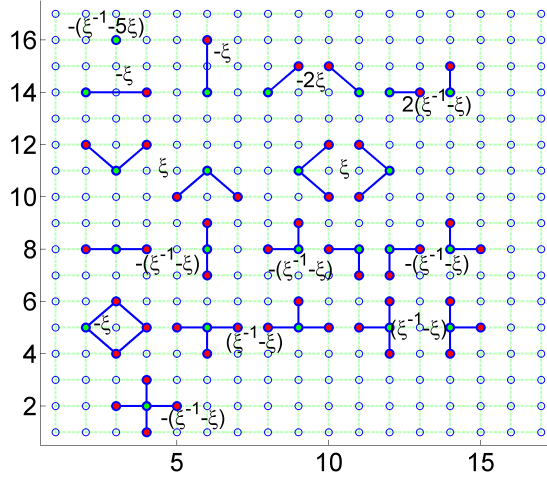


Figure 4.5: All possible configurations of single/many-body interactions derived from the added H_ξ . All solid dots represent atoms in the Rydberg state where the green dot shows the reference site, $\{k, m\}$. The ξ -dependent weight is given on the side of the corresponding configuration. Identical configurations due to translational invariance of the lattice are included into the weight coefficients. Notice that there are configurations that include nearest neighbour excitations which are forbidden in the physical subspace.

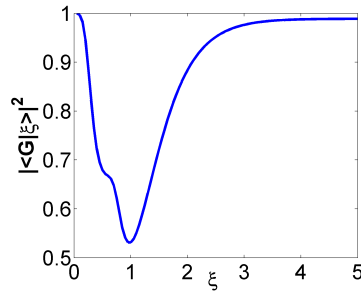


Figure 4.6: Overlap between the true ground state $|G\rangle_{\text{sqr}}$ and the approximate ground state $|\xi\rangle_{\text{num}}$ on the ξ -manifold for a 4-by-4 square lattice. The overlap never drops below 0.5 for all ξ . The curve indicates that the two ground states are very close to each other and even almost identical at small and large fugacity.

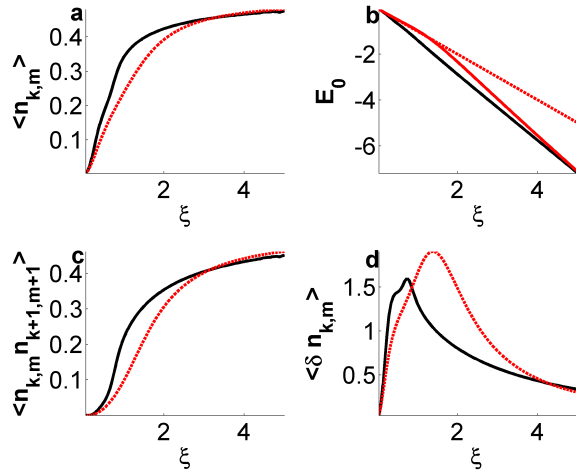


Figure 4.7: Comparison of the quantities obtained from $|\xi\rangle_{\text{num}}$ and $|G\rangle_{\text{sqr}}$ of a 4-by-4 square lattice: results obtained from the ground state, $|G\rangle_{\text{sqr}}$ of Rydberg Hamiltonian $H_{\text{Ryd}_{\text{sqr}}}$ are plotted in black solid and results obtained from the ground state, $|\xi\rangle_{\text{num}}$ of $H_{\text{R-K}_{\text{sqr}}}$ are plotted in dashed red. (a) Density of Rydberg atoms; (b) Ground state energy per atom (red solid shows result after applying perturbation theory to the red dash); (c) Density-density correlation between Rydberg atoms that are next nearest neighbours; (d) Variance of the quantity in (a).

square lattice, the Hilbert space is 2^{16} which is already a large number to deal with in terms of matrix dimension. For slightly larger system, for instance, a 6-by-6 square lattice, numerical diagonalisation is only feasible by exploring certain symmetries in the system to transform the Hamiltonian into a block diagonal form [88]. Since interesting physics often emerges with sufficiently large system size, e.g. phase transitions, overcoming numerical restrictions in quantum many-body systems is hence one of the primary reasons for physicists to explore possible alternatives in studying these systems.

As discussed, $|\xi\rangle_{\text{num}}$ is expected to be a good approximation for the true ground state, $|G\rangle_{\text{sqr}}$ within the ξ_{sqr} -manifold, and should be the closest at small and large ξ . These expectations are confirmed by the plot shown in Fig. 4.6 where we have calculated the overlap between the two ground states for the system lattice size, i.e. ${}_{\text{num}}\langle \xi | G \rangle_{\text{sqr}}$. With such large dimension in Hilbert space, it is very unlikely for two states to have a large overlap value unless they are similar. Therefore, according to Fig. 4.6, where the overlap never dropped below 0.5, one can safely conclude that $|\xi\rangle_{\text{num}}$ is a good approximation of the true ground state, $|G\rangle_{\text{sqr}}$ in the ξ_{sqr} -manifold. Moreover, at both small ξ and large ξ , the overlap even yields a value almost equal to one which suggests that the two ground states are almost identical, hence providing strong evidences in supporting the arguments made in the previous section when discussing H' and $|\xi\rangle_{\text{sqr}}$.

With the numerically calculated ground states, it is possible to further obtain

expectation values of classical observables such as the ground state energy by sandwiching the classical operator with the ground state, i.e. $\langle \hat{O} \rangle \equiv \langle G | \hat{O} | G \rangle$ with \hat{O} being an operator and $|G\rangle$ being a ground state. In particular, we have obtained the fractional Rydberg density, defined as $\langle n_{k,m} \rangle = \langle N \rangle / L$ with $\langle N \rangle$ being the expected total Rydberg atoms in the lattice, the ground state energy, E_0 , density-density correlations for Rydberg atoms located on lattice sites that are next-nearest neighbours, i.e. $\langle n_{k,m} n_{k+1,m+1} \rangle$, and variance of the fractional Rydberg density defined as $\langle \delta n_{k,m} \rangle = \langle n_{k,m}^2 \rangle - \langle n_{k,m} \rangle^2$. Using 4-by-4 square lattice, and as a function of the fugacity ξ , these quantities are plotted in Fig. 4.7 where quantities obtained from $|G\rangle_{\text{sqr}}$ are plotted in black and quantities obtained from $|\xi\rangle_{\text{num}}$ are plotted in red. In general, the plots show a good agreement between the two ground states, particularly in the region of both low and high values of ξ . In the energy plot, i.e. Fig. 4.7(b), the red solid curve shows the result when first order perturbation theory is performed with H' being the perturbing Hamiltonian such that $E_{\text{perturb}} = E_0 + \text{num} \langle \xi | H' | \xi \rangle_{\text{num}}$. The corrected ground state energy, E_{perturb} is found to be closer to the real ground state energy (black curve) than E_0 (red dash curve). At large ξ between the dashed red and black curves, the discrepancy seen can be explained by the non-zero energy contribution from the many-body terms in H' , i.e the 5-th line in Eq. (4.19). Still, these terms though affect the ground state energy, they do not affect the fractional Rydberg density as the real ground state is well approximated by $|\xi\rangle_{\text{num}}$.

Let us now summarise the results obtained so far: the Rydberg lattice gas in a two-dimensional square lattice can be well approximated by a quantum version of Baxter's classical hard-squares model within the ξ_{sqr} -manifold introduced in Eqs. (4.20). This is justified by comparing the exact numerical ground states of the Rydberg lattice gas described by $H_{\text{Ryd}_{\text{sqr}}}$ and the quantum hard-squares model described by $H_{\text{R-K}_{\text{sqr}}}$, where the overlap between the two respective ground states $|G\rangle_{\text{sqr}}$ and $|\xi\rangle_{\text{sqr}}$ is illustrated in Fig. 4.6 and other properties of the ground states are depicted in Fig. 4.7. These excellent agreements, particularly for small and large ξ suggest that $|\xi\rangle_{\text{sqr}}$ is a natural candidate for being used as a variational ansatz to approximate the true ground state even away from the ξ_{sqr} -manifold. Eventually, using such approximation, one is able to obtain a phase diagram in the parameter space. The details of this variational approach will be given in the next section. Moreover, as shown in Sec. 4.4, the transfer matrix method for determining the partition function allows the calculation of ground state properties of $|\xi\rangle_{\text{sqr}}$ for fairly large lattice size. This means that the quantum hard-squares model provides not only excellent approximation to the original Rydberg lattice gas, but also allows one to explore features that usually manifest at large system size, e.g. phase transitions.

4.7 $|\xi\rangle_{\text{sqr}}$ as a Variational Ansatz

To proceed, we now utilise the known knowledge of the quantum hard-squares model to carry out a variational study of the Rydberg lattice gas in a square lattice. The principle idea is to write $|\xi\rangle_{\text{sqr}}$ in terms of a variational parameter, η , which we denote as $|\eta\rangle$. Then, we optimise the variational state $|\eta\rangle$ by minimising the energy functional $\langle H_{\text{Ryd}_{\text{sqr}}} \rangle_{\eta} \equiv \langle \eta | H_{\text{Ryd}_{\text{sqr}}} | \eta \rangle$. For each set of laser parameters, $\{\Omega, \Delta\}$, we have an energy functional to minimise and the corresponding optimised state η will be used as an approximate ground state. This optimisation method is known as the variational principle, which can be explained in the following way. For an arbitrary Hamiltonian, H , one can express the ground state and the ground state energy as, $H|\phi_0\rangle = E_0|\phi_0\rangle$, where E_0 is the energy of the non-degenerate ground state $|\phi_0\rangle$. The variational principle states that for any normalised wavefunction $|\phi_n\rangle$, the expectation value of the Hamiltonian over $|\phi_n\rangle$ has a value greater or equal the ground state energy [61]. Mathematically, we have

$$\langle \phi_n | H | \phi_n \rangle \geq E_0. \quad (4.21)$$

This is because the ground state energy is defined as the minimum possible eigenvalue of a Hamiltonian. The equality of the above expression only holds if the trial wavefunction ϕ_n is exactly the ground state wavefunction $|\phi_0\rangle$, because $\langle \phi_0 | H | \phi_0 \rangle = \langle \phi_0 | E_0 | \phi_0 \rangle = E_0 \langle \phi_0 | \phi_0 \rangle = E_0$. Therefore, in the case where the exact ground state of a Hamiltonian cannot be obtained, the variational principle provides an upper bound of the ground state energy with a corresponding variational state (an ansatz state). Although how close the upper boundary is to the actual ground state energy cannot be determined by this method, if one minimises the expression, $\langle \phi_n | H | \phi_n \rangle$ with respect to the variational parameter, n , in this case, one eventually finds a good approximation of the ground state energy. And at this point, the variational state is closest to the actual ground state.

To compute the energy functional, we express it in terms of expectation values in the following way,

$$\langle H_{\text{Ryd}_{\text{sqr}}} \rangle_{\eta} = \Omega \sum_{k,m}^L \langle \sigma_{k,m}^x \rangle_{\eta} + \Delta \sum_{k,m}^L \langle n_{k,m} \rangle_{\eta} + \frac{V}{8} \sum_{k,m}^L (\langle n_{k,m} n_{k+1,m+1} \rangle_{\eta} + \langle n_{k,m} n_{k+1,m-1} \rangle_{\eta}),$$

where $\langle \cdot \rangle_{\eta}$ is used to denote $\langle \eta | \cdot | \eta \rangle$. We have already determined the expectation values of the classical operators in previous section by using the partition function of Baxter's classical hard-squares [51] and the transfer matrix method [117]. Interestingly, the expectation value of the non-classical operator, $\sigma_{k,m}^x$ can also be obtained [32] as one can express them in terms of the classical operators due to the

special property of the ground state $|\xi\rangle_{\text{sqr}}$. As seen previously, this ground state is annihilated by all $h_{k,m}$, i.e. $h_{k,m}|\xi\rangle_{\text{sqr}} = 0$. Therefore, any operator acting on this expression should also be zero, i.e. $\hat{X}h_{k,m}|\xi\rangle_{\text{sqr}} = 0$, with \hat{X} being an arbitrary operator. Assigning the arbitrary operator to be the quantum operator $\sigma_{k,m}^+$, i.e. $\hat{X} = \sigma_{k,m}^+$, one finds

$$\sigma_{k,m}^+ h_{k,m} |\xi\rangle_{\text{sqr}} = \sigma_{k,m}^+ \mathcal{P}_{k,m} [\sigma_{k,m}^x + \xi^{-1} n_{k,m} + \xi(1 - n_{k,m})] |\xi\rangle_{\text{sqr}}. \quad (4.22)$$

The only non-trivial solution of this equation is when $(n_{k,m} + \xi \sigma_{k,m}^+) |\xi\rangle_{\text{sqr}} = 0$. Rearranging this solution gives the relation between the quantum operator and classical operator as

$$\sigma_{k,m}^+ |\xi\rangle_{\text{sqr}} = -\frac{n_{k,m}}{\xi} |\xi\rangle_{\text{sqr}}. \quad (4.23)$$

Taking the expectation value on both sides, we arrive at $\langle \sigma_{k,m}^+ \rangle = -\langle n_{k,m} \rangle / \xi$. For the hermitian conjugate of $\sigma_{k,m}^+$, it is easy to show that $\langle \sigma_{k,m}^+ \rangle = \langle \sigma_{k,m}^- \rangle$ as $(\text{sqr} \langle \xi | \sigma_{k,m}^- | \xi \rangle)^\dagger = |\sigma_{k,m}^+ \rangle_{\text{sqr}}$. Therefore, expressing everything in terms of classical operators, the approximate ground state energy with the variational state reads,

$$\begin{aligned} \langle H_{\text{Ryd}_{\text{sqr}}} \rangle_\eta &= -\frac{2\Omega}{\xi} \sum_{k,m}^L \langle n_{k,m} \rangle_\eta + \Delta \sum_{k,m}^L \langle n_{k,m} \rangle_\eta \\ &\quad + \frac{V}{8} \sum_{k,m}^L (\langle n_{k,m} n_{k+1,m+1} \rangle_\eta + \langle n_{k,m} n_{k+1,m-1} \rangle_\eta). \end{aligned} \quad (4.24)$$

Using the transfer matrix methods, we have obtained the expectation values of each of the above observables, i.e. $\langle \sigma_{k,m}^x \rangle, \langle n_{k,m} \rangle, \langle n_{k,m} n_{k+1,m\pm 1} \rangle$, and in addition the ground state energy, E_0 in Fig. 4.8. In the limiting cases where $\xi \rightarrow 0$ and $\xi \rightarrow \infty$, the results are indeed what one expects from an analytical treatment by using the ground state $|\xi\rangle_{\text{sqr}}$ [c.f. Appendix B], where,

$$\begin{aligned} \langle n_{k,m} \rangle |_{\xi \rightarrow 0} &\approx 0; & \langle \sigma_{k,m}^x \rangle |_{\xi \rightarrow 0} &\approx 0; & \langle n_{k,m} n_{k+1,m+1} \rangle |_{\xi \rightarrow 0} &\approx 0; \\ \langle n_{k,m} \rangle |_{\xi \rightarrow \infty} &\approx \frac{1}{2}; & \langle \sigma_{k,m}^x \rangle |_{\xi \rightarrow \infty} &\approx 0; & \langle n_{k,m} n_{k+1,m+1} \rangle |_{\xi \rightarrow \infty} &\approx \frac{1}{2}. \end{aligned} \quad (4.25)$$

Knowing how the energy functional can be computed, one can perform the optimisation and see how well the optimised ground state, $|\eta\rangle$ can approximate the true ground state $|G\rangle_{\text{sqr}}$. For a 6-by-6 square lattice, by using the variational approach, as function of ξ , we plot the optimised ground state energy per lattice site and the fractional Rydberg density (black squares) in Fig. 4.9 (a). Comparing the results with the ones obtained from numerically diagonalising $H_{\text{Ryd}_{\text{sqr}}}$ (red), excel-

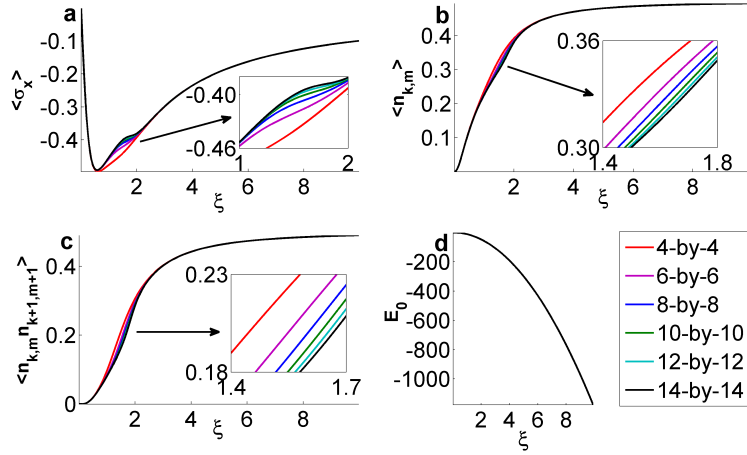


Figure 4.8: Expectation values of the observables appearing in the Hamiltonian (4.22) and the ground state energy: (a) Expectation value of $\sigma_{k,m}^x$ (b) Density of Rydberg atoms; (c) Density-density correlation of Rydberg atoms which are next nearest neighbours; (d) Ground state energy. Results for lattice size from 4-by-4 to 14-by-14 are plotted in different colours with index given on the right hand side of the energy plots. In the limiting cases, it is observed that $\langle \sigma_{k,m}^x \rangle_{\xi \rightarrow 0} = 0$, $\langle \sigma_{k,m}^x \rangle_{\xi \rightarrow \infty} = 0$; $\langle n_{k,m} \rangle_{\xi \rightarrow 0} = 0$, $\langle n_{k,m} \rangle_{\xi \rightarrow \infty} = 0.5$; $\langle n_{k,m} n_{k+1,m+1} \rangle_{\xi \rightarrow \infty} = 0$, $\langle n_{k,m} n_{k+1,m+1} \rangle_{\xi \rightarrow \infty} = 0.5$. In addition, as shown in the insets, the enlarged parts of the curves appear to be converging as lattice size increase.

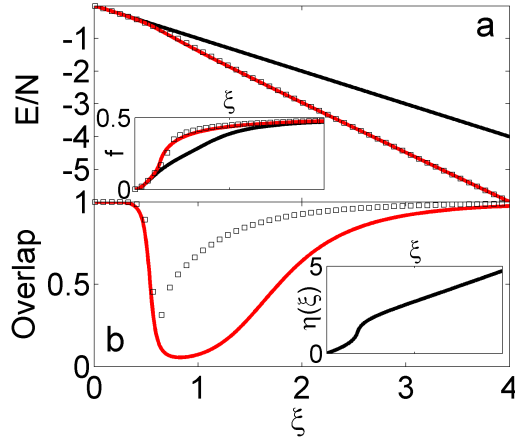


Figure 4.9: Comparing the quantities obtained from the optimised variational method to the same quantities obtained numerically from a 6-by-6 lattice on the ξ -manifold [32]. (a) Energy (main plot) and density per site (inset): exact ground state energy/density of $H_{\text{Ryd}_{\text{sqr}}}$ is plotted in red; energy/density obtained from $|\xi\rangle_{\text{sqr}}$ in the same manifold is plotted in black; energy/density obtained with the optimisation method to minimise $\langle \eta | H_{\text{Ryd}_{\text{sqr}}}(\xi) | \eta \rangle$ is plotted in black squares. (b) Red curve: overlap between $|\xi\rangle_{\text{sqr}}$ and $|G\rangle_{\text{sqr}}$; Black squares: overlap between $|\eta\rangle$ and $|G\rangle_{\text{sqr}}$; Inset: the optimising parameter η as a function of ξ .

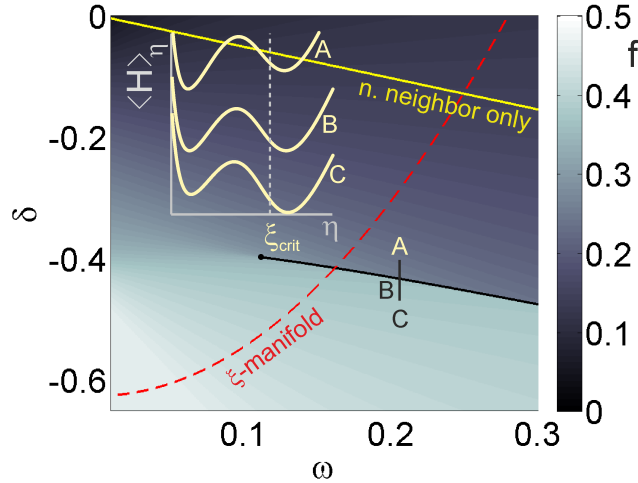


Figure 4.10: Phase diagram (in terms of density of Rydberg atoms) generated using the optimisation method with the variational state as a function of $\omega = \Omega/V$ and $\delta = \Delta/V$ for a 16-by-16 square lattice. The red dash indicates results on the ξ -manifold which is calculated in Fig. 4.9; The black line draws the phase transition line and the yellow line draws the transition line where only nearest neighbour interactions are included. The insets illustrate the energy functional at the corresponding points A, B and C, where one sees a shift in the global minimum as one crosses the transition line.

lent agreements are observed. Here we have also plotted the results obtained from the unoptimised ground state, $|\xi\rangle_{\text{sqr}}$, to demonstrate the improvement achieved by the variational method. In Fig. 4.9(b), we illustrated the obtained the overlap defined as $\text{num} \langle \xi | G \rangle_{\text{sqr}}$ in red and $\langle \eta | G \rangle_{\text{sqr}}$ in black squares. The latter indicates a drastic improvement on top of the first overlap where the overlap value never drops below 0.25 and stay higher than 0.5 for most ξ . This is a remarkable result as these many-body states in the Hilbert space has a dimension of 67 022 for a 6-by-6 lattice size. Notice that 67 022 is actually a reduced dimension from the original Hilbert space dimension of 2^{36} . This much smaller number is achieved by firstly excluding all the configurations with nearest neighbour excitations, and then by exploiting the translational and reflectional symmetries of the Hamiltonian (4.17) [32]. Still, an overlap value of higher than 0.5 indicates two states are similar. Also as expected, for small and large ξ , one sees that the overlap is nearly one, meaning the variational state, $|\eta\rangle$ is almost identical to the true ground state, $|G\rangle_{\text{sqr}}$.

4.8 Phase Diagram of the Rydberg Lattice Gas in Square Lattice

The excellent results produced by the variational method suggest that $|\xi\rangle_{\text{sqr}}$ is a suitable candidate as a variational ansatz for going beyond the ξ_{sqr} -manifold. Eventually, this allows one to explore the property of the approximate ground state in the entire parameter space described $\{\Omega, \Delta, V\}$. To obtain a phase diagram of the two-dimensional Rydberg lattice gas in the whole parameter regime, the energy functional $\langle H_{\text{Ryd}_{\text{sqr}}}\rangle_{\eta}$ is also minimised variationally in the regime away from the ξ -manifold. For convenience, we describe the entire parameter regime by two rescaled laser parameters defined as $\omega \equiv \Omega/V$ and $\delta \equiv \Delta/V$. The value of η at where the minimum energy occurs is denoted as η_{min} . With the determined η_{min} , we obtain the corresponding fractional Rydberg density, $f(\omega, \delta)$ and use it as the order-parameter for the phase diagram. The phase diagram is illustrated in Fig. 4.10. In the phase diagram, the range of values for δ and ω is chosen for the following reasons. For positive δ , Rydberg excitation is unfavoured, and hence the ground state is approximately a spin vacuum where the fractional Rydberg density $f = 0$. We consider nearest neighbour blockade where $V \gg \Omega$, hence for the results to be valid, ω has to remain small.

We now discuss the features present in the phase diagram by following a decreasing ω . Firstly, one notices that in the region $\omega > \omega_1 \approx 0.14$, the system exhibits two distinct phases, a liquid (unordered) phase and a solid (ordered) phase, where the two phases are separated by an apparent phase boundary (black line). Crossing this phase boundary from the liquid phase to the solid phase, which is illustrated along the line A - B - C, we find the energy functional $\langle H_{\text{Ryd}_{\text{sqr}}}\rangle_{\eta}$ has a double well structure with the global minimum located on either side of ξ_{crit} . In particular, as shown in the inset, around region A, the minima is on the left of ξ_{crit} . For positions very close to B, the double well has two local minima of the same height showing a competition between the two distinct phases. And finally when the laser is sufficiently negatively detuned, the laser driving is dominated by the detuning, and hence leading Rydberg atoms to form a half-filled ($f \approx 0.5$) crystalline structure. These behaviours suggest that the phase transition is discontinuous. A similar first order liquid-solid transition has also been found for Baxter's classical hard-squares model with additional (attractive) next nearest neighbour interactions [118, 119]. This suggests that our findings are not just a mere artefact of our variational approach. Along the black transition line, for $\omega_1 > \omega > \omega_2 \approx 0.1$, the system exhibits qualitatively different behaviour. Close to the phase boundary, the energy functional still has two distinct minima, however both are located below ξ_{crit} , i.e. the transition point of Baxter's classical

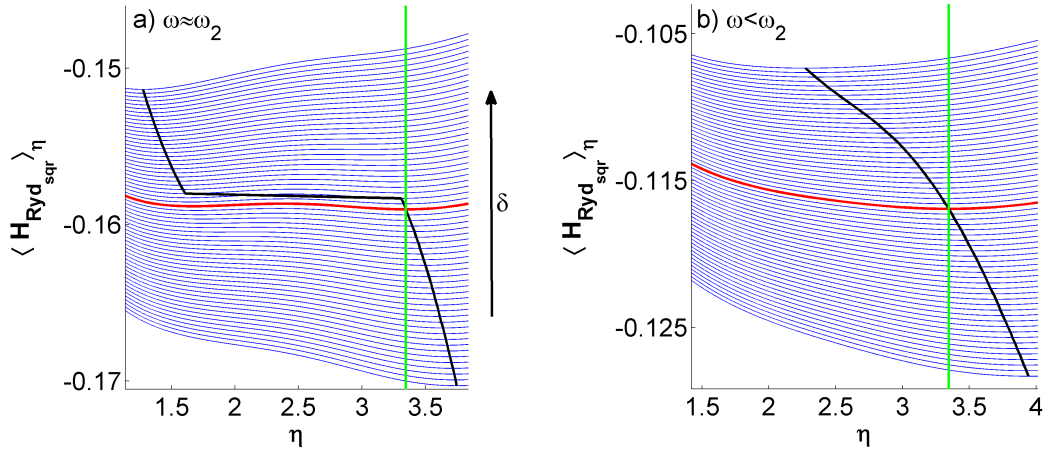


Figure 4.11: The variational energy $\langle H_{\text{Ryd}_{\text{sqr}}}\rangle_{\eta}$ as function of η . At fixed ω values where in a) $\omega \approx \omega_2$, and in b) $\omega < \omega_2$. The green line depicts the critical fugacity of the Baxter's hard-squares model. The black curve is the connected global minimum of each energy functional. The red curve indicates the approximate position where the first order transition occurs. As one can see, the only blue curves in graph (a) that have double maxima are the ones that are near the transition point. The double minima slowly merges into a single minima as one goes away from the critical point. This feature is seen more clearly in (b) where the double minima feature is completely gone at all values of δ for $\omega < \omega_2$.

hard-squares, hence indicating a first order transition from a phase with lower fractional density to a higher fractional density when reducing the detuning below $\delta \approx -0.4$. At $\omega = \omega_2$, the black transition line terminates at a critical point where one finds the two wells of the variational energy $\langle H_{\text{Ryd}_{\text{sqr}}}\rangle_{\eta}$ merges to a single minimum when deviating away from the critical values point along the δ -axis. For $\omega < \omega_2$, the variational state $|\eta\rangle$ predicts a continuous crossover from the liquid phase to the half-filled solid phase and the variational energy functional $\langle H_{\text{Ryd}_{\text{sqr}}}\rangle_{\eta}$ exhibits only a single minimum at all values of δ . Lastly, as $\omega \rightarrow 0$, it is expected that two classically ordered phases should be present according to Baxter's classical hard-squares: a quarter-filling phase for $0 > \delta > -0.5$ and the half-filling phase for $\delta < -0.5$. However, the variational state $|\eta\rangle$ is unable to resolve these phases and the corresponding discontinuous transition between the two phases for $\omega \ll \omega_2$.

Finally, we comment on the effect of longer ranged interactions, i.e. next-next-nearest neighbour interactions. When interactions beyond nearest neighbours are excluded in the system, as shown in the phase diagram in Fig. 4.10, the transition line is found to be significantly shifted (yellow). Therefore, the features in the phase diagram discussed previously can be thought as a direct consequence of

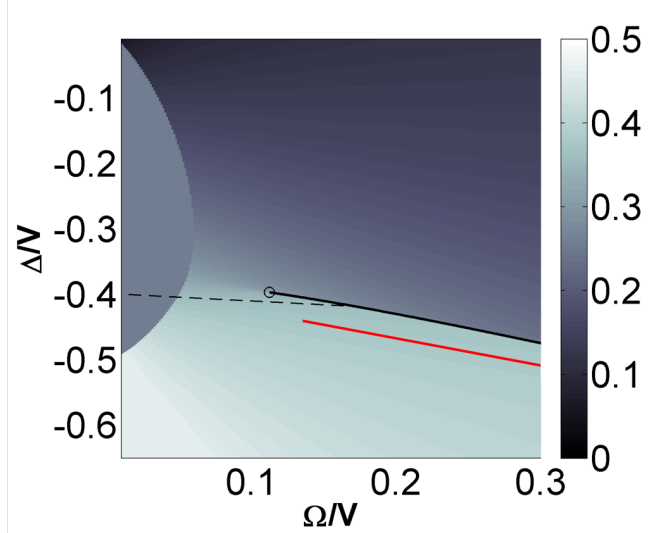


Figure 4.12: Phase diagram in the same fashion as Fig. 4.10, but with a quarter filling region determined by introducing a quarter filling state $|\phi\rangle$. Within the quarter filling lobe, the configuration energy $\langle\phi|H_{\text{Ryd}_{\text{sqr}}}| \phi\rangle_{1/4}$ is lower than the minimised variational energy $\langle\eta|H_{\text{Ryd}_{\text{sqr}}}| \eta\rangle$ for the same parameters, Ω/V and Δ/V . The circle indicates where the discontinues phase transition ends, and the dashed line illustrates the numerically obtained “extended phase boundary” described in the content.

including long range interactions between Rydberg atoms. Further including long range tails in the van der Waals interaction present in $H_{\text{Ryd}_{\text{sqr}}}$ in the quantum hard-squares model, we observe the transition line to be only marginally changed in position as shown in Fig. 4.12 in red, while the main features remain the same. Moreover, in Fig. 4.12, we have also demonstrated an extended “phase transition boundary” as a dashed line which corresponds to the laser parameters $\{\Delta/V, \Omega/V\}$ where the minimum of $\langle H_{\text{Ryd}_{\text{sqr}}} \rangle_{\eta}$ crosses the critical fugacity $\eta = \xi_c$ (c.f. Fig. 4.11). The lobe presented in this phase diagram will be discussed in detail in the next section. In the next section, we focus on the unobserved phases which are expected close to the classical limit.

4.9 Quarter-filling Variational State

In the classical limit, i.e. $\Omega = 0$, one can calculate energies of classical configurations. Hence, by comparing the energies of different configurations, one can obtain an expected phase diagram in this limit. For instance, we obtain the configuration energy to be $(-\Delta/2 + V)L$ for an ordered half-filled configuration and $-\Delta L/4$ for an ordered quarter-filling configuration. Equating these two energies, we obtain the phase boundary which occurs at $\delta = \Delta/V = -0.5$. However, as seen from the phase diagram obtained previously, the expected crystalline phase at

quarter-filling is not observed. One possible reason is that the variational ansatz used in the approximation does not possess certain symmetries and hence is unable to capture certain crystalline phases at less fillings. As discussed with Eq. (4.21), there are possible variational states that provides a better approximation, i.e. with an approximate ground state energy that is closer to the actual ground state energy. Therefore, in order to resolve the expected quarter-filling phase in the phase diagram, we introduce an alternative variational ansatz in the following form,

$$\begin{aligned}
|\phi\rangle_{1/4} = & N_\phi[|\alpha\rangle_1 |\downarrow\rangle_2 |\downarrow\rangle_3 |\downarrow\rangle_4 |\alpha\rangle_5 \dots |\downarrow\rangle_L \\
& + |\downarrow\rangle_1 |\alpha\rangle_2 |\downarrow\rangle_3 |\downarrow\rangle_4 \dots |\downarrow\rangle_L \\
& + |\downarrow\rangle_1 |\downarrow\rangle_2 |\alpha\rangle_3 |\downarrow\rangle_4 \dots |\downarrow\rangle_L \\
& + |\downarrow\rangle_1 |\downarrow\rangle_2 |\downarrow\rangle_3 |\alpha\rangle_4 \dots |\alpha\rangle_L],
\end{aligned} \tag{4.26}$$

with $N_\phi = 1/\sqrt{4 + 12\alpha^{L/2}}$ being the normalisation constant. We refer to this state as a quarter-filling state. Each of the spin product states represents one of the four degenerate quarter filling configurations. The spin state $|\alpha\rangle$ is defined as $|\alpha\rangle = (1 - \alpha^2)^{1/2} |\uparrow\rangle + \alpha^2 |\downarrow\rangle$ with the parameter α controlling whether $|\alpha\rangle$ is in the $|\downarrow\rangle$ state or $|\uparrow\rangle$ state. In the case of $\alpha = 1$, we have the spin vacuum configuration (all spins are pointing down), and when $\alpha = 0$, we have a superposition of four degenerate quarter-filling configurations and the expectation value of fractional Rydberg density is exactly $1/4$. Following methods given in Appendix C, the energy functional of the quarter filling state is given by

$$\langle H_{\text{Ryd}_{\text{sqr}}}\rangle_\alpha \equiv_{1/4} \langle \phi | H_{\text{Ryd}_{\text{sqr}}} | \phi \rangle_{1/4} = \frac{6\Omega L \alpha^{(\frac{L}{2}-1)} (1 - \alpha^2)^{\frac{1}{2}} + \Delta L (1 - \alpha^2)}{4 + 12\alpha^{\frac{L}{2}}}. \tag{4.27}$$

Treating the quarter-filling state also as an variational state with the variational parameter, α , we minimise the energy functional in the entire parameter space $\{\omega, \delta\}$. To obtain regions for which the system exhibits a quarter-filling phase, we compare the minimised $\langle H_{\text{Ryd}_{\text{sqr}}}\rangle_\alpha$ to the minimised $\langle H_{\text{Ryd}_{\text{sqr}}}\rangle_\eta$. Using fractional Rydberg density, f as the order parameter again, for any set of laser parameters $\{\omega, \delta\}$, f is determined with the use of the variational state that gives a lower energy. In Fig. 4.12, following this method, we have obtained a new phase diagram where one clearly sees a quarter-filling region ($f = 0.25$) as predicted by the new variational state $|\phi\rangle_{1/4}$.

Although introducing a quarter-filling variational state allows the determination of classically predicted crystalline phases, whether the boundary of this quarter-filling region is faithfully described by this new variational state is questionable. Moreover, the distinct boundary between the lobe and the rest of the

phase diagram cannot be simply considered as a discontinuous transition since what happens close to the boundary remains unclear with this artificial variational state. Nonetheless, to some extent, it proves the existence of different ordered phase near the classical limit.

4.10 Conclusion and Outlook

In this chapter, we carried out a detailed study of the strongly interacting Rydberg gas on a two-dimensional square lattice. In brief, we connected the Rydberg lattice gas to a quantum version of the Baxter's hard-square model and performed a variational study of the ground state of the Rydberg lattice gas by using the ground state of the quantum hard-squares model as a variational ansatz. Eventually, we obtained a phase diagram as a function of the re-scaled laser parameters, $\{\omega, \delta\}$, and using the fractional Rydberg density, f as the order parameter.

In the phase diagram, we have identified distinct phases such as an unordered phase and an ordered phase with half-filled Rydberg atoms. In addition, we have identified a discontinuous phase transition between the two phases based on the energy functional $\langle H_{\text{Ryd}_{\text{sqr}}} \rangle_\eta$ obtained through the variational approach. This is unlikely to be an artefact of the variational approach since similar transition is also seen in the Baxter's classical hard-squares model with attractive next nearest neighbour interactions [118, 119]. However, as the R-K description becomes less accurate away from the ξ_{sqr} -manifold due to the non-negligible contribution from the perturbing Hamiltonian, H' in Eq. (4.18), certain expected phases, e.g. quarter-filling phase, are not captured by the ground state, $|\xi\rangle_{\text{sqr}}$, of the quantum hard-squares model. For this reason, we have deliberately introduced a quarter-filling state, $|\phi\rangle_{1/4}$ to perform a similar variational study that focus on finding a distinct phase with quarterly filled Rydberg atoms. Although this approach indeed predicts a region in the parameter space to be a quarter-filling phase, it does not faithfully predicts the phase boundary between itself and the remaining parts of the phase diagram.

Based on the above arguments, it would be interesting to see whether adopting other techniques such as variational [120] and diffusion Monte-Carlo simulations [120, 121], and mean-field approaches will allow the determination of classical observables such as the ground state energy beyond the limit of the R-K description. Also, making effort in developing numerical methods to determine the phase diagram for adequately large system size, e.g. a 8-by-8 square lattice, might also allow us to see regions where the R-K description does not accurately describe and that alternative methods have to be used.

Another interesting direction that one can go into is to move on to three-dimensional systems. This, however, requires very advanced computational and numerical knowledge as the number of lattice sites is very large already for a small system size. e.g. a small cubic lattice with 3 sites on each side already consists of 27 lattice sites. Last, implementing inhomogeneities such as a single impurity along with the methods discussed in Chapter 3 in not only the square lattice but

also other two-dimensional geometries such as triangular and honeycomb lattices might lead to interesting results.

Chapter 5

Quantum Dynamics of the Quantum Hard-rods Model

In this chapter, we study the out-of-equilibrium evolution of a strongly interacting quantum spin chain which in principle can be realised by a modified version of the Rydberg lattice gases studied in previous chapters. By mapping this closed system onto a system consisting of hard-rods that can be coherently deposited on and removed from a lattice, we show that the system possesses thermalisation behaviour where initial states approach to an equilibrium steady state which strongly resembles a microcanonical ensemble of classical hard rods. Starting from the fully coherent evolution equation we derive a master equation for the evolution of the number of hard rods on the lattice. This equation not only captures the properties of the equilibrium state, but also describes the dynamical non-equilibrium evolution into it for the majority of initial conditions. We analyse this in detail for hard rods of varying size.

5.1 Introduction

Thermalisation, a phenomenon that describes the process in which the system reaches an equilibrium state, has long been studied in classical systems in the past [122]. It has been shown that the fundamental feature which drives a classical system toward equilibrium is dynamical chaos [123]. However, in many-body closed quantum systems, where the dynamics of the system is often described by a linear Schrödinger equation, dynamical chaos clearly does not exist. Thus, the explanation for how a closed quantum system thermalises to an equilibrium state has to be fundamentally different from the classical picture.

A straightforward approach to monitor the thermalisation process of a quantum system would involve a direct calculation of their microscopic dynamical evo-

lution. However, for an interacting many-body system, this is often a formidable task due to the exponential growth of the Hilbert space with the number of particles. Circumventing this problem requires sophisticated numerical tools and clever mathematical approaches. It is hence fair to say that our understanding of the equilibration and thermalisation of closed quantum systems is still far less developed than for their classical counterparts.

Sparked by the recent tremendous boost in experimental ultra-cold atomic and molecular physics[6, 124, 125], there has been an ever growing interest in understanding thermalisation in closed quantum systems. This is because these experiments allow one to realise almost ideal closed quantum systems by isolating them from the thermal environment[126]. In the mean time, many theories have been established to reveal the mystery of thermalisation in an isolated quantum system. For instance, the eigenstate thermalisation hypothesis (ETH) has suggested that there exists a thermal state in each eigenstate of the system Hamiltonian if the system is non-integrable [127, 128]. Recent numerical studies have proven the validity of this hypothesis [129, 130, 131], and works have been done to extend ETH to explain quantum systems that are integrable [132]. There are also alternative approaches to understand thermalisation in quantum systems, such as eigenstate randomisation hypothesis (ERH) [133] and the typicality argument [134].

Unfortunately, these hypotheses, though proved to be successful in understanding the steady state the system eventually evolves to, do not provide a detail explanation on how initial states equilibrate. Motivated by this unanswered question and intrigued by the fact that Rydberg lattice gases themselves are ideal closed quantum systems, in this chapter, we propose to study the dynamical behaviour of a generic quantum spin model. The model which belongs to the class of Ising models in a transverse field and can be mapped onto a system of quantum hard rods that are coherently removed from/deposited on a lattice, can be principally realised by the interacting Rydberg lattice gases discussed in the previous chapters. We aim to understand what exactly has happened to the initial states on their route to the steady state. To do so, we will derive an effective master equation that captures the temporal evolution of the system and the result will be compared with numerical simulations and ETH. The work presented in this chapter expands a recent work [44] and are summarised in [52].

The chapter is organised in the following way: In Sec. 5.2 we introduce the spin Hamiltonian that represents a quantum version of a hard-objects model. In Sec. 5.3, we introduce a specific graphical representation of the Hilbert space, namely the configuration network, to conveniently illustrate the dynamics of this system. The properties of the configuration network will be studied here. Utilising these properties, we will demonstrate in Sec. 5.4, with certain well justified approxima-

tions, the derivation of a master equation that describes the motion of the system in particle number space. In Sec. 5.5 the master equation is numerically studied and a steady state solution is derived. To demonstrate how well this master equation captures the actual quantum time-evolution of the system and the properties of the steady state, we compare the solution of the master equation with the exact numerical quantum evolution. This is done by numerically solving the many-body Schrödinger equation in Sec. 5.6. Conclusions and an outlook are provided in Sec. 5.7.

5.2 The System

The system under consideration describes a chain of L spin-1/2 particles which are equidistantly arranged at a nearest neighbour distance a_0 . The total physical length of the system is thus $l = L a_0$. The spins are exposed to a transverse magnetic field of field strength Ω (Rabi-frequency) which couples the local spin down-state $|\downarrow\rangle$ (ground state atom) to the spin up state $|\uparrow\rangle$ (Rydberg atom). Spins furthermore interact via a two-body interaction when they are simultaneously in the spin up state. The interaction strength is V when the two spins are located within a critical radius $r_c = \lambda a_0$. We refer λ as *blockade length* for reasons that will become clear later. Spins separated by a distance larger than r_c do not interact. The Hamiltonian of this system can be written as

$$H_{\text{spin}} = H_{\Omega} + H_V = \Omega \sum_{k=1}^L \sigma_k^x + V \sum_{k=1}^L \sum_{i=1}^{\lambda} n_k n_{k+i}, \quad (5.1)$$

with the operators having exactly the same meanings as in the previous chapters. For convenience, periodic boundary conditions are chosen, i.e. $n_L \equiv n_1$, but this is not a necessity.

In this chapter, we consider the specific regime in which $V/\Omega \rightarrow \infty$. This means that it is energetically forbidden to have spin configuration that contains two or more up-spins within a length of λ , hence the notion *blockade length*. This largely constrains the number of allowed (classical) arrangements of spins and leads to a substantially reduced dimension of the Hilbert space. In Fig. 5.1(a), we provide examples of permitted spin configurations for the cases $\lambda = 1$ and $\lambda = 2$. Due to the exclusion one can employ a description of the basis states in terms of hard rods. Each configuration of spins can be uniquely mapped into an arrangement of hard rods as illustrated in Fig. 5.1(a) for $\lambda = 1$ (dimers) and $\lambda = 2$ (trimers). Hard rods are deposited and removed by spin flips effectuated by the transverse magnetic field of strength Ω . We draw this connections to hard rods since in the course of this chapter we will make use of a number of known results from statistical mechanics that concern the counting of the possible arrangements of rods.

In relation to previous chapters, the spin model considered here can be realised by the Rydberg lattice gases studied. For instance, the coupling between the $|\downarrow\rangle$ and the $|\uparrow\rangle$ in this spin model can be realised by resonate laser couplings between the ground state and a Rydberg state of an Alkali-metal atom. In addition to the ideal nearest neighbours blockade considered in previous Rydberg lattice gases, the spin model described by Eq. (5.1) also considers a generic blockade length set by λ . This parameter λ is closely related to the physical blockade radius in the

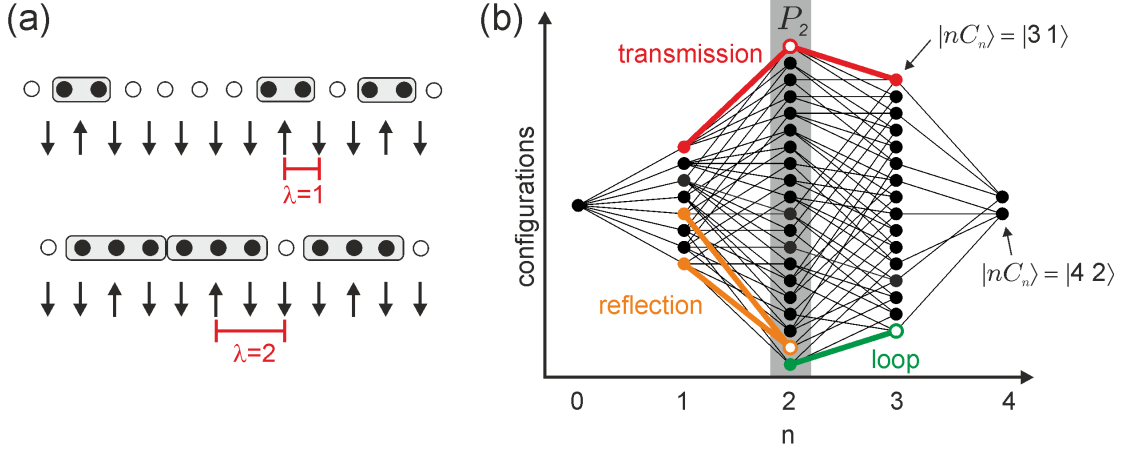


Figure 5.1: (a) Graphical representation of possible spin configuration for blockade length $\lambda = 1$ and $\lambda = 2$. Spin configurations can be also illustrated in the pictures of hard-rods where each up-spin is effectively mapped to a hard-rod occupying $\lambda + 1$ lattice sites. (b) An example of the configuration network in detail with $L = 8$ and $\lambda = 1$. Each node represents a specific classical spin configurations denoted by $|nC_n\rangle$ with n being the number of up-spins in the configuration and C_n uniquely labels the spin configuration. Two examples $|3\ 1\rangle$ and $|4\ 2\rangle$ are provided to show how the labelling works. Edge between adjacent nodes indicates that the nodes are directly coupled by H_Ω . Each column can be seen as the graphical interpretation of the expectation value of the observable, i.e. $p_n = \langle P_n \rangle$, defined in the text in Sec. 5.4. The non-zero matrix elements in the adjacency matrix \mathcal{M}^2 [see Sec. 5.4] identifies three types of transitions that describe a two-steps transition (two-spin flip operation): loop (green), reflection (orange) and transmission (red).

concept of Rydberg blockade as discussed in Chapter 2. In brief, the variation of Rydberg blockade radius, hence, λ , can be achieved by using different Rydberg states or varying the lattice spacing of the optical lattice [135].

5.3 Configuration Network

5.3.1 Structure

To get insights into the dynamics of the spin system we represent its state space through a configuration network, as shown in Fig. 5.1(b). To construct such a configuration network, we introduce the basis states $|n\mathcal{C}_n\rangle$. Each of these states represents a specific classical arrangement \mathcal{C}_n of n hard rods. These states obey the completeness relation $\sum_{n\mathcal{C}_n} |n\mathcal{C}_n\rangle\langle n\mathcal{C}_n| = \mathbb{1}$ and orthonormality relation $\langle n\mathcal{C}_n|m\mathcal{K}_m\rangle = \delta_{nm}\delta_{\mathcal{C}_n\mathcal{K}_m}$. We interpret each of the microstates $|n\mathcal{C}_n\rangle$ as a node of a network. By grouping configurations containing the same number of hard rods into columns we obtain the network structure depicted in (5.1b). The time-evolution of the system can then be imagined as a temporal change in the occupation of these nodes. Dynamics is introduced through the Hamiltonian H_Ω which leads to transitions between microstates that are represented as edges of the network. Since H_Ω causes only single spin flips, nodes in neighbouring columns are only linked directly, if their corresponding microstates can be converted into one another by the removal/deposition of one hard rod. For example, setting $\lambda = 1$ the state $|\downarrow\uparrow\downarrow\downarrow\uparrow\downarrow\uparrow\downarrow\rangle$ in the $n = 3$ column is directly linked with $|\downarrow\uparrow\downarrow\downarrow\downarrow\downarrow\uparrow\downarrow\rangle$, but not with $|\downarrow\downarrow\uparrow\downarrow\downarrow\downarrow\uparrow\downarrow\rangle$ in the $n = 2$ column. In the following we will analyse in detail the properties of the configuration network.

5.3.2 Properties of the Configuration Network

The most basic properties that define the structure of our configuration network are the number of columns and the number of nodes within each column. Fixing the length of the system to L sites, and applying periodic boundary condition, the maximum number of hard rods that each occupy $\lambda + 1$ sites (i.e., the blockade length is λ), which can be placed on the lattice is $\lfloor L/(\lambda + 1) \rfloor$, where $\lfloor x \rfloor$ denotes the closest integer smaller or equal to x . The index counting the number of hard rods can thus take the values $n = 0, 1, \dots, \lfloor L/(\lambda + 1) \rfloor$. The number of microstates ν_n contained in the n -th column is given by the number of ways in which one can distribute n indistinguishable hard rods of length $\lambda + 1$ over L lattice sites. As shown in Appendix D.1, this is a standard combinatorial problem [136]. Further proved by an alternative transfer matrix method given in Appendix D.2, ν_n has a solution that reads,

$$\nu_n = \frac{L(L - 1 - \lambda n)!}{n!(L - (\lambda + 1)n)!}. \quad (5.2)$$

Having determined the properties of the “backbone” of the network we now turn to assessing the linkage of the nodes. In particular, we calculate the mean number

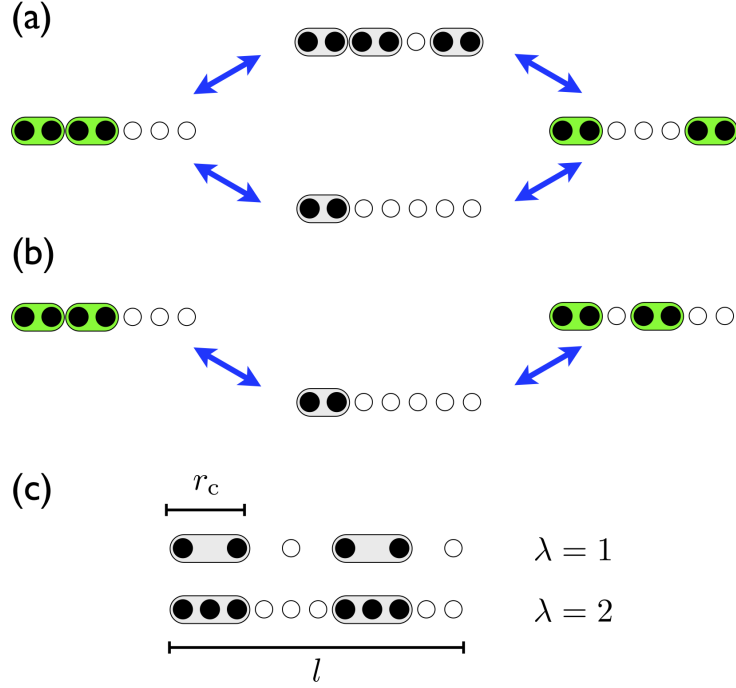


Figure 5.2: (a,b) Graphical illustration of the reflection processes. Two configurations can at most be connected by two reflection pathways (a). However, since rods must not overlap, the path containing an additional hard rod during the intermediate step is often forbidden (b). (c) For the numerical study we fix the physical system length l and the critical radius r_c . The parameter λ is varied by increasing the number of lattice sites.

of different possibilities $T_{n \rightarrow n \pm 1}$ to go from a state with n hard rods to one in the adjacent columns. This quantity can be expressed as $T_{n \rightarrow n \pm 1} = c_{n, n \pm 1} / \nu_n$, where $c_{n, n \pm 1}$ denotes the *total* number of links between columns n and $n \pm 1$ and hence $c_{n \pm 1, n} = c_{n, n \pm 1}$. (Note that this symmetry does not hold for the $T_{n \rightarrow m}$.) Moreover, we know that $T_{n \rightarrow n-1} = n$, as in a configuration of n hard rods there are n possibilities for removing one hard rod reaching a state with $n-1$ hard rods. Using these relations the total number of links between two columns evaluates to

$$\begin{aligned}
 c_{n, n-1} &= T_{n \rightarrow n-1} \nu_n = \frac{L(L-1-\lambda n)!}{(n-1)!(L-(\lambda+1)n)!}, \\
 c_{n+1, n} &= T_{n+1 \rightarrow n} \nu_{n+1} = \frac{L(L-1-\lambda(n+1))!}{n!(L-(\lambda+1)(n+1))!},
 \end{aligned}
 \tag{5.3}$$

which can then be used to calculate $T_{n \rightarrow n+1}$.

Let us continue by analysing the second order processes shown in Fig. 5.1(b), i.e. loops, reflections and transmissions, as they will enter in the derivation of the master equation. Selecting a node from the network, the number of loop transitions from that node equals the number of links that this node has with

other nodes. Therefore, the mean number of loop transitions from a state with n hard rods is given by

$$\overline{N_{\text{loop}}^{(n)}} = T_{n \rightarrow n+1} + T_{n \rightarrow n-1}. \quad (5.4)$$

Reflections connect two configurations that contain the same number of hard rods but differ in the position of exactly one hard rod [cf. Fig. 5.2]. Two configurations that are randomly selected from one column will typically differ by the positioning of more than one hard rod and are thus not connected by a reflection. If two microstates happen to be connected there are at most two paths as illustrated in Fig. 5.2: a de-excitation followed by an excitation or vice versa. For $n \gg 1$ (at high density) there is often even only one path available [c.f. Fig. 5.2(b)]. Similar considerations can also be made for transmission diagrams, i.e., the average number of paths connecting two microstates containing n and $n \pm 2$ hard rods is ~ 1 . In fact the mean number of reflections (transmissions) $\overline{N_{\text{refl}}^{(n)}}$ ($\overline{N_{\text{trans}}^{(n)}}$) between two *randomly* selected states can be calculated analytically:

$$\begin{aligned} \overline{N_{\text{refl}}^{(n)}} &= \frac{T_{n+1 \rightarrow n}(T_{n+1 \rightarrow n} - 1)\nu_{n+1}}{\nu_n(\nu_n - 1)} + \frac{T_{n-1 \rightarrow n}(T_{n-1 \rightarrow n} - 1)\nu_{n-1}}{\nu_n(\nu_n - 1)}, \\ \overline{N_{\text{trans}}^{(n)}} &= \frac{T_{n+2 \rightarrow n+1}T_{n+1 \rightarrow n} + T_{n-2 \rightarrow n-1}T_{n-1 \rightarrow n}}{\nu_n}. \end{aligned} \quad (5.5)$$

To illustrate that loop transitions are far more abundant than reflections and transmissions we present some numerical examples in Table (5.1). Here we compare $\overline{N_{\text{loop}}^{(n)}}$, $\overline{N_{\text{refl}}^{(n)}}$ and $\overline{N_{\text{trans}}^{(n)}}$ for a number of lattice and hard rod sizes. This leads to two observations. First, the relative weight of loop transitions largely increases with increasing systems size L , as due to the larger dimension of the Hilbert space each state can have more connections to other configurations. Second, the probability that two states within a column of the network are connected by a reflection is vanishingly small in the "bulk" of the network ($1 \ll n \ll \lfloor L/(\lambda + 1) \rfloor$). The same is also true for transmissions between columns n and $n \pm 2$. Note, that near the boundaries of the network, i.e. columns close to the maximum/minimum n -value, the condition $\overline{N_{\text{loop}}^{(n)}} \gg \overline{N_{\text{trans}}^{(n)}}$, $\overline{N_{\text{refl}}^{(n)}}$ are less well satisfied. However, this concerns only an exponentially small subset of states forming the configuration network. These two observations on the statistics of the configuration network are of central importance in the derivation of the effective master equation for $p_n(t)$ that we are going to present in the following section.

L	λ	n	$\overline{N_{\text{loop}}^{(n)}}$	$\overline{N_{\text{refl}}^{(n)}}$	$\overline{N_{\text{trans}}^{(n)}}$
12	1	2	8.22	0.54	2.22
		4	5.71	0.17	0.51
300	1	2	296	0.026	2
		75	174.78	1.27×10^{-57}	1.39×10^{-57}
	5	2	280.1	0.026	2
		25	93.39	1.64×10^{-27}	3.18×10^{-27}
	14	2	244.78	0.025	2
		10	68	3.11×10^{-13}	1.73×10^{-12}

Table 5.1: Relative importance of the three transition types in terms of the defined averages. The symbols have their usual meanings. Notice that we have chosen a relatively small lattice size and a large one and for each lattice sites, we use various blockade length to see how average transitions change. Furthermore, we choose n in the way such that $n = 2$ corresponds to the configurations near the edges (when $n = 1$, there is only reflection toward one side) and $n \sim L/\lambda$ corresponds to the configurations in the centre of the configuration network.

5.4 Derivation of the master Equation

Our aim is to derive an equation of motion which describes the evolution of the system in particle number space. This means that we are not interested in the actual population of individual nodes within the graph shown in Fig. 5.1(b) but rather in the probability p_n of the system to reside in a specific column n . We will see that this eventually leads to a master equation which has a steady state where $p_n(t \rightarrow \infty)$ is proportional to the number of classical configurations making up the n -th column. This strongly suggests that this steady state corresponds to a microcanonical equilibrium state in which all permitted classical spin configurations are populated with equal probability.

5.4.1 Configuration States and Probability Distribution

The probability p_n is defined as $p_n = \text{Tr} \rho(t) P_n$, where $\rho(t)$ is the density matrix of the system and $P_n = \sum_{\mathcal{C}_n} |n\mathcal{C}_n\rangle \langle n\mathcal{C}_n|$ is a projector which projects onto the subspace spanned by all microstates contained in the n -th column of the configuration network [c.f. Fig. 5.1(b)]. The set of expectation values p_n can be thought as the distribution function which describes the probability of finding n up-spins in the system at a given time. Throughout the rest of the chapter, we are interested in a situation where the initial state of the system $\rho(0)$ has a fixed number of hard-rods, i.e. $[P_n, \rho(0)] = 0$.

To begin with the formal derivation of the Master equation, let us momentarily return to the case of finite V and transform Hamiltonian (5.1) into the interaction

picture with respect to H_V according to Appendix E.1. In the spin configuration basis, i.e. $|n\mathcal{C}_n\rangle$, the spin Hamiltonian H_{spin} in the interaction picture reads,

$$H_I(t) = \sum_{n\mathcal{C}_n, m\mathcal{K}_m} h_{n\mathcal{C}_n, m\mathcal{K}_m} e^{-i(\omega_{m\mathcal{K}_m} - \omega_{n\mathcal{C}_n})t} |n\mathcal{C}_n\rangle \langle m\mathcal{K}_m|, \quad (5.6)$$

where $\omega_{n\mathcal{C}_n} = \langle n\mathcal{C}_n | H_V | n\mathcal{C}_n \rangle$ and $h_{n\mathcal{C}_n, m\mathcal{K}_m} = \langle n\mathcal{C}_n | H_\Omega | m\mathcal{K}_m \rangle$.

Proceeding with the second order von Neumann equation derived in Appendix E.2 and further using the exact master Equation derived in Appendix E.3 based on the second order von Neumann equation, one finds that $p_n = \text{Tr}\rho(t)P_n = \langle P_n \rangle$ evolves in time according to

$$\begin{aligned} \partial_t \langle P_n \rangle_t = & - \int_0^t ds \text{Tr} \{ P_n H_I(t) H_I(s) \rho(s) + H_I(s) H_I(t) P_n \rho(s) \\ & - H_I(s) P_n H_I(t) \rho(s) - H_I(t) P_n H_I(s) \rho(s) \}, \end{aligned} \quad (5.7)$$

where H_I is the H_{spin} in the interaction picture as obtained in Eq. (5.6).

Eq. (5.7) is still exact at this stage. To make progress we make an approximation which is to perform the replacement $\rho(s) \rightarrow \rho(t)$. At this point it is illusive why this is sensible but we will provide a numerical justification of this step *a posteriori*. Now, we return to the ideal blockade regime where $V/\Omega \rightarrow \infty$, in which allowed spin configurations have the same configuration energy, $\omega_{n\mathcal{C}_n} = 0$. Adopting this fact, one notices that the exponential factor in $H_I(t)$ becomes $e^{-i0t} = 1$. As a result, the interaction picture Hamiltonian becomes time-independent in the ideal blockade regime, i.e. $H_I(t) \rightarrow H_\Omega$. Therefore, the time-integration in Eq. (5.7) simply amounts to a multiplication by t .

Accepting the steps so far, one finds that Eq. (5.7) depends on matrices of the form

$$H_I^2(0) = \sum_{\substack{n\mathcal{C}_n \\ p\mathcal{L}_p}} \langle n\mathcal{C}_n | H_\Omega^2 | p\mathcal{L}_p \rangle |n\mathcal{C}_n\rangle \langle p\mathcal{L}_p|, \quad (5.8)$$

where the matrix elements $\langle n\mathcal{C}_n | H_\Omega^2 | p\mathcal{L}_p \rangle$ read,

$$\langle n\mathcal{C}_n | H_\Omega^2 | p\mathcal{L}_p \rangle = \sum_{m\mathcal{K}_m} \langle n\mathcal{C}_n | H_\Omega | m\mathcal{K}_m \rangle \langle m\mathcal{K}_m | H_\Omega | p\mathcal{L}_p \rangle.$$

The aim now is to obtain the value of these matrix elements for any arbitrary choices of the two microstates $|n\mathcal{C}_n\rangle$ and $|p\mathcal{L}_p\rangle$ in Eq. (5.8).

Revisiting the configuration network where each basis state, $|n\mathcal{C}_n\rangle$ is represented by a unique node with the edges connecting nodes illustrating possible direct transition driven by H_Ω , one finds that the transitions between nodes can be described by an adjacency matrix, \mathcal{M} [137]. In network theory, an adjacency

matrix is a K -by- K matrix that illustrates the number of transitions between adjacent nodes in a graph containing total of K nodes. In our case, as seen in the configuration network in Fig. 5.1(b), if two nodes, i and j , where i, j are short hand notation for $n\mathcal{C}_n, m\mathcal{C}_m$, are directly connect by an edge, the corresponding entry of this adjacency matrix, $\mathcal{M}_{i,j}$ is one, and is zero otherwise. Since our configuration network is undirected, \mathcal{M} is symmetric; and since there is no edges that directly links a node to its self, the diagonal elements of \mathcal{M} is zero. The matrix elements of an adjacency matrix to the power of s , i.e. $(\mathcal{M}^s)_{i,j}$, represents the total number of different s -steps transitions along the edges between the nodes in a graph. And $(\mathcal{M}^s)_{i,j} = 0$ simply means a transition of s -steps between the i -th and the j -th nodes does not exist. Since H_Ω^2 describes a two-step transition from a node to another, we can therefore map the squared Hamiltonian, H_I^2 to an adjacency matrix to the power of two, i.e. \mathcal{M}^2 . The matrix elements $(\mathcal{M}^2)_{i,j}$ thus corresponds to $\langle n\mathcal{C}_n | H_\Omega^2 | p\mathcal{L}_p \rangle$.

The idea of mapping the squared Hamiltonian H_Ω^2 to \mathcal{M}^2 builds up a connection between the matrix elements of H_I^2 and the configuration network. For instance, for two microstates that are not connected by a direct two-step transition in the configuration network, one immediately knows that the corresponding matrix element is zero. Then, by exploiting the nature of H_Ω , which is to couple spin configurations in neighbouring columns, one immediately sees that both $m = n \pm 1$ and $p = m \pm 1$ have to be satisfied for the matrix element to yield a non-zero value (see Eq. (5.8) for the meaning of indices). In these cases, the non-zero matrix elements amount to three distinct types of transitions in relationship to the configuration network in Fig. 5.1(b): (i) loops (green) with $|p\mathcal{L}_p\rangle = |n\mathcal{C}_n\rangle$, where the initial and final states are identical, (ii) reflections (orange) with $|p\mathcal{L}_p\rangle = |n\mathcal{C}'_n\rangle$, where the initial and final state are not identical but are located in the same column, and (iii) transmissions (red) with $|p\mathcal{L}_p\rangle = |n \pm 2\mathcal{L}_{n\pm 2}\rangle$, where the initial and final state are located in two columns with a difference in excitation number being $|n - p| = 2$. As a result, the calculation of the matrix elements $\langle n\mathcal{C}_n | H_\Omega^2 | p\mathcal{L}_p \rangle$ is related to counting the number of the three possible transitions. Using Fig. 5.1 as an example, for the state $|3\ 1\rangle$, we have $\langle 3\ 1 | H_\Omega^2 | 3\ 1 \rangle = 4$, $\langle 3\ 1 | H_\Omega^2 | 3\ 2 \rangle = 1$, \dots , since they are 4 possible loop transitions, 1 reflection transition that arrives at $|3\ 2\rangle$, and so on. The question now is how to count these numbers for large system size since the complexity of these configuration networks scales exponentially with the increasing lattice size.

As demonstrated in the previous section, of all three types of two-step transitions, loop transition significantly dominates over the other two types of transition, i.e. $\overline{N}_{\text{loop}}^{(n)} \gg \overline{N}_{\text{trans}}^{(n)}, \overline{N}_{\text{refl}}^{(n)}$. This result allows us to make an essential approximation at this stage which is to neglect all matrix elements that correspond to reflection

and transmission. Mathematically, this approximation corresponds to only keeping the diagonal elements (loop transitions) in \mathcal{M}^2 . Accepting this step, Eq. (5.8) can be approximated as,

$$H_I^2(0) \approx \sum_{n\mathcal{C}_n} \langle n\mathcal{C}_n | H_\Omega^2 | n\mathcal{C}_n \rangle | n\mathcal{C}_n \rangle \langle n\mathcal{C}_n |, \quad (5.9)$$

where

$$\langle n\mathcal{C}_n | H_\Omega^2 | n\mathcal{C}_n \rangle = \sum_{m\mathcal{K}_m} |\langle n\mathcal{C}_n | H_\Omega | m\mathcal{K}_m \rangle|^2,$$

with $m = n \pm 1$.

The final approximation consists of neglecting the variation of the matrix elements of H_Ω^2 with \mathcal{C}_n within a given column of the configuration network, by replacing the matrix element with its average taken over all microstates within a column,

$$\langle n\mathcal{C}_n | H_\Omega^2 | n\mathcal{C}_n \rangle \rightarrow \Omega^2 \overline{N_{\text{loop}}^{(n)}},$$

and with,

$$\Omega^2 \overline{N_{\text{loop}}^{(n)}} = \Omega^2 (T_{n \rightarrow n+1} + T_{n \rightarrow n-1}), \quad (5.10)$$

where we have used the analytical form of $\overline{N_{\text{loop}}^{(n)}}$ calculated in previous section. This is a valid approximation for large system sizes as the number of loops for different \mathcal{C}_n in the n -th column are nearly the same and is much larger than the variation among them. Even, for small system size, like the one shown in Fig. 5.1(b), the number of loops for nodes in the same column is roughly the same.

Accepting all approximations made so far and using the first term in Eq. (5.7) as an example, with a particular n value, one finds that

$$\begin{aligned} \int_0^t \text{Tr}[P_n H_I(t) H_I(s) \rho(s)] &\approx \Omega^2 t \overline{N_{\text{loop}}^{(n)}} \text{Tr} \left[\sum_{\mathcal{C}_n} |n\mathcal{C}_n\rangle \langle n\mathcal{C}_n| \rho(t) \right] \\ &\approx \Omega^2 t (T_{n \rightarrow n+1} + T_{n \rightarrow n-1}) p_n, \end{aligned} \quad (5.11)$$

where we have used the definition of $p_n = \text{Tr}[P_n \rho(t)]$ and $P_n = \sum_{\mathcal{C}_n} |n\mathcal{C}_n\rangle \langle n\mathcal{C}_n|$. Applying the same treatment to the other three terms in Eq. (5.7) and grouping terms of p_n with the same index number n , one arrives at the final master equation,

$$\begin{aligned} \partial_t p_n(t) &= 2\Omega^2 t [T_{n+1 \rightarrow n} p_{n+1}(t) + T_{n-1 \rightarrow n} p_{n-1}(t)] \\ &\quad - 2\Omega^2 t [T_{n \rightarrow n-1} p_n(t) + T_{n \rightarrow n+1} p_n(t)]. \end{aligned} \quad (5.12)$$

To solve these coupled differential equations, we express them in a matrix form

that reads,

$$\dot{\mathbf{p}}(t) = 2\Omega^2 t \mathbf{A} \mathbf{p}(t), \quad (5.13)$$

where $\mathbf{p}(t)$ is the vector form of the distribution function,

i.e. $\mathbf{p}(t) = (p_1, p_2, \dots, p_{L/(\lambda+1)})^\dagger$ and \mathbf{A} , with a size of $(n_{\max} + 1)$ -by- $(n_{\max} + 1)$ and $n_{\max} = L/(\lambda + 1) + 1$, is the coefficient matrix described by the rates functions. The matrix elements of \mathbf{A} follows

$$A_{ij} = -(T_{i-1 \rightarrow i} + T_{i-1 \rightarrow i-2})\delta_{i,j} + T_{i \rightarrow i-1}\delta_{i+1,j} + T_{i-1 \rightarrow i}\delta_{i,j+1}, \quad (5.14)$$

and with special boundary condition $A_{ii} = -T_{i-1 \rightarrow i}$ when $i = 1$ and $A_{ii} = -T_{i-1 \rightarrow i-2}$ when $i = n_{\max} + 1$. One immediately sees that the coefficient matrix obeys detailed balance where each matrix column has a sum of zero, thus suggesting a steady state solution [138]. To solve the differential equation, we introduce the substitution of $\tau = t^2/2$ with $d\tau/dt = t$. Since $\frac{\partial \mathbf{p}(\tau)}{\partial t} = \frac{\partial \mathbf{p}(\tau)}{\partial \tau} \frac{d\tau}{dt}$, we have

$$\frac{\partial \mathbf{p}(\tau)}{\partial \tau} = 2\Omega^2 \mathbf{A} \mathbf{p}(\tau). \quad (5.15)$$

The solution to the above differential equation is standard and reads $\mathbf{p}(\tau) = e^{2\Omega^2 \tau \mathbf{A}} \mathbf{p}(0)$. Substituting $\tau = t^2/2$ back, one finds,

$$\mathbf{p}(t) = e^{\Omega^2 t^2 \mathbf{A}} \mathbf{p}(0). \quad (5.16)$$

By determining the analytical form of the matrix elements of \mathbf{A} , one is able to solve the master equation analytically for the probability distribution p_n .

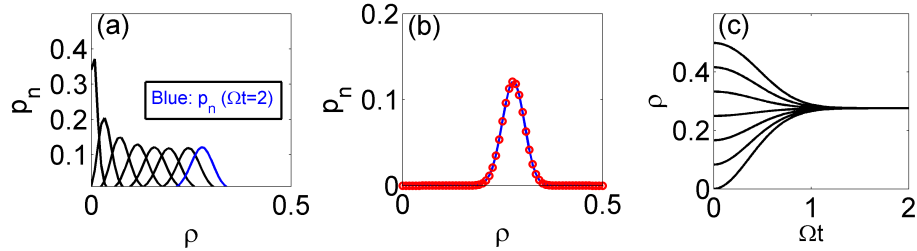


Figure 5.3: The time evolution of the distribution functions $p_n(t)$ by solving the master equation with nearest neighbour blockade only, i.e. $\lambda = 1$. The system considered has a lattice length to blockade length ratio $l/r_c = 120$. p_n are drawn at the time intervals: $\Omega t = 0.02, 0.1, 0.2, 0.3, 0.4, 0.5, 0.6, 0.8$ and $\Omega t = 2$ (blue) from left to right, as shown in (a). The initial distribution function used is $p_0 = 1$ which is a delta function. The steady state distribution is explicitly demonstrated in (b) in blue and compared with the numerical results obtained directly from Eq. (5.17) (red circles). The two curves match perfectly. To investigate the dependence of the time-evolution on initial distributions, we start with distributions with different densities ranging from $\rho = 0$ ($p_0 = 1$) to $\rho = 0.5$ ($p_{60} = 1$). As seen, the steady state is independent of the chosen initial state.

5.5 Time Evolution and the Steady State of the master Equation

Since the coefficient matrix \mathbf{A} calculated in Eq. (5.14) obeys detailed balance, i.e. each column of \mathbf{A} sums to zero, there exists a steady state for the distribution function p_n^{eq} which reads

$$p_n^{\text{eq}} = \frac{\nu_n}{\sum_{n=0}^{L/(\lambda+1)} \nu_n}, \quad (5.17)$$

and with $p_n^{\text{eq}} T_{n \rightarrow n+1} = p_{n+1}^{\text{eq}} T_{n+1 \rightarrow n}$. Both the time evolution of the initial state and the steady state solution can be numerically studied by using Eq. (5.16). Here, we fix the lattice length to critical radius ratio as $l/r_c = 120$ and we investigate the time-evolution of distribution functions and the properties of the steady states.

In particular, as shown in Fig. 5.3, by fixing the blockade length to $\lambda = 1$, we demonstrate the temporal evolution of the distribution function $p_0 = 1$, the steady state solution and the dependence on initial conditions. In (a), at the beginning of the temporal evolution, one sees a quick diffusive dynamic which can be explained as the spreading of the occupation of the nodes in the configuration network. Then, the overall shape of the distribution does not change much but the position continuously moves toward the right until it reaches the steady state. The steady state distribution obtained from the master equation (blue) is illustrated together with the steady state predicted by Eq. (5.17) (red circles) in (b), where one sees a perfect match between the two curves. Lastly, we look at the dependence on

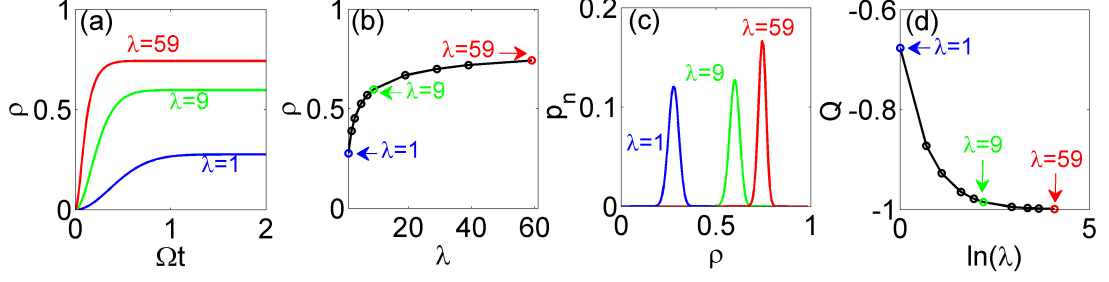


Figure 5.4: In (a), to see the dependence on the blockade length, we show the time-evolution of the distribution function $p_0 = 1$ with different blockade radii $\lambda = 1$ (blue), $\lambda = 9$ (green) and $\lambda = 59$ (red). The densities of the steady states are explicitly plotted in (b) to further demonstrate the increase of density of the steady state with increasing blockade length. Values of λ in the plot include 1 (blue), 2, 3, 5, 7, 9 (green), 19, 29, 39, and 59 (red). At particular blockade length where $\lambda = 1, 9$, and 59 , distribution functions at equilibrium ($\Omega t = 2$) are plotted in blue, green and red respectively in (c). The Mandel Q -factor has been calculated for all steady state distributions and illustrated in (d) with x-axis being the natural log of λ . The Mandel Q -factor saturates to -1 at large blockade length.

initial distributions where $p_n(t = 0)$ are chosen to have a density ranging from $\rho = 0$ to $\rho = 0.5$ at an equal step size $0.5/6$. The density ρ is calculated by using $\rho = nr_c/l = n\lambda/L$. Distributions with these densities correspond to delta functions from $p_0 = 1$ to $p_{60} = 1$. Notably, all curves reach the same steady state approximately at the same time $\Omega t \approx 1.2$ independent of the chosen initial states.

To see the effect of changing blockade length, we fixed the initial state to be $p_0 = 1$ and let it evolve under the master equation with blockade radii ranging from $\lambda = 1$ to $\lambda = 59$. Time-evolutions at these blockade radii and the properties of their steady states are illustrated in Fig. 5.4. Results at $\lambda = 1, 9$, and 59 are particularly highlighted in the present figure in the colours blue, green, and red respectively. In (a), one finds that the higher the blockade length, the faster the system reaches the steady state. The densities of the steady states, which have been explicitly plotted in (b), also increase with increasing blockade length. The distribution functions at equilibrium are shown in (c). The results here coincide with those studied in Ref. [40]. Finally, we calculate the Mandel Q -factor, defined as $Q = \frac{\langle n^2 \rangle - \langle n \rangle^2}{\langle n \rangle} - 1$ [139], for each steady state distribution in (d). The Q -value compares a distribution function to a Poisson and a Poisson distribution is defined to have a Q -value being zero. For a distribution having a negative Q -value, it indicates a sub-Poissonian behaviour and as it approaches -1 , variance is approximately zero which suggests the absence of fluctuation in experimental detections of the density of the steady state [140].

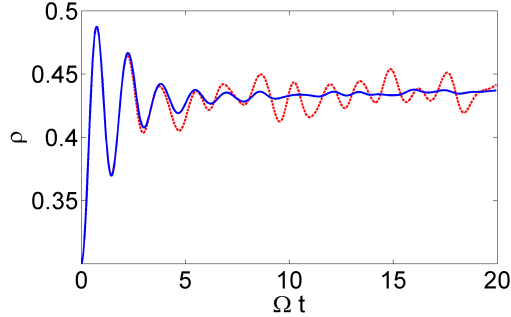


Figure 5.5: For $\lambda = 3$ and $l/r_c = 10$, the quantum evolution of the density of a randomly chosen spin configuration in $k = 0$ momentum subspace (red dash) and in complete momentum subspace (blue). The initial pin configuration has 3 up-spins and does not have translational symmetry (see text).

5.6 Exact Numerical Quantum Evolution

After having discussed the main features of the time evolution and the steady state of the master equation we will now compare its predictions to the exact quantum dynamics of the system. The quantum evolution of a spin configuration, $|\Phi(0)\rangle$, can be described by the solution to the Schrödinger equation as,

$$|\Phi(t)\rangle = e^{-iH_c t} |\Phi(0)\rangle, \quad (5.18)$$

where H_c denotes the spin Hamiltonian (5.1) in the spin configuration basis $|n\mathcal{C}_n\rangle$ representation. For a system containing L lattice sites, the dimension of the Hilbert space grows exponentially as L increases. Thus, exact numerical calculation is restricted by the system size. In order to perform numerical calculations of sufficiently large system sizes efficiently, we will work with a different set of basis states which eventually allows us to block-diagonalise the Hamiltonian as illustrated in Ref. [88]. In the following section, we will derive this set of basis states, which we will refer to as quasi-momentum basis states. The name will become apparent as the derivation proceeds.

5.6.1 Quasi-momentum Basis States

To start the derivation, it is convenient to introduce some notations. Here, to differentiate the notation for the microstates, i.e. $|n\mathcal{C}_n\rangle$, we introduce, for a lattice size of L , a more general notation of the spin configuration, $|n_1, n_2, n_3, \dots, n_L\rangle$ where $n_i = 1, 0$ corresponds to a presence of an up-spin or not respectively. Periodic boundary conditions apply such that $n_{L+1} = n_1$. Now, we define a translational

Number of up-spins	Reference State Notation	Configuration	$N(r_i, n)$
0	$ r_1, 0\rangle$	$ \downarrow\downarrow\downarrow\downarrow\downarrow\downarrow\downarrow\downarrow\rangle$	1
1	$ r_1, 1\rangle$	$ \uparrow\downarrow\downarrow\downarrow\downarrow\downarrow\downarrow\downarrow\rangle$	8
2	$ r_1, 2\rangle$	$ \uparrow\downarrow\uparrow\downarrow\downarrow\downarrow\downarrow\downarrow\rangle$	8
2	$ r_2, 2\rangle$	$ \uparrow\downarrow\uparrow\downarrow\uparrow\downarrow\downarrow\downarrow\rangle$	8
2	$ r_3, 2\rangle$	$ \uparrow\downarrow\downarrow\downarrow\uparrow\downarrow\downarrow\downarrow\rangle$	4
3	$ r_1, 3\rangle$	$ \uparrow\downarrow\uparrow\downarrow\uparrow\downarrow\downarrow\downarrow\rangle$	8
3	$ r_2, 3\rangle$	$ \uparrow\downarrow\uparrow\downarrow\downarrow\downarrow\uparrow\downarrow\rangle$	8
4	$ r_1, 4\rangle$	$ \uparrow\downarrow\uparrow\downarrow\uparrow\downarrow\uparrow\downarrow\rangle$	2

Table 5.2: The basis constructed by exploiting the translational symmetry of the periodic lattice with a lattice size of $L = 8$ and blockade length $\lambda = 1$.

operator, T , which shift the spins by one to the right, i.e.,

$$T|n_1, n_2, n_3, \dots, n_L\rangle = |n_L, n_1, n_2, \dots, n_{L-1}\rangle. \quad (5.19)$$

This corresponds to a decrease in the spin index by one. It can be proved that the translational operator commutes with the Hamiltonian in Eq. (5.1). The eigenstates of the translational operator can be calculated as,

$$T^N|\phi(k)\rangle = e^{ik}|\phi(k)\rangle, \quad (5.20)$$

where the eigenvalue e^{ik} is obtained from the fact that $T^N = 1$, i.e. translating N times of a given state will bring it back to the given state. Therefore, we have N non-equivalent solutions to the value of k ,

$$k = m\frac{2\pi}{N}, \text{ with } m = 0, 1, \dots, N - 1. \quad (5.21)$$

Before constructing the new set of basis states, let us first define a set of reference states, denoted as $|r_i, n\rangle$ with n being the number of up-spins in the spin configuration, and r_i denoting the reference state with i uniquely labelling each distinct configuration state. These reference states have the following properties: (i) Every reference state has a corresponding, equivalent microstate. (ii) Reference states are unique in the sense that a reference state cannot be expressed by any other reference states under translational operations. (iii) Microstates that do not have their counterpart reference states can be expressed in terms of a particular reference state under translational operations. To give an example of how to obtain the reference states, we have identified and provided the complete eight reference states for a system of eight lattice sites with blockade length being $\lambda = 1$ in Table (5.2). From the table, one can demonstrate the above three properties of a reference state. For instance, it is not possible to express any of the reference

states in terms of any other reference states with translational operations. Also, spin configurations that are not shown in the table can be expressed in terms of a reference state under translational operation, e.g. $|\downarrow\downarrow\uparrow\downarrow\downarrow\downarrow\downarrow\rangle = T^2|r_1, 1\rangle$.

With these reference states and the eigenvalues of the translational operator, we can now construct the new basis states in the following way,

$$|s_i, n\rangle_k = \frac{1}{\sqrt{N(s_i, n)}} \sum_{N=1}^{N(s_i, n)} e^{-ikN} T^N |r_i, n\rangle, \quad (5.22)$$

where $N(s_i, n)$ is the normalisation constant, and the value of it is basically the number of translations the reference state needs to take to arrive back to itself, i.e. $T^{N(s_i, n)}|r_i, n\rangle = |r_i, n\rangle$. A basis state $|s_i, n\rangle_k$ is associated to the particular reference state $|r_i, n\rangle$ with an allowed k -value. And the basis state can be interpreted as a superposition of all configuration states that can be translated from the associated reference state. Due to the properties of the reference states discussed earlier on, it is easy to prove that the constructed basis states obey orthogonality, i.e. ${}_k\langle s_i, n | s_j, n' \rangle_{k'} = \delta_{i,j} \delta_{n,n'} \delta_{k,k'}$.

The form of the new basis states resembles that of a discrete momentum state, hence, we refer to these basis states as quasi-momentum basis states with quasi-momenta k . The advantage of using these basis states is that the Hilbert space can be divided into uncoupled blocks with different quasi-momenta. We refer to each block as a k -subspace, with k being the allowed quasi-momenta determined in Eq. (5.21). As a result, instead of diagonalising the entire Hamiltonian at once, one can diagonalise each block separately. The dimension of most of the blocks is roughly $1/L$ of the dimension of the entire Hilbert space with L being the lattice size. The use of the quasi-momentum basis states will reduce the effort in numerical calculation of the quantum evolution of the system. Moreover, this also allows one to perform numerical calculation with larger system sizes.

Finally, we perform a change of basis to write the microstates, i.e. $|n\mathcal{C}_n\rangle$ in the quasi-momentum basis state representation,

$$\begin{aligned} |n\mathcal{C}_n\rangle &= \sum_k \sum_i \sum_{n'} {}_k\langle s_i, n' | n\mathcal{C}_n \rangle |s_i, n'\rangle_k \\ &= \sum_k \frac{e^{ikm}}{\sqrt{N(s_i, n)}} |s_i, n\rangle_k, \end{aligned} \quad (5.23)$$

with m being the number of translational operations required for the reference state to be translated into the spin configuration corresponding to the microstate, $|n\mathcal{C}_n\rangle$. Notice that ${}_k\langle s_i, n' | n\mathcal{C}_n \rangle$ is only non-zero when $n = n'$, and moreover, there is only one reference state that the spin configuration $|n\mathcal{C}_n\rangle$ can be translated

into under the translational operation. These facts allow us to drop the two summations in the second step.

Therefore, the quantum evolution of a microstate in the quasi-momentum basis representation, according to Eq. (5.18) reads,

$$|\Phi(t)\rangle = \frac{1}{\sqrt{N(s_i, n)}} \sum_k e^{-iH_k t} e^{ikm} |s_i, n\rangle_k, \quad (5.24)$$

with $N(s_i, n)$ being the normalisation constant of the quasi-momentum basis states $|s_i, n\rangle_k$ introduced in Eq. (5.22), k being the allowed wave vectors, H_k being the Hamiltonian in the quasi-momentum basis representation. Knowing the state $|\Phi(t)\rangle$, one can calculate the expectation value, $\langle n \rangle$ of the number operator n by

$$\begin{aligned} \langle n \rangle &= \langle \Phi(t) | n | \Phi(t) \rangle \\ &= \frac{1}{N(s_i, n)} \sum_k \langle s_i, n | e^{iH_k t} e^{-ikm} n e^{-iH_k t} e^{-ikm} | s_i, n \rangle_k. \end{aligned} \quad (5.25)$$

From this expression, one sees that to obtain $\langle n \rangle$, instead of diagonalising the entire Hamiltonian H_{spin} , one can diagonalise the Hamiltonian in each individual k -subspace, i.e., H_k , separately, and perform the summation on the results.

If one chooses a state having translational symmetry such that $N(s_i, n) < L$, i.e. it takes less than L steps of translation to get back to the state itself, one sees that this state only evolves in certain k -subspaces. For instance, the vacuum state where all spins are in the down-spin state has $N(s_i, n) = 1$, and the only allowed wave vector is $k = 0$. In this special situation, $\langle n \rangle = \langle n \rangle_0$, and thus one only needs to consider the temporal evolution in $k = 0$ subspace. However, if one randomly chooses a spin configuration state, it is more likely that the state does not have any special translational symmetry such that $N(s_i, n) = L$. In this case, it is necessary to consider the complete momentum space. We demonstrate the above argument in Fig. 5.5, where an example of the temporal evolution of a randomly chosen spin configuration in the $k = 0$ subspace has been plotted in (red dash) and the temporal evolution of the same state in the complete momentum space has been plotted in blue. The latter curve shows a more pronounced dephasing comparing with the red dashed curve.

5.6.2 Comparison to the solutions of the master Equation

To finally compare our analytical solution of the master Equation to the exact quantum evolution, we have adopted the above numerical method for systems up to $L = 30$ sites. The left column of Fig. 5.6 shows the numerically exact quantum evolution of the hard rod density together with the prediction of the

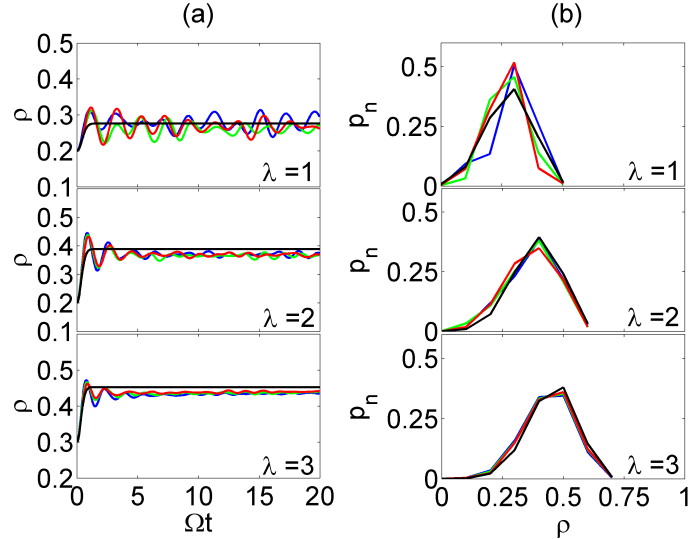


Figure 5.6: (a) Quantum evolution of microstates in complete momentum space and (b) the distribution functions of the steady states. In vertical direction, we increase the blockade radius where $\lambda = 1, 2, 3$ with a fixed $l/r_c = 10$. In all plots, the temporal evolutions described by the master equation and the distribution function of the steady states are plotted in black. For each blockade radius, we randomly chose 3 different initial states for the numerical simulation of the quantum evolution. Then the quantum evolution and the distribution functions of the resultant steady states are illustrated in red, green, and blue respectively for each of the initial states.

master equation (in black). The ratio of system length to critical radius is fixed to $l/r_c = 10$ and we choose $\lambda = 1, 2, 3$ from the top to the bottom panel. Note that the dimension of the Hilbert space increases from top to bottom. The differently coloured curves in each panel show solutions to the Schrödinger equation starting from randomly chosen initial states $|n_0 \mathcal{C}_{n_0}\rangle$ with the same number of hard rods n_0 but different spin configurations \mathcal{C}_{n_0} . The initial number of hard rods is chosen such that the initial state lies in a region of the configuration network with large connectivity, i.e., where the statistical assumptions underlying the derivation of the master equation are well met. The right column shows the corresponding probability distributions p_n at $\Omega t = 20$. For both $\langle n \rangle \lambda / L$ and p_n the agreement between the results of the exact quantum calculation and the prediction of the master equation is remarkably good. In particular, for long times the results of the full quantum calculation and solution of the master equation only differ by roughly one per cent. For short times the quadratic time dependence of $\langle n \rangle \lambda / L$ as well as its dependence on λ are well reproduced (see insets). For longer times the full quantum solutions exhibit oscillations around the equilibrium value of $\langle n \rangle \lambda / L$. Being a simple rate equation our master equation does not reproduce these. However, the quantum oscillations decrease with increasing dimension of

the Hilbert space. For $\lambda = 1$ this behaviour was also reported in reference [44].

At long times we observe a small systematic offset of $\langle n \rangle \lambda / L$ obtained from the exact numerics from the steady state values predicted by the master equation. In the cases shown in Fig. 5.6(a), where the initial state contains fewer hard rods than the equilibrium state, the quantum calculations suggest a slightly lower value of the average hard rod density at long times. In contrast, for initial states with a higher hard rod density than the equilibrium value the quantum results lie slightly above the prediction of the master equation. Due to this systematic dependence on the initial state, we attribute this small offset to the presence of memory effects in the quantum dynamics that were completely neglected in the derivation of the master equation. Furthermore, the data of the full quantum calculation for $\lambda = 3$ exhibit a very slow drift of $\langle n \rangle \lambda / L$ towards the steady state of our rate equation. This effect is seen more clearly in Fig. 5.7, where we follow the time evolution of the hard rod density for $\lambda = 4$ to much longer times. The observed shift might be indicative of a pre-equilibration process in the quantum system, in which $\langle n \rangle \lambda / L$ quickly reaches a quasi-equilibrium state, which then very slowly equilibrates to the “true” steady state. However, the drift might also stem from a long wavelength oscillation present in the full quantum calculation due to the finite size of the system. Since the full quantum calculations are limited to small system sizes it is difficult to further explore this effect, which seems to be more pronounced with increasing λ .

Let us finally return to the observation made in Fig. 5.6(b) that distribution functions p_n calculated fully quantum mechanically and using the master equation agree very well at long times. In order to quantify the degree of agreement we use the following overlap measure [141],

$$\mathcal{D} = 1 - \frac{1}{2} \sum_{n=0}^{L/(\lambda+1)} |\bar{p}_n - p_n^{\text{eq}}|. \quad (5.26)$$

Here p_n^{eq} denotes the steady state solution of the master equation and \bar{p}_n is the equilibrium distribution obtained from the solution of the Schrödinger equation, time averaged over a time interval Δt , i.e., $\bar{p}_n = \int_t^{t+\Delta t} d\tau p_n(\tau) / \Delta t$. The distribution functions are identical when $\mathcal{D} = 1$, and $\mathcal{D} = 0$ for distribution functions that are completely non-overlapping. For the three situations discussed in Fig. 5.6 we have selected 100 randomly chosen initial spin configurations for $L = 10, \lambda = 1$ and 500 randomly chosen initial spin configurations for $L = 20, \lambda = 2$ and $L = 30, \lambda = 3$, and have used them as initial states of the quantum evolution. The time average in order to compute \bar{p}_n was taken over the interval $\Delta t = [20/\Omega, 40/\Omega]$. We have collected the results of these simulations in the histograms shown in Fig. 5.8. Here

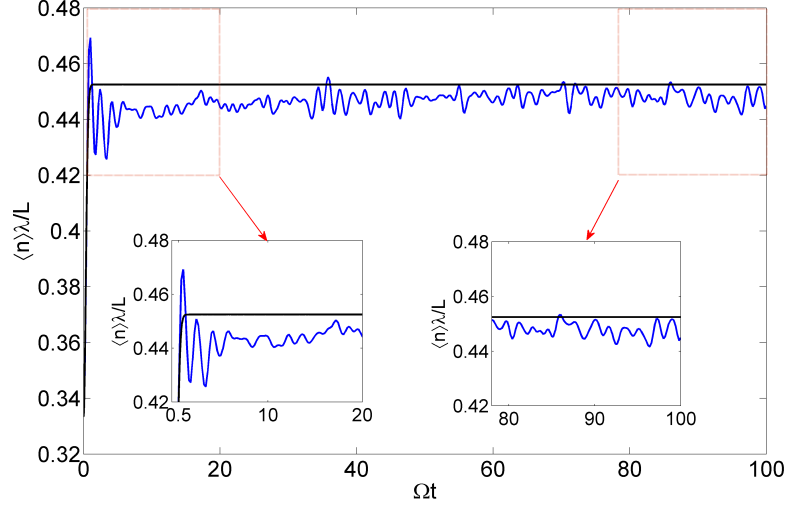


Figure 5.7: Long time quantum evolution of the hard rod density starting from a randomly chosen initial state with $n_0 = 3$ hard rods for $\lambda = 4$ and $l/r_c = 9$. The evolution predicted by the master equation is plotted in black. To highlight the shift, the time evolution from $\Omega t = 0.5$ to $\Omega t = 20$ is enlarged and shown in the left inset, and the evolution from $\Omega t = 80$ to $\Omega t = 100$ is enlarged and shown in the right inset.

we see that for the vast majority of initial conditions \mathcal{D} is close to one with only a few outliers. This indicates that indeed equilibration is largely independent of the initial state. In order to demonstrate that the used set of initial conditions is representative we have looked at the distribution of the number of hard rods contained in the initial states. As an example the inset in Fig. 5.8 shows this distribution for the parameters of the bottom panel. Comparing this to the microcanonical steady state distribution we see that indeed each number is represented with the correct weight. Finally, looking at the histograms shown in Fig. 5.8 as a function of the dimension of the Hilbert space we see that the system equilibrates better with increasing number of available microstates, confirming similar observations made in [44] for the case $\lambda = 1$. In the thermodynamic limit, the master equation in Eq. (5.12) therefore indeed provides an excellent description of the non-equilibrium dynamics in particle number space.

5.6.3 Eigenstate Thermalisation Hypothesis

In this section, we show numerically that our closed quantum system obeys the ETH. To do this, we numerically diagonalise Hamiltonian (5.1) to obtain the eigenstates and eigenenergies, and denote them as $|\epsilon_i\rangle$ and ϵ_i respectively. Thus, $H_{\text{spin}}|\epsilon_i\rangle = \epsilon_i|\epsilon_i\rangle$. For any initial state $|\phi\rangle$, we can rewrite it in terms of the

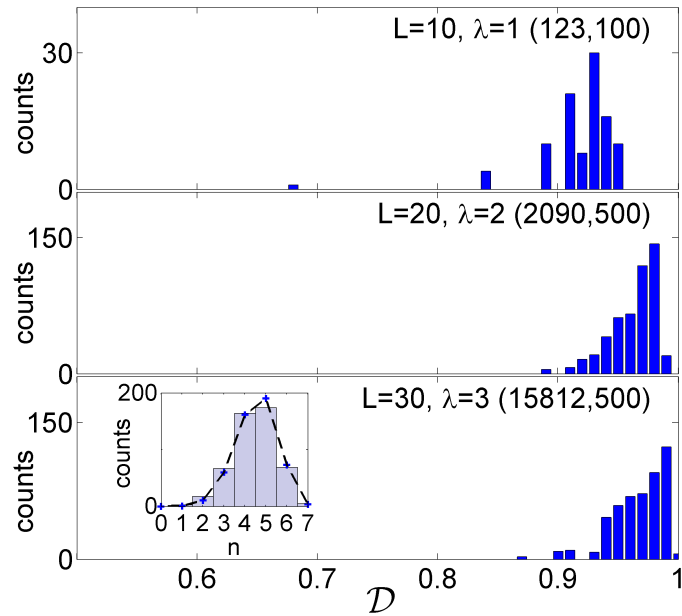


Figure 5.8: Histogram of the parameter \mathcal{D} , defined in Eq. (5.26), for the three parameter sets used in Fig. 5.6. The numbers in the parentheses show the dimension of the Hilbert space and the number of initial states used to create the histogram, respectively. For the bottom panel we also show the distribution of the number of hard rods contained in the initial states as an inset. The black dashed line with blue cross marks in the inset shows the microcanonical steady state distribution of the number of hard rods for comparison.

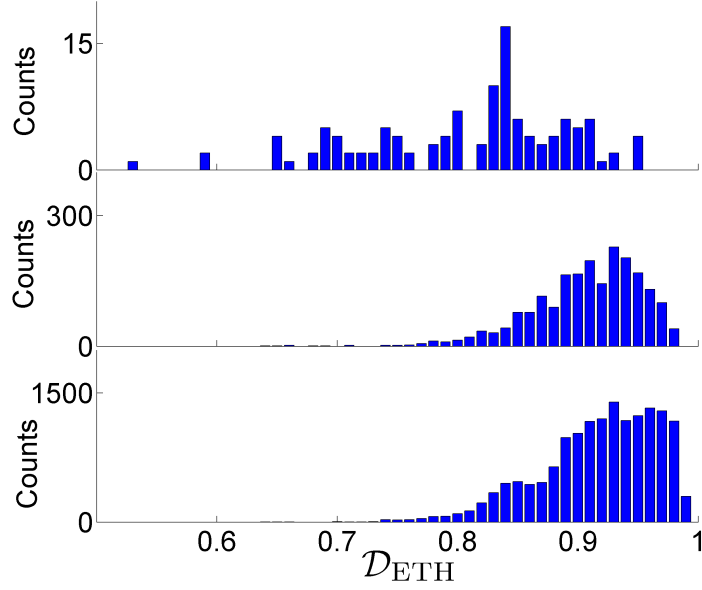


Figure 5.9: Histogram of the overlap \mathcal{D}_{ETH} , defined in 5.29. The parameter sets are equivalent to those in 5.8. The histogram is constructed using all eigenstates for the respective parameter set.

eigenstates basis, such that $|\phi\rangle = \sum_i |\epsilon_i\rangle \langle \epsilon_i | \phi \rangle$, and we further denote $\langle \epsilon_i | \phi \rangle = E_i$. For an arbitrary initial state, it is then possible to write down the expectation value of the projector $P_n = \sum_{\mathcal{C}_n} |n\mathcal{C}_n\rangle \langle n\mathcal{C}_n|$ at time t as,

$$\langle \phi | P_n | \phi \rangle(t) = \sum_{i,j} E_i^* E_j e^{-i(\epsilon_j - \epsilon_i)t} \langle \epsilon_i | P_n | \epsilon_j \rangle. \quad (5.27)$$

According to ETH, in the infinite time limit where $\tau \rightarrow \infty$ the time average value of $\langle P_n \rangle(\tau) \equiv \langle \phi | P_n | \phi \rangle(\tau)$ can be calculated as,

$$\begin{aligned} \overline{\langle P_n \rangle(\tau)} &= \lim_{\tau \rightarrow \infty} \frac{1}{\tau} \int_0^\tau dt \langle \phi | P_n | \phi \rangle(t) \\ &= \sum_i E_i^* E_i \langle \epsilon_i | P_n | \epsilon_i \rangle + i \lim_{\tau \rightarrow \infty} \left[\sum_{i \neq j} \frac{E_i^* E_j \langle \epsilon_i | P_n | \epsilon_j \rangle}{\epsilon_j - \epsilon_i} \left(\frac{e^{-i(\epsilon_j - \epsilon_i)\tau} - 1}{\tau} \right) \right] \\ &= \sum_i E_i^* E_i \langle \epsilon_i | P_n | \epsilon_i \rangle, \end{aligned} \quad (5.28)$$

provided that $\langle \epsilon_i | P_n | \epsilon_i \rangle$ only weakly depend on ϵ_i .

In the following we will perform a comparison between the distribution function calculated in the eigenstates, denote as $p_n^{\epsilon_i} \equiv \overline{\langle P_n \rangle(\tau)}$ and the equilibrium distribution p_n^{eq} defined in Eq. (5.17). This analysis follows closely the one presented in the previous section: We first numerically diagonalize Hamiltonian (5.1).

Subsequently, we calculate the overlap

$$\mathcal{D}_{\text{ETH}} = 1 - \frac{1}{2} \sum_{n=0}^{L/(\lambda+1)} |p_n^{\epsilon_i} - p_n^{\text{eq}}| \quad (5.29)$$

for all eigenstates $|\epsilon_i\rangle$ and produce a histogram of the results. The corresponding data is shown in 5.9, with the parameter sets being equivalent to those in 5.8. Each histogram is constructed using all eigenstates for the respective parameter set. The result shows features that are very similar to Fig. 5.8. For example, the number of states giving rise to a distribution function with high overlap with p_n^{eq} increases as the Hilbert space dimension grows. In general this indicates that our system satisfies the ETH.

It is interesting to note that the actual time-evolution produces states whose distribution functions have higher overlap with p_n^{eq} than the average energy-eigenstate. This indicates that for the systems sizes and observable considered here the off-diagonal terms which have been neglected in deriving Eq. (5.28) still contribute significantly.

5.7 Conclusion and Outlook

In conclusion, we analysed in detail the time-evolution of a driven quantum spin system through a derived master equation. The master equation which describes the temporal behaviour of the observable p_n reliably predicted the actual time-evolution that one obtains from numerical treatment of the quantum system. The master equation, unlike the numerics where system size is the limiting issue, was found to be capable of calculating results for very large system sizes in a considerable short time and it could be applied to arbitrary blockade length (quantum hard-rods with varying sizes). By showing what happens en route to the equilibrium in our results, we showed that the expectation value of p_n can be calculated at a finite time from a statistical ensemble that corresponds to the partition of a hard-rods gas.

One of the interesting findings in the results is the gradual shift of the blue curves (numerical result) toward the steady state observed in Fig. 5.7 which indicates the presence of a new (very slow) timescale. The master equation we have derived fails to capture this small but obvious shift that one obtains in the numerics. With further analysis involving different initial states, it is found that such a phenomenon always presents. A similar phenomenon has been observed in other systems and are named prethermalisation [142, 143, 144]. Therefore, it is intriguing to understand what causes this shifting and why does it occur in a

non-integrable, closed quantum system described by H_{spin} .

In deriving the master equation, we only considered a second order expansion of the von Neumann equation [c.f. Appendix E.3]. As a result, we arrive at a master equation which contains a squared Hamiltonian H_I^2 such that only second order processes, e.g. reflections, are considered. In fact, it is possible to go beyond the second order expansion. For instance, a fourth order expansion can be achieved by continuously replacing $\rho(s)$ in Eq. (E.10) with the $\rho(t)$ obtained in Eq. (E.9) for two more times. Then, by expanding all the commutators, apart from the second order terms described by H_I^2 , one will also obtain 16 terms with each term depends on H_I^4 . Since there is no clear evidence for us to argue that these higher order terms are negligible, it is interesting to see how they might affect our results. As a fourth order process contains more information in describing the dynamics, it is expected that they might reduce the memory effect as discussed along with the results produced in Fig. 5.6. The matrix elements of these more complicated H_I^4 can be also mapped to adjacency matrices in the form of \mathcal{M}^4 which will be calculable by using the combinatoric results obtained.

A few other things that one can calculate for this system are for instance the level-spacing distribution of our Hamiltonian to see whether it gives a Wigner distribution, a Poisson distribution or something in-between. Due to the fact that our system is non-integrable, but contains symmetries such as the translational symmetry used in constructing momentum eigenbasis, we expect the spectrum of the level spacing distribution to be something in between the Wigner and Poisson distributions.

Appendices

Appendix A

Interaction Picture and the Effective Hamiltonian

The Hamiltonian of the Rydberg lattice gas as given in Eq. (2.33), takes the following form,

$$H_{\text{Ryd}} = \sum_{\mathbf{k}}^L \Omega_{\mathbf{k}} \sigma_{\mathbf{k}}^x + \sum_{\mathbf{k}}^L \Delta_{\mathbf{k}} n_{\mathbf{k}} + \frac{1}{2} \sum_{\langle \mathbf{k}, \mathbf{m} \rangle}^L V_{|\mathbf{k}-\mathbf{m}|} n_{\mathbf{k}} n_{\mathbf{m}}, \quad (\text{A.1})$$

and the corresponding Schrödinger equation reads,

$$i \frac{\partial}{\partial t} \Psi = H_{\text{Ryd}} \Psi, \quad (\text{A.2})$$

with Ψ being the wavefunction.

To transform the Hamiltonian into an interaction picture with respect to the nearest neighbour interaction, we apply the unitary transformation,

$$U = \exp \left\{ -itV \sum_{\langle \mathbf{k}, \mathbf{k}' \rangle}^L n_{\mathbf{k}} n_{\mathbf{k}'} \right\} = \prod_{\langle \mathbf{k}, \mathbf{k}' \rangle} e^{-itV n_{\mathbf{k}} n_{\mathbf{k}'}} , \quad (\text{A.3})$$

where the notation $\langle \mathbf{k}, \mathbf{k}' \rangle$ indicates that \mathbf{k} and \mathbf{k}' are indices of atoms who are nearest neighbours of each other. The state vector in the interaction picture is then given by $\Psi_I = U^\dagger \Psi$, or $\Psi = U \Psi_I$. Therefore, the Schrödinger equation can be written as,

$$i \frac{\partial}{\partial t} (U \Psi_I) = H_{\text{Ryd}} (U \Psi_I), \quad (\text{A.4})$$

Using the product rule, the left hand side becomes $i(\frac{\partial}{\partial t} U) \Psi_I + iU(\frac{\partial}{\partial t} \Psi_I)$. Then, applying U^\dagger on both sides, and rearranging the equation, one finds,

$$i \frac{\partial}{\partial t} \Psi_I = [U^\dagger H_{\text{Ryd}} U - iU^\dagger (\frac{\partial}{\partial t} U)] \Psi_I, \quad (\text{A.5})$$

where $U^\dagger H_{\text{Ryd}} U - iU^\dagger (\frac{\partial}{\partial t}) U$ acts as an effective Hamiltonian, and it can be calculated as,

$$\begin{aligned}
H_{\text{eff}} &= U^\dagger H_{\text{Ryd}} U - iU^\dagger \frac{\partial}{\partial t} U \\
&= U^\dagger H_{\text{Ryd}} U - U^\dagger \left[V \sum_{\langle \mathbf{k}, \mathbf{k}' \rangle}^L n_{\mathbf{k}} n_{\mathbf{k}'} \right] U \\
&= U^\dagger \left[\sum_{\mathbf{k}}^L \Omega_{\mathbf{k}} \sigma_{\mathbf{k}}^x + \sum_{\mathbf{k}}^L \Delta_{\mathbf{k}} n_{\mathbf{k}} + \frac{1}{2} \sum_{|\mathbf{k}-\mathbf{m}|>1}^L V_{|\mathbf{k}-\mathbf{m}|} n_{\mathbf{k}} n_{\mathbf{m}} \right] U. \quad (\text{A.6})
\end{aligned}$$

To carry on the calculation, since the unitary transformation commutes with the number operators, i.e. $n_{\mathbf{k}}$, one only needs to consider the term $U^\dagger \sigma_{\mathbf{k}}^x U$.

Using the fact that number operators are projection operators, i.e. $n_{\mathbf{k}}^2 = n_{\mathbf{k}}$, and using the Taylor expansion of an exponential, one can rewrite an exponential in the following way,

$$\begin{aligned}
e^{itV n_a n_b} &= 1 + itV n_a n_b + \frac{(itV n_a n_b)^2}{2!} + \dots \\
&= 1 + n_a n_b [-1 + 1 + itV + \frac{(itV)^2}{2!} + \dots] \\
&= 1 + n_a n_b [e^{itV} - 1]. \quad (\text{A.7})
\end{aligned}$$

Using this fact, one finds that

$$\begin{aligned}
U^\dagger \sigma_{\mathbf{k}}^x U &= \prod_{\langle \mathbf{k}, \mathbf{m} \rangle} e^{itV n_{\mathbf{k}} n_{\mathbf{m}}} \sigma_{\mathbf{k}}^x \prod_{\langle \mathbf{k}, \mathbf{k}' \rangle} e^{-itV n_{\mathbf{k}} n_{\mathbf{k}'}} \\
&= \prod_{\langle \mathbf{k}, \mathbf{k}' \rangle} [1 + n_{\mathbf{k}} n_{\mathbf{k}'} (e^{itV} - 1)] \sigma_{\mathbf{k}}^x \\
&\quad \times \prod_{\langle \mathbf{k}, \mathbf{k}' \rangle} [1 + n_{\mathbf{k}} n_{\mathbf{k}'} (e^{-itV} - 1)]. \quad (\text{A.8})
\end{aligned}$$

Then, writing $\sigma_{\mathbf{k}}^x$ as $\sigma_{\mathbf{k}}^+ + \sigma_{\mathbf{k}}^-$, we can expand the brackets by using the following relations:

$$\begin{aligned}
n_{\mathbf{k}} \sigma_{\mathbf{k}}^x &= \sigma_{\mathbf{k}}^+, & n_{\mathbf{k}} \sigma_{\mathbf{k}}^+ &= \sigma_{\mathbf{k}}^+, & n_{\mathbf{k}} \sigma_{\mathbf{k}}^- &= 0, \\
\sigma_{\mathbf{k}}^x n_{\mathbf{k}} &= \sigma_{\mathbf{k}}^-, & \sigma_{\mathbf{k}}^- n_{\mathbf{k}} &= \sigma_{\mathbf{k}}^-, & \sigma_{\mathbf{k}}^+ n_{\mathbf{k}} &= 0.
\end{aligned}$$

One eventually finds that

$$U^\dagger \sigma_{\mathbf{k}}^x U = \sigma_{\mathbf{k}}^+ \prod_{\mathbf{k}'} [1 - n_{\mathbf{k}'} + n_{\mathbf{k}'} e^{itV}] + h.c., \quad (\text{A.9})$$

where h.c. stands for the hermitian conjugate of the present part, and the indices \mathbf{k}' are again the nearest neighbours of \mathbf{k} . In the limit of $V \gg \Omega_{\mathbf{k}}, \Delta_{\mathbf{k}}$, we apply rotating wave approximation where the rapid oscillating phases, $e^{\pm itV}$, can be neglected since these terms will quickly average to zero over time. In addition, defining a plaquette operator, $\mathcal{P}_{\mathbf{k}} = \prod_{\mathbf{k}'} [1 - n_{\mathbf{k}'}]$, one arrives at

$$U^\dagger \sigma_{\mathbf{k}}^x U = \sigma_{\mathbf{k}}^x \mathcal{P}_{\mathbf{k}}. \quad (\text{A.10})$$

Therefore, the effective Hamiltonian reads

$$H_{\text{eff}} = \sum_{\mathbf{k}}^L \Omega_{\mathbf{k}} \sigma_{\mathbf{k}}^x \mathcal{P}_{\mathbf{k}} + \sum_{\mathbf{k}}^L \Delta_{\mathbf{k}} n_{\mathbf{k}} + \frac{1}{2} \sum_{|\mathbf{k}-\mathbf{m}|>1}^L V_{|\mathbf{k}-\mathbf{m}|} n_{\mathbf{k}} n_{\mathbf{m}}. \quad (\text{A.11})$$

Appendix B

Expectation Values of the Observables in the Limiting Cases

The ground state ξ in the two limiting cases can be expressed as,

$$|\xi\rangle_{\xi \rightarrow 0} = \left[\left| \begin{pmatrix} \downarrow & \downarrow & \downarrow & \cdots \\ \downarrow & \downarrow & \downarrow & \cdots \\ \downarrow & \downarrow & \downarrow & \cdots \\ \vdots & & & \ddots \end{pmatrix} \right\rangle - \xi \left[\left| \begin{pmatrix} \uparrow & \downarrow & \downarrow & \cdots \\ \downarrow & \downarrow & \downarrow & \cdots \\ \downarrow & \downarrow & \downarrow & \cdots \\ \vdots & & & \ddots \end{pmatrix} \right\rangle + \left| \begin{pmatrix} \downarrow & \uparrow & \downarrow & \cdots \\ \downarrow & \downarrow & \downarrow & \cdots \\ \downarrow & \downarrow & \downarrow & \cdots \\ \vdots & & & \ddots \end{pmatrix} \right\rangle + \cdots \right], \quad (\text{B.1})$$

$$|\xi\rangle_{\xi \rightarrow \infty} = \left[\left| \begin{pmatrix} \uparrow & \downarrow & \uparrow & \cdots \\ \downarrow & \uparrow & \downarrow & \cdots \\ \uparrow & \downarrow & \uparrow & \cdots \\ \vdots & & & \ddots \end{pmatrix} \right\rangle - \frac{1}{\xi} \left[\left| \begin{pmatrix} \downarrow & \downarrow & \uparrow & \cdots \\ \downarrow & \uparrow & \downarrow & \cdots \\ \uparrow & \downarrow & \uparrow & \cdots \\ \vdots & & & \ddots \end{pmatrix} \right\rangle + \left| \begin{pmatrix} \uparrow & \downarrow & \downarrow & \cdots \\ \downarrow & \uparrow & \downarrow & \cdots \\ \uparrow & \downarrow & \uparrow & \cdots \\ \vdots & & & \ddots \end{pmatrix} \right\rangle + \cdots \right]. \quad (\text{B.2})$$

where we have denoted \uparrow as an occupied site, and \downarrow as an unoccupied site. In the $\xi \rightarrow 0$ case, atoms do not want to be excited, thus allowing us to approximate the ground state as the all unoccupied configuration plus very small corrections where each configuration has only one excitation. In the limit of $\xi \rightarrow \infty$, the ground state is approximated by configuration that contains maximum excitation, i.e. half of the total number of sites, $L/2$ in addition with configurations with one less occupation. The coefficients in front of the corrections ensures that they are vanishingly small.

Using the states, $|\xi\rangle_{\xi \rightarrow \infty}$ and $|\xi\rangle_{\xi \rightarrow 0}$ defined in Sec. 4.7 and denote $\langle \cdot \rangle \equiv \langle \xi | \cdot | \xi \rangle$,

for $\xi \rightarrow 0$, we have

$$\begin{aligned}
\langle \sum_{k,m} n_{k,m} \rangle &= \langle 0 | \sum_{k,m} n_{k,m} | 0 \rangle - \xi \langle 0 | \sum_{k,m} n_{k,m} | 1 \rangle \\
&\quad - \xi \langle 1 | \sum_{k,m} n_{k,m} | 0 \rangle + \xi^2 \langle 1 | \sum_{k,m} n_{k,m} | 1 \rangle \\
&= \xi^2 L
\end{aligned} \tag{B.3}$$

where L is the total number of sites, and we have abbreviated the configurations in the way that the number represents the number of up-spins, and for empty configuration, we have $|0\rangle$. Thus, $n_{k,m}|0\rangle = 0$. Using same notations, we have

$$\begin{aligned}
\langle \sum_{k,m} \sigma_{k,m}^x \rangle &= \langle 0 | \sum_{k,m} \sigma_{k,m}^x | 0 \rangle - \xi \langle 0 | \sum_{k,m} \sigma_{k,m}^x | 1 \rangle \\
&\quad - \xi \langle 1 | \sum_{k,m} \sigma_{k,m}^x | 0 \rangle + \xi^2 \langle 1 | \sum_{k,m} \sigma_{k,m}^x | 1 \rangle \\
&= 0 - \xi L - \xi L + 0. \\
&= -2\xi L
\end{aligned} \tag{B.4}$$

Lastly, we have

$$\langle \sum_{k,m} n_{k,m} n_{k+1,m+1} \rangle = 0, \tag{B.5}$$

since no configuration contains two up-spins, all terms will be zero.

In the $\xi \rightarrow \infty$ case, we have,

$$\begin{aligned}
\langle \sum_{k,m} n_{k,m} \rangle &= \langle \frac{L}{2} | \sum_{k,m} n_{k,m} | \frac{L}{2} \rangle - \frac{1}{\xi} \langle \frac{L}{2} - 1 | \sum_{k,m} n_{k,m} | \frac{L}{2} \rangle \\
&\quad - \frac{1}{\xi} \langle \frac{L}{2} | \sum_{k,m} n_{k,m} | \frac{L}{2} - 1 \rangle + \frac{1}{\xi^2} \langle \frac{L}{2} - 1 | \sum_{k,m} n_{k,m} | \frac{L}{2} - 1 \rangle \\
&= \frac{L}{2} - 0 - 0 + \frac{L}{2\xi^2} (\frac{L}{2} - 1) \\
&= \frac{L}{2} \left(1 + \frac{L-2}{2\xi^2} \right).
\end{aligned} \tag{B.6}$$

Notice that due to the nearest neighbour exclusion, the maximum occupation is half of the total number of sites, i.e. $\frac{L}{2}$. Also, the different ways of having $\frac{L}{2} - 1$

occupations is $\frac{L}{2}$.

$$\begin{aligned}
\langle \sum_{k,m} \sigma_{k,m}^x \rangle &= \langle \frac{L}{2} | \sum_{k,m} \sigma_{k,m}^x | \frac{L}{2} \rangle - \frac{1}{\xi} \langle \frac{L}{2} - 1 | \sum_{k,m} \sigma_{k,m}^x | \frac{L}{2} \rangle \\
&\quad - \frac{1}{\xi} \langle \frac{L}{2} | \sum_{k,m} \sigma_{k,m}^x | \frac{L}{2} - 1 \rangle + \frac{1}{\xi^2} \langle \frac{L}{2} - 1 | \sum_{k,m} \sigma_{k,m}^x | \frac{L}{2} - 1 \rangle \\
&= 0 - \frac{1}{\xi} \frac{L}{2} - \frac{1}{\xi} \frac{L}{2} + 0 \\
&= -\frac{L}{\xi}.
\end{aligned} \tag{B.7}$$

Finally,

$$\begin{aligned}
\langle \sum_{k,m} n_{k,m} n_{k+1,m+1} \rangle &= \langle \frac{L}{2} | \sum_{k,m} n_{k,m} n_{k+1,m+1} | \frac{L}{2} \rangle - \frac{1}{\xi} \langle \frac{L}{2} - 1 | \sum_{k,m} n_{k,m} n_{k+1,m+1} | \frac{L}{2} \rangle \\
&\quad - \frac{1}{\xi} \langle \frac{L}{2} | \sum_{k,m} n_{k,m} n_{k+1,m+1} | \frac{L}{2} - 1 \rangle \\
&\quad + \frac{1}{\xi^2} \langle \frac{L}{2} - 1 | \sum_{k,m} n_{k,m} n_{k+1,m+1} | \frac{L}{2} - 1 \rangle \\
&= \frac{L}{2} - 0 - 0 + \frac{1}{\xi^2} \frac{L}{2} \left(\frac{L}{2} - 2 \right) \\
&= \frac{L}{2} \left[1 + \frac{1}{\xi^2} \left(\frac{L}{2} - 2 \right) \right].
\end{aligned} \tag{B.8}$$

Now, we can substitute in the limiting condition into these approximated expectation values and divide everything by L to calculate the mean expectation, we have

$$\begin{aligned}
\langle n_{k,m} \rangle |_{\xi \rightarrow 0} &\approx 0, & \langle \sigma_{k,m}^x \rangle |_{\xi \rightarrow 0} &\approx 0, & \langle n_{k,m} n_{k+1,m+1} \rangle |_{\xi \rightarrow 0} &\approx 0, \\
\langle n_{k,m} \rangle |_{\xi \rightarrow \infty} &\approx \frac{1}{2}, & \langle \sigma_{k,m}^x \rangle |_{\xi \rightarrow \infty} &\approx 0, & \langle n_{k,m} n_{k+1,m+1} \rangle |_{\xi \rightarrow \infty} &\approx \frac{1}{2}.
\end{aligned} \tag{B.9}$$

Appendix C

Configuration Energy of the Quarter Filling State

Using the definition of the quarter filling state defined in Sec. 4.9, where

$$\begin{aligned}
 |\phi\rangle_{1/4} = & N_\phi [|\alpha\rangle_1 |\downarrow\rangle_2 |\downarrow\rangle_3 |\downarrow\rangle_4 |\alpha\rangle_5 \dots |\downarrow\rangle_L \\
 & + |\downarrow\rangle_1 |\alpha\rangle_2 |\downarrow\rangle_3 |\downarrow\rangle_4 \dots |\downarrow\rangle_L \\
 & + |\downarrow\rangle_1 |\downarrow\rangle_2 |\alpha\rangle_3 |\downarrow\rangle_4 \dots |\downarrow\rangle_L \\
 & + |\downarrow\rangle_1 |\downarrow\rangle_2 |\downarrow\rangle_3 |\alpha\rangle_4 \dots |\alpha\rangle_L],
 \end{aligned} \tag{C.1}$$

with $|\alpha\rangle = (1 - \alpha^2)^{1/2} |\uparrow\rangle + \alpha |\downarrow\rangle$ one finds the following $\langle\alpha|\alpha\rangle = 1$ and $\langle\alpha|\downarrow\rangle = \langle\downarrow|\alpha\rangle = \alpha$, and α being real. The configuration energy can be calculated as,

$$\begin{aligned}
 {}_{1/4}\langle\phi|H_{\text{Ryd}_{\text{sqr}}}| \phi\rangle_{1/4} = & N_\phi^2 [\langle\textcircled{1}| + \langle\textcircled{2}| + \langle\textcircled{3}| + \langle\textcircled{4}|] \\
 & \left\{ \Omega \sum \sigma_{k,m}^2 + \Delta \sum n_{k,m} \right\} [|\textcircled{1}\rangle + |\textcircled{2}\rangle + |\textcircled{3}\rangle + |\textcircled{4}\rangle],
 \end{aligned} \tag{C.2}$$

with $|\textcircled{1}\rangle$, and etc. denote the sub-states in ϕ . The interaction term in $H_{\text{Ryd}_{\text{sqr}}}$ is neglected due to the lack of interactions of the quarter filling configuration. Expanding the expression, one finds that

$$\begin{aligned}
 \langle\textcircled{1}|H_{\text{Ryd}_{\text{sqr}}}| \textcircled{1}\rangle = & \frac{L}{4} \{ {}_1\langle\alpha|\Delta n_1|\alpha\rangle_1 {}_2\langle\downarrow|\downarrow\rangle_2 {}_3\langle\downarrow|\downarrow\rangle_3 \dots \} \\
 = & \frac{L}{4} \Delta (1 - \alpha^2).
 \end{aligned} \tag{C.3}$$

The coefficient $L/4$ is due to quarter filling, i.e. maximum Rydberg atom the system can have is $L/4$. And there are total of four equivalent terms in the energy

calculation which in the end gives ΔL . The cross terms in the energy reads

$$\begin{aligned}
\langle \textcircled{1} | H_{\text{Ryd}_{\text{sq}}} | \textcircled{2} \rangle &= \langle \alpha | \Omega \sigma_1^x | \downarrow \rangle_1 \langle \downarrow | \alpha \rangle_2 \langle \downarrow | \downarrow \rangle_3 \langle \downarrow | \downarrow \rangle_4 \langle \alpha | \downarrow \rangle_5 \cdots \\
&= \frac{L}{2} \Omega \alpha^{(\frac{L}{2}-1)} (1 - \alpha^2)^{\frac{1}{2}}.
\end{aligned} \tag{C.4}$$

There are total of 12 equivalent cross terms and together with $\langle \textcircled{1} | H_{\text{Ryd}_{\text{sq}}} | \textcircled{1} \rangle$, we have the quarter filling state energy as,

$${}_{1/4} \langle \phi | H_{\text{Ryd}_{\text{sq}}} | \phi \rangle_{1/4} = \frac{6\Omega L \alpha^{(\frac{L}{2}-1)} (1 - \alpha^2)^{\frac{1}{2}} + \Delta L (1 - \alpha^2)}{4 + 12\alpha^{\frac{L}{2}}}. \tag{C.5}$$

Appendix D

Calculation of Configuration Network Properties

D.1 The Combinatorial Method

The first method to calculate the mean connectivities considers counting ν_n and $c_{n \rightarrow n \pm 1}$ directly. The idea is to consider each hard-rod as an effective particle and all hard-rods are indistinguishable. The problem then becomes a standard combinatorial one which is to count the number of ways to arrange indistinguishable particles on a lattice [136]. Here, each hard-rod occupies $\lambda + 1$ original lattice sites and will be counted as if it occupies one effective lattice site. In general, the number of ways to arrange indistinguishable particles on a lattice can be calculated by using the combinatorics as $\nu_n = \frac{L_{\text{eff}}!}{n!(L_{\text{eff}} - n)!}$ with L_{eff} being the total number of effective lattice sites and n being the number of hard-rods on the lattice. For an open boundary one-dimensional lattice chain, with n hard-rods (n up-spins), one finds that $L_{\text{eff}} = L - \lambda n$. To further include the periodic boundary condition in the counting mechanism, we assign the first hard-rod with a known position. There are in total L different ways to place this hard-rod. For each way, one can count the number of ways to arrange the remaining $n - 1$ hard-rods, and eventually multiply by L . However, due to indistinguishability of the particles, there will be n repetitions for a total of n hard-rods since each one of the $n - 1$ hard-rods can be interchanged with the first assigned hard-rod. The amount of effective lattice sites on which to arrange the remaining $n - 1$ hard-rods, becomes $L_{\text{eff}} = L - (\lambda + 1) - \lambda(n - 1)$. Finally, substituting L_{eff} and $n - 1$ into the general combinatorics, and together with the L/n factor derived from assigning the first hard-rod and avoiding repetitions, one finds that the number of nodes contained

in the n -th column can be calculated as,

$$\nu_n = \frac{L(L-1-\lambda n)!}{n!(L-(\lambda+1)n)!}. \quad (\text{D.1})$$

To calculate the total number of edges between neighbouring columns, i.e. $c_{n \rightarrow n \pm 1}$ with $c_{n-1 \rightarrow n} = c_{n \rightarrow n-1}$ and $c_{n+1 \rightarrow n} = c_{n \rightarrow n+1}$, one can use the relation that $c_{n \rightarrow n-1} = T_{n \rightarrow n-1} \nu_n$ and $c_{n+1 \rightarrow n} = T_{n+1 \rightarrow n} \nu_{n+1}$. Now, let us consider $T_{n \rightarrow n-1}$ from a physical perspective. For a spin configuration containing n up-spins, e.g. $|\downarrow\uparrow\downarrow\uparrow\rangle$ with $n = 2$, there are obviously n different possible ways to flip one up-spin to arrive at spin configurations with $n - 1$ up-spins, e.g. $|\downarrow\downarrow\downarrow\uparrow\rangle$ and $|\downarrow\uparrow\downarrow\downarrow\rangle$ by flipping one up-spin from the example above. This simply means $T_{n \rightarrow n-1} = n$. Therefore, we have,

$$\begin{aligned} c_{n \rightarrow n-1} &= T_{n \rightarrow n-1} \nu_n = \frac{L(L-1-\lambda n)!}{(n-1)!(L-(\lambda+1)n)!}, \\ c_{n+1 \rightarrow n} &= T_{n+1 \rightarrow n} \nu_{n+1} = \frac{L(L-1-\lambda(n+1))!}{n!(L-(\lambda+1)(n+1))!}, \end{aligned} \quad (\text{D.2})$$

and these results can be further used to obtain $T_{n \rightarrow n+1}$ and $T_{n-1 \rightarrow n}$.

D.2 Transfer Matrix Method

The alternative method, which is the one used in Ref. [44] is to introduce a spin-coherent state similar to the one provided in [31],

$$\begin{aligned} |\xi\rangle &= \frac{1}{\sqrt{N_\xi}} \prod_k^L (1 - \xi \left[\prod_{i=k-\lambda, i \neq k}^{k+\lambda} (1 - n_i) \right] \sigma_k^+) |0\rangle \\ &= \frac{1}{\sqrt{N_\xi}} \{ |0\rangle - \xi |1\rangle + \xi^2 |2\rangle - \dots \}, \end{aligned} \quad (\text{D.3})$$

where the sub-state, $|n\rangle$, is a superposition state of all allowed microstates with n up-spins, e.g. $|1\rangle = |\uparrow\downarrow\downarrow\downarrow \dots\rangle + |\downarrow\uparrow\downarrow\downarrow \dots\rangle + |\downarrow\downarrow\uparrow\downarrow \dots\rangle + \dots + |\dots \downarrow\downarrow\downarrow\uparrow\rangle$. Thus, the state in Eq. (D.3) is a weighted sum over all allowed microstates under the constraint of having a blockade length, λ . The weight of all microstates is controlled by a single parameter, ξ . The normalisation constant of the state $|\xi\rangle$, N_ξ can be

expressed as,

$$\begin{aligned}
N_\xi &= \langle \xi | \xi \rangle \\
&= \langle 0 | 0 \rangle + \xi^2 \langle 1 | 1 \rangle + \xi^4 \langle 2 | 2 \rangle + \dots \\
&= \nu_0 + z\nu_1 + z^2\nu_2 + \dots \\
&= \sum_{n=0}^{L/(\lambda+1)} z^n \nu_n,
\end{aligned} \tag{D.4}$$

where we have set $z = \xi^2$, and ν_n counts the number of sub-sub-states in the sub-state $|n\rangle$. One immediately sees that N_ξ is nothing but a generating function for a series of numbers $\{\nu_0, \nu_1, \nu_2, \dots\}$ [145]. In general, an ordinary generating function is expressed as $G(a_n; x) = \sum_1^\infty a_n x^n$ for a series a_1, a_2, a_3, \dots . To extract the n -th number, a_n from this series, the expression $a_n = \left. \frac{1}{n!} \frac{\partial^n}{\partial x^n} G(a_n; x) \right|_{x=0}$ can be used. The derivatives ensure that numbers before a_n give zero and evaluating at $x = 0$ makes terms after a_n vanish. Therefore, ν_n can be calculated as,

$$\nu_n = \left. \frac{1}{n!} \frac{\partial N_\xi}{\partial z} \right|_{z=0}. \tag{D.5}$$

In Ref. [31], it is shown that in the case of $\lambda = 1$, i.e. nearest neighbour blockade, the normalisation constant, N_ξ is equivalent to the partition function of a hard-dimer gas. Here, we have generalised the spin-coherent state to include a general blockade length, λ . As a result, the corresponding normalisation constant N_ξ eventually can be mapped to partition function of a hard-rod gas where each hard rod occupies adjacent $\lambda + 1$ lattice sites. Using the partition function of a hard-trimer gas derived in Appendix F with a zero chemical potential $2 \ln(\xi) = 0 \rightarrow \xi = 1$, i.e. all configuration states have the same weight, and by mathematical induction, one finds that

$$\nu_n = \frac{L}{n!} \prod_{j=2n+1}^{3n-1} (L - j), \tag{D.6}$$

and this agrees with the obtained expression in the combinatorial method with $\lambda = 2$ [see Eq. (D.1)].

The next step is to calculate the total number of edges between neighbouring columns, $c_{n \rightarrow n \pm 1}$, which is mathematically given by,

$$c_{n \rightarrow n \pm 1} = \langle n \pm 1 | \sum_k \sigma_k^- | n \rangle, \tag{D.7}$$

where $|n\rangle = \sum_{\mathcal{C}_n} |n\mathcal{C}_n\rangle$. Let us now consider $c_{n \rightarrow n-1}$ as an example and to calculate $\langle n-1 | \sum_k \sigma_k^- | n \rangle$, we use a property of the spin state in Eq. (D.3), where the

expectation value of the off-diagonal operator σ_k^- can be written in terms of the expectation values of diagonal operator n_k as $\langle \xi | \sum_k \sigma_k^- | \xi \rangle = -\xi^{-1} \langle \xi | \sum_k n_k | \xi \rangle$. Using this expression, one can define a generating function for $c_{n \rightarrow n-1}$ as,

$$\begin{aligned}
\Lambda^-(z) &= \sum_k \langle \xi | n_k | \xi \rangle \\
&= -\xi \langle \xi | \sum_k \sigma_k^- | \xi \rangle \\
&= -\xi (\langle 0 | - \xi \langle 1 | + \xi^2 \langle 2 | - \dots) \sum_k \sigma_k^- (|0\rangle - \xi |1\rangle + \dots) \\
&= \xi \left(\xi \langle 0 | \sum_k \sigma_k^- |1\rangle + \xi^3 \langle 1 | \sum_k \sigma_k^- |2\rangle + \xi^5 \langle 2 | \sum_k \sigma_k^- |3\rangle + \dots \right) \\
&= \xi^2 c_{1 \rightarrow 0} + \xi^4 c_{2 \rightarrow 1} + \xi^6 c_{3 \rightarrow 2} + \dots \\
&= \sum_n z^n c_{n \rightarrow n-1}. \tag{D.8}
\end{aligned}$$

Again, using mathematical induction, one finds that,

$$c_{n \rightarrow n-1} = \frac{1}{n!} \frac{\partial^n}{\partial z^n} \Lambda^-(z) \Big|_{z=0} = \frac{L}{(n-1)!} \prod_{j=2n+1}^{3n-1} (L-j). \tag{D.9}$$

Following similar steps, one can also induct an analytical expression for $c_{n \rightarrow n+1}$ which reads,

$$c_{n \rightarrow n+1} = \frac{1}{n!} \frac{\partial^n}{\partial z^n} \Lambda^+(z) \Big|_{z=0} = \frac{L}{n!} \prod_{j=2n+3}^{3n-2} (L-j). \tag{D.10}$$

These two expressions also agree with the combinatorial results calculated in Eq. (D.2) in the case of $\lambda = 2$, if one expand the products.

Up to now, one sees that both methods mentioned in this section can be used to calculate the mean connectivities. However, the transfer matrix method is rather complicated compared to the combinatorics as the calculation of the partition function involve diagonalising a transfer matrix with size $(\lambda + 1) - \text{by} - (\lambda + 1)$ analytically. Thus, the complexity of the calculation increases as the blockade length, λ increases. However, it is worth to point out that the combinatoric method only works in the regime where all microstates (nodes in the configuration network) are equally probable, and this corresponds to $\xi = 1$ in the transfer matrix method. Therefore, in a more general case where $\xi \neq 1$, the transfer matrix method has to be adopted.

Appendix E

Derivation of a master Equation from a General Hamiltonian

E.1 Unitary Transformation and the Interaction Picture

We start by introducing a complete and orthonormal basis $|\alpha\rangle$ and write a general Hamiltonian in matrix form separating the diagonal and off-diagonal part:

$$\begin{aligned} H &= \mathbb{1}H\mathbb{1} \\ &= \left\{ \sum_{\alpha} |\alpha\rangle\langle\alpha| \right\} H \left\{ \sum_{\alpha} |\alpha\rangle\langle\alpha| \right\} \\ &= \sum_{\alpha} |\alpha\rangle\langle\alpha| H_{\text{diag}} |\alpha\rangle\langle\alpha| + \sum_{\alpha,\beta} |\alpha\rangle\langle\alpha| H_{\text{off-diag}} |\beta\rangle\langle\beta| \\ &= \sum_{\alpha} \langle\alpha| H_{\text{diag}} |\alpha\rangle |\alpha\rangle\langle\alpha| + \sum_{\alpha,\beta} \langle\alpha| H_{\text{off-diag}} |\beta\rangle |\alpha\rangle\langle\beta| \\ &= \sum_{\alpha} \omega_{\alpha} |\alpha\rangle\langle\alpha| + \sum_{\alpha,\beta} h_{\alpha,\beta} |\alpha\rangle\langle\beta|, \end{aligned} \tag{E.1}$$

where $\omega_{\alpha} = \langle\alpha| H_{\text{diag}} |\alpha\rangle$, $h_{\alpha,\beta} = \langle\alpha| H_{\text{off-diag}} |\beta\rangle$ and $\alpha \neq \beta$. To study the dynamics of the system described by H , it is often useful to transform the Hamiltonian into the interaction picture such that both the Hamiltonian and state vectors are time dependent. To transform from the Schrödinger picture to the interaction picture, we introduce the unitary operator $\hat{U}(t) = \exp[-iH_{\text{diag}}t]$ where we set $\hbar = 1$. The

unitary operator satisfies $UU^\dagger = \mathbb{1}$. In terms of the general basis $|\alpha\rangle$,

$$\begin{aligned}\hat{U}(t) &= \exp\left\{-i \sum_{\alpha} \omega_{\alpha} |\alpha\rangle\langle\alpha|t\right\} \\ &= \exp\{-i\omega_0|0\rangle\langle 0|t\} \exp\{-i\omega_1|1\rangle\langle 1|t\} \cdots \\ &= \prod_{\alpha} \exp\{-i\omega_{\alpha} |\alpha\rangle\langle\alpha|t\},\end{aligned}\tag{E.2}$$

where we have used the fact that diagonal operators commute, i.e. $[|\alpha_i\rangle\langle\alpha_i|, |\alpha_j\rangle\langle\alpha_j|] = 0$. Taylor expanding the exponential gives,

$$\begin{aligned}\hat{U}(t) &= \prod_{\alpha} \left[\mathbb{1} + (-i\omega_{\alpha} |\alpha\rangle\langle\alpha|t) + \frac{(-i\omega_{\alpha} |\alpha\rangle\langle\alpha|t)^2}{2!} + \cdots \right] \\ &= \prod_{\alpha} \left[\mathbb{1} + |\alpha\rangle\langle\alpha| \left(i\omega_{\alpha}t + \frac{(i\omega_{\alpha}t)^2}{2!} + \cdots \right) \right] \\ &= \prod_{\alpha} [\mathbb{1} + (e^{-i\omega_{\alpha}t} - 1) |\alpha\rangle\langle\alpha|],\end{aligned}\tag{E.3}$$

where we have used the fact that $|\alpha\rangle\langle\alpha|$ is a projection operator such that $(|\alpha\rangle\langle\alpha|)^2 = |\alpha\rangle\langle\alpha|$. We then perform the unitary transformation to transfer the Hamiltonian into an interaction picture where the effective Hamiltonian reads $H_I(t) = \hat{U}^\dagger(t)H_{\text{off-diag}}\hat{U}(t)$. After termwise application, the interaction picture Hamiltonian then reads,

$$\begin{aligned}H_I &= \sum_{\alpha,\beta} \left\{ \mathbb{1} + (e^{i\omega_{\alpha}t} - 1)|\alpha\rangle\langle\beta| \right\} h_{\alpha,\beta} |\alpha\rangle\langle\beta| \left\{ \mathbb{1} + (e^{-i\omega_{\beta}t} - 1)|\beta\rangle\langle\beta| \right\} \\ &= \sum_{\alpha,\beta} h_{\alpha,\beta} \left\{ \mathbb{1}|\alpha\rangle\langle\beta|\mathbb{1} + (e^{i\omega_{\alpha}t} - 1)|\alpha\rangle\langle\beta|\mathbb{1} + \right. \\ &\quad \left. + \mathbb{1}(e^{-i\omega_{\beta}t} - 1)|\alpha\rangle\langle\beta| + (e^{i\omega_{\alpha}t} - 1)(e^{-i\omega_{\beta}t} - 1)|\alpha\rangle\langle\beta| \right\} \\ &= \sum_{\alpha,\beta} h_{\alpha,\beta} |\alpha\rangle\langle\beta| \left\{ 1 + e^{i\omega_{\alpha}t} - 1 + e^{-i\omega_{\beta}t} - 1 + e^{i\omega_{\alpha}t}e^{-i\omega_{\beta}t} - e^{i\omega_{\alpha}t} - e^{-i\omega_{\beta}t} + 1 \right\} \\ &= \sum_{\alpha,\beta} h_{\alpha,\beta} e^{-i(\omega_{\beta}-\omega_{\alpha})t} |\alpha\rangle\langle\beta|,\end{aligned}\tag{E.4}$$

again with $\omega_{\alpha} = \langle\alpha|H_{\text{diag}}|\alpha\rangle$, $h_{\alpha,\beta} = \langle\alpha|H_{\text{off-diag}}|\beta\rangle$ and $\alpha \neq \beta$. By transforming into the interaction picture, the Hamiltonian $H_I(t)$ is now time-dependent. We will then continue to derive the master equation in the interaction picture.

E.2 The von Neumann Equation in the Interaction Picture

The von Neumann equation can be derived starting from the Schrödinger equation in the interaction picture,

$$i\partial_t|\psi_I\rangle = H_I|\psi_I\rangle, \quad (\text{E.5})$$

where $|\psi_I\rangle$ is the time-dependent state vector in the interaction picture, i.e. $|\psi_I\rangle = \hat{U}^\dagger|\psi_S\rangle$ with $|\psi_S\rangle$ being the state vector in the Schrödinger picture, and we have set $\hbar = 1$. Since the Hamiltonian, H_I is hermitian, one can also write

$$-i\partial_t\langle\psi_I| = \langle\psi_I|H_I. \quad (\text{E.6})$$

Taking the derivatives of the density operator, $\rho(t) = |\psi_I\rangle\langle\psi_I|$ with respect to t , one finds that

$$\begin{aligned} \partial_t\rho(t) &= \partial_t(|\psi_I\rangle\langle\psi_I|) \\ &= (\partial_t|\psi_I\rangle)\langle\psi_I| + |\psi_I\rangle(\partial_t\langle\psi_I|). \end{aligned} \quad (\text{E.7})$$

Now substitute the Schrödinger equation for the wavefunction into the above equation, one finds

$$\begin{aligned} \partial_t\rho(t) &= -iH_I|\psi_I\rangle\langle\psi_I| + i|\psi_I\rangle\langle\psi_I|H_I \\ &= -i[H_I\rho(t) - \rho(t)H_I] \\ &= -i[H_I, \rho(t)], \end{aligned} \quad (\text{E.8})$$

which is known as the von Neumann equation. Formally integrating both sides of the equation from 0 to t gives,

$$\rho(t) - \rho(0) = -i \int_0^t ds [H_I(s), \rho(s)]. \quad (\text{E.9})$$

Rearrange the equation and inserting $\rho(t)$ into the right-hand-side of the von Neumann equation gives

$$\dot{\rho} = -i[H_I(t), \rho(0)] - \int_0^t ds [H_I(t), [H_I(s), \rho(s)]]. \quad (\text{E.10})$$

In principle, one can repeatedly make the substitution of $\rho(s)$ into the commutator and obtain an equation containing higher orders. However, we will only consider the above second order process here as it is sufficient to describe dynamics of the system we consider in the main text.

E.3 An Exact master Equation

The expectation value of an arbitrary observable, \hat{O} in terms of the density matrix is given as,

$$\langle \hat{O} \rangle = \text{Tr}(\rho \hat{O}). \quad (\text{E.11})$$

Using the integral form of the von Neumann equation derived in Eq. (E.10), one can write the time evolution of \hat{O} as,

$$\begin{aligned} \partial_t \langle \hat{O} \rangle_t &= \partial_t \text{Tr}(\rho \hat{O}) \\ &= \text{Tr}(\dot{\rho} \hat{O}) \\ &= -\text{Tr}\{i\hat{O}[H_I(t), \rho(0)]\} - \int_0^t ds \text{Tr}\{\hat{O}[H_I(t), [H_I(s), \rho(s)]]\}, \end{aligned} \quad (\text{E.12})$$

where we have used the cyclic property of trace to move \hat{O} in the front. Expanding the first commutator and using cyclic property of trace again, one finds that,

$$\begin{aligned} -\text{Tr}\{i\hat{O}[H_I(t), \rho(0)]\} &= -i\text{Tr}\{\hat{O}H_I\rho(0) - \hat{O}\rho(0)H_I\} \\ &= -i\text{Tr}\{\rho(0)\hat{O}H_I - \hat{O}\rho(0)H_I\} \\ &= -i\text{Tr}\{[\rho(0), \hat{O}]H_I\}. \end{aligned} \quad (\text{E.13})$$

Thus, if one chooses the observable \hat{O} and the initial state to be commute, one can eventually neglect the first term in Eq. (E.12). Expanding the commutators in the second term in Eq. (E.12), and moving ρ terms to the most right, one finds,

$$\begin{aligned} \partial_t \langle \hat{O} \rangle_t &= -\int_0^t ds \text{Tr}\{\hat{O}H_I(t)H_I(s)\rho(s) + H_I(s)H_I(t)\hat{O}\rho(s) - \\ &\quad -H_I(s)\hat{O}H_I(t)\rho(s) - H_I(t)\hat{O}H_I(s)\rho(s)\}. \end{aligned} \quad (\text{E.14})$$

Up to now, we have derived an exact master equation describing the temporal behaviour of an arbitrary observable, \hat{O} .

Appendix F

Partition Function of a Hard-trimer Gas

The partition function of hard-rods can be calculated using the transfer matrix method [87]. In this section, we will calculate the partition function of hard rods with $\lambda = 2$, i.e. hard-trimers, by using the transfer matrix method. For such a blockade radius, the Hamiltonian is given by,

$$H_{\text{hard-trimer}} = \sum_k^L (V n_k n_{k+1} + W n_k n_{k+2}) - 2 \ln(\xi) \sum_k^L n_k \quad (\text{F.1})$$

which considers both nearest and next-nearest neighbours interactions with $V \rightarrow \infty$ and $W \rightarrow \infty$. $2 \ln(\xi)$ acts as an effective chemical potential. The partition function of the Hamiltonian can be calculated as,

$$\begin{aligned} Z_{\text{trimer}} &= \text{Tr} [e^{-H_{\text{hard-trimer}}}] \\ &= \sum_{n_1 n_2} \sum_{n_3 n_4} \dots \sum_{n_{L-1} n_L} \\ &\quad \left\{ e^{-\left[\frac{V}{2}(n_1 n_2 + 2n_2 n_3 + n_3 n_4) + W(n_1 n_3 + n_2 n_4) + \ln(\xi)(n_1 + n_2 + n_3 + n_4)\right]} \right\} \cdot \\ &\quad \cdot \left\{ e^{-\left[\frac{V}{2}(n_3 n_4 + 2n_4 n_5 + n_5 n_6) + W(n_3 n_5 + n_4 n_6) + \ln(\xi)(n_3 + n_4 + n_5 + n_6)\right]} \right\} \dots \\ &\quad \dots \cdot \left\{ e^{-\left[\frac{V}{2}(n_{L-1} n_L + 2n_L n_1 + n_1 n_2) + W(n_{L-1} n_1 + n_L n_2) + \ln(\xi)(n_{L-1} + n_L + n_1 + n_2)\right]} \right\}, \end{aligned} \quad (\text{F.2})$$

where we have expanded the exponential of the Hamiltonian in such a way that each bracket contains terms with four different indices n_i to n_{i+3} and the next bracket starts from n_{i+2} . The factor of one-half in the front ensures no double counting. This allows us to express the trace in terms of series of sums $\sum_{n_1 n_2} \sum_{n_3 n_4} \dots \sum_{n_{L-1} n_L}$ where we have grouped every two indices as an effective

new index. The new index has four degrees of freedom, i.e. $n_1 n_2 = 1, 1; 1, 0; 0, 1; 0, 0$. However, in the limit of $V \rightarrow \infty$, one can exclude the configuration $n_1 n_2 = 1, 1$. Now, we can treat each bracket as a matrix \mathbf{T} with $n_i n_{i+1}$ being the labels of the matrix elements, i.e.,

$$T_{n_1 n_2, n_3 n_4} = e^{-[\frac{V}{2}(n_1 n_2 + 2n_2 n_3 + n_3 n_4) + W(n_1 n_3 + n_2 n_4) + \ln(\xi)(n_1 + n_2 + n_3 + n_4)]}. \quad (\text{F.3})$$

Then, taking into account the three possible configurations of the indices, one can write out the matrix as

$$\mathbf{T}_{n_1 n_2, n_3 n_4} = \begin{pmatrix} T_{10,10} & T_{10,01} & T_{10,00} \\ T_{01,10} & T_{01,01} & T_{01,00} \\ T_{00,10} & T_{00,01} & T_{00,00} \end{pmatrix} = \begin{pmatrix} \xi^2 e^{-W} & \xi^2 & \xi \\ \xi^2 e^{-V} & \xi^2 e^{-W} & \xi \\ \xi & \xi & 1 \end{pmatrix}. \quad (\text{F.4})$$

Notice that if the $n_1 n_2 = 1, 1$ configuration is not excluded, the transfer matrix will be a 4-by-4 matrix with first row and first column yielding a zero entry in the nearest neighbour blockade regime, i.e. $e^{-V} \rightarrow 0$ and

$$e^{-W} \rightarrow 0$$

. The exclusion of this configuration simplifies the calculation since it reduces the matrix size. The partition function can then be calculated,

$$Z_{\text{trimer}} = \sum_{n_1 n_2} \sum_{n_3 n_4} \cdots \sum_{n_{L-1} n_L} T_{n_1 n_2, n_3 n_4} T_{n_3 n_4, n_5 n_6} \cdots T_{n_{L-1} n_L, n_1 n_2}. \quad (\text{F.5})$$

The sums are simply matrix multiplication since $A_{i,j} = \sum_k B_{i,k} C_{k,j}$ with matrix-A is the product of matrix-B and C, i.e. $\mathbf{A} = \mathbf{B} \cdot \mathbf{C}$. Since the matrix element of the matrix \mathbf{T} only depends on the possible configurations that $n_i n_{i+1}$ can take and is independent of the what value of i takes, one can write the partition function as,

$$Z_{\text{trimer}} = \sum_{n_1 n_2} T_{n_1 n_2, n_1 n_2}^{L/2} = \text{Tr}(\mathbf{T}^{L/2}), \quad (\text{F.6})$$

where the matrix \mathbf{T} is usually named as transfer matrix. The power $L/2$ arises from the summing index, which runs through odd numbers only and the summation is nothing but a trace since $\text{Tr} \mathbf{A} = \sum_i A_{ii}$. To compute $\mathbf{T}^{L/2}$, it is convenient to diagonalise the transfer matrix first. In the limit $V, W \rightarrow \infty$, and introducing

fugacity defined as $z \equiv \xi^2$. The analytical form of the partition function reads,

$$\begin{aligned}
Z_{\text{trimer}} = & 2^{-L} 3^{-L/2} \left\{ \left[4 - \frac{4(-2)^{1/3}(1+6z)}{\eta(z)^{1/3}} + 2(-2)^{2/3}\eta(z)^{1/3} \right]^{L/2} \right. \\
& + 2^{L/2} \left[2 + \frac{2(2)^{1/3}(1+6z)}{\eta(z)^{1/3}} + 2^{2/3}\eta(z)^{1/3} \right]^{L/2} \\
& \left. + \left[4 + \frac{4(-1)^{2/3}(2)^{1/3}(1+6z)}{\eta(z)^{1/3}} + 2(-1)^{1/3}(2)^{2/3}\eta(z)^{1/3} \right]^{L/2} \right\} \quad (\text{F.7})
\end{aligned}$$

, with $\eta(z) = (2 + 9z(2 + 3z) + 3\sqrt{3z^3(4 + 27z^2)})^{\frac{1}{3}}$. Notice that in the limit where $L \rightarrow \infty$, the first term and the last term (square bracket) are vanishingly small compared to the middle term due to the $2^{L/2}$ pre-factor of the middle term.

Bibliography

- [1] I. Bloch, J. Dalibard, and W. Zwerger. Many-body physics with ultracold gases. *Rev. Mod. Phys.*, 80:885–964, Jul 2008.
- [2] M. H. Anderson, J. R. Ensher, M. R. Matthews, C. E. Wieman, and E. A. Cornell. Observation of bose-einstein condensation in a dilute atomic vapor. *Science*, 269(5221):198–201, 1995.
- [3] C. Bradley, C. Sackett, J. Tollett, and R. Hulet. Evidence of bose-einstein condensation in an atomic gas with attractive interactions. *Phys. Rev. Lett.*, 75:1687–1690, Aug 1995.
- [4] K. Davis, M. Mewes, M. Andrews, N. van Druten, D. Durfee, D. Kurn, and W. Ketterle. Bose-einstein condensation in a gas of sodium atoms. *Phys. Rev. Lett.*, 75:3969–3973, Nov 1995.
- [5] B. DeMarco and D. S. Jin. Onset of fermi degeneracy in a trapped atomic gas. *Science*, 285(5434):1703–1706, 1999.
- [6] M. Greiner, O. Mandel, T. Esslinger, T. W. Hansch, and I. Bloch. Quantum phase transition from a superfluid to a mott insulator in a gas of ultracold atoms. *Nature*, 415(6867):39–44, 01 2002.
- [7] C. Regal, M. Greiner, and D. Jin. Observation of resonance condensation of fermionic atom pairs. *Phys. Rev. Lett.*, 92:040403, Jan 2004.
- [8] M. Bartenstein, A. Altmeyer, S. Riedl, S. Jochim, C. Chin, J. Denschlag, and R. Grimm. Crossover from a molecular bose-einstein condensate to a degenerate fermi gas. *Phys. Rev. Lett.*, 92:120401, Mar 2004.
- [9] T. Bourdel, L. Khaykovich, J. Cubizolles, J. Zhang, F. Chevy, M. Teichmann, L. Tarruell, S. Kokkelmans, and C. Salomon. Experimental study of the bec-bcs crossover region in lithium 6. *Phys. Rev. Lett.*, 93:050401, Jul 2004.

- [10] J. Barrow-Green. *Poincaré and the Three Body Problem*. History of mathematics. American Mathematical Society, 1997.
- [11] A. Chenciner. Three body problem. *Scholarpedia*, 2(10):2111, 2007.
- [12] H. Behte. Theorie der metalle. erster teil. eigenwerte und eigenfunktionen der linearen atomischen kette. *Z. Phys.*, 71:205–226, 1931.
- [13] E. Lieb, T. Schultz, and D. Mattis. Two soluble models of an antiferromagnetic chain. *Annals of Physics*, 16(3):407–466, 1961.
- [14] C. K. Majumdar and D. K. Ghosh. On nextnearestneighbor interaction in linear chain. i. *Journal of Mathematical Physics*, 10(8):1388–1398, 1969.
- [15] I. Affleck, T. Kennedy, E. Lieb, and H. Tasaki. Rigorous results on valence-bond ground states in antiferromagnets. *Phys. Rev. Lett.*, 59:799–802, Aug 1987.
- [16] S. White. Density matrix formulation for quantum renormalization groups. *Phys. Rev. Lett.*, 69:2863–2866, Nov 1992.
- [17] P. Hohenberg and W. Kohn. Inhomogeneous electron gas. *Phys. Rev.*, 136: B864–B871, Nov 1964.
- [18] M. Plenio and P. Knight. The quantum-jump approach to dissipative dynamics in quantum optics. *Rev. Mod. Phys.*, 70:101–144, Jan 1998.
- [19] T. Gallagher. *Rydberg Atoms*. Cambridge University Press, 1994.
- [20] T. F. Gallagher. Rydberg atoms. *Reports on Progress in Physics*, 51(2):143, 1988.
- [21] M. Viteau, M. G. Bason, J. Radogostowicz, N. Malossi, D. Ciampini, O. Morsch, and E. Arimondo. Rydberg excitations in bose-einstein condensates in quasi-one-dimensional potentials and optical lattices. *Phys. Rev. Lett.*, 107:060402, 2011.
- [22] I. Bloch. Ultracold quantum gases in optical lattices. *Nat Phys*, 1(1):23–30, 10 2005.
- [23] D. Jaksch, J. I. Cirac, P. Zoller, S. L. Rolston, R. Côté, and M. D. Lukin. Fast quantum gates for neutral atoms. *Phys. Rev. Lett.*, 85:2208–2211, Sep 2000.

- [24] L. Isenhower, E. Urban, X. Zhang, A. Gill, T. Henage, T. Johnson, T. Walker, and M. Saffman. Demonstration of a neutral atom controlled-not quantum gate. *Phys. Rev. Lett.*, 104:010503, Jan 2010.
- [25] T. Wilk, A. Gaëtan, C. Evellin, J. Wolters, Y. Miroshnychenko, P. Grangier, and A. Browaeys. Entanglement of two individual neutral atoms using rydberg blockade. *Phys. Rev. Lett.*, 104:010502, Jan 2010.
- [26] R. Heidemann, U. Raitzsch, V. Bendkowsky, B. Butscher, R. Löw, L. Santos, and T. Pfau. Evidence for coherent collective rydberg excitation in the strong blockade regime. *Phys. Rev. Lett.*, 99:163601, Oct 2007.
- [27] M. Reetz-Lamour, T. Amthor, J. Deiglmayr, and M. Weidemüller. Rabi oscillations and excitation trapping in the coherent excitation of a mesoscopic frozen rydberg gas. *Phys. Rev. Lett.*, 100:253001, Jun 2008.
- [28] E. Urban, T. A. Johnson, T. Henage, L. Isenhower, D. D. Yavuz, T. G. Walker, and M. Saffman. Observation of rydberg blockade between two atoms. *Nat Phys*, 5(2):110–114, 02 2009.
- [29] A. Gaetan, Y. Miroshnychenko, T. Wilk, A. Chotia, M. Viteau, D. Comparat, P. Pillet, A. Browaeys, and P. Grangier. Observation of collective excitation of two individual atoms in the rydberg blockade regime. *Nature Physics*, 5(2):115–118, 2009.
- [30] H. Weimer, R. Löw, T. Pfau, and H. P. Büchler. Quantum critical behavior in strongly interacting rydberg gases. *Phys. Rev. Lett.*, 101:250601, Dec 2008.
- [31] I. Lesanovsky. Many-body spin interactions and the ground state of a dense Rydberg lattice gas. *Phys. Rev. Lett.*, 106:025301, 2011.
- [32] S. Ji, C. Ates, and I. Lesanovsky. Two-dimensional rydberg gases and the quantum hard-squares model. *Phys. Rev. Lett.*, 107:060406, Aug 2011.
- [33] E. Sela, M. Punk, and M. Garst. Dislocation-mediated melting of one-dimensional rydberg crystals. *Phys. Rev. B*, 84:085434, 2011.
- [34] A. Lauer, D. Muth, and M. Fleischhauer. Transport-induced melting of crystals of rydberg dressed atoms in a one-dimensional lattice. *New Journal of Physics*, 14(9):095009, 2012.
- [35] W. Zeller, M. Mayle, T. Bonato, G. Reinelt, and P. Schmelcher. Spectra and ground states of one- and two-dimensional laser-driven lattices of ultracold rydberg atoms. *Phys. Rev. A*, 85:063603, Jun 2012.

- [36] S. Ji, C. Ates, J. P. Garrahan, and I. Lesanovsky. Equilibration of quantum hard rods in one dimension. *Journal of Statistical Mechanics: Theory and Experiment*, 2013(02):P02005, 2013.
- [37] K. Saha, S. Sinha, and K. Sengupta. Phases and collective modes of rydberg atoms in an optical lattice. *Phys. Rev. A*, 89:023618, Feb 2014.
- [38] I. Lesanovsky. Liquid ground state, gap, and excited states of a strongly correlated spin chain. *Phys. Rev. Lett.*, 108:105301, 2012.
- [39] H. Katsura. Existence of an energy gap in a one-dimensional lesanovsky model. *Phys. Rev. A*, 88:065602, Dec 2013.
- [40] C. Ates and I. Lesanovsky. Entropic enhancement of spatial correlations in a laser-driven Rydberg gas. *Phys. Rev. A*, 86:013408, 2012.
- [41] E. Levi and I. Lesanovsky. Non-classical correlations in a class of spin chains with long-range interactions and exactly solvable ground states. *New Journal of Physics*, 16(9):093053, 2014.
- [42] R. M. W. van Bijnen, S. Smit, K. A. H. van Leeuwen, E. J. D. Vredenburg, and S. J. J. M. F. Kokkelmans. Adiabatic formation of rydberg crystals with chirped laser pulses. *Journal of Physics B: Atomic, Molecular and Optical Physics*, 44(18):184008, 2011.
- [43] B. Olmos, R. Gonzalez-Ferez, I. Lesanovsky, and L. Velazquez. Universal time evolution of a Rydberg lattice gas with perfect blockade. *Journal of Physics A: Mathematical and Theoretical*, 45:325301, 2012.
- [44] C. Ates, J. P. Garrahan, and I. Lesanovsky. Thermalization of a strongly interacting closed spin system: From coherent many-body dynamics to a fokker-planck equation. *Phys. Rev. Lett.*, 108:110603, 2012.
- [45] J. Schachenmayer, I. Lesanovsky, A. Micheli, and A. J. Daley. Dynamical crystal creation with polar molecules or rydberg atoms in optical lattices. *New Journal of Physics*, 12(10):103044, 2010.
- [46] T. Pohl, E. Demler, and M. D. Lukin. Dynamical crystallization in the dipole blockade of ultracold atoms. *Phys. Rev. Lett.*, 104:043002, 2010.
- [47] G. Pupillo, A. Micheli, M. Boninsegni, I. Lesanovsky, and P. Zoller. Strongly correlated gases of rydberg-dressed atoms: quantum and classical dynamics. *Physical review letters*, 104(22):223002, 2010.

- [48] M. Höning, D. Muth, D. Petrosyan, and M. Fleischhauer. Steady-state crystallization of rydberg excitations in an optically driven lattice gas. *Phys. Rev. A*, 87:023401, Feb 2013.
- [49] D. Petrosyan. Two-dimensional crystals of rydberg excitations in a resonantly driven lattice gas. *Phys. Rev. A*, 88:043431, Oct 2013.
- [50] P. Schauß, J. Zeiher, T. Fukuhara, S. Hild, M. Cheneau, T. Macrì, T. Pohl, I. Bloch, and C. Gross. Dynamical crystallization in a low-dimensional Rydberg gas. *ArXiv e-prints*, April 2014.
- [51] R. J. Baxter. *Exactly Solved Models in Statistical Mechanics*. Academic Press, Ltd., London, 1982.
- [52] S. Ji, C. Ates, J. P. Garrahan, and I. Lesanovsky. Equilibration of quantum hard rods in one dimension. *Journal of Statistical Mechanics: Theory and Experiment*, 2013(02):P02005, 2013.
- [53] I. Martinson and L. J. Curtis. Janne Rydberg his life and work. *Nuclear Instruments and Methods in Physics Research B*, 235:17–22, July 2005.
- [54] N. Bohr. I. on the constitution of atoms and molecules. *Philosophical Magazine Series 6*, 26(151):1–25, 1913.
- [55] W. C. Mariin and R. Zalubas. Energy levels of sodium, no i through na xi. 1981.
- [56] H. A. Bethe and E. A. Salpeter. *Quantum Mechanics of One and Two Electron Atoms*. Academic Press, 1957.
- [57] A. A. Radzig and B. M. Smirnov. *Reference Data on Atoms, Molecules, and Ions*. Springer, 1985.
- [58] R. Jastrow. On the rydberg-ritz formula in quantum mechanics. *Phys. Rev.*, 73:60–67, Jan 1948.
- [59] B. Sanguinetti, H. O. Majeed, M. L. Jones, and B. T. H. Varcoe. Precision measurements of quantum defects in the $n p 3/2$ rydberg states of 85 rb. *Journal of Physics B: Atomic, Molecular and Optical Physics*, 42(16):165004, 2009.
- [60] L. Zhang, Z. Feng, A. Li, J. Zhao, C. Li, and S. Jia. Measurement of quantum defects of $n s$ and $n d$ states using field ionization spectroscopy in ultracold cesium atoms. *Chinese Physics B*, 18(5):1838, 2009.

- [61] D. J. Griffiths. *Introduction to Quantum Mechanics*. Prentice Hall, 2004.
- [62] F. Gounand, M. Hugon, and P. R. Fournier. Radiative lifetimes of highly excited states in rubidium. *J. Phys. France*, 41(2):119–121, 1980.
- [63] A. L. de Oliveira, M. W. Mancini, V. S. Bagnato, and L. G. Marcassa. Measurement of rydberg-state lifetimes using cold trapped atoms. *Phys. Rev. A*, 65:031401, Feb 2002.
- [64] D. M. Cook. *The Theory of the Electromagnetic Field*. Courier Dover, 1975.
- [65] V. A. Davydkin, V. D. Ovsyannikov, and B. A. Zon. Oscillator strengths, polarizabilities, and hyperpolarizabilities of rydberg states. *Laser Physics*, 3(2), 1993.
- [66] P. M. Koch. *Rydberg States of Atoms and Molecules*. Cambridge University Press, 1983.
- [67] A. C. Riviere and D. S. Sweetman. *Atomic Collision Processes*. North Holland, 1964.
- [68] J. E. Bayfield and P. M. Koch. Multiphoton ionization of highly excited hydrogen atoms. *Phys. Rev. Lett.*, 33:258–261, Jul 1974.
- [69] N. F. Ramsey. *Molecular Beams*. Oxford University Press, 1956.
- [70] J. A. Schiavone, D. E. Donohue, D. R. Herrick, and R. S. Freund. Electron-impact excitation of helium: Cross sections, n , and l distributions of high rydberg states. *Phys. Rev. A*, 16:48–61, Jul 1977.
- [71] J. A. Schiavone, S. M. Tarr, and R. S. Freund. Electron-impact excitation of the rare-gas atoms to high-rydberg states. *Phys. Rev. A*, 20:71–81, Jul 1979.
- [72] F. P. Schäfer. *Dye Lasers*. Springer-Verlag, 1990.
- [73] F. J. Duarte and L. W. Hillman. *Dye Laser Principles*. Academic, 1990.
- [74] C. C. Gerry and P. L. Knight. *Introductory Quantum Optics*. Cambridge University Press, 2005.
- [75] J. Deiglmayr, M. Reetz-Lamour, T. Amthor, S. Westermann, A.L. de Oliveira, and M. Weidemller. Coherent excitation of rydberg atoms in an ultracold gas. *Optics Communications*, 264(2):293 – 298, 2006. ISSN 0030-4018.

- [76] L. Béguin, A. Vernier, R. Chicireanu, T. Lahaye, and A. Browaeys. Direct measurement of the van der waals interaction between two rydberg atoms. *Phys. Rev. Lett.*, 110:263201, Jun 2013.
- [77] M. D. Lukin, M. Fleischhauer, R. Cote, L. M. Duan, D. Jaksch, J. I. Cirac, and P. Zoller. Dipole blockade and quantum information processing in mesoscopic atomic ensembles. *Phys. Rev. Lett.*, 87:037901, Jun 2001.
- [78] B. Olmos and I. Lesanovsky. Rydberg rings. *Phys. Chem. Chem. Phys.*, 13:4208–4219, 2011.
- [79] D. Tong, S. M. Farooqi, J. Stanojevic, S. Krishnan, Y. P. Zhang, R. Côté, E. E. Eyler, and P. L. Gould. Local blockade of rydberg excitation in an ultracold gas. *Phys. Rev. Lett.*, 93(6):063001, 2004.
- [80] K. Singer, M. Reetz-Lamour, T. Amthor, L. G. Marcassa, and M. Weidemüller. Suppression of excitation and spectral broadening induced by interactions in a cold gas of rydberg atoms. *Phys. Rev. Lett.*, 93:163001, Oct 2004.
- [81] M. Saffman, T. G. Walker, and K. Mølmer. Quantum information with rydberg atoms. *Rev. Mod. Phys.*, 82:2313–2363, Aug 2010.
- [82] C. Ates, T. Pohl, T. Pattard, and J. M. Rost. Many-body theory of excitation dynamics in an ultracold rydberg gas. *Phys. Rev. A*, 76:013413, 2007.
- [83] W. R. Anderson, J. R. Veale, and T. F. Gallagher. Resonant dipole-dipole energy transfer in a nearly frozen rydberg gas. *Phys. Rev. Lett.*, 80:249–252, Jan 1998.
- [84] I. Mourachko, D. Comparat, F. de Tomasi, A. Fioretti, P. Nosbaum, V. M. Akulin, and P. Pillet. Many-body effects in a frozen rydberg gas. *Phys. Rev. Lett.*, 80:253–256, Jan 1998.
- [85] D. S. Rokhsar and S. A. Kivelson. Superconductivity and the quantum hard-core dimer gas. *Phys. Rev. Lett.*, 61:2376–2379, 1988.
- [86] C. Castelnovo, C. Chamon, C. Mudry, and P. Pujol. From quantum mechanics to classical statistical physics: Generalized rokhsarkivelson hamiltonians and the stochastic matrix form decomposition. *Annals of Physics*, 318(2):316 – 344, 2005. ISSN 0003-4916.

- [87] N. Goldenfield. *Lectures on Phase Transitions and the Renormalization Group*. Westview Press, 1992.
- [88] A. W. Sandvik. Computational studies of quantum spin systems. *AIP Conf.Proc.*, 1297:135, 2010.
- [89] T. F. Gallagher and W. E. Cooke. Interactions of blackbody radiation with atoms. *Phys. Rev. Lett.*, 42:835–839, Mar 1979.
- [90] C. E. Theodosiou. Lifetimes of alkali-metal⁻atom rydberg states. *Phys. Rev. A*, 30:2881–2909, Dec 1984.
- [91] W. P. Spencer, A. G. Vaidyanathan, D. Kleppner, and T. W. Ducas. Measurements of lifetimes of sodium rydberg states in a cooled environment. *Phys. Rev. A*, 24:2513–2517, Nov 1981.
- [92] D B Branden, T Juhasz, T Mahlokozera, C Vesa, R O Wilson, M Zheng, A Kortyna, and D A Tate. Radiative lifetime measurements of rubidium rydberg states. *Journal of Physics B: Atomic, Molecular and Optical Physics*, 43(1):015002, 2010.
- [93] T. A. Johnson, E. Urban, T. Henage, L. Isenhower, D. D. Yavuz, T. G. Walker, and M. Saffman. Rabi oscillations between ground and rydberg states with dipole-dipole atomic interactions. *Phys. Rev. Lett.*, 100:113003, Mar 2008.
- [94] P. Schauß, M. Cheneau, M. Endres, T. Fukuhara, S. Hild, A. Omran, T. Pohl, C. Gross, S. Kuhr, and I. Bloch. Observation of mesoscopic crystalline structures in a two-dimensional Rydberg gas. *arXiv:1209.0944*, 2012.
- [95] A. E. Ferdinand and M. E. Fisher. Bounded and inhomogeneous ising models. i. specific-heat anomaly of a finite lattice. *Phys. Rev.*, 185:832–846, Sep 1969.
- [96] W.F. Wolff and J. Zittartz. Correlations in inhomogeneous ising models. *Zeitschrift fr Physik B Condensed Matter*, 50(2):131–140, 1983. ISSN 0722-3277.
- [97] C. Fan and B. M. McCoy. One-dimensional ising model with random exchange energy. *Phys. Rev.*, 182:614–623, Jun 1969.
- [98] H. Bock, I. Lesanovsky, and P. Schmelcher. Neutral two-body systems in inhomogeneous magnetic fields: the quadrupole configuration. *Journal of Physics B: Atomic, Molecular and Optical Physics*, 38(7):893, 2005.

- [99] D. C. Li and Z. L. Cao. Entanglement in the anisotropic heisenberg xyz model with different dzyaloshinskii-moriya interaction and inhomogeneous magnetic field. *The European Physical Journal D*, 50(2):207–214, 2008. ISSN 1434-6060.
- [100] Y. Ma and S. Chen. Geometric phase and quantum phase transition in an inhomogeneous periodic xy spin- $\frac{1}{2}$ model. *Phys. Rev. A*, 79:022116, Feb 2009.
- [101] V. Gurarie, L. Pollet, N. V. Prokof'ev, B. V. Svistunov, and M. Troyer. Phase diagram of the disordered bose-hubbard model. *Phys. Rev. B*, 80:214519, Dec 2009.
- [102] I. L. Aleiner, B. L. Altshuler, and G. V. Shlyapnikov. A finite-temperature phase transition for disordered weakly interacting bosons in one dimension. *Nat Phys*, 6(11):900–904, 11 2010.
- [103] M. White, M. Pasienski, D. McKay, S. Q. Zhou, D. Ceperley, and B. De-Marco. Strongly interacting bosons in a disordered optical lattice. *Phys. Rev. Lett.*, 102:055301, Feb 2009.
- [104] P. Fendley, K. Sengupta, and S. Sachdev. Competing density-wave orders in a one-dimensional hard-boson model. *Phys. Rev. B*, 69:075106, Feb 2004.
- [105] S. Isaiah and T. R. Lynn. Quasidegenerate perturbation theories. a canonical van vleck formalism and its relationship to other approaches. *The Journal of Chemical Physics*, 73(11):5711–5717, 1980.
- [106] C. N. Yang and C. P. Yang. One-dimensional chain of anisotropic spin-spin interactions. i. proof of bethe's hypothesis for ground state in a finite system. *Phys. Rev.*, 150:321–327, Oct 1966.
- [107] H. Weimer, R. Löw, T. Pfau, and H. P. Büchler. Quantum critical behavior in strongly interacting rydberg gases. *Phys. Rev. Lett.*, 101:250601, 2008.
- [108] R. Löw, H. Weimer, U. Krohn, R. Heidemann, V. Bendkowsky, B. Butscher, H. P. Büchler, and T. Pfau. Universal scaling in a strongly interacting rydberg gas. *Phys. Rev. A*, 80:033422, Sep 2009.
- [109] Shaojin Qin, Michele Fabrizio, Lu Yu, Masaki Oshikawa, and Ian Affleck. Impurity in a luttinger liquid away from half-filling: A numerical study. *Phys. Rev. B*, 56:9766–9774, Oct 1997.

- [110] M. L. Wall, , and L. D. Carr. Dipole-dipole interactions in optical lattices do not follow an inverse cube power law. *New Journal of Physics*, 15(12):123005, 2013.
- [111] I. Lesanovsky and H. Katsura. Interacting fibonacci anyons in a rydberg gas. *Phys. Rev. A*, 86:041601, Oct 2012.
- [112] L. Onsager. Crystal statistics. i. a two-dimensional model with an order-disorder transition. *Phys. Rev.*, 65:117–149, Feb 1944.
- [113] S. Sachdev. *Quantum Phase Transitions*. Cambridge University Press, 2011.
- [114] F. Verstraete, M. M. Wolf, D. Perez-Garcia, and J. I. Cirac. Criticality, the area law, and the computational power of projected entangled pair states. *Phys. Rev. Lett.*, 96:220601, Jun 2006.
- [115] N. Schuch, M. M. Wolf, F. Verstraete, and J. I. Cirac. Computational complexity of projected entangled pair states. *Phys. Rev. Lett.*, 98:140506, Apr 2007.
- [116] X. Chen, B. Zeng, Z. Gu, B. Yoshida, and I. L. Chuang. Gapped two-body hamiltonian whose unique ground state is universal for one-way quantum computation. *Phys. Rev. Lett.*, 102:220501, Jun 2009.
- [117] W. Guo and H. W. J. Blöte. Finite-size analysis of the hard-square lattice gas. *Phys. Rev. E*, 66:046140, Oct 2002.
- [118] D. A. Huse. Tricriticality of interacting hard squares: Some exact results. *Phys. Rev. Lett.*, 49:1121–1124, Oct 1982.
- [119] R. J. Baxter and P. A. Pearce. Hard squares with diagonal attractions. *Journal of Physics A: Mathematical and General*, 16(10):2239, 1983.
- [120] W. M. C. Foulkes, L. Mitas, R. J. Needs, and G. Rajagopal. Quantum monte carlo simulations of solids. *Rev. Mod. Phys.*, 73:33–83, Jan 2001.
- [121] D. M. Ceperley and B. J. Alder. Ground state of the electron gas by a stochastic method. *Phys. Rev. Lett.*, 45:566–569, Aug 1980.
- [122] D. Flamm. History and outlook of statistical physics. *arXiv:physics/9803005*, 1998.
- [123] G. Gallavotti. *Statistical Mechanics: A Short Treatise*. Texts and monographs in physics. Springer, 1999.

- [124] S. Hofferberth, I. Lesanovsky, B. Fischer, T. Schumm, and J. Schmiedmayer. Non-equilibrium coherence dynamics in one-dimensional Bose gases. *Nature*, 449:324, 2007.
- [125] I. Bloch, J. Dalibard, and W. Zwerger. Many-body physics with ultracold gases. *Reviews of Modern Physics*, 80(3):885–964, 07 2008.
- [126] T. Kinoshita, T. Wenger, and D. S. Weiss. A quantum Newton’s cradle. *Nature*, 440:900, 2006.
- [127] J. M. Deutsch. Quantum statistical mechanics in a closed system. *Phys. Rev. A*, 43:2046–2049, Feb 1991.
- [128] M. Srednicki. Chaos and quantum thermalization. *Phys. Rev. E*, 50:888, 1994.
- [129] M. Rigol, V. Dunjko, and M. Olshanii. Thermalization and its mechanism for generic isolated quantum systems. *Nature*, 452:854, 2008.
- [130] M. Eckstein and M. Kollar. Nonthermal Steady States after an Interaction Quench in the Falicov-Kimball Model. *Phys. Rev. Lett.*, 100:120404, 2008.
- [131] A. Pal and D. A. Huse. Many-body localization phase transition. *Phys. Rev. B*, 82:174411, 2010.
- [132] M. Rigol and M. Srednicki. Alternatives to eigenstate thermalization. *Phys. Rev. Lett.*, 108:110601, Mar 2012.
- [133] T. N. Ikeda, Y. Watanabe, and M. Ueda. Eigenstate randomization hypothesis: Why does the long-time average equal the microcanonical average? *Phys. Rev. E*, 84:021130, Aug 2011.
- [134] P. Reimann. Typicality for generalized microcanonical ensembles. *Phys. Rev. Lett.*, 99:160404, Oct 2007.
- [135] D. Comparat and P. Pillet. Dipole blockade in a cold rydberg atomic sample [invited]. *JOSA B*, 27(6):A208–A232, 2010.
- [136] R. Bowley and M. Sánchez. *Introductory Statistical Mechanics*. Oxford science publications. Clarendon Press, 1999.
- [137] G. Chartrand. *Introductory Graph Theory*. Dover Publications, 1985.
- [138] C. W. Gardiner. *Handbook of Stochastic Methods*. Springer, New York, 2004.

- [139] L. Mandel. Physical significance of operators in quantum optics. *Phys. Rev.*, 136:B1221–B1224, Nov 1964.
- [140] M. Viteau, P. Huillery, M. G. Bason, N. Malossi, D. Ciampini, O. Morsch, E. Arimondo, D. Comparat, and P. Pillet. Cooperative excitation and many-body interactions in a cold rydberg gas. *Phys. Rev. Lett.*, 109:053002, 2012.
- [141] I. Bengtsson and K. Życzkowski. *Geometry of Quantum States: An Introduction to Quantum Entanglement*. Cambridge University Press, 2006.
- [142] J. Berges, Sz. Borsányi, and C. Wetterich. Prethermalization. *Phys. Rev. Lett.*, 93:142002, Sep 2004.
- [143] M. Kollar, F. A. Wolf, and M. Eckstein. Generalized gibbs ensemble prediction of prethermalization plateaus and their relation to nonthermal steady states in integrable systems. *Phys. Rev. B*, 84:054304, Aug 2011.
- [144] M. Gring, M. Kuhnert, T. Langen, T. Kitagawa, B. Rauer, M. Schreitl, I. Mazets, D. Adu Smith, E. Demler, and J. Schmiedmayer. Relaxation and prethermalization in an isolated quantum system. *Science*, 337(6100):1318–1322, 2012.
- [145] S. K. Lando. *Lectures on Generating Functions*. Student mathematical library. American Mathematical Soc., 2003.